ADVANCED NONLINEAR ANALYSIS OF MASONRY ARCH BRIDGES

A thesis submitted to Imperial College London in partial fulfilment of the requirements for the degree of Doctor of Philosophy in the Faculty of Engineering

by

Yanyang Zhang

BEng, MSc

Computational Structural Mechanics Group

Department of Civil and Environmental Engineering

Imperial College London

London, SW7 2AZ

January 2015

This work is dedicated to my parents

Qiang Zhang and Hongyan Wang

DECLARATION

The work presented in this thesis was carried out in the Structures Section of the Department of Civil and Environmental Engineering at Imperial College London. This thesis is the results of my own work and any quotation from, or description of the work of others is acknowledged herein by reference to the sources, whether published or unpublished.

This thesis is not the same as any that I have submitted for any degree, diploma or other qualification at any other university. No part of this document has been or is being concurrently submitted for any such degree, diploma or other qualification.

Yanyang Zhang

London, January 2015

ABSTRACT

This research investigates the nonlinear response up to collapse of masonry arches and arch bridges using advanced numerical descriptions. Past research has shown that the mesoscale modelling approach for brick-masonry, where bricks and mortar joints are modelled separately, may offer a realistic representation of the mechanical behaviour of masonry components. However, because of the significant computational cost, thus far the use of this modelling strategy has been mainly restricted to 2D analysis of masonry arches and arch bridges. In some cases this may lead to a crude representation of the response which is inherently three-dimensional, especially when the analysed structure is subjected to eccentric loading or is characterised by a complex geometry (e.g. skew arches).

In this work, masonry arches and arch bridges are analysed using a partitioned mesoscale approach, which enables the use of a detailed model for describing material nonlinearity at structural scale. This is combined with a partitioned approach allowing for parallel computation which guarantees computational efficiency. In the 3D mesoscale description, brick units and mortar interfaces are modelled separately accounting for the actual texture and arrangement of masonry. 3D elastic continuum solid elements are used to model brick units while mortar interfaces are modelled by means of 2D nonlinear interface elements. In analysing masonry bridges, the backfill material is modelled as an elasto-plastic continuum, while the physical interface between the continuum and mesoscale domain for masonry is represented by nonlinear zero-thickness interface elements allowing separation and plastic sliding.

The proposed modelling approach has been applied to the analysis of multi-ring square and skew arches and masonry arch bridges. The numerical results, which also include numerical-experimental comparisons, confirm the accuracy of the adopted numerical strategy.

Moreover numerical simulations have been performed to investigate the effects of the arch geometry, loading positions, material characteristics and potential settlements at the supports. The results obtained offer important information and a detailed description on the complex response of these critical structural systems under different loading and boundary conditions.

ACKNOWLEDGEMENTS

Four-year PhD study is one of the most invaluable memories in my life. When I came to write the acknowledgements of my thesis, I realised that there are many people whom I want to thank.

First, I wish to express my thanks to my supervisors Dr Lorenzo Macorini and Professor Bassam A. Izzuddin for their insightful supervision, strong support and constant motivation. Particularly, I want to express my deepest thanks to my principal supervisor Dr Lorenzo Macorini. I appreciate the large amount of time that he spent in supervising my research and his patient guidance in the past four years. He gave me profound encouragement and assistance during my low points.

Furthermore, I wish to thank my parents, Qiang Zhang and Hongyan Wang, who raised me up and provided utmost solicitude for me. Thanks for their understanding, encouragement, care and sacrifices throughout my life. Without their unconditional love, I could not indulge in my study and enjoy the fullest research life. I love you all.

Moreover, I wish to express my special thanks to my boyfriend Dr Libin Fang for his truly, deeply love and concern. His company and support encouraged me to overcome difficulties. All memories spent with him are the most priceless treasure in my life.

I also would like to thank all my best friends, Rui Sun, Xin Liu, Yating Liang, Jiaping Gu, Jie Wang, Ou Zhao, and Wei Qiu at Imperial College London. Their great help during my four-year study is very much appreciated. They lightened my PhD life and made it more meaningful.

I am particularly grateful for the help from Marcus Heo Nong H N and Alan Rodriguez Villares. Their contribution is greatly valuable for my research.

Last but not least, I would like to thank my colleagues H. Francisco Brás Xavier, Alejandro Barrero Hamed Zolghadr Jahromi, Shirin Jowhari Moghadam, Amir Khojasteh and Eleni Minga. Thanks for their invaluable advice either in my research work or my life.

TABLE OF CONTENTS

LIST OF FIGURES

LIST OF TABLES

LIST OF SYMBOLS

Latin upper case letters

C	Cohesion in equation 3-3
D	Material parameter governing the shape of the cap surface; elastic stiffness matrix
DL	Dead load
E, E_m, E_f, E_b	Young's modulus
F_{MC}	Classic Mohr-Coulomb function
F_{SHMC}	Hyperbolic Mohr-Coulomb function
G_{fI}, G_{f1}	Mode-I (tension) fracture energy
G_{fII}, G_{f2}	Mode-II (shear) fracture energy
G_m	Mortar shear modulus
H	Height
$\mathbf{I}_6$	6×6 identity matrix
$[\mathbf{J}]_{n,i}$	Jacobian matrix
$\mathbf{K}$	Tangent stiffness matrix
K_{ab}	Abutment stiffness
$K_{e,exp}$	Experimental elastic (initial) stiffness
ΔK_e	Elastic (initial) stiffness

L_d	Length of direct span
LL	Live load
$LL_{u,exp}$	Experimental ultimate load
$LL_{u,num}$	Numerical ultimate load
ΔLL_u	Change of ultimate load
P	Load
P	Projection 7×6 matrix on the six-dimensional stress space
Q	Plastic potential
S	Speed-up
S_{max}	Maximum speed-up
T	Ring thickness
T_m	Wall-clock time for the monolithic simulation
W	Arch width
W_{pl1} (W_{cr1}), W_{pl2}	Distinct historical parameters (plastic works)
X, Y, Z	Descriptors used to indicate the number of subdivisions

Latin lower case letters

c_q	Cohesion in equation 3-27
d_x	Element relative displacements in x direction
d_y	Element relative displacements in y direction
d_z	Element relative displacements in z direction
h_j	Mortar joint thickness

$\boldsymbol{k}_0$	Diagonal elastic stiffness matrix
$k_{n0,}\, k_{t0x,}\, k_{t0y}$	Normal and two tangential stiffness values in matrix $\boldsymbol{k}_0$

Greek lower case letters

$\boldsymbol{\varepsilon}$	Strain vector
$d\boldsymbol{\varepsilon}_n$	Increment of strain vector
$\boldsymbol{\varepsilon}_{pl}$	Plastic deformation vector
$d\boldsymbol{\varepsilon}_{pl,n}$	Increment of plastic deformation vector
$\varepsilon_{pl,VM}$	Equivalent von Mises plastic deformation
α	Radian of each block
σ	Normal stresses
$\sigma_1\,,\ \sigma_2\,,\ \sigma_3$	Principal stresses
σ_c	Compressive strength
σ_m	Mean total stress
σ_t, f_t	Tensile strength
σ_{VM}	Equivalent von Mises stress
$\boldsymbol{\sigma}_n$	Actual stress vector
$\boldsymbol{\sigma}_{trial,n}$	Trial elastic stress vector
$\bar{\sigma}$	Deviatoric stress
$d\lambda_n$	Increment of the plastic multiplier
τ_x	Shear stresses in x direction

τ_y	Shear stresses in y direction
ϕ, φ	Friction angle
θ	Material parameter in equation 3-4; skew angle in Table 3-1; Lode's angle in equation 3-12;
θ_T	Specific transition angle in equation 3-21
v	Poisson's ratio
φ_q	Dilatancy angle
ρ, ρ_b, ρ_f	Density
δ_{im}	Horizontal inward of support
δ_{ss}	Horizontal spread of support
δ_{vs}	Vertical settlement of support

CHAPTER 1

Introduction

1.1 Past and Present

Masonry arch bridges represent a substantial part of existing bridges, which have been built since antiquity with different sizes and construction features. These structural systems are generally made up of a single or multi-span masonry arch, which is the critical structural component supporting the fill material and the road surface. Lateral masonry walls confine the fill and often act as barriers for safety purposes.

The European railway network includes tens of thousands of masonry bridges, where only in the UK about 70,000 masonry bridges are still in service (Ashour & Garrity, 1998). These structures were mainly built from the time of the Romans until the early twentieth century to support the growth of cities and towns and the development of the road, railway and waterway systems. Notable examples of these structures are displayed in Figure 1-1 and 1-2. Figures 1-1 shows a skew masonry arch bridge carrying the existing lines from Heaton Lodge junction towards Mirfield in West Yorkshire. Figure 1-2 presents the Wye Bridge across the River Wye in Monmouth, Wales, which was first erected as a wooden bridge in the Middle Ages, and then was rebuilt between 1615-1617 using masonry with a total length of 71m.

Besides, it was estimated that in China there exists four million masonry arch bridges, many of which were built more than a thousand years ago (Ning & O, 2008). Figure 1-3 displays the world's oldest open-spandrel stone segmental arch bridge, Zhaozhou (Anji) Bridge, which was constructed in the years 595-605. Apparently, such a beautiful ancient bridge is more than a component of the public transportation system, representing a work of engineering art which influenced the design of bridges thereafter. Therefore, most of these old structures not only play an essential role in public transport systems all over the world, but also belong to the engineering and architectural heritage, representing valuable examples of past engineering achievements (McKibbins et al., 2006).

Old masonry bridges were designed according to empirical bases and considering reduced loading. Thus at present, most of these old structures are carrying much heavier traffic loads and undergoing much higher transportation speed, which is far beyond the original design expectation and requirements (McKibbins et al., 2006; Corradi, 1998). In this respect, according to the European Standard, in recent years the maximum allowable gross vehicle weight has increased from 38t to 44t, and the maximum axle load from 10t to 11.5t (Gramsammer, Kerzreho & Odeon, 1999). Therefore, a growing demand to determine their actual capacity under traffic loading condition is to be met over the coming decades, considering also that old masonry bridges may have gradually deteriorated in time. Thus it is becoming also crucial to identify effective strengthening measures to enhance their load capacity and general structural condition (Brencich & Colla, 2002).

In past years, a number of modelling approaches for masonry bridges have been proposed. Most of them are based on the 2D analysis of the main masonry arch, neglecting the interaction among the different structural components. Only recently, the need for using more advanced descriptions to represent the 3D geometry of masonry bridges has been emerging (Brencich, 2009). This has been also confirmed by experimental research (Melbourne et al., 2007; Cavicchi & Gambarotta, 2005; Melbourne & Gilbert, 1995; Melbourne & Walker, 1989; Page, 1989; Walker & Melbourne, 1988; Page, 1987; Hendry et al., 1986b) which has

shown that the response of masonry bridges is strongly influenced by the interaction between the different structural and non-structural components. This confirms that an accurate prediction of the bridge behaviour can only be achieved using advanced numerical tools, which account for the actual geometry and mechanical characteristics, along with the interaction among the main parts of the bridge.

Figure 1-1: Wood lane Bridge, UK

Figure 1-2: Wye Bridge, UK

Figure 1-3: Zhaozhou (Anji) Bridge, China

1.2 Objectives and Scope

The principal aim of this research is to develop and validate numerical modelling strategies for high-fidelity nonlinear analysis of masonry arches and arch bridges, allowing for an accurate response prediction of these complex structural components and heterogeneous systems under monotonic static loading conditions up to collapse.

Past research (McKibbins et al., 2006) has shown that the behaviour of masonry bridges is generally determined by the interaction between different structural and non-structural components, which can be described using three-dimensional (3D) models. Besides, 3D models are also required for analysing skew masonry arches, which are characterised by a complex 3D response associated with the specific masonry arrangement.

Thus far, 3D descriptions for masonry bridges (e.g. Boothby & Roberts, 2001) have been developed mainly using macroscopic approaches for masonry (Lourenço, 1996), which do not allow the representation of the actual anisotropic behaviour and the consideration of potential defects in the brickwork. On the other hand, the use of more detailed mesoscale

strategies for masonry (Lourenço & Rots, 1997; Macorini & Izzuddin, 2011), where the masonry components are modelled independently enabling an accurate description of the actual masonry bond, is too computationally demanding. This renders mesoscale modelling impractical for the analysis of large masonry arch structures when adopting conventional computational resources.

The research objectives of this research can be summarised as follows:

- To develop an advanced 3D mesoscale representation for square and skew brick\block-masonry arches, accounting for material and geometric nonlinearity under static loading conditions, and to verify the accuracy and efficiency of the proposed approach when analysing realistic masonry arch structures.
- To use the developed numerical strategy for masonry arches in nonlinear numerical simulations, providing a deep insight into the complex behaviour of both square and skew arches. Attention is paid not only to behaviour at collapse and the prediction of specific failure modes (e.g. four-hinge mechanism, ring separation, shear sliding etc.) but also to the performance at serviceability, taking into account the influence of the variation of the loading position, critical defects in the brickwork and support movements.
- To develop and validate an advanced 3D modelling approach for accurate nonlinear analysis of masonry arch bridges, allowing for the interaction between different structural and non-structural components (e.g. the arch barrel, the backfill and the spandrel walls).
- To investigate the effects of geometric, material and loading parameters, typical defects in the brickwork and support movements on the static response up to collapse of realistic single-span masonry bridges.

This research will benefit from the use of an advanced mesoscale description for masonry (Macorini & Izzuddin, 2011) and a domain partitioning approach allowing for parallel computation (Macorini & Izzuddin, 2013a)) both recently developed at Imperial College. Previous research (Macorini & Izzuddin, 2013a,b) has shown that the use of partitioned mesoscale modelling for masonry structures, where the mesoscale model is incorporated

within a partitioning strategy to improve computational efficiency, guarantees the accuracy provided by the monolithic mesoscale description in the analysis of large masonry structures.

1.3 Layout of the Thesis

This thesis comprises seven chapters as follows:

Chapter 1 outlines the main objectives and the scope of this research.

Chapter 2 provides a general overview of masonry arch bridges including arch components, construction characteristics and possible types of failure. Various approaches which have been implemented for analysing and assessing masonry arch bridges are then reviewed. Previous efforts devoted to experimental work on full and model scale tests are also summarised. The development of analysis and assessment techniques for masonry arch bridges is then discussed. Following that, previous numerical modelling strategies for masonry, masonry arches and masonry arch bridges based on the finite element method are presented and critically discussed.

In Chapter 3, the advanced numerical modelling approaches for masonry arches and bridges which are used in this research are described. This includes a 3D mesoscale modelling method for representing material nonlinearity in masonry, a partitioned modelling approach based on the use of parallel computing resources, a geometric description for skew arches and a modelling strategy for the interaction between the arch and the backfill.

Chapter 4 considers the validation of the proposed mesoscale description for masonry arches. To check the accuracy of the proposed modelling strategy, numerical results are compared against experimental data on the response of masonry square and skew arches. Numerical studies considering the influence of material properties and the modelling strategy on the response predictions are presented and discussed. Finally, the effectiveness in using a partitioning approach (Macorini & Izzuddin, 2013a) for the mesoscale analysis of masonry arches is investigated.

Chapter 5 presents the results of extensive parametric studies on the behaviour of square and skew masonry arches. The responses of arches characterised by different geometrical characteristics are compared, and the effects on the arch response of (i) the loading position, (ii) defects in the brickwork, (iii) stiffness of the supports and (iv) potential movements at the abutments are investigated.

Chapter 6 presents the results obtained from the use of the proposed modelling strategy for masonry arch bridges. The results obtained using an efficient strip-model are initially discussed. These include numerical experimental comparisons and parametric studies on the influence of the fill material properties, defects in the brickwork, variations in the loading position, geometry of the arch and movements at the abutments. Subsequently, results obtained by using full 3D models are discussed focusing on the transverse behaviour of a brick-masonry bridge. Finally the efficiency provided by the partitioning approach (Macorini & Izzuddin, 2013a) applied to the analysis of masonry bridges is analysed.

Finally, in Chapter 7, conclusions and achievements of this research are summarised followed by recommendations for future work on masonry arch bridges.

CHAPTER 2

Review of Literature

2.1 Introduction

In this chapter, after describing the main types, components and characteristics of masonry arch bridges, previous research aimed at investigating the response up to collapse of these complex structural systems is presented and critically discussed.

Existing masonry bridges were built mainly considering empirical rules in the nineteenth century and well before. At present most of these structures are still in service playing a critical role within the railway and roadway networks in Europe and around the world, while carrying traffic loads substantially higher than those they were designed for. Thus, since after the Second World War, a growing interest in studying their behaviour up to collapse and assessing their ultimate load capacity has developed.

Large experimental programs were carried out, where several full-scale and model-scale bridges were tested under vertical loading. These physical experiments allowed the understanding of the actual failure modes and pointed out the complex interaction between the different bridge components.

The first structural assessment methods were based upon elastic principles providing only an approximate estimate of the load capacity. Afterwards plastic analysis procedures were proposed and only recently, thanks to the tremendous progress of the computational resources,

more advanced numerical modelling strategies have been set out allowing for a more accurate description of the bridge geometry and nonlinear behaviour.

Most of the advanced modelling approaches for masonry bridges consider the use of the finite element method. One-, two- and three-dimensional finite element modelling strategies for masonry bridges have been proposed thus far. Three-dimensional models provide the most realistic description of the complex longitudinal and transverse interaction between the different bridge components, but their use has been limited by the significant computational demand. In any case the accuracy of the numerical results strongly depends upon the ability of the adopted models to describe the nonlinear behaviour of masonry, which is a heterogeneous and anisotropic material comprising brick units and mortar joints. Due to this complex nature, its structural response is dominated not only by the mechanical characteristics of the basic components but also by the specific masonry arrangement.

2.2 Masonry arch bridges

A typical masonry arch bridge comprises different components, which include the arch, the backfill, the abutments, the spandrel and the wing walls (Figure 2.1). A stone arch barrel is built from voussoirs with a keystone in the centre, while brick-masonry arches are made up of one or more rings of bricks (Figure 2-1).

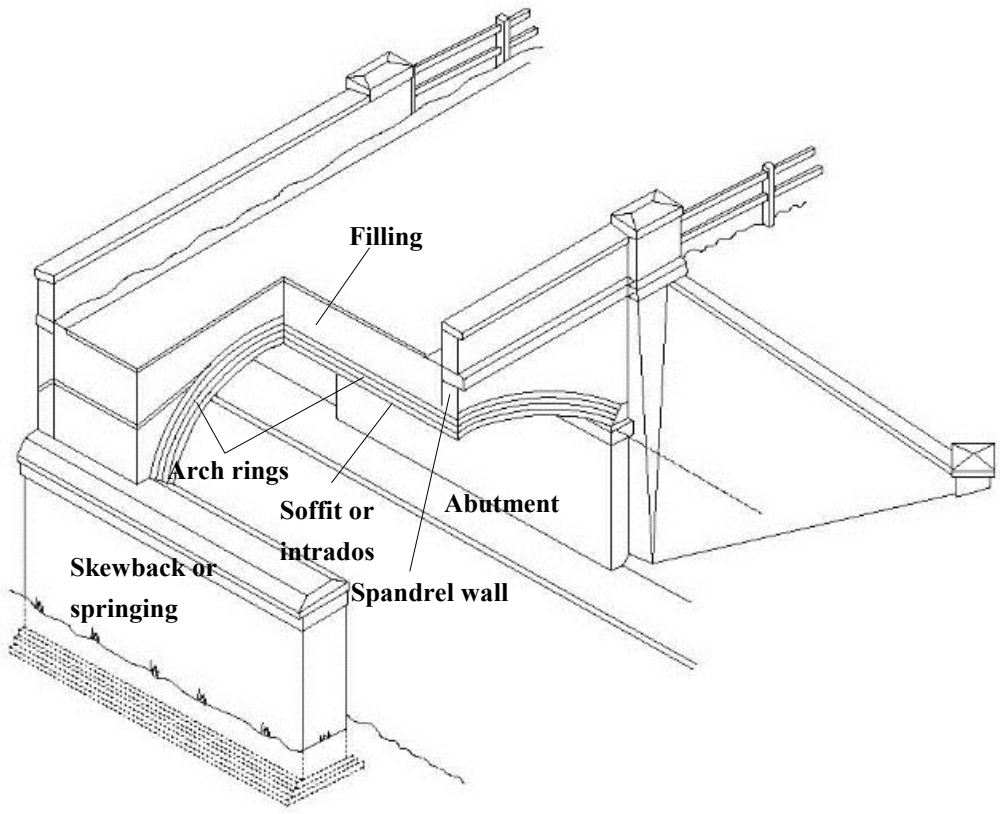

Figure 2-1: Main components in a masonry arch bridge (McKibbins et al., 2006)

(a) Single ring (b) Multi-ring (c) Multi-ring with headers

Figure 2-2: Masonry bond in brick-masonry arches (Melbourne et al., 2007)

Brick arches with small span are usually built with a single ring (Figure 2-2a), but longer arches require two or more rings which are typically bonded using the stretcher or the header method. When using the stretcher method (Figure 2-2b), the bond between adjoining rings is

guaranteed by continuous circumferential mortar joints. Conversely according to the latter construction technique, headers are used to interconnect adjacent rings (Figure 2-2c).

Existing masonry bridges were constructed with different forms (Page, 1993); arch barrels were built in semi-circular, segmental, semi-elliptical, multi-centre circular or parabolic shapes. In all these structures, the voussoir or the bricks at either end of the arch barrel are supported upon the skewback at a surface named springing. The skewback is located at the abutment or the piers (Figure 2-1). The spandrel walls restrain the fill and carry the parapets and also stiffen and strengthen the arch barrel as a whole. The wing walls are built by extending the spandrels on each side of the arch ring to resist the outward pressures from the backfill. The backfill is usually made up of soil materials excavated during the construction of the foundations, examples include clay and limestone. When the bridge span is greater than about 12m, masonry ribs or internal spandrel walls are normally adopted to lighten and stiffen the structure providing resistance to the outward pressure from the backfill.

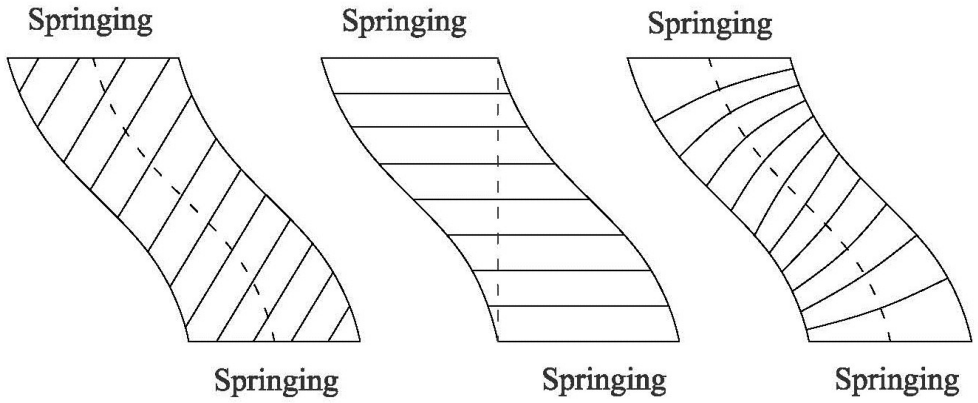

(a) Helicoidal or English method (b) "False" method (c) Orthogonal or French method

Figure 2-3: Cylindrical projection of the soffit of a 45 degree skew arch

In addition to the regular square arch bridges, existing masonry bridges comprise a large number of skew arch bridges. These are characterised by abutments which are parallel to each other but offset to some degree resulting in springings which are not perpendicular to

the edges of the arch (Harvey, 2004). The first skew arch in the British Isles was constructed by Chapman in 1787 (Page, 1993) on the Kildare Canal in Ireland. Chapman devised a design method for skew arches in which the joints between the courses of voussoirs are placed at right angles to the skew of the arch (Figure 2-3a). This method was later named as the Helicoidal or English method. Two decades later, Outram (Page, 1993) built several bridges with up to about 20° skew angles using un-skewed masonry blocks. These bridges were designed with the joints between the courses of voussoirs parallel to the abutments as in Figure 2.3b. This technique for high skew angles is considered as a "false" method, as it can easily lead to unavoidable abutment movements and partial failures (Page, 1993). According to a later method, known as the Orthogonal or the French method (Figure 2-3c), all the voussoirs are perpendicular to the skew of the arch and meet the springing asymptotically. This requires a complex arrangement, where the units must have varying sizes and different shapes posing restriction on the construction material and type of masonry units. For this reason the French method was mainly adopted to build skew arches with ashlar stones but not with brick units. Conversely the arches of most brick-masonry skew bridges were built following the English method, which enables the use of identical units increasing cost efficiency. The main drawback of this construction technique is that it requires untidy edge details for multi-ring skewed brickwork arches.

2.3 Experimental research on masonry arch bridges

A number of physical experiments including model-scale laboratory tests and full-scale on site tests were carried to investigate the response of masonry arches and arch bridges up to collapse. The results from these experimental studies are of paramount importance to understand the real behaviour of the main bridge components (e.g. masonry arches) as well as their interaction, and to identify the critical loading conditions and the actual failure modes. In the following, the results of some relevant experimental studies are presented distinguishing full-scale from model scale tests. Finally the failure mechanisms observed in the tests are discussed.

2.3.1 Load tests on full-scale arches and arch bridges

Since 1953 the Transport Research Laboratory (TRL) has led a research programme in the UK to investigate the behaviour of masonry arch bridges under vertical static loading. Both real bridges and laboratory model bridges were tested up to collapse.

Within this program, Davey (Davey, 1953; Davey, 1949; Davey, 1947) tested three real bridges, where two bridges were loaded at the crown and one bridge at the quarter span. It was found that the latter loading case is the more critical and that the infill contribution significantly increases the loading capacity of the bridge. However Davey observed significant deformations at the abutments which did not behave as perfectly rigid supports.

Hendry et al. (Hendry et al., 1986b; Hendry, Davies & Royles, 1985) carried out full scale tests to collapse on two single span bridges, the Bargower and the Bridgemill Bridge. The Bridgemill Bridge was a square bridge constructed with a parabolic shape and 18.3m span, while the Bargower bridge was characterised by a 10m span, a 16 degree skew and a segmental shape. In the Bridgemill Bridge test, a line load across the full width of the arch was applied at the quarter span; progressive damage in the lateral walls and in the arch was observed by increasing the load, and collapse occurred when a mechanism with four radial cracks formed in the arch (Figure 2-4). The Bargower Bridge was tested applying a line load at the third span; in this case longitudinal and radial cracks developed within the arch. However a hinge mechanism did not form as the arch was restrained laterally by rock material above the abutments. The bridge collapse was caused by a local compressive failure in the arch, close to where the load was applied.

Figure 2-4: Collapse of the Prestwood Bridge due to a four-hinge mechanism (Page, 1993)

Page (Page, 1993; Page, 1989; Page, 1987) performed full scale destructive tests on six redundant bridges. One of the experiments on a segmental single-span bridge at Prestwood was considered to check the adequacy of the plastic mechanism method (details are discussed in 2.4.3). It was found that the actual collapse mode was in good agreement with that predicted by the 2D plastic assessment method. In this case the stiffening contribution of the spandrel walls was not significant, as an early separation of the two lateral walls took place because of existing defects in the bridge.

The early experimental studies on the response of masonry bridges were focused on the analysis of the longitudinal behaviour of the arch barrels interacting with the backfill. More recently, Fanning and Boothby (Fanning & Boothby, 2001) considered the transverse effects due to the interaction with the spandrel walls. Analysing the results of experimental tests on real stone masonry bridges under service loading (static truck loading), it was observed that the stiffening effect of lateral walls leads to transverse bending in the arch barrel which, at higher loading levels, may cause the development of longitudinal cracks in the arch.

Concerning experimental studies on masonry bridge components, Wang (Wang, 2004) carried out a series of laboratory tests on full scale brick-masonry arches, including both square and skew arches. Wide square arches built using strong and weak brick units were tested applying point loads. Moreover different support conditions were considered, and the response of arches supported at the two abutments was compared to that of similar arches propped also along the span by point supports. The results obtained showed some important features of the 3D response of masonry arches, as a non-uniform distribution of vertical displacements along the arch width. Within the same experimental campaign, two realistic brick-masonry arches with 45 degree skew angle were analysed applying patch loads which were increased up to collapse. It was shown that the three-dimensional failure mode of skew arches which is characterised by the development of five radial cracks (hinges) is different from the typical four-hinge mechanism of square arches.

2.3.2 Load tests on model scale bridges

Pippard collaborated with other researchers on a series of experiments (Pippard & Baker, 1968; Pippard & Chitty, 1941; Pippard, Tranter & Chitty, 1936). Masonry arches with lime-stone or concrete voussoirs bonded by cement mortar or lime mortar were loaded up to collapse. The backfill contribution was allowed for by "hanging" some additional weights on the arches. The experimental results were used to validate an assessment method developed by the same authors.

More recently a number of bridge model tests were conducted at the University of Edinburgh (Ponniah, Fairfield & Prentice, 1997; Prentice & Ponniah, 1996; Fairfield & Ponniah, 1994; Fairfield & Ponniah, 1993) to investigate the beneficial contribution of the backfill to the ultimate loading capacity of masonry bridges.

The interaction between the different bridge components was studied by Royles and Hendry, who carried out a series of collapse tests on model scale arch bridge (Royles & Hendry, 1991). The experimental results clearly highlighted the limitations of simplified 2D

assessment methods for masonry bridges which disregard the interaction among the arch barrel, the spandrel and wing walls, and the backfill material.

Finally it is important to mention the significant contribution made by Melbourne and his collaborators towards the understanding of the actual behaviour of masonry bridges (Melbourne, 1998; Melbourne, Gilbert & Wagstaff, 1995; Melbourne & Hodgson, 1995). They performed a number of model scale tests considering different types of bridges, including single span, multi-span, semi-circular and skew arch bridges. It was shown that masonry bridges may collapse not only because of the classic four-hinge mechanism, but also owing to ring separation and support movements, which may dramatically reduce the ultimate loading capacity. The arch-fill interaction was also investigated, as well as the stiffening and strengthening effects due to the spandrel walls. In the tests on skew bridges (Melbourne & Hodgson, 1995), the influence of the skew angle on the structural behaviour was examined. These tests probably represent the first attempt to study the specific failure mechanisms of skew bridges. Concerning multi-span bridges, it was found that the typical collapse mode involves the whole bridge rather than the loaded span, and that the critical loading position is at the crown and not at the third or quarter span.

2.3.3 Failure mechanism

The results of real scale and model scale experimental tests allowed for the definition of the potential failure mechanisms for masonry arch bridges (Melbourne et al., 2007; Hughes & Blackler, 1997; Page, 1993). These comprise failure due to (i) four-hinge mechanism, (ii) shear sliding, (iii) ring separation, (iv) abutment movement, (v) masonry crushing and (vi) arch buckling.

The hinge mechanism is the most common failure mode for masonry bridges which results from the development of radial fracture lines in the arch barrel. Usually four radial cracks (hinges) transform the arch into a mechanism leading to the collapse of the bridge (Figure 2-5). In single ring arches an individual large crack in one mortar bed joint represents a hinge,

but in multi-ring brickwork arch barrels a group of radial cracks may develop within a small portion of the arch forming a diffused hinge (Gilbert, 1993).

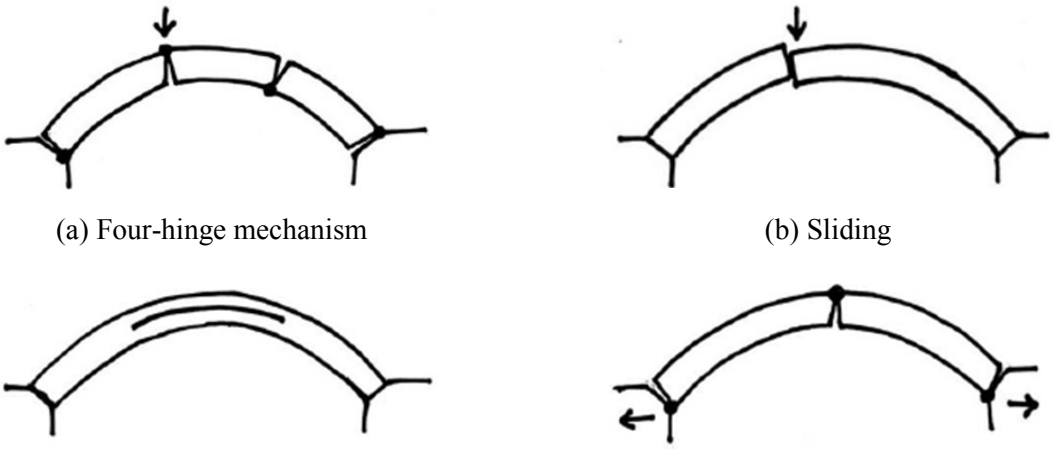

(a) Four-hinge mechanism (b) Sliding

(c) Ring separation (d) Abutment movement

Figure 2-5: Failure modes for masonry arches (Melbourne et al., 2007)

Figure 2-5 depicts other failure modes for masonry arches which comprise ring separation, shear sliding and failure caused by movements at the abutments.

Ring separation usually occurs in brick-masonry multi-ring arches, especially when they are built following the stretcher method. In this case the circumferential mortar joints which connect adjacent rings (Figure 2-2b) represent weak surfaces.

Shear sliding corresponds to a local failure mode, which takes place when a sliding crack develops along the arch, usually close to where a concentrated load is applied.

When a masonry arch is subject to relative movements at the abutments (e.g. settlements), failure may occur after the development of only three hinges at the two springings and at about the crown of the arch.

The arch of a masonry bridge may also collapse because of material failure (e.g. crushing) which arises when internal stresses in the arch exceed the compressive strength of masonry.

Finally shallow arches may fail due to snap-through buckling (Wang, 2004) which may develop before the formation of four hinges or material failure.

The discussion above concerns the behaviour of square arches at collapse. In the case of skew arches, more complex three-dimensional failure modes are expected (Hodgson, 1996) which are associated with the three-dimensional arrangement of mortar bed and perpendicular joints.

2.4 Classic design and assessment methods

While for many centuries masonry arch bridges had been built using empirical rules, the first systematic design and assessment methods were based upon elastic and plastic theories. The main characteristics of these classic methods, whose more advanced versions are currently adopted in practical design and assessment for masonry bridges, are discussed below.

2.4.1 Early methods

Ancient masonry bridges were designed following empirical rules forged on previous experience and associated with specific proportions between the mass and the geometrical characteristics of the arch barrel (e.g. thickness, span and rise of the arch barrel).

In 1675, Robert Hook (LimitState Ltd, 2011) was the first modern scientist and engineer to consider the masonry arch stability problem. He provided a solution in the form of a Latin anagram as “Ut pendet continuum flexile, sic stabit contiguum rigidum inversum” which can be translated as “as hangs the flexible line, so but inverted will stand the rigid arch”. He also stated that he had found “a true mathematical and mechanical form of all manner of arches for buildings” but he did not present the solution.

In the eighteenth century, Couplet and La Hire (Hamilton, 1952) conducted theoretical analyses and experimental tests aimed at determining the state of masonry arches at collapse. They independently elaborated design and assessment theories based on the line of thrust.

2.4.2 Elastic methods

The development of the elastic methods, which were aimed at reducing the effects of tensile stresses preventing the formation of cracks within the arch barrel, began in the nineteenth century.

Navier (Navier, 1833) proposed a theory called the straight line law for the distribution of the pressure on the bearing surface of voussoirs. These were assumed to be made up of a linear elastic material. He stated that, in order to avoid the occurrence of tension and the formation of cracks, the resulting line of force (the line of thrust) must lay in the middle third of the voussoir cross-section.

Moseley (Moseley, 1835) set out an elastic method similar to that proposed by Navier. He stated that the thrust line had to be within the arch depth and its inclination to each arch joint had to be smaller than the friction angle of the arch material. It should be noted that Moseley was the first British scientist who worked out a thrust line principle.

Barlow (Barlow, 1846) developed a very conservative method using a graphical technique to calculate the thrust line within the arch. He concluded that there are many possible thrust line locations that guarantee the stability of the arch. The work conducted by Navier and Barlow led to the development of the well-known middle third rule.

Rankine (Rankine, 1862) developed a design method based on the middle third rule. He proposed to assume the shape of the arch intrados parallel to the line of trust due to a system of symmetrically distributed vertical loads. Moreover he found that in order to satisfy equilibrium at the arch crown, a system of horizontal pressures have to be considered.

Castigliano (Castigliano, 1879) applied the minimum strain energy principle to the analysis and design of masonry arches. This allowed the calculation of the arch deformations and internal forces. He conceived an iterative design procedure where the geometry of the arch

must be changed until the trust line is included within the middle third part of any cross section of the arch.

Pippard (Pippard & Chitty, 1951) proposed an elastic assessment method based on the minimum strain energy theorem. According to this approach, in the case of a pin-ended parabolic elastic arch subject to a concentrated live load W at the crown (Figure 2-6), the thrust H and the central bending moment M_c, resulting from the combined effects of the live load and the dead weight of the arch, are calculated as:

$$H = \frac{l}{a}\left[\rho lh\left(\frac{a}{21}+\frac{h+d}{4}\right)+\frac{25}{128}W\right] \tag{2-1}$$

and

$$M_c = \frac{l}{4}\left(\frac{lah}{42}\rho-\frac{7}{32}\mathrm{W}\right) \tag{2-2}$$

where l is the span of the arch, a is the rise at midspan, ρ is the density of the arch and the fill (assumed to be the same), d is the arch ring thickness at the crown and $2h$ is the width of the arch. This is obtained assuming a 45° load spread angle and considering that h is the fill depth at the crown.

Pippard considered two limit loads which are associated with the development of the first crack W_1 (2-3) and the material failure in compression W_2 (2-4):

$$W_1 = \frac{32\rho lh\left[2a^2+4ad+21d\left(h+d\right)\right]}{21\left(28a-25d\right)} \tag{2-3}$$

$$W_2 = \frac{\frac{256fhd}{l}+128\rho lh\left(\frac{a}{28d}-\frac{1}{21}-\frac{h+d}{4a}\right)}{\left(\frac{25}{a}+\frac{42}{d}\right)} \tag{2-4}$$

where f is the material strength in compression.

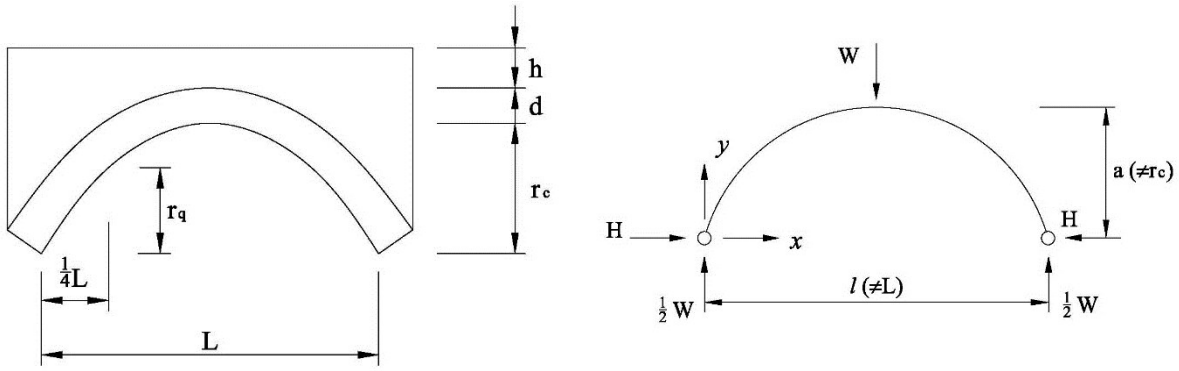

Figure 2-6: Pippard's bridge model (Page, 1993)

During and shortly after World War Two, Pippard's approach was implemented by the Military Engineering Experimental Establishment (MEXE) into a practical assessment procedure, named MEXE method, which also at present represents the most popular semi-empirical method for estimating the load capacity of masonry arch bridges. According to this approach, considering Pippard's parabolic pin-ended arch, the provisional axle load (PAL) W (kN) can be calculated as:

$$W = \frac{740\left(d+h\right)^2}{L^{1.3}} \tag{2-5}$$

To account for different geometrical and mechanical characteristics of actual masonry bridges, the original MEXE method has been enhanced leading to the modified MEXE method which is included in the current provisions for the assessment of existing masonry bridges (Department of Transport, 2001). In particular a series of empirical factors are considered leading to a maximum permissible axle load:

$$W_{\mathrm{m}} = F_{sr}F_pF_mF_jF_cW \tag{2-6}$$

where F_{sr} is the span to rise factor, F_{p} is the profile factor, F_{m} is the material factor, F_{j} is the joint factor, and F_{c} is the condition factor. Further details on the modified MEXE method can

be found in the Advice Note BA 16/97, Amendment No.2 (Department of Transport, 2001). Even though this widely adopted assessment approach has the great merit of simplicity and practicality, it not always provides consistent results. Anomalies in the application of this method are discussed in (Agrawal, 1973) and (Larnach, 1987) and more recently in (Wang et al. 2010), where it is pointed out that this assessment procedure may lead to unsafe predictions, especially in the analysis of short span bridges.

2.4.3 Plastic methods

As opposed to the elastic methods which offer lower bound solutions, the plastic approaches based upon the upper bound theorem enable the determination of the critical failure modes for masonry arch bridges, providing an estimate of their load carrying capacity. Evidently the accuracy of the plastic predictions depends upon the ability of the adopted models in representing material nonlinearity in the masonry arch and the interaction among the different bridge components.

Pippard (Pippard & Baker, 1968; Pippard & Chitty, 1951; Pippard & Chitty, 1941; Pippard, Tranter & Chitty, 1936) collaborated with other researchers on the development of a "mechanism procedure" for assessing the stability of voussoir arches. Although the authors did not consider their approach as a plastic analysis method, it can be regarded as an early attempt of plastic analysis for masonry arches. In the proposed method, it is assumed that the arch barrel is made up rigid blocks with negligible tensile resistance and infinite compressive strength. Moreover it is considered that the friction between adjacent blocks prevents shear sliding. In this way, assuming the ultimate state with four cracks (hinges) dividing the arch in three parts (Figure 2-7), the collapse load W can be calculated using equilibrium considerations and accounting for the self-weight of the three blocks V_1, V_2 and V_3, which include the arch ring and the backfill. Moreover it is considered that two hinges develop below the live load W and at the far springing, whereas the positions of the remaining two hinges are defined using a tabular method.

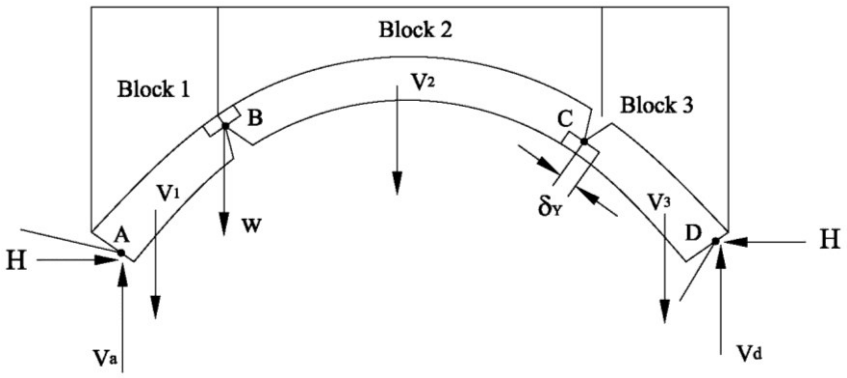

Figure 2-7: Mechanism with equilibrating forces (Page, 1993)

Subsequently, Heyman (Heyman, 1982; 1980; 1969) proposed an assessment method based on the theorems of plastic analysis. According to this strategy, a masonry arch made up of rigid voussoirs can transform into a mechanism as a result of the development of a sufficient number of plastic hinges. As in Pippard's method, Heyman neglected masonry tensile strength and disregarded potential sliding and crushing failure. Thus a masonry bridge is assumed to be safe if it is possible to find a thrust line within the arch in equilibrium with the external loading and the bridge self-weight. This approach, as the elastic methods discussed before, does not account for the interaction between the different bridge components (e.g. arch, backfill and lateral walls).

Crisfield and Packham (Crisfield & Packham, 1987) proposed an enhanced plastic method using an automated procedure to obtain the critical mechanism and loading position. This is an advance from Heyman's early approach, as a realistic compressive strength for masonry is considered, and the frictional contribution of the fill material is accounted for to determine its lateral resistance which opposes the sway of the arch. According to this more advanced plastic approach, the ultimate load W can be calculated considering the virtual work relationship (Figure 2-7):

$$\begin{aligned} & W\Delta p + V_1\Delta_1 = V_2\Delta_2 + V_3\Delta_3 + H_f\Delta_h \\ & + \frac{1}{2}\left[d_a^2\sigma_y + d_b^2\sigma_y\left(1+\Delta\theta_2\right) + d_c^2\sigma_y\left(\Delta\theta_2+\Delta\theta_3\right) + d_d^2\sigma_y\Delta\theta_3 \right] \end{aligned} \tag{2-7}$$

where $V_{i=1..3}$ are the dead weights of the arch and fill blocks 1 to 3, $\Delta_{i=1..3}$ are the virtual displacements at the centroids of the blocks 1 to 3, Δ_h is the horizontal virtual displacement at the centroid of block 3, $\Delta\theta_{i=1..3}$ are the virtual rotations, σ_y is a compressive strength of the brickwork/stonework, $d_{a\text{-}d}$ are the depths of the compressive "yield blocks". Finally H_f is the horizontal force corresponding to the passive resistance of the fill which is given by:

$$H_f = \frac{1}{2}\rho_f k_p \left(d_0^2 - d_c^2\right) \tag{2-8}$$

where ρ_f is the density of the fill, d_0 and d_c are the depth of backfill from the surface to D and C, and k_p is the passive resistance factor:

$$k_p = \frac{1+\sin\varphi}{1-\sin\varphi} \tag{2-9}$$

where φ is the angle of friction of the fill. The force H_f acts at a distance $\bar{y}$ above D where:

$$\bar{y} = d_0 - \frac{2\left(d_0^3 - d_c^3\right)}{2\left(d_0^2 - d_c^2\right)} \tag{2-10}$$

and:

$$\Delta_h = \bar{y}\Delta\theta_3 \tag{2-11}$$

Based on basic kinematics, the relationships between $\Delta_{i=1..3}$ and Δ_h can be found. The depth of the "yield blocks" is calculated from statics using an iterative technique. The minimum collapse load W_{min} can then be worked out by applying equation (2-7) on various hinge locations. Even though this procedure has the merit of allowing for arch-fill interaction, it does not consider three-dimensional effects and the interaction with the spandrel walls.

Similar plastic methods were developed by other authors, including Harvey (Harvey, 1988) who considered Heyman's safe theory and extended the concept of "thrust line" defining "thrust zones". In this approach, as in Crisfield's method (Crisfield & Packham, 1987), the

arch compressive strength is considered adopting a compressive rectangular stress block at plastic hinge. Later this modelling strategy was implemented in a commercial computer software named *Archie-M*, which is currently employed for designing new or assessing existing masonry bridges. In particular for specific bridge geometry and loading condition, possible thrust zone locations are defined (Figure 2-8). If the thrust zone remains within the cross-section along the arch barrel, the whole structure is assumed to be stable and safe. The plastic solution is determined allowing for the backfill contribution, where the interaction between the arch and the backfill is taken into account by adopting a simplified strategy based on the calculation of passive and active pressures. In assessing existing bridges, the program provides the maximum loading capacity by increasing the live load until the zone of thrust reaches the edge of the arch.

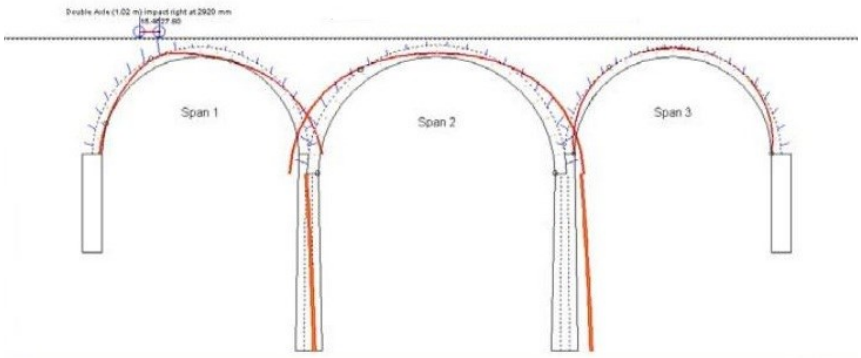

Figure 2-8: Analysis by means of Archie-M (Melbourne et al., 2007)

Melbourne and Walker (Melbourne & Walker, 1989) developed a simplified rigid block model accounting for the interaction among the arch, the backfill and the lateral walls. This was later improved by Gilbert (Melbourne & Gilbert, 1995; 1994). The enhanced version of this method considers a large number of rigid blocks to model a masonry arch allowing also shear sliding between adjacent block. Ring separation in multi-ring arches can be represented using this model (see Figure 2-9), as well as the interaction with the spandrel walls. Further improvements of the method (Gilbert & Melbourne, 1998) allowed the ultimate loading prediction for multi-span arches. Later Gilbert (Gilbert, 2001) implemented an improved

version of this approach in the computer software RING (LimitState Ltd, 2011) which is currently used for practical design.

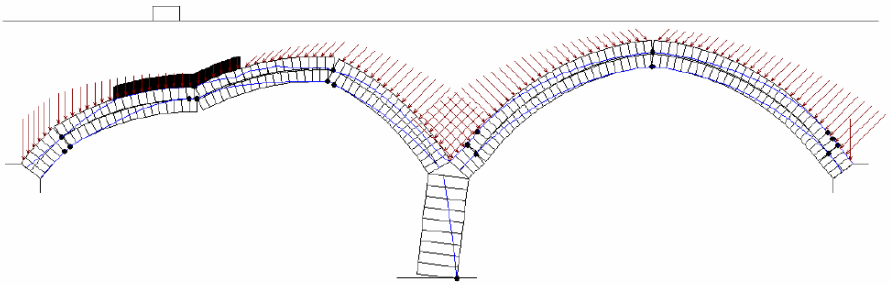

Figure 2-9: Analysis by means of RING (Melbourne et al., 2007)

The models discussed before are mainly based upon a 2D description of the masonry bridge response. The first attempt of adopting a 3D plastic approach with rigid blocks is due to Livesley, who initially developed a 2D rigid block automatic procedure to calculate the collapse load of masonry arches (Livesley, 1978). This was later extended to 3D analysis (Livesley, 1992) and was applied to investigate masonry walls, square arches (Figure 2-10) and domes.

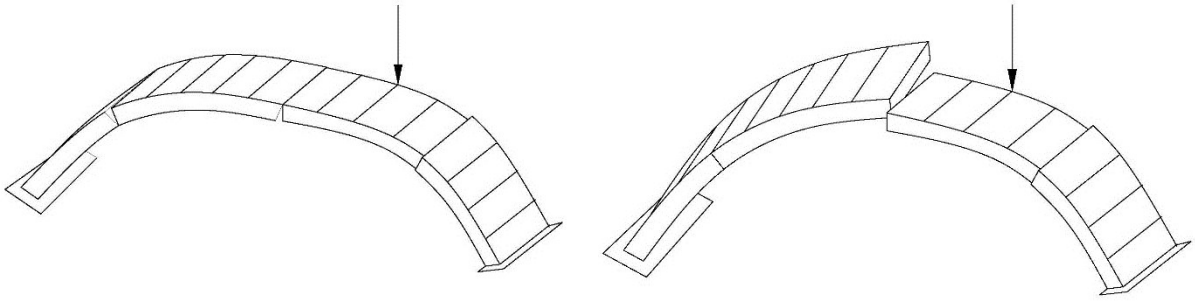

Figure 2-10: Livesley's rigid block method (Livesley, 1992)

2.5 Advanced modelling approaches

The recent progress of computational resources has enabled the development of advanced yet computationally expensive modelling techniques for masonry arch bridges. These overcome

the intrinsic limits of the conventional rigid-plastic methods, which allow only for a simple description of the bridge 3D geometry and nonlinear behaviour and an approximate representation of the interaction between the masonry arch and the other bridge components. Moreover as opposed to rigid-plastic approaches, the more advanced modelling techniques enable not only the prediction of the ultimate load capacity, but the representation of the response including the development of damage and cracks at different loading levels and the consideration of abutment movement. Most of the advanced modelling techniques are based upon the finite element method (FEM), while alternative modelling strategies consider the discrete element method (Azevedo & Sincraian, 2001) and the discontinuous deformation analysis (Thavalingam et al., 2001b).

The FEM represents a general structural analysis approach, which can be coupled with sophisticated nonlinear material descriptions for masonry enabling an accurate description of the actual bridge geometry, material characteristics and boundary conditions. Thus far different FE models have been developed to investigate the response of masonry bridges up to collapse. These comprise simple 1D and 2D models and more computational demanding 3D descriptions. In the following, the main characteristics of previous FE models for masonry arches and bridges including also recent modelling approaches to represent material nonlinearity in the masonry are discussed.

2.5.1 One-dimensional modelling approaches

Dawe (Dawe, 1974b; 1974a) developed FE models with curved beam elements for shallow and deep arches, but he did not apply these FE descriptions to the analysis of masonry arch bridges. Probably the first effort of using the FE method for the analysis of masonry arches was due to Towler (Towler & Sawko, 1982). He adopted FE models for the simulation of test results on model-scale brickwork arches. In particular, a masonry arch was modelled using a set of one-dimensional straight beam elements, in which realistic geometric and material properties were assumed. This research showed the potential of the FE method for computing

the arch ultimate load capacity and predicting the development of cracks under live loads. Successively, Towler (Towler, 1985) enhanced the description for material nonlinearity setting out procedures to determine the required material parameters based on experimental measurements, and investigated the influence of the backfill on the strength of the arch. Finally he suggested that, as an explicit modelling of the backfill is computationally expensive requiring a long computing time, it should be considered only in special cases.

Rouf (Rouf, 1984) extended Towler's work by applying curved beam elements to model the arch. He found that apart from material failure, arch failure could also be caused by the formation of a mechanism and stated that also shearing failure could lead to the arch collapse. However this method does not allow for a realistic redistribution of stresses after the development of cracks.

Apart from the above work, Crisfield (Crisfield & Packham, 1987; Crisfield & Wills, 1986; Crisfield, 1985b; Crisfield, 1985a; Crisfield, 1984) made significant contributions in applying curved beam elements to model masonry arch bridges. He compared the numerical results against several experimental tests showing the accuracy of the FE predictions. In Crisfield's FE modelling strategy, the arc-length approach was applied for representing the softening post-peak response of the arch. In the first version of this modelling strategy the arch-backfill interaction was ignored. Afterwards, Crisfield and his co-workers performed a comparative research on the contribution of the backfill, where an arch with low span-to-rise ratio was analysed taking into account or neglecting the lateral resistance of the backfill, where 1D nonlinear elements (springs) were employed to simulate the backfill contribution (Figure 2-11a). In this modelling strategy for the backfill, the nonlinear elements are activated only when the arch ring moves horizontally into the backfill (1D element in compression). The stress-strain relationship of these elements is bi-linear as shown in Figure 2-11b. Moreover, according to Crisfield's modelling strategy, the imposed loading on the road surface is distributed on to the arch barrel through the backfill considering a dispersal angle θ, which

may vary from 0° to 45° (Figure 2-12) and can be calculated assuming that the fill behaves as a semi-infinite elastic plane of unit thickness.

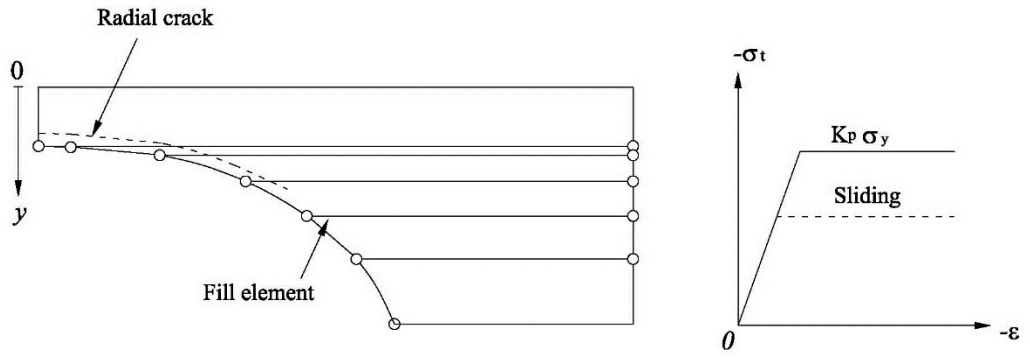

(a) 1D nonlinear elements for the backfill (b) Stress-strain relationship

Figure 2-11: 1D nonlinear elements for the backfill (Choo, Coutie & Gong, 1991b; Crisfield & Packham, 1987)

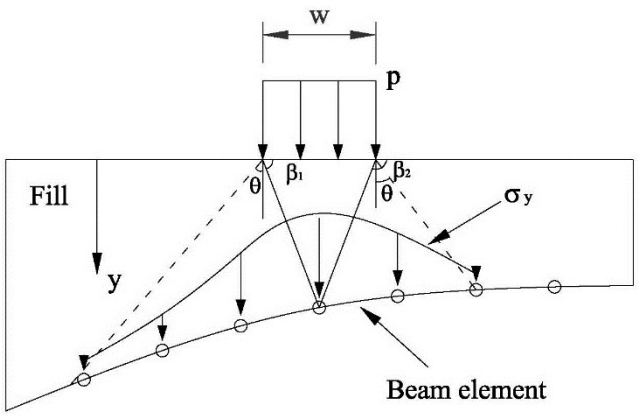

Figure 2-12: Load distribution through the backfill on the arch barrel (Choo, Coutie & Gong, 1991b; Crisfield & Packham, 1987)

Choo et al (Choo, Coutie & Gong, 1991b; 1991a; 1990b; 1990a) suggested the use of tapered beam elements with negligible tensile strength and elastic-perfectly plastic behaviour in compression to represent the arch barrel. Consequently, after the development of cracks (Figure 2-13), the arch failure is determined by masonry crushing in compression, where the

crushed zones form when the compressive stresses approach the crushing (yielding) strength of the masonry. Concerning the backfill modelling, also in this model nonlinear spring elements are employed to simulate the lateral resistance offered by the backfill (Figure 2-10). The proposed model was verified through comparisons between numerical load-deflection curves and experimental curves from real stone arch bridges tested up to collapse. A good agreement was obtained only when adopting a Young's modulus and a compressive strength much lower than those obtained from the laboratory measurements.

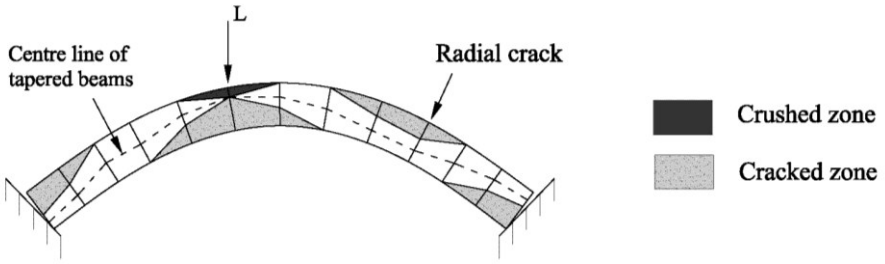

Figure 2-13: 1D model with nonlinear beam elements

More recently, Brencich and Francesco (Brencich & De Francesco, 2006) proposed to use 1D elastic-plastic models with no tensile resistance to model multi-span bridges. In this modelling strategy, bridge piers are simulated by one-dimensional beams similar to those employed for the arch barrel. The proposed model (Figure 2-14) can provide an adequate description of the bridge deformations and the location of plastic hinges at different loading levels.

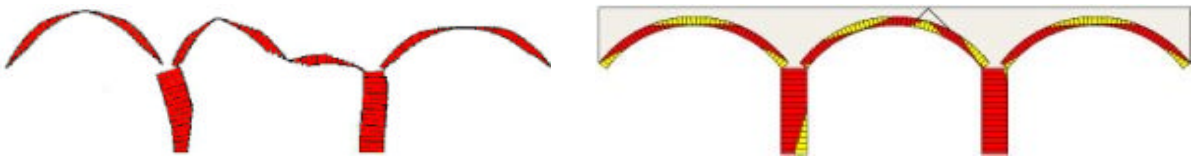

(a) Collapse mechanism (b) Distribution of plastic hinges

Figure 2-14: 1D elastic-plastic modelling for multi-span bridges (Brencich & De Francesco, 2006)

The most recent one-dimensional FE models clearly represent an advance when compared against elastic and rigid-plastic formulations. However they still introduced significant simplifications in the description of the bridge geometry and the interaction among the different bridges components.

2.5.2 Two-dimensional modelling approaches

To increase the accuracy of the numerical predications, two-dimensional (2D) FE approaches may be considered. Brencich (Brencich, 2009) defined two-dimensional models for masonry arch bridges as "models that neglect all the three-dimensional aspects of the bridge response, like the effect of external and internal spandrels, reducing the bridge geometry to the arch barrel, the fill and the piers, if any".

According to the 2D FE modelling strategy, the masonry arch and the fill are represented by means of 2D elements under the plane strain or the plane stress conditions. The use of plane strain elements corresponds to implicitly assuming perfectly rigid spandrels, which prevent the lateral deformations of the backfill. On the other hand, the plane stress condition allows for excessive transverse deformations in the backfill.

Choo et al (Choo, Coutie & Gong, 1991b) put forward a 2D model for masonry arch bridges (Figure 2-15a) which accounts for arch-fill interaction and enables the prediction of tangential cracking leading to ring separation. Eight-noded quadratic elements with the plane stress assumption are used to simulate multi-ring brickwork. Nodal separation is allowed to represent cracking development within the arch barrel. The proposed model can describe both radial and tangential cracks, which form when the tensile stresses are larger than the material tensile strength. After the formation of tangential cracks, the two adjacent rings are connected by joint elements with high axial but negligible shear stiffness (Figure 2-15b). This model was employed in numerical simulations of multi-ring masonry bridges examining the influence of ring separation. It was shown that ring separation largely reduces the bridge stiffness and loading capacity.

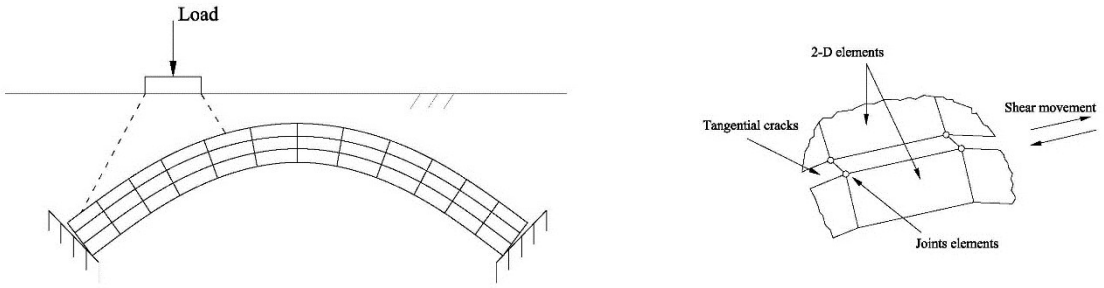

(a) 2D model for a masonry bridge (b) Joint elements for arch-fill interaction

Figure 2-15: 2D FE modelling approach for masonry bridges (Choo, Coutie & Gong, 1990b)

Loo and Yang (1991b; Loo & Yang, 1991a) developed a FE numerical procedure to investigate the response up to failure of semi-circular masonry arch bridges subject to concentrated loads. A two-dimensional "smeared crack" macro model approach (Chen & Baladi, 1985) was implemented within a stress redistribution scheme. This allowed the prediction of the development of cracks in the arch barrel. This model takes into account both the arch barrel and the backfill and can provide information about the formation of cracking, the failure mechanism and the ultimate loading capacity. This model was also adopted to investigate the influence of the abutment movement on the bridge response. In this respect it was found that also small support movements significantly affect the load-deflection characteristics and the load capacity of the bridge.

Ng et al. (Ng, Fairfield & Sibbald, 1999) used the general-purpose FE program LUSAS (Finite Element Analysis Ltd, 1993) to assess the ultimate load of three masonry arch bridges. A 2D modelling approach was employed, where the arch barrel and the backfill were modelled using eight-noded quadrilateral elements. Comparisons were performed not only against a series of experimental data but also against the ultimate load predictions obtained using alternative approaches, including the ARCHIE program (see Section 2.3.3) and the MEXE method (see Section 2.3.2). It was found that the MEXE method, even though based on the elastic theory, does not always provide conservative solutions. Moreover the results obtained using the ARCHIE program, which considers the mechanism method, are affected

by a largely approximate representation of the backfill leading to unrealistic stress distributions in the arch barrel.

Thavalingam et al. (Thavalingam et al., 2001a) conducted a comparative study on different 2D computational modelling schemes including a nonlinear FE description. In the FE model (Figure 2-16), 1D nonlinear interface elements are adopted to represent the interaction between the arch and the backfill and the development of cracks in the mortar joints of the arch.

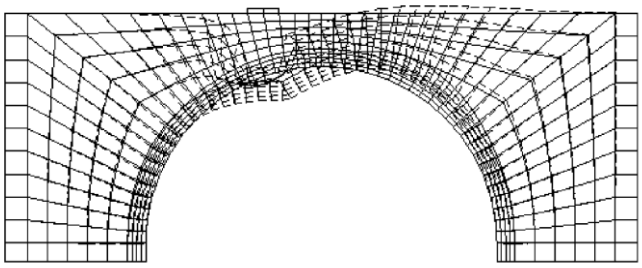

Figure 2-16: 2D FE model with nonlinear interfaces (Thavalingam et al., 2001a)

Cavicchi and Gambarotta (Cavicchi & Gambarotta, 2007; 2005) analysed several multi-span masonry bridges using two-dimensional FE models. The objective of the study was to examine the effect of the arch-backfill interaction on the structural behaviour of masonry arch bridges. In these numerical models, arches and piers are described using nonlinear beams with an elastic-plastic no-tension material. The backfill is simulated using a two-dimensional modelling technique with a modified Mohr–Coulomb failure criterion under plane strain conditions.

Another 2D model was developed by Ford et al. (Ford, Augarde & Tuxford, 2003) using the commercial FE package Strand7 (Strand7 Pty Ltd., 2010). A micro-modelling approach was employed, where the arch barrel was divided into masonry unit and mortar joint which were modelled adopting 1D nonlinear interface elements. It should be noted that not only the arch

barrel and the backfill but also the pavement layer are represented to allow for a more realistic distribution of the live load onto the bridge structure.

The 2D FE models discussed before, which use planar elements to represent the longitudinal response of masonry bridges, cannot predict the specific 3D behaviour of skew arches and bridges. In this respect, Choo and Gong (Choo & Gong, 1995) proposed a modelling approach with shell elements and a simple material description to examine the influence of skew angle on the structural behaviour of masonry skew bridges. According to this approach, eight-noded quadratic shell elements are used and the development of cracking and crushing in the masonry is accounted for by reducing the thickness the arch.

2.5.3 Three-dimensional modelling approaches

The main drawback of 2D FE models with planar elements is mainly due to the approximate representation of the bridge domain and the interaction between the different bridge components. Moreover 2D models cannot capture the lateral effects (e.g. failure of the lateral walls due to the fill lateral pressure) and the three-dimensional (3D) failure modes, including the typical collapse mechanisms of skew arches and bridges, and cannot provide a realistic response prediction in the case of eccentric loading. To overcome these inherent limitations, 3D modelling approaches need to be deployed, although these are more computationally demanding.

Boothby and Roberts (Boothby & Roberts, 2001) employed 3D FE models using the commercial finite element package ANSYS (De Salvo, Gorman & Imgrund, 1987) to examine the lateral effects due to the backfill on the overall structural response of masonry bridges subject to vertical loading. In the 3D models, the arch barrel, the backfill, the spandrel walls, the parapets and the wing walls were described using a continuous approach with eight-noded solid elements (Figure 2-17), where a macroscopic description was adopted for modelling masonry which was assumed as a homogeneous and isotropic material. In particular a smeared cracking model was adopted to represent material nonlinearity in

masonry and a Drucker-Prager material law (Drucker & Prager, 1952) was assumed for the backfill. Moreover frictional elements were adopted to capture the interaction between the backfill and the masonry components. The results obtained using the 3D models were compared against 2D predictions achieved using simpler 2D "strip" models. It was shown that the latter strategy does not allow the prediction of potential transverse failure modes which correspond to the failure of the spandrel walls subject to the transverse fill pressure, the edge failure and the longitudinal failure (e.g. longitudinal cracks) of the arch barrel. Moreover it was found that a variation in the masonry tensile strength has a greater influence on the numerical response obtained using 3D models than on the results determined by a 2D "strip" model, and that the type of backfill does not influence the potential transverse failure modes of the bridge.

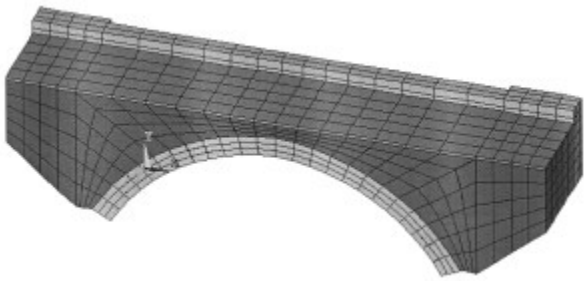

Figure 2-17: 3D macro-model for a single span masonry bridge (Boothby & Roberts, 2001)

In a later study (Fanning, Boothby & Roberts, 2001), the same 3D modelling strategy was adopted to analyse single- and double-span bridges (Figure 2-18) subjected to truck loading conditions. It was shown that the distribution of tyre pressure through the fill requires the consideration of 3D effects. Moreover this pressure induces significant transverse bending in the arch barrel and a give rise to a complex interaction between the arch and the lateral walls.

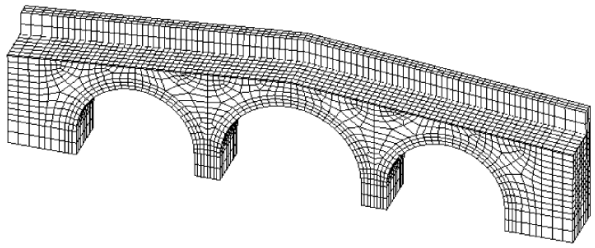

Figure 2-18: 3D macro-model for a double-span bridge (Fanning, Boothby & Roberts, 2001)

Wang (Wang, 2004) proposed a numerical modelling approach based on the use of the commercial FE package ANSYS (De Salvo, Gorman & Imgrund, 1987) to study the 3D behaviour of masonry arches. 3D FE models were developed to predict the response up to collapse under vertical loading. Square and skew arches were analysed using solid elements (Figures 2-19a,b) with a macroscopic elasto-plastic description for masonry, which was represented as a homogeneous and isotropic material. The numerical predictions were compared against the results from physical tests on brick-masonry arches (Wang, 2004). The type of failure mechanism was correctly predicted in the case of square and skew arches, but the numerical curves show a stiffer response with higher ultimate loads. Parametric studies were also conducted indicating that the prediction of the maximum load capacity and failure mechanism is mainly influenced by the masonry tensile strength.

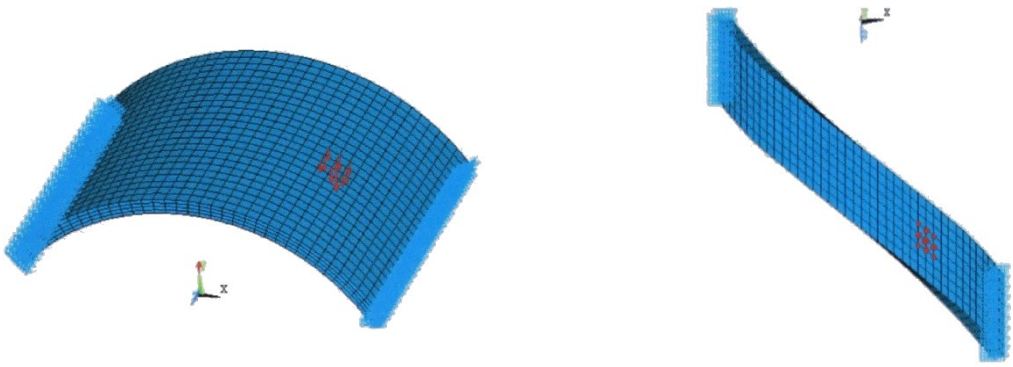

(a) 3D model for a square arch (b) 3D model for a skew arch

Figure 2-19: 3D models for masonry arches using ANSYS (Wang, 2004)

Recently Milani and Lourenco (Milani & Lourenço, 2012) proposed an advanced modelling approach for investigating the three-dimensional behaviour of masonry bridges. According to this strategy, the masonry components are modelled using a macro-scale homogenised approach with parallelepiped rigid elements and nonlinear interface elements, where the FE mesh for the arch barrel considers the actual masonry bond on the longitudinal face of the arch, but not along the arch width (Figure 2-20a,b). The fill material is represented by elastic-plastic solid elements with an isotropic Mohr-Coulomb material model with cut-off in tension and softening. The authors performed numerical simulations where the numerical predictions were compared against the results from experimental tests and the numerical solutions obtained using 2D descriptions. It was found that the 3D modelling strategy generally provides a better approximation of the bridge response and it is mainly required in the case of skewed bridges and bridges subject to unsymmetrical loading.

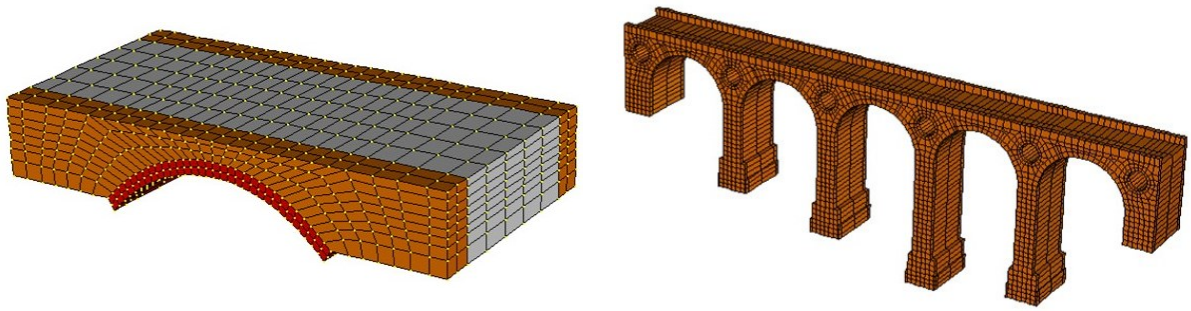

(a) Skew masonry arch bridge (b) Five-span arch bridge

Figure 2-20: 3D macro-scale homogenised models (Milani & Lourenço, 2012)

2.5.4 Modelling material nonlinearity

When analysing masonry arches and bridges, the accuracy of the numerical predictions depends not only upon the ability of the adopted numerical strategy to describe the arch geometry (e.g. 1D, 2D and 3D models), but also on the material model used to represent the nonlinear behaviour of masonry. This is a heterogeneous and anisotropic material whose

response is influences by the mechanical and geometrical characteristics of the individual components (e.g. masonry units and mortar joints) and by the particular masonry bond, where masonry joints represent preferential fracture planes Dhanasekar et al. (1985). Thus far several modelling strategies for capturing the nonlinear response of masonry have been developed. These mainly include macroscale and microscale descriptions (Lourenço, 1996) which are associated with different scales of representation for masonry and different computational costs. The most detailed and accurate micromodels represent masonry units, mortar joints and unit-joint interface separately (Figure 2-21a) using continuum and interface elements. In a simplified and more efficient mesoscale description (Figure 2-21b), nonlinear interface elements can be used to represent both mortar joints and unit-mortar interfaces, while continuum elements are still used for units (Lourenço & Rots, 1997). Finally according to the macroscale strategy, masonry is assumed as a homogeneous and isotropic material (Figure 2-21c) and a description with only continuum elements with specific plasticity- or damage-based models is adopted to represent material nonlinearity. This latter strategy is the most computationally efficient, thus until now has been the most employed approach for advanced numerical simulations of masonry bridges (Fanning & Boothby, 2001; Boothby & Roberts, 2001). However this approach does not allow the representation of masonry anisotropy and an accurate representation of critical failure modes like those associated with ring separation. Moreover it provides accurate results only when selecting specific material parameters which are not always associated with the actual mechanical characteristics of the masonry constituents. On the other hand, the use of detailed micro-modelling is impractical also for the analysis of relatively small masonry components due to the high computational demand. The mesocale approach for masonry represents a good compromise between accuracy and efficiency, but it has been mainly employed for 2D analysis of masonry bridges (Thavalingam et al., 2001a), while its use in 3D models is still prevented by a high computational cost.

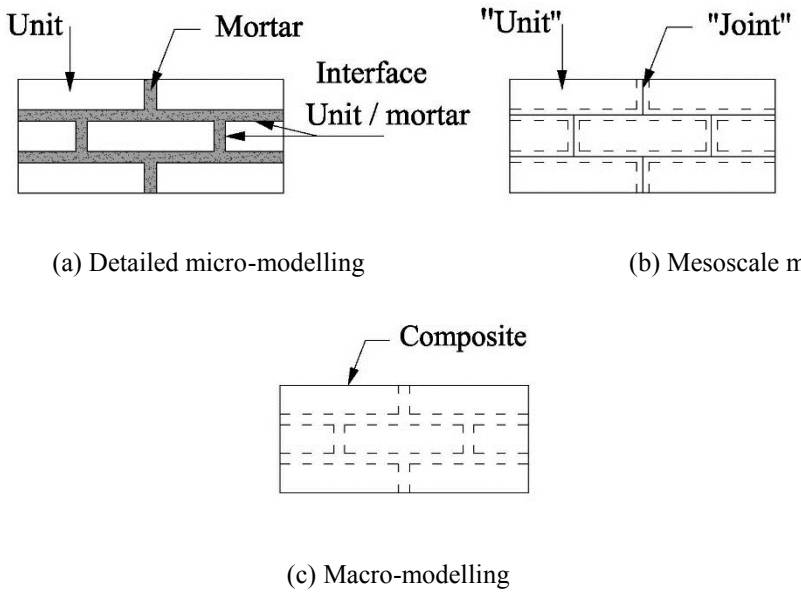

(a) Detailed micro-modelling (b) Mesoscale modelling

(c) Macro-modelling

Figure 2-21: Modelling approaches for masonry (Lourenço & Rots, 1997)

2.6 Conclusion

Significant experimental research has been conducted to study the complex behaviour of masonry bridges up to collapse. This has allowed the determination of the critical failure mechanisms, which derive from the interaction between the different bridge components generally leading to the collapse of the arch barrel. Early assessment methods based upon elastic and plastic principles do not enable an accurate description of the bridge response. Most advanced procedures, generally based upon the use of the finite element method, provide a more accurate response prediction at different loading levels including the elastic behaviour, the development of damage and cracking, and the collapse mode. In this respect, only the use of 3D models enables the consideration of the actual bridge geometry (especially for skew arches which are difficult to model with 1D/2D models, mechanical characteristics, where the transverse effects, and the response under eccentric load can be adequately represented. However these models are very computationally demanding, and thus far they have been mainly used with a simplified macroscopic material description for masonry. This

cannot represent the inherent masonry anisotropy and cannot allow a realistic prediction of the critical failure modes associated with the specific masonry bond (e.g. ring separation).

To sum up, accurate detailed mesoscale descriptions, where mortar and units are modelled separately, offer a realistic representation of the behaviour of masonry components at different loading level up to collapse. However the use of such detailed FE modelling for masonry arches and realistic masonry arch bridges, which are relatively large structures, is computationally demanding, thus so far it has been mainly employed in 2D plane strain analysis. In many cases, this is a too crude kinematic assumption, as the response of masonry arches and arch bridges is intrinsically three-dimensional even under simple loading conditions. To overcome these limitations, an advanced mesoscale modelling approach for masonry arches and arch bridges accounting for partitioned approach is developed in the current research. Detailed description of the proposed numerical modelling strategies will be presented in the next chapter.

CHAPTER 3

Numerical Modelling Strategies for Masonry Arch Bridges

3.1 Introduction

A masonry arch bridge is a three-dimensional (3D) heterogeneous structure, where different structural components perform their own function within the integral system and cooperate with each other to guarantee an adequate structural performance. Therefore, for a realistic prediction of the bridge response up to collapse, a numerical description capable of representing the nonlinear behaviour of the main bridge components (e.g. masonry arch and backfill) as well as their mutual interaction is required.

This chapter presents the proposed numerical strategy for masonry arch bridges. This is based upon the use of the finite element method (FE) and allows for an accurate 3D nonlinear analysis of the bridge response. Unlike numerical strategies based on limit analysis concepts, which can provide only an estimate of the ultimate loading capacity, the adopted numerical modelling technique enables the prediction of the bridge nonlinear response, including the elastic behaviour and the evolution of damage, plastic deformations and cracks under different loading conditions up to collapse.

In the following, attention is given to the 3D mesoscale modelling approach for brick-block masonry which is used here to model masonry arches. This advanced numerical strategy was

developed previously at Imperial College (Macorini & Izzuddin, 2011) and implemented in ADAPTIC, a general finite element code for nonlinear analysis of structures developed at Imperial College (Izzuddin, 1991). Thus far it has been successfully applied to the nonlinear analysis of brick/block-masonry wall components and structures under static and extreme dynamic loading (Macorini & Izzuddin, 2014). According to this approach, 2D nonlinear interface elements are used to represent mortar joints and to capture potential cracks in masonry units.

Subsequently, the numerical description adopted for the backfill material is discussed. 3D elasto-plastic solid elements are employed to represent the backfill domain. An elasto-plastic material model suitable for describing soil materials has been implemented in ADAPTIC (Izzuddin, 1991) and used to account for material nonlinearity in the 3D analysis of the backfill. This model is based upon the use of the rounded hyperbolic Mohr-Coulomb yield criterion proposed by Abbo & Sloane (1995), which allows for a practical yet accurate representation of the development of inelastic deformations in different types of soils. As opposed to more sophisticated descriptions for soil materials, this constitutive law has the advantage of requiring only few material parameters, which are familiar not only to soil mechanics specialists but also to practising structural engineers and can be obtained through simple tests.

According to the proposed modelling approach for masonry arch bridges, the interaction between the backfill and the masonry arch is modelled by using nonlinear interface elements, which can effectively represent the cohesive and frictional nature of the physical interface between the two domains.

The mesoscale description for masonry arches and the continuous elastic-plastic model for the backfill are incorporated within a partitioning framework allowing for parallel computation. This has been recently developed at Imperial College (Jokhio & Izzuddin, 2013; Jokhio, 2012), and it guarantees computational efficiency also in the analysis of large structural systems, which could not be investigated using standard serial codes. The main

characteristics of this advanced computational strategy are discussed in the final part of this chapter, focusing on its applications to masonry arch bridges. More detailed information on this approach can be found in (Jokhio & Izzuddin, 2013; Jokhio, 2012), while previous applications on large masonry wall structures are discussed in (Macorini & Izzuddin, 2013b).

3.2 Numerical Modelling for Masonry Arches

The accuracy of the response prediction for masonry arches, which are the main structural components in masonry bridges, is mainly associated with the ability of the adopted mechanical model to represent material nonlinearity in masonry. As discussed in Chapter 2, masonry is a heterogeneous and strongly nonlinear material whose behaviour depends on the orientation of the loading direction with respect to the masonry bond, where mortar joints represent preferential fracture planes (Page, 1981). In this respect, a detailed mechanical model for brick/block-masonry should take into account not only the mechanical characteristics of units and mortar but also the actual 3D masonry texture. This is disregarded in most of the numerical strategies currently used for nonlinear analysis of masonry arches, where the arch domain is represented using a 2D model usually based on the plane strain assumption. While this could be generally acceptable for the analysis of square arches subjected to line loads, it may lead to erroneous results when investigating the response of arches under patch loads or skew arches showing an inherent 3D response (Melbourne et al., 2007). The adopted numerical strategy for brick/block-masonry, which is based on a mesoscale description previously developed at Imperial College (Macorini & Izzuddin, 2011), allows for an accurate representation of the 3D domain of any masonry arch, as the actual 3D masonry bond is represented using two or more elastic solid elements for each brick and 2D nonlinear interface element for mortar joints. In the following, this modelling strategy is briefly presented providing also some details on the proposed geometrical description for skew arches built using the helicoidal method (Melbourne & Hodgson, 1995).

3.2.1 3D mesoscale modelling approach

To represent the actual masonry bond and model the development of cracks in real brick/stone-masonry arches, a discrete modelling strategy is used. Unlike the continuous approach which assumes masonry a homogeneous material, zero-thickness nonlinear interface elements are adopted to represent mortar joints and solid elements to model masonry units. This way the typical fracture lines, which characterise the nonlinear response up to collapse of masonry arches in masonry bridges under gravity and traffic loading, can be represented. These correspond to radial cracks, circumferential cracks leading to ring separation in multi-ring arches and longitudinal cracks caused by transverse bending (Gilbert, Melbourne & Smith, 2006). While the first two types of crack generally take place in the mortar joints, longitudinal cracks may pass also through the masonry units. Thus nonlinear interface elements are placed also in the middle of each brick to capture the potential development of cracks. This renders the FE mesh for brick-masonry arches relatively simple, as it is made up of identical solid elements connected to each other by nonlinear interface elements as shown in Figures 3-1 and 3-2.

In particular 20-noded elastic solid elements formulated according to standard FE procedures (Bathe, 1996) are used together with specific 2D nonlinear interface elements accounting for material and geometric nonlinearity. In the following only the main characteristics of the adopted nonlinear interface elements are provided as more detailed information can be found in (Macorini & Izzuddin, 2011).

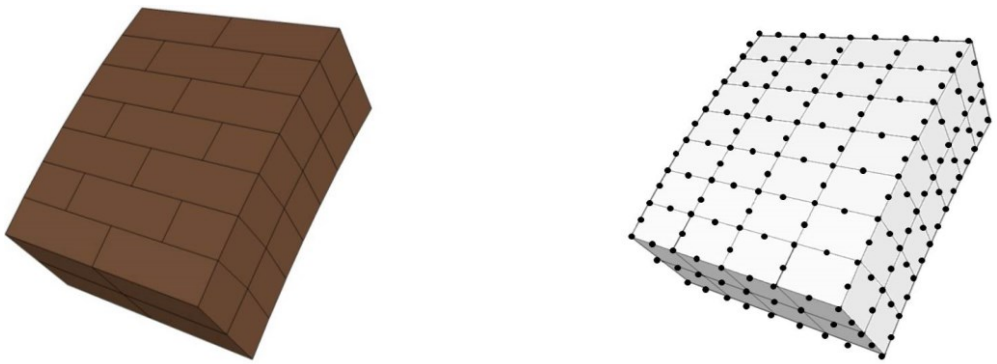

Figure 3-1: 3D mesoscale model for masonry arches

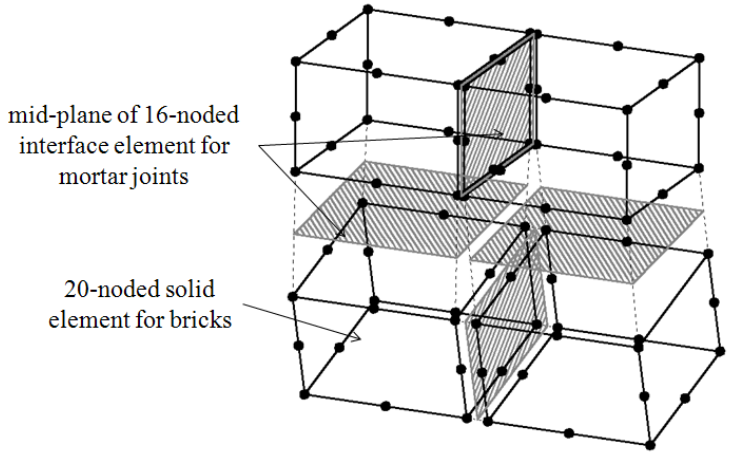

Figure 3-2: Solid elements connected by nonlinear interfaces (Macorini & Izzuddin, 2011)

The nonlinear interface elements used to represent mortar joints and capture potential cracks in masonry units have sixteen nodes, each of which features three translational freedoms.

As shown in Figure 3-3, nodes 1-8 lie on the top face of the element, while nodes 9-16 lie on the bottom face. These two faces, which are coincident in the initial undeformed configuration, can represent either the two faces of two masonry units connected by a mortar joint or adjacent faces of the same brick or block (Figure 3-2). The three local strain components correspond to the normal and the two in plane relative displacements (separations) d_z, d_x, and d_y calculated on the interface mid-plane. The associated stresses σ, τ_x, and τ_y represent traction forces.

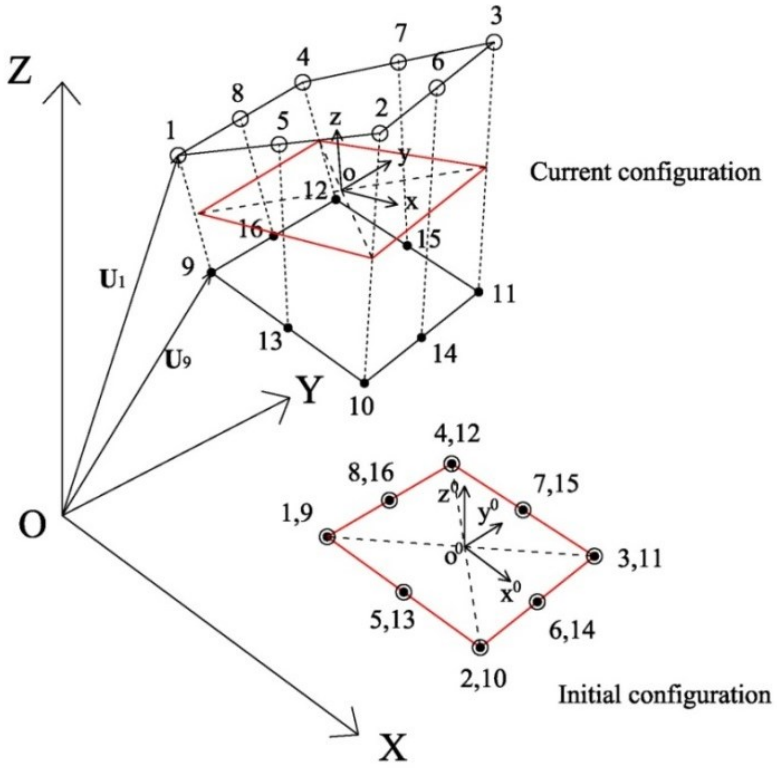

Figure 3-3: Nonlinear interface element (Macorini & Izzuddin, 2011)

An interface element modelling a mortar joint allows also a practical description of the joint elastic behaviour, where the three stress components are calculated using Hooke's law and a diagonal elastic stiffness matrix $\boldsymbol{k}_0$. This collects the normal k_{n0} and two tangential stiffness values k_{t0x} and k_{t0y} (usually $k_{t0x} = k_{t0y} = k_{t0}$).

$$\mathbf{k}_0 = \begin{bmatrix} k_{t0x} & 0 & 0 \\ 0 & k_{t0y} & 0 \\ 0 & 0 & k_{n0} \end{bmatrix} \tag{3-1}$$

According to previous research (Rots, 1997), in the case of thin mortar joints k_{n0} and k_{t0} can be calculated considering the joint geometry and the mortar elastic properties as below:

$$k_{t0} = \frac{G_m}{h_j},\ k_{n0} = \frac{E_m}{h_j} \tag{3-2}$$

where G_m and E_m are the mortar shear and Young's modulus and h_j is the mortar joint thickness. Similar expressions accounting also for the masonry unit dimensions and material

properties were suggested for thick mortar joints (Rots, 1997). However previous studies (e.g. (Da Porto et al., 2010) showed that these analytical expressions generally lead to overestimating the joint stiffness. More recent research (Chisari et al., 2013) has suggested to consider more advanced strategies coupling numerical and experimental techniques for the calculation of realistic elastic stiffness parameters for mortar joints.

In the constitutive model for the adopted interface element, material nonlinearity is taken into account by employing a cohesive model (Brocks, Cornec & Scheider, 2003), which enables an effective representation of damage, cracks and plastic separations. In particular a multi-surface plasticity criterion is utilised. Figure 3-4 depicts the two separate yield functions, where a hyperbolic failure surface based on the Coulomb slip criterion determines the boundaries of elastic domain in tension and shear representing Mode-I and Mode-II fracture. It reads:

$$F_1 = \tau_x^2 + \tau_y^2 - (C - \sigma \tan\phi)^2 + (C - \sigma_t \tan\phi)^2 \tag{3-3}$$

where C, ϕ and σ_t are the cohesion, friction angle and tensile strength for a mortar joint or a brick-brick interface. A non-associated flow rule is employed and a plastic potential Q_1 similar to function F_1 (3-3), but with a different friction angle parameter, is adopted to model the actual dilatancy. This is due to the roughness of the fractured shear surface and can be measured in tests on interfaces.

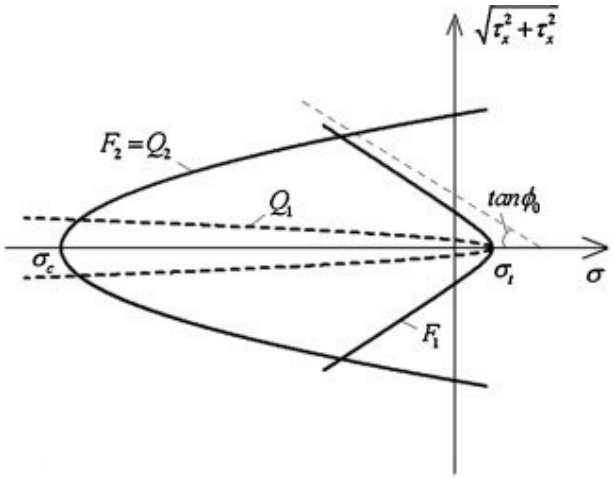

Figure 3-4: Yield functions and plastic potentials (Macorini & Izzuddin, 2011)

The second yield function corresponds to a cap model in compression and it is given by another hyperbolic function:

$$F_2 = \tau_x^2 + \tau_y^2 - (D - \sigma \tan\theta)^2 + (D - \sigma_c \tan\theta)^2 \tag{3-4}$$

where σ_c is the compressive strength of masonry while D and θ are material parameters governing the shape of the cap surface.

For a realistic representation of the development of cracks in brickwork, a work-softening plasticity approach is employed and two distinct historical parameters expressed in the form of plastic work values, namely W_{pl1}, W_{pl2} are used. These are associated with the two yield functions F_1 and F_2 governing the degradation of the model material parameters. W_{pl1} and W_{pl2} are given by:

$$dW_{pl1} = \begin{cases} \boldsymbol{\sigma} d\mathbf{u}_{pl1} & (\sigma \geq 0) \\ \left(\sqrt{\tau_x^2 + \tau_y^2} + \sigma \tan\phi\right) \sqrt{du_{x,pl\,1}^2 + du_{y\,pl\,1}^2} & (\sigma < 0) \end{cases} \tag{3-5}$$

$$dW_{pl2} = \boldsymbol{\sigma} d\mathbf{u}_{pl2} \tag{3-6}$$

where $\boldsymbol{u}_{pl1}$ and $\boldsymbol{u}_{pl2}$ are the vectors collecting the three plastic deformation components associated with the functions F_1 and F_2 (Macorini & Izzuddin, 2011).

In particular, the tensile strength and the friction angle converge to their residual values (material parameters) when W_{pl1} approaches the Mode-I (tension) fracture energy G_{f1}; similarly the cohesion at the interface reaches its residual value when W_{pl1} converges to the Mode-II (shear) fracture energy G_{f2}. Figures 3-5a,b show the traction-separation response in tension and shear. It can be seen that the use of very large G_{f1} values moves towards a perfectly plastic behaviour with no strength degradation in tension.

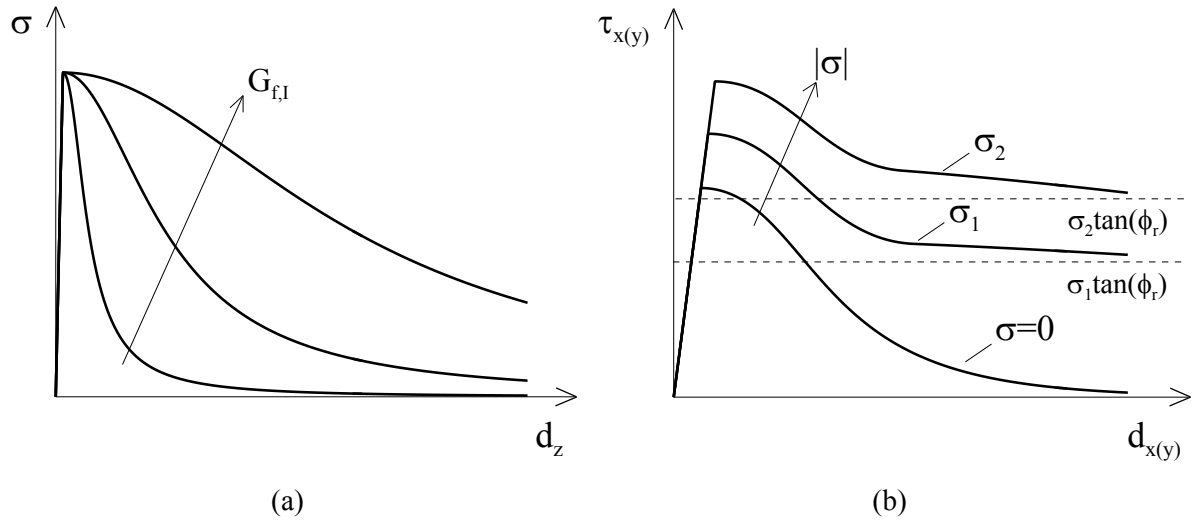

Figure 3-5: Traction-separation curves in (a) tension and (b) shear (Macorini & Izzuddin, 2011)

3.2.2 Geometrical description for skew arches

When using the mesoscale description presented before for analysing brick-masonry components of unreinforced masonry buildings, the construction of the FE mesh is relatively straightforward, as sets of equal solid and interface elements are arranged in two or three perpendicular directions forming masonry walls. Similarly, also the mesh for single or multi-ring square semi-circular or segmental arches can be defined quite easily, as the bed mortar joints are arranged along radial directions, and the joints connecting different rings in

multi-ring arches run along circumferential lines. Conversely the mesh construction for skew arches is more problematic as, according to the adopted mesoscale strategy, it should represent the actual arrangement of masonry units and mortar joints which in skew arches is relatively complex. In this research, skew arches built according to the English or helicoidal method (Hodgson, 1996; Melbourne & Hodgson, 1995) are considered. This method was developed in the 19th century (George, 1880) and was extensively used to build brick-masonry skew bridges, as it allows for the use of masonry units of identical dimensions (bricks) which are arranged according to a specific geometry to form skew arches. In Buck's manual (George, 1880) construction rules for brick skew arches are provided. These are based upon descriptive geometry principles, which are used here to establish the nodal coordinates (Figure 3-6) for all the solid elements of the FE mesh for a brick skew arch. In this way, the nodal coordinates of a generic solid element (block) for a segmental single-ring skew arch can be obtained considering the sketches in Figure 3-7, where the arch is represented by a strip of N_c parts including (N_c – 2) hexahedrons and two triangular prisms for the untidy edges of the arch (see also Figure 3-6). In Figure 3-7, W, L_d, *H, T* and θ represent the arch width, the direct span, the rise, the ring thickness and the skew angle. The intrados of the arch can be considered as part of a cylindrical surface with radius R_0, while the radius for the extrados is (R_0+T). The direct span L_d of the arch is equal to the diameter of the cylinder, while the oblique span L_o is equal to $L_d/\sin\theta$. Each hexahedron corresponds to a generic solid element (half brick) with eight nodes at the four corners. The x, y and z coordinates for the corner nodes of a generic block i can be calculated using the expressions given in Table 3-1, where α represents the angle for each block as shown in Figure 3-6. Evidently the coordinates for the mid-side nodes in the 20-noded solid elements can be obtained from the coordinates of the corner nodes through liner interpolations.

The expressions provided in Table 3-1 can be used to construct the mesh for segmental and semi-circular brick skew arches. Moreover the same principles can be applied for elliptical skew arches, where an elliptical arch can be divided into several parts approximated by circular arch segments.

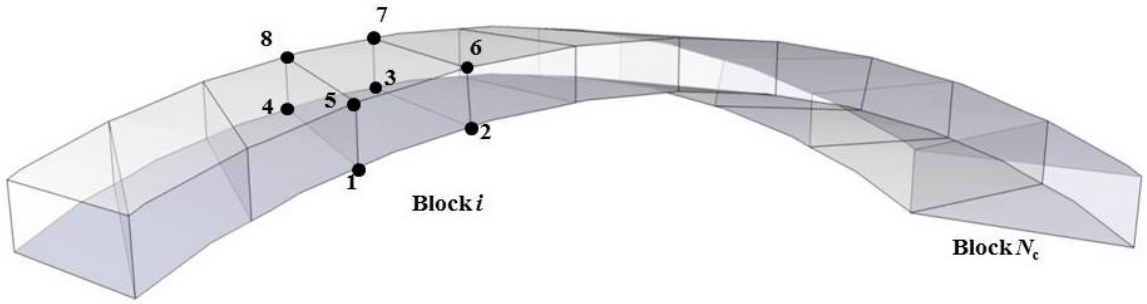

Figure 3-6: Nodal position of a solid element within the FE mesh for a portion of single-ring skew arch

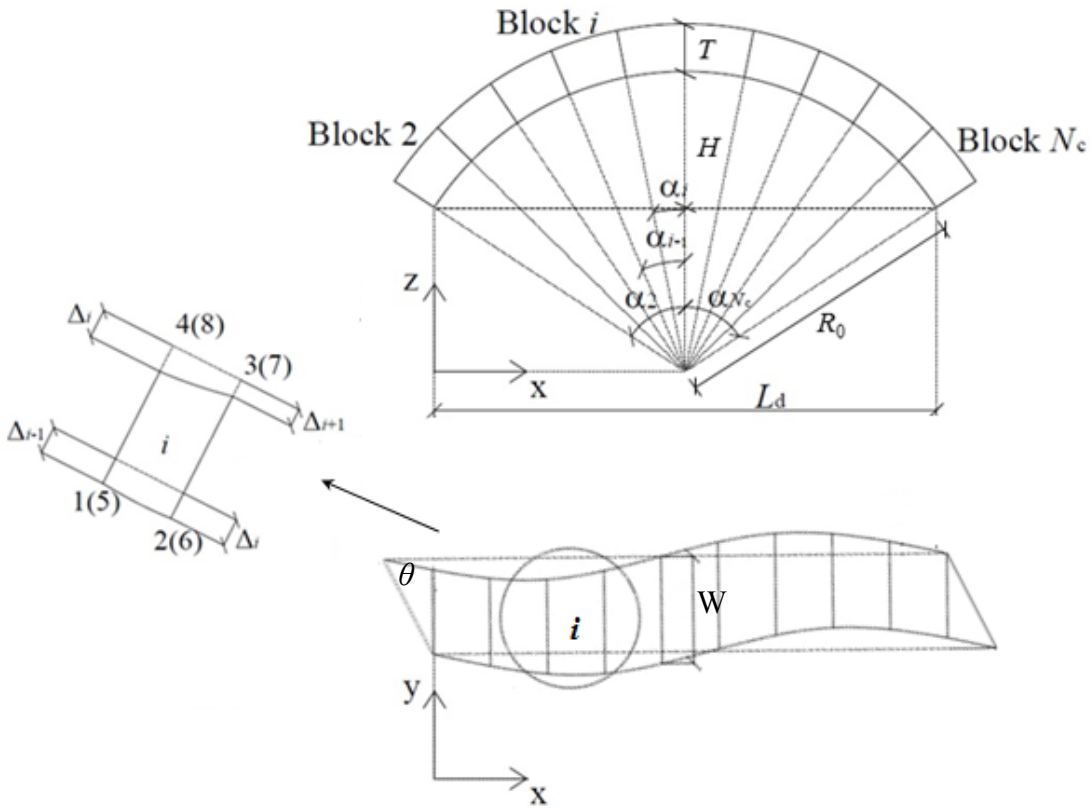

Figure 3-7: Elevation view and projection in plan of the extrados of a skew arch showing the position of a generic solid element

Table 3-1: Nodal coordinates for the FE mesh for a skew arch

Node No.	x	y	z
i_1	$\frac{L_d}{2} - R_0 \cdot \sin\alpha_{i-1}$	$-\Delta_{i-1}$	$R_0 \cdot \cos\alpha_{i-1}$
i_2	$\frac{L_d}{2} - R_0 \cdot \sin\alpha_i$	$-\Delta_i$	$R_0 \cdot \cos\alpha_i$
i_3	$\frac{L_d}{2} - R_0 \cdot \sin\alpha_i$	$W \cdot \sin\theta - \Delta_{i+1}$	$R_0 \cdot \cos\alpha_i$
i_4	$\frac{L_d}{2} - R_0 \cdot \sin\alpha_{i-1}$	$W \cdot \sin\theta - \Delta_i$	$R_0 \cdot \cos\alpha_{i-1}$
i_5	$\frac{L_d}{2} - \left(R_0 + T\right) \cdot \sin\alpha_{i-1}$	Δ_{i-1}	$\left(R_0 + T\right) \cdot \cos\alpha_{i-1}$
i_6	$\frac{L_d}{2} - \left(R_0 + T\right) \cdot \sin\alpha_i$	Δ_i	$\left(R_0 + T\right) \cdot \cos\alpha_i$
i_7	$\frac{L_d}{2} - \left(R_0 + T\right) \cdot \sin\alpha_i$	$W \cdot \sin\theta - \Delta_{i+1}$	$\left(R_0 + T\right) \cdot \cos\alpha_i$
i_8	$\frac{L_d}{2} - \left(R_0 + T\right) \cdot \sin\alpha_{i-1}$	$W \cdot \sin\theta - \Delta_i$	$\left(R_0 + T\right) \cdot \cos\alpha_{i-1}$

$$\alpha = \cos^{-1}\frac{R_0 - H}{R_0}$$

$$\alpha_i = \left(1 - \frac{2\left(i-1\right)}{N_c - 1}\right)\alpha,\ \alpha_0 = \alpha_1,\ \alpha_{N_c+1} = \alpha_{N_c}$$

$$\Delta_i = \begin{cases} R_0 \cdot \cot\theta \cdot \sin\dfrac{2\left(i-1\right)\alpha_0}{N_c - 1} - L_d \cdot \dfrac{i-1}{N_c - 1} \cdot \cot\theta, & i \le \dfrac{N_c + 1}{2} \\ L_d \cdot \dfrac{i-1}{N_c - 1} \cdot \cot\theta - R_0 \cdot \cot\theta \cdot \sin\dfrac{2\left(i-1\right)\alpha_0}{N_c - 1}, & i > \dfrac{N_c + 1}{2} \end{cases}$$

$$\Delta_0 = \Delta_1,\ \Delta_{N_c+1} = \Delta_{N_c}$$

3.3 Numerical Description for Backfill

Masonry arch bridges are heterogeneous systems where the fill material plays a critical role spreading the loads applied on the road/rail surface below to the arch barrel, while providing transverse resistance and passive pressure to the deformed arch. Thus, a realistic representation of the fill behaviour and its interaction with the arch barrel is critical for an accurate response prediction of masonry arch bridges. Some of the most recent FE modelling approaches for masonry bridges (Milani & Lourenço, 2012; Melbourne et al., 2007; Boothby, 2001; Fanning & Boothby, 2001) consider the backfill as a continuous elasto-plastic material, where specific plastic criteria are adopted to describe the development of plastic deformations. The same strategy is employed in the proposed 3D modelling description, where 15-noded elasto-plastic tetrahedral elements (Figure 3-8) are utilised to model the fill domain.

In the following the main characteristics of the adopted plastic model for the fill material are provided. This has been implemented in ADAPTIC and its accuracy has been checked in numerical comparisons.

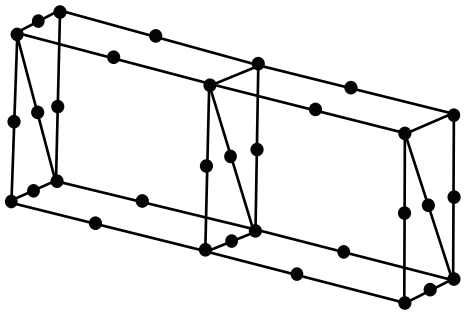

Figure 3-8: 15-noded tetrahedral elements for the backfill domain

3.3.1 Material model for backfill

The backfill in existing masonry bridges is largely made up of soil materials, thus realistic soil models should be considered for an accurate description of the backfill contribution in masonry arch bridges. Thus far a number of constitutive models have proposed for representing the nonlinear behaviour of soil materials (Potts & Zdravkovic, 2001). These

models are generally formulated within the elasto-plastic framework utilising different plastic criteria. Usually the most advanced models, capable of reproducing the complex soil response with high accuracy, require a large number of input parameters which cannot be easily obtained from conventional tests. Consequently in structural simulations to investigate soil-structure interaction, as in the analysis of masonry bridges, simpler isotropic elastic perfectly-plastic models like the Mohr-Coulomb or the Drucker-Prager models are usually adopted (Milani & Lourenço, 2012; Melbourne et al., 2007; Boothby, 2001; Fanning & Boothby, 2001). The first model results from the combination of Hooke's law and Coulomb's failure criterion and requires two elastic parameters, Young's modulus and Poisson's ratio, and only two inelastic parameters, namely cohesion and friction angle, for defining the plastic surface. The Mohr-Coulomb model allows for an accurate description of the soil behaviour at failure, but adopting constant Young's modulus and Poisson's ratio values, it provides only an approximate linear response prediction before reaching the plastic limit.

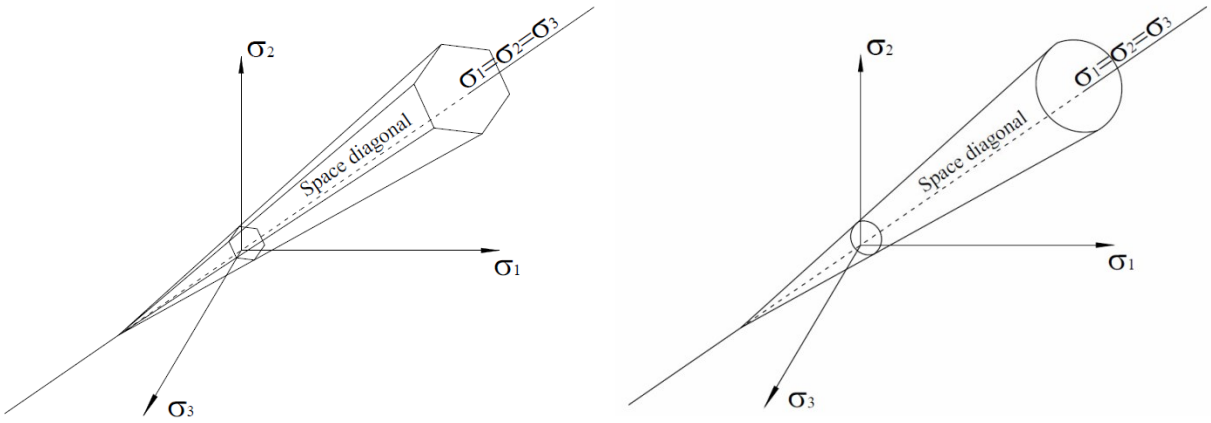

(a) (b)

Figure 3-9: (a) Mohr-Coulomb and (b) Drucker-Prager yield surfaces in the principal stress space

The Drucker-Prager model (Drucker & Prager, 1952) is a simplification of the Mohr-Coulomb model, as it substitutes the irregular hexagonal cone for the failure contour (Figure 3-9a) with a cylindrical cone in the principal stress space (Figure 3-9b) providing significant computational advantages. However, as traditional soil mechanics predictions are based on

the Mohr-Coulomb model, whose material parameters can be obtained in standard tests, it is preferable to adopt the Mohr-Coulomb formulation also in numerical simulations (Potts & Zdravkovic, 2001). Nevertheless some computational difficulties must be solved, mainly to deal with the corners of the yield and plastic potential (for non-associated plastic flow) surfaces. In particular at the edges of the hexagonal cone, the gradients of the yield function and the plastic potential and the gradient derivatives cannot be univocally defined, thus preventing the solution of the local plastic problem using standard techniques (Simo & Hughes, 1998).

In this research, an elasto perfectly-plastic model based on the use of a smooth rounded hyperbolic Mohr-Coulomb failure criterion (Abbo & Sloan, 1995), which circumvents the computational difficulties associated with the traditional Mohr-Coulomb formulation, has been implemented in ADAPTIC and used for analysing the backfill contribution in masonry bridges. In the following, some details of this constitutive model and the procedure adopted for the solution of the local plastic problem which has been implemented in ADAPTIC are discussed.

3.3.1.1 Basic variables and elastic behaviour

The local three-dimensional material model for the backfill is formulated in terms of 6 strain $\boldsymbol{\varepsilon}$ (3-7) and 6 stress $\boldsymbol{\sigma}$ (3-8) components, which are shown with reference to a solid element in Figure 3-10.

$$\boldsymbol{\varepsilon} = \begin{bmatrix} \varepsilon_x & \varepsilon_y & \varepsilon_z & \gamma_{xy} & \gamma_{zx} & \gamma_{yz} \end{bmatrix}^T \tag{3-7}$$

$$\boldsymbol{\sigma} = \begin{bmatrix} \sigma_x & \sigma_y & \sigma_z & \tau_{xy} & \tau_{zx} & \tau_{yz} \end{bmatrix}^T \tag{3-8}$$

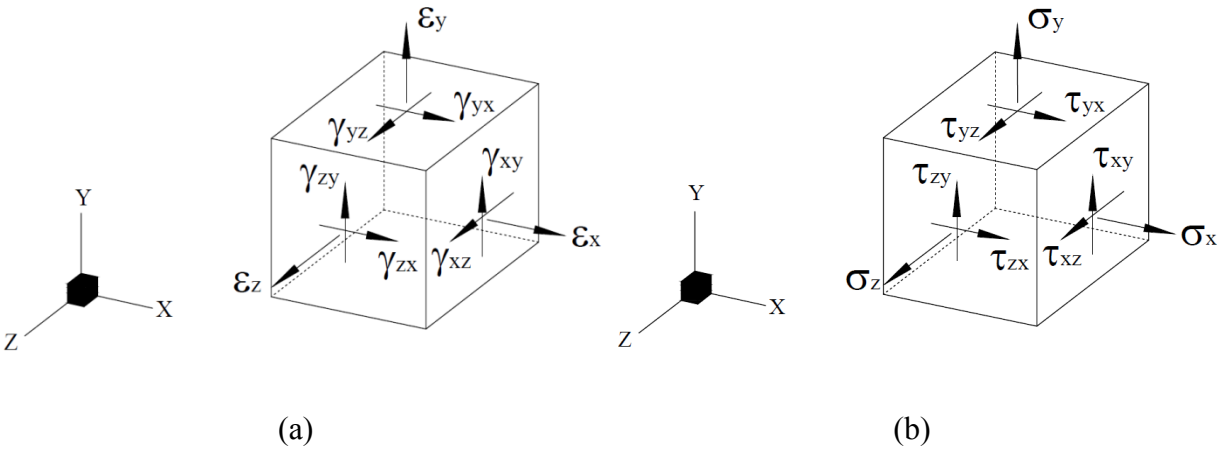

(a) (b)

Figure 3-10: Definition of (a) 3D strain and (b) 3D stress variables

According to the adopted elasto-plastic description, the backfill is assumed as an isotropic material, which behaves elastically before reaching the failure surface. Only two independent elastic material parameters, namely Young's modulus E and Poisson's ratio ν, are used with the Hooke's law to represent the elastic behaviour, where the symmetric elastic matrix is given by:

$$\mathbf{D} = \frac{E}{(1+\nu)(1-2\nu)} \begin{bmatrix} 1-\nu & \nu & \nu & 0 & 0 & 0 \\ \nu & 1-\nu & \nu & 0 & 0 & 0 \\ \nu & \nu & 1-\nu & 0 & 0 & 0 \\ 0 & 0 & 0 & \frac{1-2\nu}{2} & 0 & 0 \\ 0 & 0 & 0 & 0 & \frac{1-2\nu}{2} & 0 \\ 0 & 0 & 0 & 0 & 0 & \frac{1-2\nu}{2} \end{bmatrix} \tag{3-9}$$

Thus within the elastic domain, the accumulated total stresses can be expressed as below:

$$\boldsymbol{\sigma} = \mathbf{D} \cdot \boldsymbol{\varepsilon} \tag{3-10}$$

where the total strain **ε** is elastic (it is assumed that the material has never reached the plastic limit).

3.3.1.2 Failure criterion

The boundaries of the elastic domain are defined by a smooth hyperbolic Mohr-Coulomb function F_{SHMC}, which requires only two material parameters, i.e. cohesion c and frictional angle φ. This has been derived in (Abbo & Sloan, 1995) considering the classic Mohr-Coulomb failure surface $F_{MC} = 0$ which can be expressed in terms of the principal stresses $\sigma_1 \geq \sigma_2 \geq \sigma_3$ as:

$$F_{MC} = (\sigma_1 - \sigma_3) + (\sigma_1 + \sigma_3)\sin\varphi - 2c\cos\varphi = 0 \tag{3-11}$$

Alternatively using the three stress invariants: the mean total stress σ_m, the deviatoric stress $\bar{\sigma}$ and Lode's angle θ, it becomes (Nayak & Zienkiewicz, 1972):

$$F_{MC} = \sigma_m \sin\varphi + S(\theta)\bar{\sigma} - c\cos\varphi = 0 \tag{3-12}$$

where

$$S(\theta) = \cos\theta - \frac{1}{\sqrt{3}}\sin\varphi\sin\theta \tag{3-13}$$

$$\sigma_m = \frac{1}{3}(\sigma_x + \sigma_y + \sigma_z) \tag{3-14}$$

$$\bar{\sigma} = \sqrt{\frac{1}{2}(s_x^2 + s_y^2 + s_z^2) + \tau_{xy}^2 + \tau_{yz}^2 + \tau_{zx}^2} \tag{3-15}$$

$$\theta = \frac{1}{3}\sin^{-1}\left(-\frac{3\sqrt{3}}{2}\frac{J_3}{\bar{\sigma}^3}\right) \tag{3-16}$$

where $-30^\circ \leq \theta \leq 30^\circ$ and

$$J_3 = s_x s_y s_z + 2\tau_{xy}\tau_{yz}\tau_{zx} - s_x\tau_{yz}^2 - s_y\tau_{zx}^2 - s_z\tau_{xy}^2 \tag{3-17}$$

in which

$$s_x = \sigma_x - \sigma_m \tag{3-18}$$

$$s_y = \sigma_y - \sigma_m \tag{3-19}$$

$$s_z = \sigma_z - \sigma_m \tag{3-20}$$

To avoid singularities in the octahedral plane (the deviatoric plane in three-dimensional stress space), Abbo & Sloan (Abbo & Sloan, 1995) recommended to substitute $S(\theta)$ with a piecewise function $\overline{S}(\theta)$ which reads:

$$\overline{S}(\theta) = \begin{cases} \cos\theta - \dfrac{\sqrt{3}}{3}\sin\varphi\sin\theta & |\theta| \le \theta_T \\ S_1 - S_2\sin 3\theta & |\theta| > \theta_T \end{cases} \tag{3-21}$$

where θ_T is a specific transition angle, and

$$S_1 = \frac{1}{3}\cos\theta_T\left(3 + \tan\theta_T\tan 3\theta_T + \frac{\sqrt{3}}{3}\operatorname{sign}(\theta)\left(\tan 3\theta_T - 3\tan\theta_T\right)\sin\varphi\right) \tag{3-22}$$

$$S_2 = \frac{1}{3\cos 3\theta_T}\left(\operatorname{sign}(\theta)\sin\theta_T + \frac{\sqrt{3}}{3}\sin\varphi\cos\theta_T\right) \tag{3-23}$$

in which

$$\operatorname{sign}(\theta) = \begin{cases} -1 & \text{for } \theta < 0^\circ \\ +1 & \text{for } \theta \ge 0^\circ \end{cases} \tag{3-24}$$

The value of the transition angle is included in the interval $0° \le \theta_T \le 30°$, where the upper limit provides a better approximation of the classic Mohr-Coulomb criterion in the octahedral plane. However the use of a too large transition angle may lead to numerical problems (ill-conditioning), thus a value $\theta_T = 25°$ is suggested in (Abbo & Sloan, 1995).

Moreover, as the classic Mohr-Coulomb yield criterion (3-12) exhibits a linear relationship between the mean total stress and the deviatoric stress for a constant Lode's angle, an additional singularity point is located at the intersection between the yield function and the horizontal axis ($\bar{\sigma} = 0$) in the meridional plane (Figure 3-11).

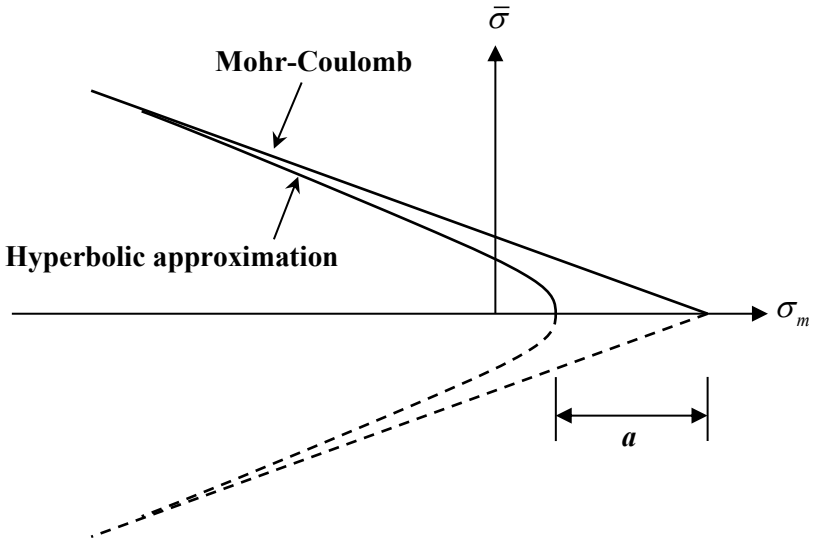

Figure 3-11: Hyperbolic approximation to Mohr-Coulomb yield surface (Abbo & Sloan, 1995)

To remove this singularity, in (Abbo & Sloan, 1995) a hyperbolic approximation is proposed (Figure 3-11). Thus the original yield function (3-11) is transformed into the rounded hyperbolic Mohr-Coulomb expression given below:

$$F_{RHMC} = \sigma_m \sin\varphi + \sqrt{\bar{\sigma}^2 \bar{S}^2 + a^2 \sin^2\varphi} - c\cos\varphi \tag{3-25}$$

where:

$$a = a_1 c \cot\varphi \tag{3-26}$$

with $a_1 \leq 0.25$. In (Abbo & Sloan, 1995) it is recommended to use $a_1 = 0.05$, which provides very accurate results, close to the original Mohr-Coulomb predictions.

The modified Mohr-Coulomb function (3-25), being rounded in both the meridian and octahedral planes (Figure 3-12), is continuous and differentiable for all stress states. Thus it

can be readily used within an implicit Euler backward scheme (Simo & Hughes, 1998) for the integration of the stress-strain relationships in the plastic regime. Besides, the discrepancy with the original Mohr-Coulomb yield criterion can be limited by a proper selection of the two additional parameters a_1 and θ_T. In particular when $a_1 = 0$ and $\theta_T = 30°$, the modified yield function coincides with the classic Mohr-Coulomb surface.

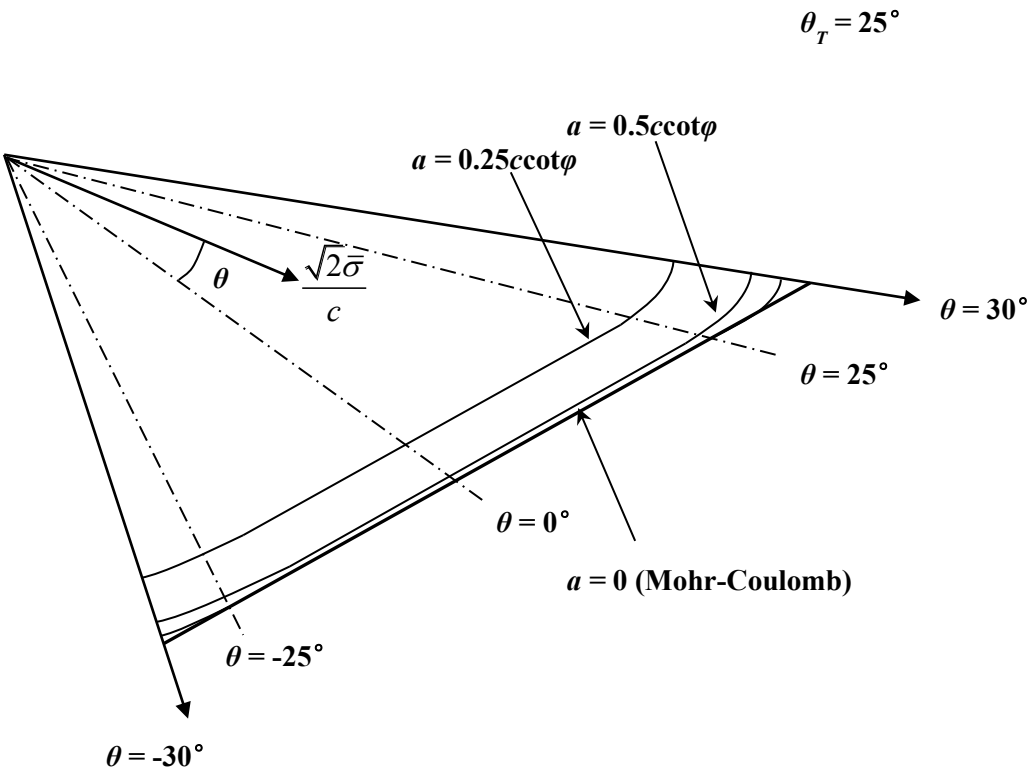

Figure 3-12: Rounded hyperbolic Mohr-Coulomb yield surface (Abbo & Sloan, 1995) in the octahedral plane

3.3.1.3 Plastic potential

In modelling the elasto-plastic behaviour of soils the use of a plastic potential Q independent from the yield function may be considered. This allows a more realistic representation of the dilatancy, which characterises the plastic response of frictional materials exhibiting significant pressure-sensitivity. In the adopted constitutive model for the backfill, a

hyperbolic plastic potential similar to the yield function (3-25) but with different material parameters is proposed. This is given by:

$$Q = \sigma_m \sin\varphi_q + \sqrt{\bar{\sigma}^2 \overline{S_q}^2 + a^2 \sin^2\varphi_q} - c_q \cos\varphi_q \tag{3-27}$$

where c_q can be taken equal to the cohesion c, the dilatancy angle φ_q can be assumed different from the friction angle φ (non-associated plastic formulation) and $\overline{S_q}$ can be calculated using the equation (3-21) where the angle φ is substituted by φ_q.

3.3.1.4 Solution procedure for local plasticity problem

An incremental strategy is adopted to calculate the solution of the elasto-plastic problem (Figure 3-183). The strain increment $d\boldsymbol{\varepsilon}_n$ is the primary variable calculated applying a differential operator to the variation of displacements at the current time/load step n (Bathe, 1996). A trial elastic stress vector $\boldsymbol{\sigma}_{trial,n}$ is calculated using the elastic stiffness matrix **D** to obtain:

$$\boldsymbol{\sigma}_{trial,n} = \boldsymbol{\sigma}_{n-1} + \mathbf{D} d\boldsymbol{\varepsilon}_n \tag{3-28}$$

where $\boldsymbol{\sigma}_{n-1}$ is the stress solution at the previous time step.

When the trial stresses cross the plastic surface (3-25), the solution for the plasticity problem is determined by using the implicit backward Euler method and the Kuhn-Tucker complementarity conditions (Simo & Hughes, 1998).

The total strain increment is divided into an elastic $d\boldsymbol{\varepsilon}_{el}$ and a plastic component $d\boldsymbol{\varepsilon}_{pl}$:

$$d\boldsymbol{\varepsilon}_n = d\boldsymbol{\varepsilon}_{el,n} + d\boldsymbol{\varepsilon}_{pl,n} \tag{3-29}$$

$$d\boldsymbol{\varepsilon}_{pl,n} = d\lambda_n \frac{\partial Q}{\partial \boldsymbol{\sigma}} \tag{3-30}$$

where $d\lambda_n$ is the increment of the plastic multiplier which is calculated together with the actual stress vector $\boldsymbol{\sigma}_n$ by solving the nonlinear equation system:

$$\begin{cases} \mathbf{R}_{\sigma,n} = \boldsymbol{\sigma}_n - \mathbf{D}\left(d\boldsymbol{\varepsilon}_n - d\lambda_n \left.\dfrac{\partial Q}{\partial \boldsymbol{\sigma}}\right|_n \right) - \boldsymbol{\sigma}_{n-1} = 0 \\ \mathrm{R}_{d\lambda,n} = F_{RHMC}\left(\boldsymbol{\sigma}_n\right) = 0 \end{cases} \tag{3-31}$$

where $\mathbf{R}_n = \left\langle \mathbf{R}_\sigma \quad \mathrm{R}_{d\lambda} \right\rangle_n^T$ is the vector of the residuals.

An iterative solution procedure based on the Netwon-Raphson method is adopted and the system in (3-31) is linearized, leading for the i^{th} iteration to:

$$\mathbf{R}_{n,i+1} \cong \mathbf{R}_{n,i} + \left[\mathbf{J}\right]_{n,i} \left\langle d\boldsymbol{\sigma} \quad d\lambda \right\rangle_{n,i}^{\mathrm{T}} = 0 \tag{3-32}$$

Thus,

$$\left\langle d\boldsymbol{\sigma} \quad d\lambda \right\rangle_{n,i}^{\mathrm{T}} = -\left[\mathbf{J}\right]_{n,i}^{-1} \mathbf{R}_{n,i} \tag{3-33}$$

where the 7×7 Jacobian matrix $\left[\mathbf{J}\right]_{n,i}$ is given by:

$$\left[\mathbf{J}\right]_{n,i} = \begin{bmatrix} \left\{ \mathbf{I}_6 + \mathbf{D} d\lambda \dfrac{\partial^2 Q}{\partial \boldsymbol{\sigma}^2} \right\} & \left\{ \mathbf{D} \dfrac{\partial Q}{\partial \boldsymbol{\sigma}} \right\} \\ \left\{ \dfrac{\partial F}{\partial \boldsymbol{\sigma}} \right\} & 0 \end{bmatrix}_{n,i} \tag{3-34}$$

where $\mathbf{I}_6$ is the 6×6 identity matrix.

Finally the local solution at the time\load step *n* can be found simply by iterative correction of the unknown variables until convergence, which is attained when the norm of the residuals is less than a tolerance δ:

$$\boldsymbol{\sigma}_n = \boldsymbol{\sigma}_{n-1} + \sum_j d\boldsymbol{\sigma}_{n,j} \tag{3-35}$$

with *j* increased until

$$\sqrt{\mathbf{R}_{n,j}\mathbf{R}_{n,j}} \le \delta \tag{3-36}$$

At the end of the iterative process, the consistent tangent stiffness matrix **K** can be obtained as the first derivative of the stresses with respect to the strains:

$$\mathbf{K} = \left[\frac{\partial \boldsymbol{\sigma}}{\partial \boldsymbol{\varepsilon}}\right]_n \tag{3-37}$$

This can be determined by linearizing the non-linear equations for the stress components, represented by $\mathbf{R}_{\sigma,n}$. Thus the stiffness **K** is calculated using the Jacobian $\mathbf{J}_n$, obtained at the convergence within the expression:

$$\mathbf{K}_n = \mathbf{P}^T \mathbf{J}_n^{-1} \mathbf{P} \mathbf{D} \tag{3-38}$$

where **P** corresponds to the projection 7×6 matrix on the six-dimensional stress space:

$$\mathbf{P} = \begin{bmatrix} \mathbf{I}_6 & \mathbf{0}_{6\times 1} \end{bmatrix}^T \tag{3-39}$$

in $\mathbf{0}_{6\times 1}$ is a 6×1 null matrix.

The accumulated plastic deformation at the end of the time/load step *n* is calculated by adding the plastic deformation increment $d\boldsymbol{\varepsilon}_{pl,n}$ (3-30) to the total plastic deformation at the previous step as below:

$$\boldsymbol{\varepsilon}_{pl,n} = \boldsymbol{\varepsilon}_{pl,n-1} + d\boldsymbol{\varepsilon}_{pl,n} \tag{3-40}$$

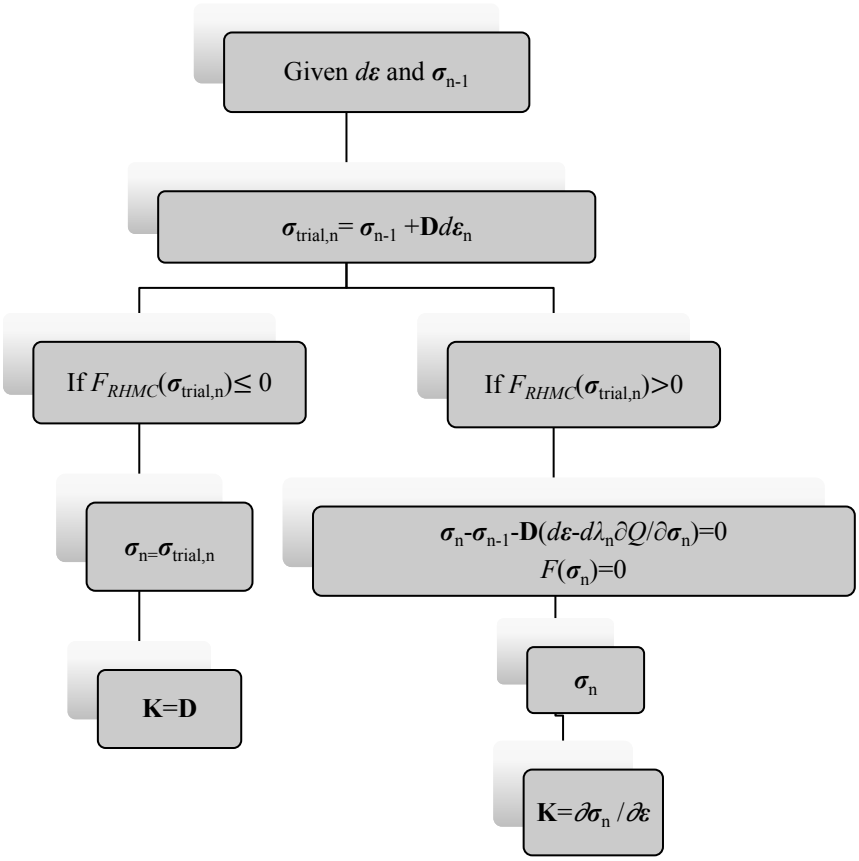

Figure 3-13: Solution procedure for the local plasticity problem

Finally, for completeness, the first and the second derivatives of the yield function and the plastic potential derived in (Abbo & Sloan, 1995), which are required for the solution of the local plastic problem (e.g. in equation (3-25)) are provided below.

Using the chain rule of differentiation the first derivative of the yield function F (or the plastic potential Q) can be expressed as:

$$\frac{\partial F}{\partial \boldsymbol{\sigma}} = C_1 \frac{\partial \sigma_m}{\partial \boldsymbol{\sigma}} + C_2 \frac{\partial \bar{\sigma}}{\partial \boldsymbol{\sigma}} + C_3 \frac{\partial J_3}{\partial \boldsymbol{\sigma}} \tag{3-41}$$

where:

$$C_1 = \frac{\partial F}{\partial \sigma_m} \tag{3-42}$$

$$C_2 = \frac{\partial F}{\partial \bar{\sigma}} - \frac{\tan 3\theta}{\bar{\sigma}} \frac{\partial F}{\partial \theta} \tag{3-43}$$

$$C_3 = -\frac{\sqrt{3}}{2\cos 3\theta \bar{\sigma}^3} \frac{\partial F}{\partial \theta} \tag{3-44}$$

$$\frac{\partial \sigma_m}{\partial \boldsymbol{\sigma}} = \frac{1}{3}\begin{bmatrix} 1 & 1 & 1 & 0 & 0 & 0 \end{bmatrix}^T \tag{3-45}$$

$$\frac{\partial \bar{\sigma}}{\partial \boldsymbol{\sigma}} = \frac{1}{2\bar{\sigma}}\begin{bmatrix} s_x & s_y & s_z & 2\tau_{xy} & 2\tau_{zx} & 2\tau_{yz} \end{bmatrix}^T \tag{3-46}$$

$$\frac{\partial J_3}{\partial \boldsymbol{\sigma}} = \begin{bmatrix} s_y s_z - \tau_{yz}^2 \\ s_x s_z - \tau_{xz}^2 \\ s_x s_y - \tau_{xy}^2 \\ 2\left(\tau_{yz}\tau_{zx} - s_z \tau_{xy}\right) \\ 2\left(\tau_{xz}\tau_{xy} - s_x \tau_{yz}\right) \\ 2\left(\tau_{xy}\tau_{yz} - s_y \tau_{xz}\right) \end{bmatrix} + \frac{\bar{\sigma}^2}{3}\begin{bmatrix} 1 \\ 1 \\ 1 \\ 0 \\ 0 \\ 0 \end{bmatrix} \tag{3-47}$$

Thus:

$$C_1 = \sin\varphi \tag{3-48}$$

$$C_2 = \alpha\left(\bar{S} - \tan 3\theta \frac{d\bar{S}}{d\theta}\right) \tag{3-49}$$

$$C_3 = \alpha\left(-\frac{\sqrt{3}}{2\cos 3\theta \bar{\sigma}^2} \frac{d\bar{S}}{d\theta}\right) \tag{3-50}$$

where:

$$\alpha = \frac{\bar{\sigma}\bar{S}}{\sqrt{\bar{\sigma}^2\bar{S}^2 + a^2 \sin^2\phi}} \tag{3-51}$$

$$\frac{d\bar{S}}{d\theta}=\begin{cases}-3S_2\cos 3\theta & |\theta|>\theta_T\\ -\sin\theta-\frac{1}{\sqrt{3}}\sin\phi\cos\theta & |\theta|\le\theta_T\end{cases} \tag{3-52}$$

Finally:

$$\frac{\partial F}{\partial\boldsymbol{\sigma}}=\begin{bmatrix}\frac{\partial F}{\partial\sigma_x}\\ \frac{\partial F}{\partial\sigma_y}\\ \frac{\partial F}{\partial\sigma_z}\\ \frac{\partial F}{\partial\tau_{xy}}\\ \frac{\partial F}{\partial\tau_{yz}}\\ \frac{\partial F}{\partial\tau_{zx}}\end{bmatrix}=\begin{bmatrix}\frac{C_1}{3}+C_2\frac{s_x}{2\bar{\sigma}}+C_3\left(s_ys_z-\tau_{yz}^2+\frac{\bar{\sigma}^2}{3}\right)\\ \frac{C_1}{3}+C_2\frac{s_y}{2\bar{\sigma}}+C_3\left(s_xs_z-\tau_{xz}^2+\frac{\bar{\sigma}^2}{3}\right)\\ \frac{C_1}{3}+C_2\frac{s_z}{2\bar{\sigma}}+C_3\left(s_xs_y-\tau_{xy}^2+\frac{\bar{\sigma}^2}{3}\right)\\ C_2\frac{\tau_{xy}}{\bar{\sigma}}+2C_3\left(\tau_{yz}\tau_{zx}-s_z\tau_{xy}\right)\\ C_2\frac{\tau_{yz}}{\bar{\sigma}}+2C_3\left(\tau_{xy}\tau_{zx}-s_z\tau_{yz}\right)\\ C_2\frac{\tau_{zx}}{\bar{\sigma}}+2C_3\left(\tau_{xy}\tau_{yz}-s_z\tau_{zx}\right)\end{bmatrix} \tag{3-53}$$

The second derivative of the plastic potential reads:

$$\frac{\partial^2 Q}{\partial\boldsymbol{\sigma}^2}=\frac{\partial C_2}{\partial\boldsymbol{\sigma}}^T\frac{\partial\bar{\sigma}}{\partial\boldsymbol{\sigma}}+C_2\frac{\partial^2\bar{\sigma}}{\partial\boldsymbol{\sigma}^2}+\frac{\partial C_3}{\partial\boldsymbol{\sigma}}^T\frac{\partial J_3}{\partial\boldsymbol{\sigma}}+C_3\frac{\partial^2 J_3}{\partial\boldsymbol{\sigma}^2} \tag{3-54}$$

where:

$$\frac{\partial C_2}{\partial\boldsymbol{\sigma}}=C_2\frac{\partial\alpha}{\partial\boldsymbol{\sigma}}+\alpha\frac{\partial\theta}{\partial\boldsymbol{\sigma}}\left(\frac{d\bar{S}}{d\theta}(1-3\sec^2 3\theta)-\tan 3\theta\frac{d^2\bar{S}}{d\theta^2}\right) \tag{3-55}$$

$$\frac{\partial C_3}{\partial\boldsymbol{\sigma}}=C_3\frac{\partial\alpha}{\partial\boldsymbol{\sigma}}+\alpha\frac{\sqrt{3}}{2\bar{\sigma}^2\cos 3\theta}\left(\frac{2}{\bar{\sigma}}\frac{d\bar{S}}{d\theta}\frac{\partial^2\bar{\sigma}}{\partial\boldsymbol{\sigma}^2}-\frac{\partial\theta}{\partial\boldsymbol{\sigma}}\left(\frac{d^2\bar{S}}{d\theta^2}+3\tan 3\theta\frac{d\bar{S}}{d\theta}\right)\right) \tag{3-56}$$

$$\frac{\partial\alpha}{\partial\boldsymbol{\sigma}}=\frac{1-\alpha^2}{\sqrt{\bar{\sigma}^2\bar{S}^2+\alpha^2\sin^2\varphi}}\left(\bar{S}\frac{\partial\bar{\sigma}}{\partial\boldsymbol{\sigma}}+\bar{\sigma}\frac{d\bar{S}}{d\theta}\frac{\partial\theta}{\partial\boldsymbol{\sigma}}\right) \tag{3-57}$$

$$\frac{\partial^2 \bar{\sigma}}{\partial \boldsymbol{\sigma}^2} = \frac{1}{\bar{\sigma}} \begin{bmatrix} \frac{1}{3} - \frac{s_x s_x}{4\bar{\sigma}^2} & -\frac{1}{6} - \frac{s_x s_y}{4\bar{\sigma}^2} & -\frac{1}{6} - \frac{s_x s_z}{4\bar{\sigma}^2} & -\frac{s_x \tau_{xy}}{2\bar{\sigma}^2} & -\frac{s_x \tau_{zx}}{2\bar{\sigma}^2} & -\frac{s_x \tau_{yz}}{2\bar{\sigma}^2} \\ -\frac{1}{6} - \frac{s_x s_y}{4\bar{\sigma}^2} & \frac{1}{3} - \frac{s_y s_y}{4\bar{\sigma}^2} & -\frac{1}{6} - \frac{s_y s_z}{4\bar{\sigma}^2} & -\frac{s_y \tau_{xy}}{2\bar{\sigma}^2} & -\frac{s_y \tau_{zx}}{2\bar{\sigma}^2} & -\frac{s_y \tau_{yz}}{2\bar{\sigma}^2} \\ -\frac{1}{6} - \frac{s_x s_z}{4\bar{\sigma}^2} & -\frac{1}{6} - \frac{s_y s_z}{4\bar{\sigma}^2} & \frac{1}{3} - \frac{s_z s_z}{4\bar{\sigma}^2} & -\frac{s_z \tau_{xy}}{2\bar{\sigma}^2} & -\frac{s_z \tau_{zx}}{2\bar{\sigma}^2} & -\frac{s_z \tau_{yz}}{2\bar{\sigma}^2} \\ -\frac{\tau_{xy} s_x}{2\bar{\sigma}^2} & -\frac{\tau_{xy} s_y}{2\bar{\sigma}^2} & -\frac{\tau_{xy} s_z}{2\bar{\sigma}^2} & 1 - \frac{\tau_{xy} \tau_{xy}}{\bar{\sigma}^2} & -\frac{\tau_{xy} \tau_{zx}}{\bar{\sigma}^2} & -\frac{\tau_{xy} \tau_{yz}}{\bar{\sigma}^2} \\ -\frac{\tau_{zx} s_x}{2\bar{\sigma}^2} & -\frac{\tau_{zx} s_y}{2\bar{\sigma}^2} & -\frac{\tau_{zx} s_z}{2\bar{\sigma}^2} & -\frac{\tau_{zx} \tau_{xy}}{\bar{\sigma}^2} & 1 - \frac{\tau_{zx} \tau_{zx}}{\bar{\sigma}^2} & -\frac{\tau_{zx} \tau_{yz}}{\bar{\sigma}^2} \\ -\frac{\tau_{yz} s_x}{2\bar{\sigma}^2} & -\frac{\tau_{yz} s_y}{2\bar{\sigma}^2} & -\frac{\tau_{yz} s_z}{2\bar{\sigma}^2} & -\frac{\tau_{yz} \tau_{xy}}{\bar{\sigma}^2} & -\frac{\tau_{yz} \tau_{zx}}{\bar{\sigma}^2} & 1 - \frac{\tau_{yz} \tau_{yz}}{\bar{\sigma}^2} \end{bmatrix} \tag{3-58}$$

$$\frac{\partial^2 J_3}{\partial \boldsymbol{\sigma}^2} = \frac{1}{3} \begin{bmatrix} s_x - s_y - s_z & 2s_z & 2s_y & 2\tau_{xy} & 2\tau_{zx} & -4\tau_{yz} \\ 2s_z & s_y - s_x - s_z & 2s_x & 2\tau_{xy} & -4\tau_{zx} & 2\tau_{yz} \\ 2s_y & 2s_x & s_z - s_x - s_y & -4\tau_{xy} & 2\tau_{zx} & 2\tau_{yz} \\ 2\tau_{xy} & 2\tau_{xy} & -4\tau_{xy} & -6s_z & 6\tau_{yz} & 6\tau_{zx} \\ 2\tau_{zx} & -4\tau_{zx} & 2\tau_{zx} & 6\tau_{yz} & -6s_y & 6\tau_{xy} \\ -4\tau_{yz} & 2\tau_{yz} & 2\tau_{yz} & 6\tau_{zx} & 6\tau_{xy} & -6s_x \end{bmatrix} \tag{3-59}$$

where C_1, C_2 and C_3 are calculated using the material properties for the plastic potential (e.g. dilatation angle).

3.3.2 Numerical comparisons

Before using the elasto-plastic material model for the backfill to investigate the response of masonry bridges, numerical simulations have been carried out comparing the results obtained using ADAPTIC against the numerical and analytical predictions found in the literature on the response of a strip footing. Zienkiewicz et al. (Zienkiewicz, Humpheson & Lewis, 1975) investigated the behaviour of a flexible and frictionless strip footing resting on clay. The footing was subjected to a uniformly distributed loading, which was increased up to failure neglecting the soil self-weight contribution. A 2D plane strain description with 32 8-noded parabolic elements was adopted together with the associated Mohr-Coulomb model for the

soil material with Young's modulus E = 207MPa, Poisson's ratio υ = 0.3, friction angle φ = 20° and cohesion c = 0.069MPa. The geometry, the loading and the boundary conditions of the analysed system are shown in Figure 3-14, where a fixed support condition is assumed at the bottom of the 3660mm deep uniform soil layer and roller supports at the two lateral vertical sides. Figure 3-15 shows the FE mesh in ADAPTIC.

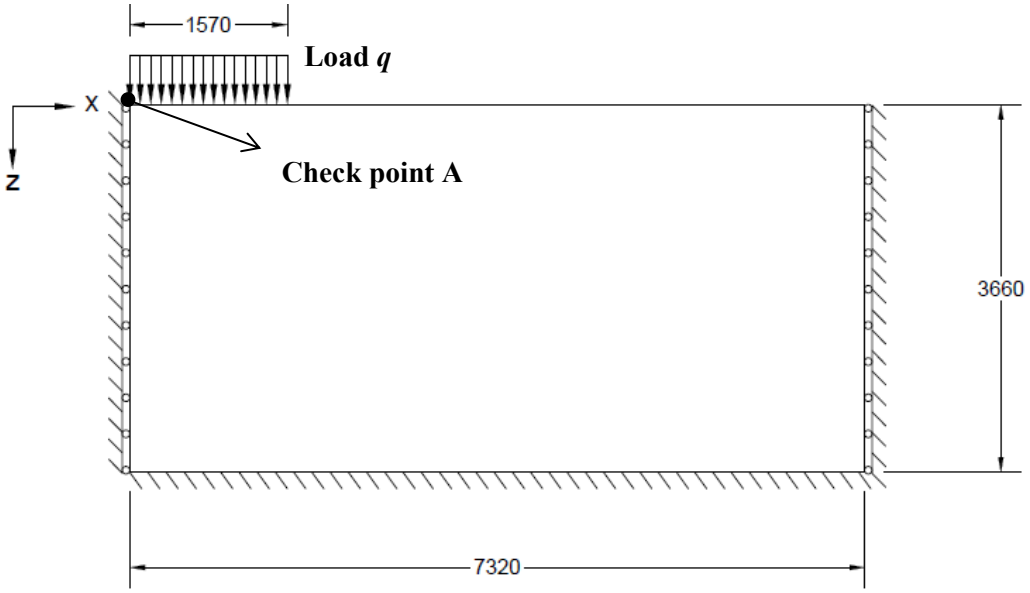

Figure 3-14: Strip footing

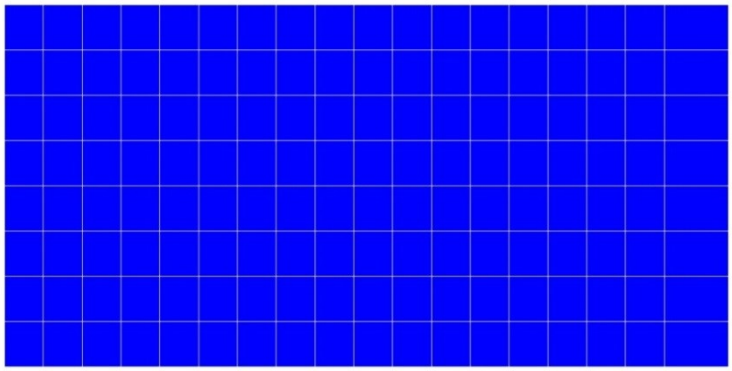

Figure 3-15: FE mesh in ADAPTIC for the strip footing on clay

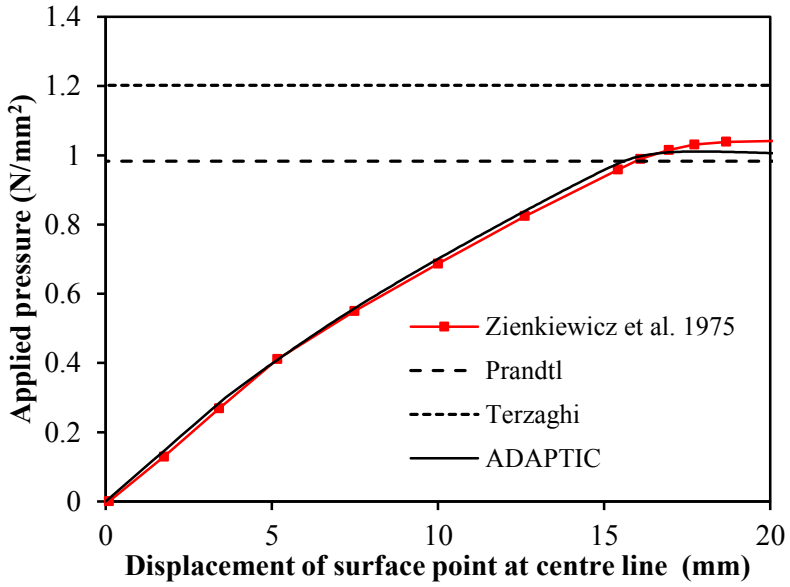

Figure 3-16: Numerical results for the strip footing

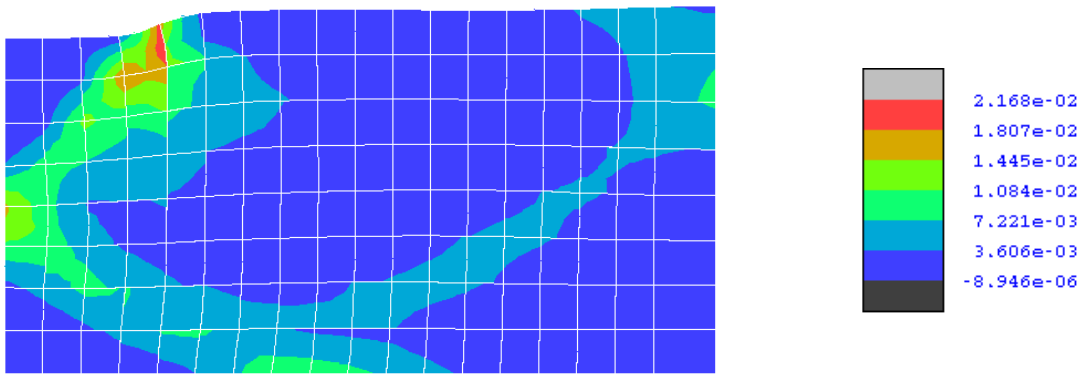

Figure 3-17: Equivalent von Mises plastic deformations in the soil material

The ADAPTIC numerical curve showing the variation of the vertical displacement at the right end of the footing (point A in Figure 3-14) with the applied pressure q is plotted in Figure 3-16, where it is also compared against the numerical response obtained in (Zienkiewicz, Humpheson & Lewis, 1975) using the original Mohr-Coulomb model and the Prandtl and Terzaghi ultimate load predictions. It can be seen that the model implemented in ADAPTIC provides results very close to the Zienkiewicz et al. (Zienkiewicz, Humpheson & Lewis, 1975) prediction, where the maximum load supported by the footing is close to the

Prandtl solution. This is reached when significant equivalent von Mises plastic deformations $\varepsilon_{pl,VM}$ ($\varepsilon_{pl,VM} = \sqrt{2/3\,\boldsymbol{\varepsilon}_{pl} : \boldsymbol{\varepsilon}_{pl}}$) develop within the soil domain as shown in Figure 3-17.

As discussed in section 3.3.1, the two parameters θ_T, and a_1 are utilized to adjust the shape of RHMC failure surface to approximate the classic Mohr-Coulomb failure envelope. Although Abbo (Abbo, 1997) proposed to use θ_T = 25° and a_1 = 0.05, the influence of these two parameters has not been quantitatively discussed. Numerical results obtained by varying the transition angle and a_1 are shown in Figure 3-18 and Figure 3-20. The influence of these two parameters on the ultimate loading capacity of the strip footing is illustrated in Figure 3-19 and Figure 3-21. It can be seen that all the numerical curves are very close to the Zienkiewicz et al. prediction which was obtained adopting the original Mohr-Coulomb model. The relative error, calculated assuming the Zienkiewicz et al. ultimate load prediction as exact, does not change significantly when the transition angles varies from 5° to 28°. On the other hand, by increasing a_1 the relative error increases accordingly as the rounded approximation moves away from the Mohr-Coulomb elastic boundaries. Very similar results have been obtained also in term of plastic deformations. This is shown in Figure 3-22 and Figure 3-23, where the equivalent von Mises plastic deformations $\bar{\varepsilon}_{pl}$ at the last step of the numerical simulations, when the displacement at the check point A reaches 20mm, are displayed. Only negligible differences can be noticed comparing the cases with different θ_T and a_1 values.

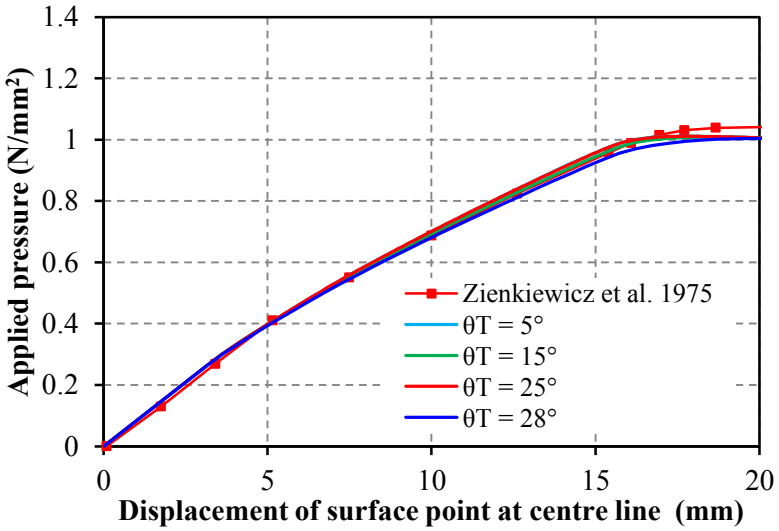

Figure 3-18: Numerical results for different transition angle θ_T values

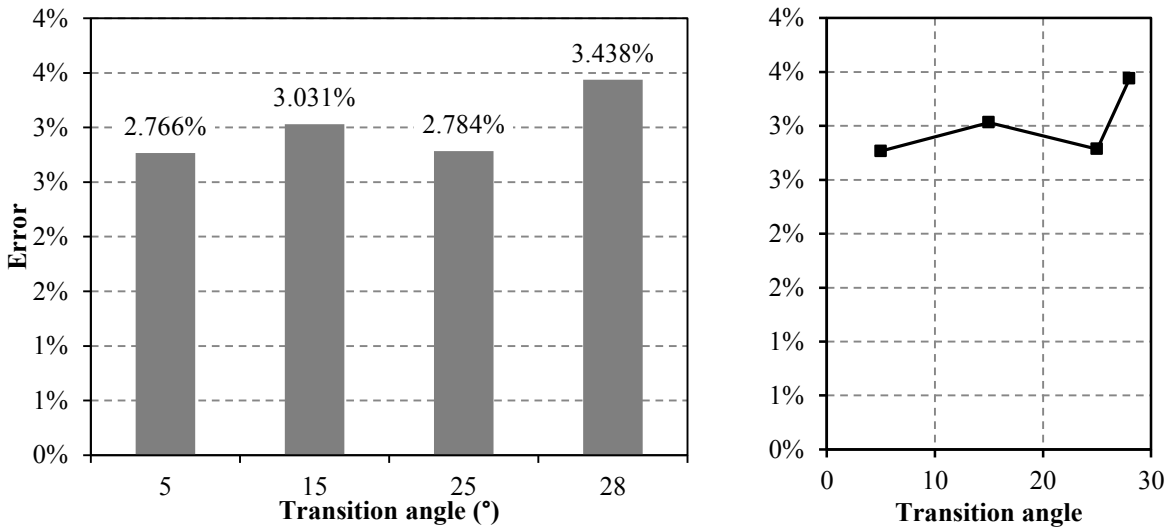

Figure 3-19: Influence of different transition angle θ_T on the ultimate load

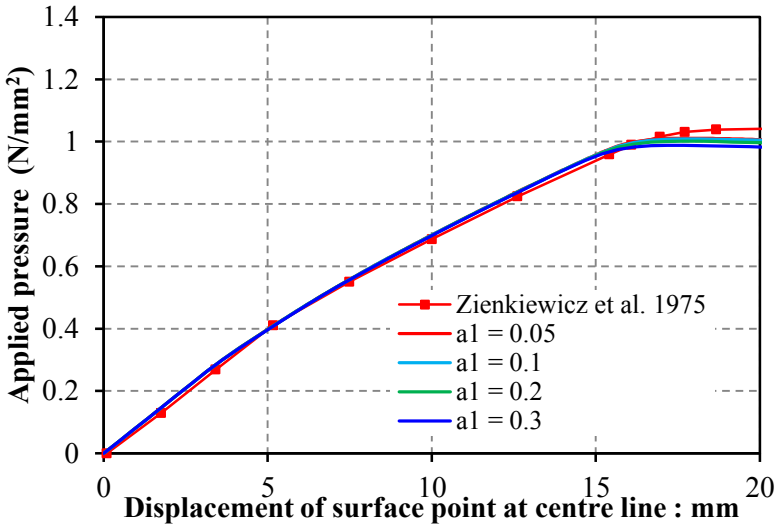

Figure 3-20: Numerical results for different values of a_1

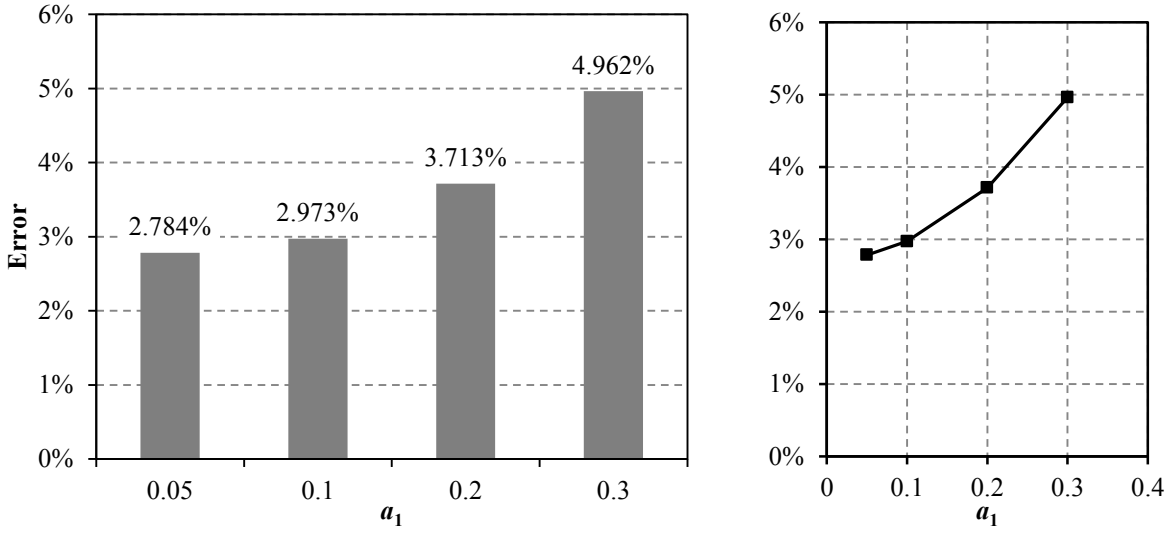

Figure 3-21: Influence of different values of a_1 on the ultimate load

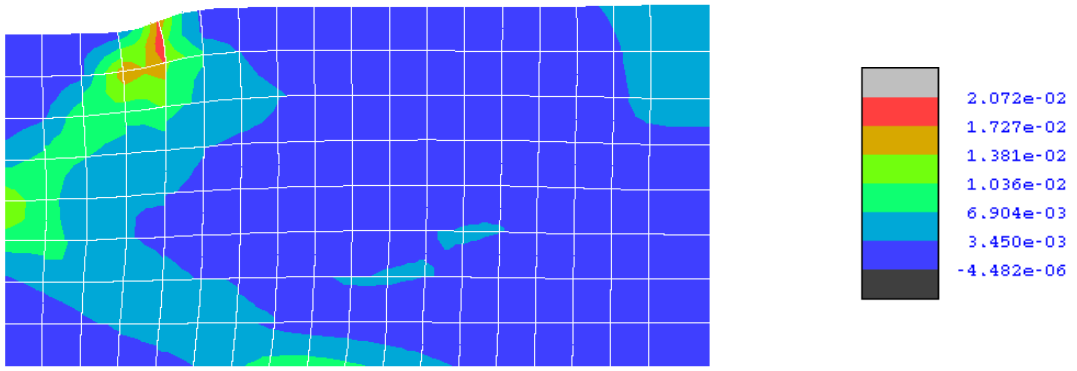

(a)

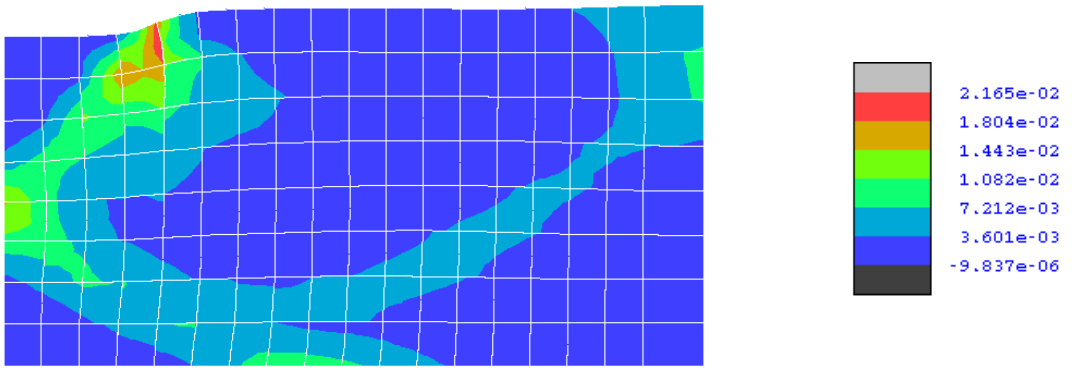

(b)

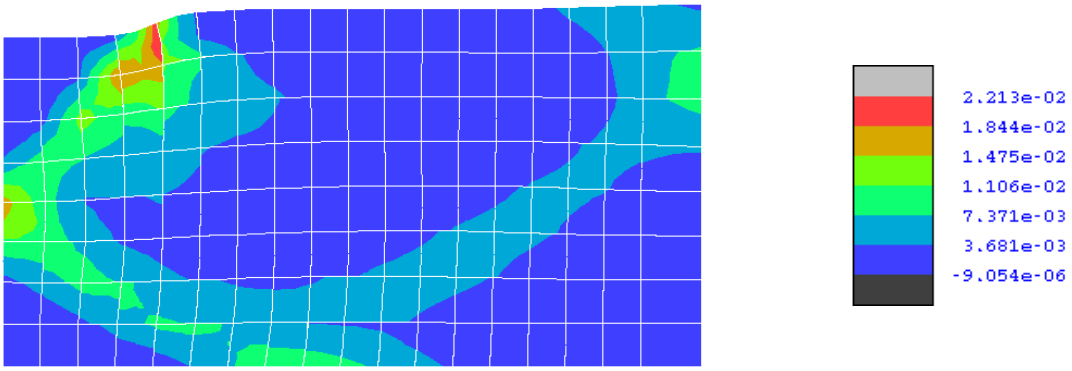

(c)

Figure 3-22: Equivalent von Mises plastic deformations for (a) $\theta_T = 5°$, (b) $\theta_T = 15°$ and (c) $\theta_T = 28°$

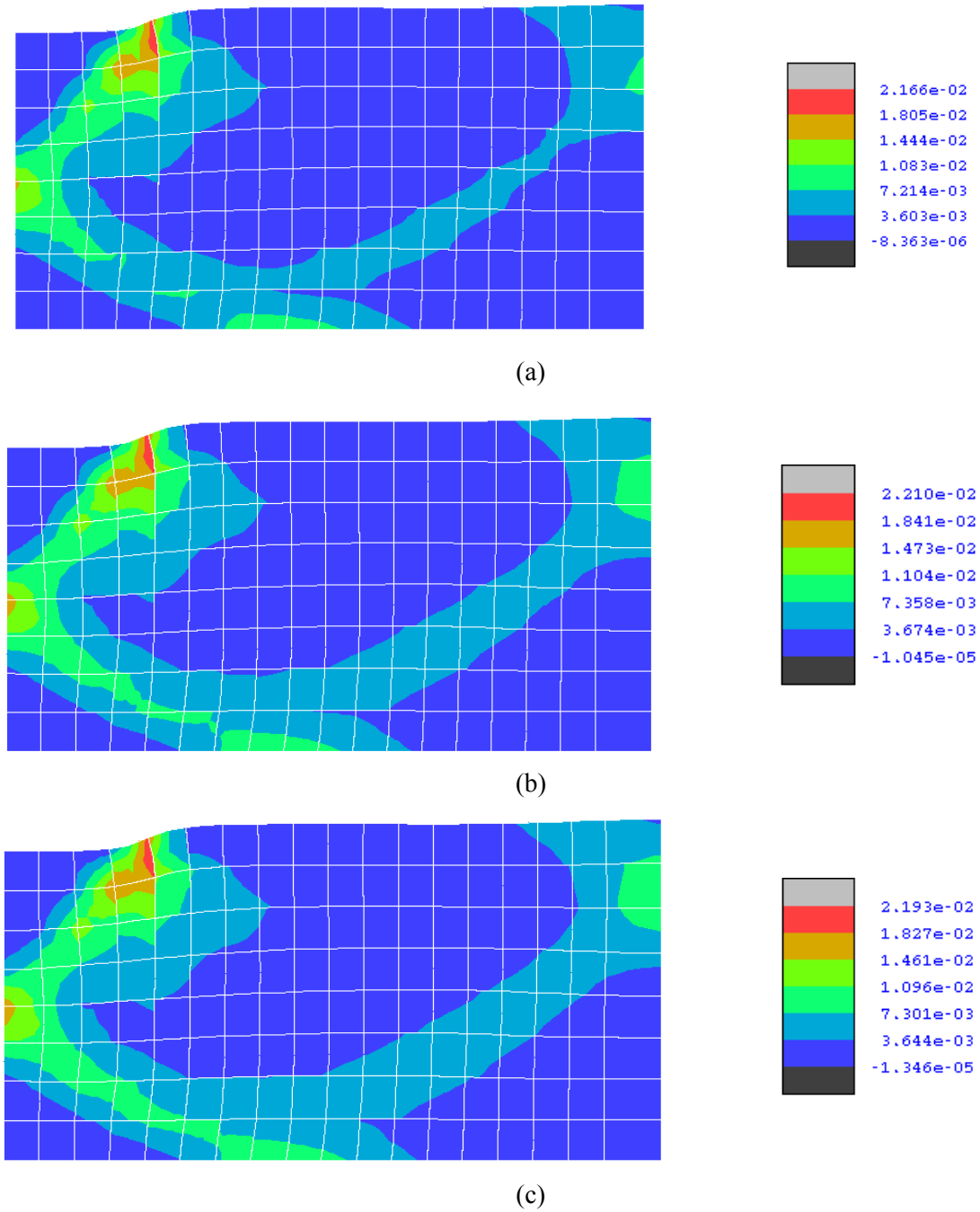

Figure 3-23: Equivalent von Mises plastic deformations in the soil material for (a) $a_1 = 0.1$, (b) $a_1 = 0.2$ and (c) $a_1 = 0.3$

3.4 Numerical modelling of arch-fill interaction and spandrel walls

The elasto-plastic formulation for soil materials presented before allows for a realistic description of the backfill behaviour, but not the interaction at the interface between the fill and the masonry arch. Physical tests on real masonry bridges (Page, 1989; Page, 1987) and laboratory models (Melbourne & Gilbert, 1995; Melbourne & Walker, 1989; Walker & Melbourne, 1988) showed that at collapse significant sliding at the arch-fill interface may develop together with extensive cracks in the masonry components of the bridge. In this respect, a rigid connection among the nodes of the arch and the fill at their interface does not enable the representation of potential separation and sliding between the two domains, and may also restrain the development of radial and longitudinal cracks in the masonry arch. Thus in the proposed 3D modelling strategy for masonry arch bridges, the discrete model with solid elements and nonlinear interfaces for the masonry arch and the continuous model for the backfill are connected by nonlinear interface elements, enabling relative movements between the two domains. In particular, the FE mesh for the backfill is constructed with the rectangular face of the 15-noded prismatic solid elements at the bottom of the backfill, where it rests on the arch, coincident with the top face of the solid elements representing masonry bricks at the extrados of the arch. In this way, as shown in Figure 3-24, 16-noded nonlinear interface elements can be easily arranged to connect the two separate domains, where one interface element connects the top face of one 20-noded solid element modelling a portion of the arch and the bottom rectangular face of the corresponding 15-noded solid element for the fill. The two faces with 8 nodes coincide in the initial undeformed configuration.

The same nonlinear model employed for representing cracks in the brick-masonry mesoscale description is also considered for modelling the nonlinear interaction between the backfill and the arch. This corresponds to a phenomenological description, which accounts not only for the frictional characteristics of the physical interface between the two domains, but also it

describes the nonlinear behaviour of a portion of the backfill close to the arch which is subjected to finite deformations when large relative movements between the arch and the backfill take place. Evidently this highly nonlinear behaviour cannot be effectively described using a standard continuous elasto-plastic model for the backfill.

In the proposed 3D numerical description for masonry arch bridges, the contribution of the spandrel walls is also taken into account. In this case only a simplified model is adopted, as the use of the brick-masonry mesoscale description employed for the masonry arch is quite problematic. This is due to the specific masonry bond of the lateral wall which does not allow a direct connection of the mesoscale mesh for wall to the arch, being the faces of the adjacent bricks at the interface of the two masonry components not coincident. Moreover, the use of the mesoscale description for the lateral walls would render the connection between the wall and the inner backfill impractical. In this case, the vertical 6-noded triangular faces solid elements for the backfill cannot be connected to the 8-noded rectangular faces of the solid elements modelling the bricks in the spandrel walls by standard interface elements representing the frictional characteristics of the physical interface. Because of these difficulties, in the proposed modelling approach, the spandrel wall contribution is modelled adopting the same strategy used for the backfill. Thus the continuous approach is employed and elasto-plastic solid elements with the Mohr-Coulomb model are used to describe the two lateral walls, where the FE mesh for each spandrel wall is a simple lateral extension of the FE mesh for the backfill. Evidently this can provide only an approximated description of the spandrel wall nonlinear response, but it allows an adequate representation of the contribution of the spandrel walls to restrain lateral expansion of the backfill, which takes place when vertical loads are applied on the road/rail supported by the bridge.

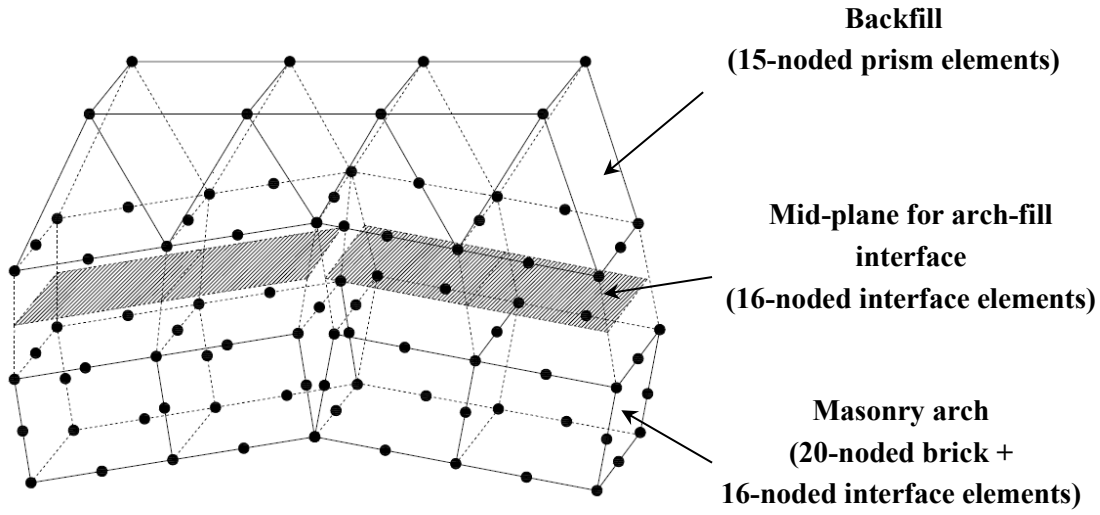

Figure 3-24: Modelling arch-fill interaction using 2D nonlinear interface elements

3.5 3D Mesoscale partitioned modelling for masonry arch bridges

When analysing large masonry structures, the use of the detailed 3D mesoscale strategy for brick/block masonry is impractical, because it requires an excessive computational effort. To overcome this intrinsic limitation, a novel computational strategy for brick\block-masonry has been recently proposed (Macorini & Izzuddin, 2013a), where the mesoscale description is incorporated within an advanced partitioned strategy. This has been previously developed at Imperial College (Jokhio & Izzuddin, 2013; Jokhio, 2012) to increase the computational efficiency in the analysis of large structural systems. The use of this advanced partitioning strategy allows realistic response predictions also for large masonry structures, where the accuracy is guaranteed by the use of a detailed mesoscale description at the structural scale.

According to this strategy, a large masonry component is modelled by a parent structure which comprises super-elements representing the partitioned subdomains. Dual super-elements are used for modelling the partitions as separate processes, where two-way

communication between each pair of dual parent/child super-elements allows effective parallelisation of the nonlinear structural analysis simulation (Jokhio & Izzuddin, 2013; Jokhio, 2012).

(Macorini & Izzuddin, 2013b) showed that the partitioned mesoscale approach for brick/block-masonry allows a significant speed-up *S*. This is an objective measure of computational efficiency, which, in this specific case, corresponds to the ratio between the wall-clock time required for the analysis of a masonry component modelled by the mesoscale approach using a serial code (monolithic simulation), and the time required for analysing the same structure employing the partitioned mesoscale strategy and parallel computing resources. In general, the speed-up increases when a large number of partitions is adopted, but it may decrease when the size of the parent structure, collecting the nodes at the partition boundary, becomes excessively large (Macorini & Izzuddin, 2013b).

More recently further enhancements have been introduced into the mesoscale partitioned approach to improve computational efficiency (Macorini & Izzuddin, 2013b). These include the use of hierarchic partitioning (Jokhio, 2012) and rigid constraints to reduce the number of freedoms at the partition boundary (Jokhio, 2012). The first enhancement enables the use of multi-level partitions, where the original child partitions are further subdivided by higher level super-elements. This way, partitions at one level are children to those at the upper level and parent to those at the lower level. This is shown in Figures 3-25b,c, where a two-level partitioning scheme for a masonry arch is sketched. The second improvement to the original partitioned mesoscale strategy considers to use master-slave hard coupling to connect several nodes on the slave surface at the partition boundaries with only one 6 freedoms master node (Figures 3-25d,e). Thus the displacements at each node on the slave surface can be fully determined from the displacements of the master node. This allows a significant reduction of the size (e.g. number of freedoms) of the parent structure, but with the expense of introducing unrealistic rigid constraints which may alter the strain/stress distribution at the partition boundaries (Macorini & Izzuddin, 2013b).

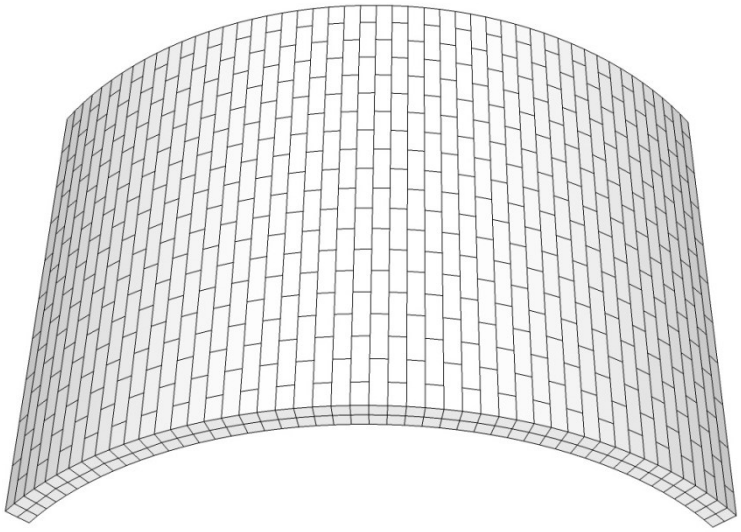

(a)

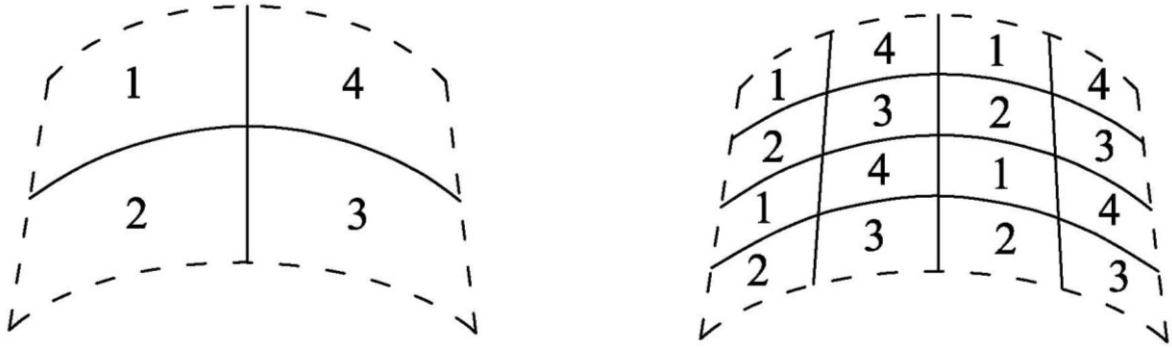

(b)

Figure 3-25: Partitioned modelling for (a) typical masonry arch barrel, (b) different levels of super elements for (c) hierarchic partitioning approach, (d) multi-dimensional coupling at the partition boundary and (e) mesoscale partitioning with multi-dimensional coupling for a masonry arch (Cont'd …)

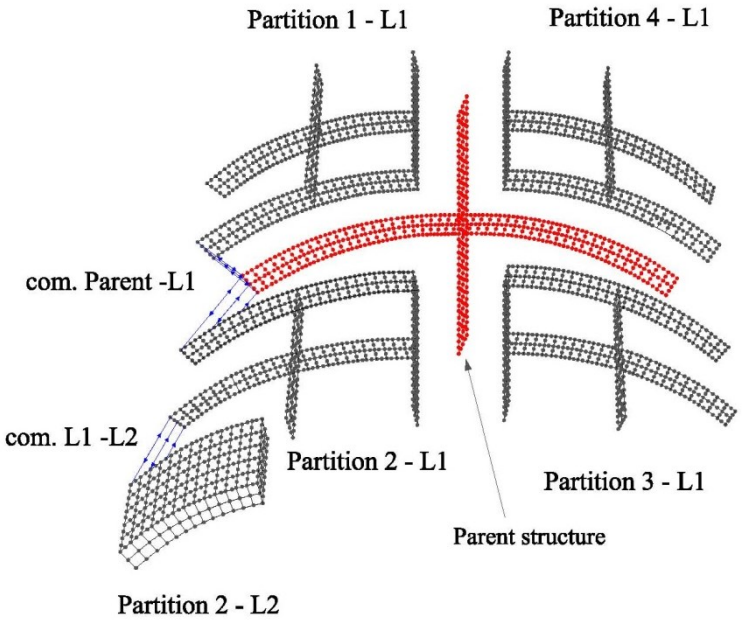

(c)

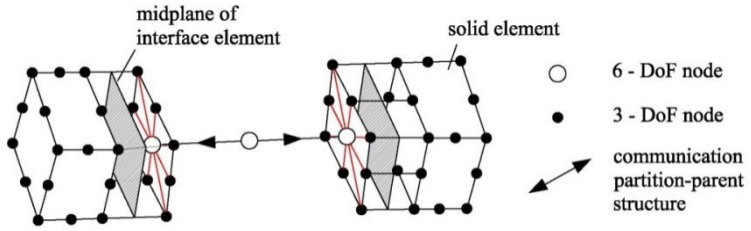

(d)

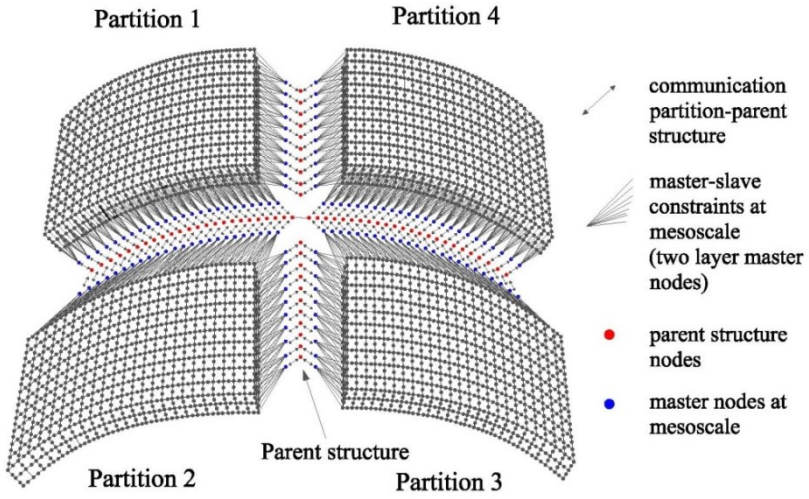

(e)

Figure 3-25: Partitioned modelling for (a) typical masonry arch barrel, (b) different levels of super elements for (c) hierarchic partitioning approach, (d) multi-dimensional coupling at the partition boundary (e) mesoscale partitioning with multi-dimensional coupling for a masonry arch

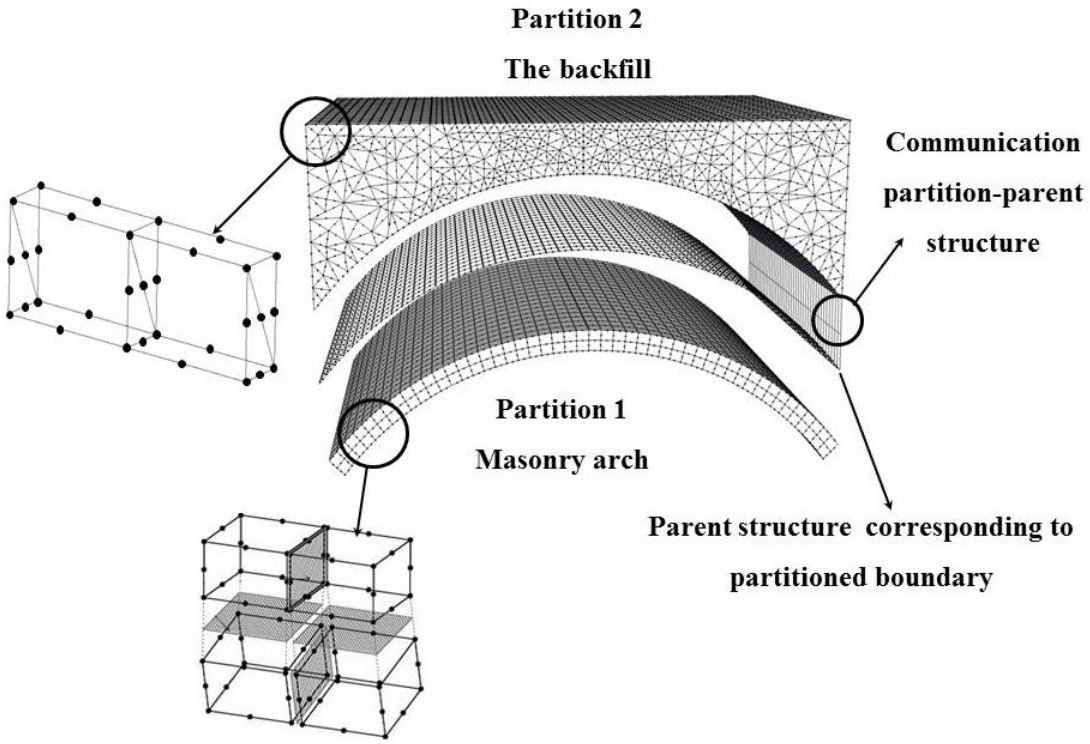

Figure 3-26: Partitioned modelling for masonry arch bridges

In the proposed 3D modelling strategy for brick/block masonry bridges, the enhanced partitioned strategy previously used for analysing large masonry structures (Macorini & Izzuddin, 2013b) is adopted. In this case, the basic partitioned model representing a realistic masonry arch bridge encompasses two partitions (Figure 3-26): one for the fill domain and the spandrel walls, which are modelled using the continuous approach with elasto-plastic solid elements considering different material properties, and the other for the whole masonry arch which is described using the mesoscale strategy with solid and nonlinear interface elements. Moreover, the second partition includes also the nonlinear interfaces representing the arch-fill interaction. The parent structure corresponds to the set of nodes at the partitioned boundary which are located the interface between the two separate domains (Figure 3-26). Evidently, to improve computational efficiency, hierarchic partitioning and master-slave coupling at the partitioned boundary can be used. This is shown in Figure 3-27, where a subdivision in higher level partitions for the masonry arch is sketched. In particular, for convenience, it has been assumed that the level of partitioning and the distribution of the

partitions can be defined independently for the two domains (arch and backfill with lateral walls), while the parent file collects all the nodes at the interface between the arch and the backfill.

To allow for a practical use of the proposed mesoscale partitioned strategy for masonry bridges, an automatic FE mesh generator has been recently developed (Rodriguez-Villares, 2014). This is coupled with Gmsh (Geuzaine & Remacle, 2009), a general 3D FE mesh generator for monolithic models, and it automatically generates the partition and parent input files for ADAPTIC.

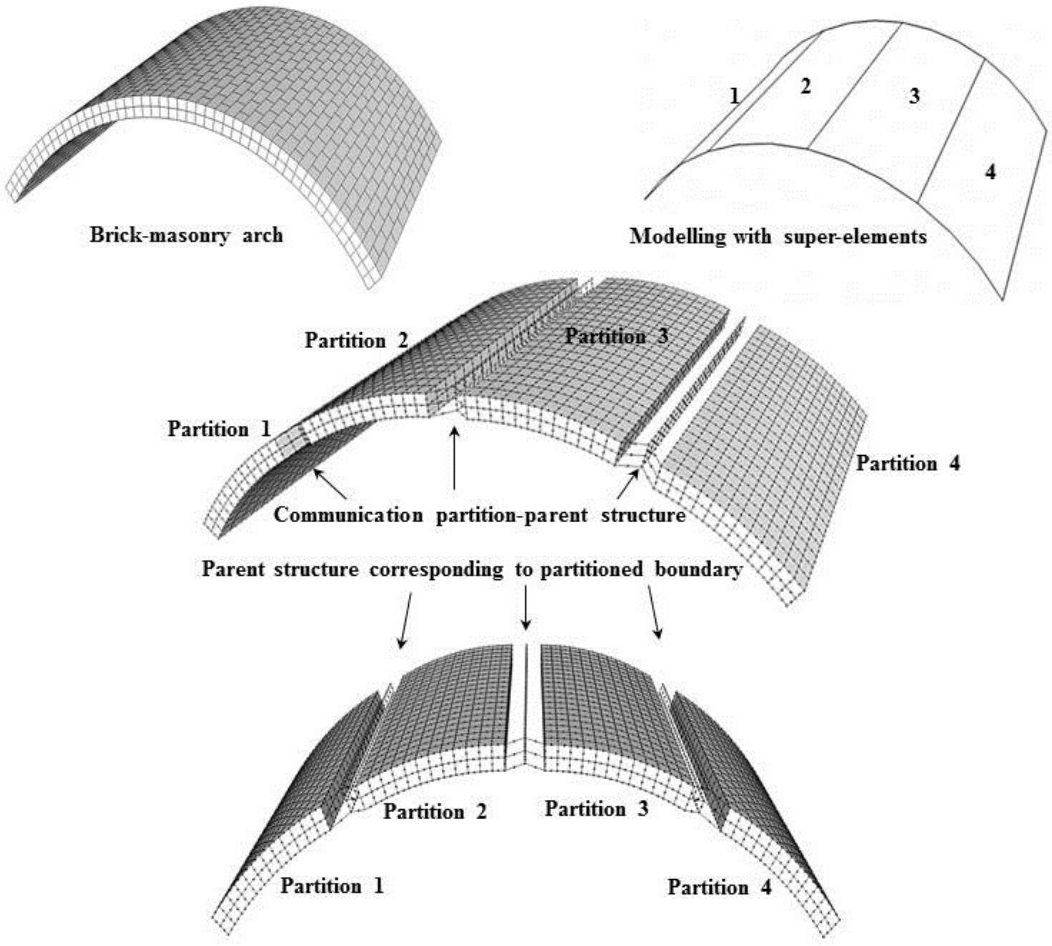

Figure 3-27: Higher level partitions for the masonry arch

3.6 Conclusions

In this chapter, an advanced FE modelling strategy for masonry arches and bridges has been presented. It is based upon a detailed 3D mesoscale modelling strategy, which employs solid and nonlinear interface elements to offer an accurate prediction of the development of damage and cracks in the masonry. A specific geometrical description for skew arches is provided. This enables the consideration of the actual arrangement of masonry units and mortar joints for skew arches built according to the helicoidal method. In the analysis of masonry bridges, elasto-plastic solid elements are employed for representing the backfill and the lateral walls, while the arch-backfill interaction is modelled by nonlinear interface elements, which consider the frictional characteristics of the physical interface between the two domains. As the computational cost of mesoscale simulations may become excessive, the detailed modelling approach for masonry arches and bridges is used within a partitioning strategy allowing for parallel computation, thus increasing computational efficiency.

CHAPTER 4

Validation of Mesoscale Modelling for Masonry Arches

4.1 Introduction

In previous research (Macorini & Izzuddin, 2014; Macorini & Izzuddin, 2011), the detailed mesoscale approach for brick/block-masonry described in Chapter 3 has been used in static and dynamic analysis of masonry walls, and its accuracy has been checked in several numerical-experimental comparisons. In the following, this approach is employed for the analysis of brick-masonry arches subjected to static loading, and numerical predictions are compared against experimental results. To this end, recent full-scale laboratory tests have been considered, where the analysed structures represent realistic arches similar to those found in existing masonry bridges. Multi-ring arches characterised by different failure mechanisms are analysed. These include square arches which fail due to the formation of radial cracks leading to a "hinge mechanism" or because of ring separation (Melbourne et al., 2007) and a skew arch characterised by a 3D failure mode (Wang, 2004). Such complex failure mechanisms can be accurately represented only by using specific material descriptions for masonry which account for the actual masonry bond, as the adopted 3D mesoscale modelling technique where bricks and brick-mortar joints are modelled separately. The full mesoscale description is also compared against models utilising a lower number of solid and nonlinear interface elements so as to identify the most accurate and computationally efficient strategy for modelling square and skew arches.

In the final part of this chapter, the mesoscale strategy for brick-masonry is combined with the partitioning approach previously developed at Imperial College (Jokhio, 2012) to the analysis of a large square arch. A partitioned mesoscale description allowing for parallel computation is used here to overcome the intrinsic limitation of detailed mesoscale models which is associated with high computational demand preventing the use of such models for the analysis of large structures. The results obtained using different partitioning strategies are compared, and the most efficient yet accurate strategy is selected. This will be then used in the analysis of realistic masonry bridges in Chapter 6, where the interaction between the masonry arch and the other components of masonry bridges (e.g. backfill) will be investigated.

Finally, it is important to note that focus is given not only to the ability of the proposed numerical descriptions to predict the ultimate arch capacity under static loading, but more in general to represent the complete structural response including the elastic behaviour and the progressive development of damage, which should be taken into account for an accurate safety assessment. This is in tune with recent research (Wang, Haynes & Melbourne, 2013; Melbourne & Tomor, 2004), which pointed out that the analysis of the response under serviceability loading is particularly important for the safety evaluation of masonry structures subjected to substantial repeated loading like masonry bridges. In these cases, damage accumulated in time under service loading may lead to a significant reduction of the ultimate capacity (Melbourne, Wang & Tomor, 2007).

4.2 Analysis of Square Arches

The accuracy of the proposed mesoscale description for the analysis of brick-masonry square arches has been checked considering the experimental results obtained in a series of laboratory tests on multi-ring arches under static loading. These were carried out at the University of Salford within the scope of the Sustainable Bridges research project (Melbourne et al., 2007).

4.2.1 Experimental tests

The masonry specimens comprise multi-ring 3m and 5m span arches with segmental circular shape and the same 4:1 span-to-rise ratio. These were constructed without headers to connect the two rings and employing class A engineering bricks (strong bricks) or Britley Olde English bricks (weak bricks). The strong bricks were used to represent high quality brickwork, while the weak bricks to represent aged brickwork as found in typical historical masonry bridges of the railway networks in Europe. All the bricks used in the tests are characterised by 215mm stretcher, 102.5mm thickness and 65mm header, while the mortar joints are 10mm thick with a volumetric cement:lime:sand ratio of 1:2:9. Reinforced concrete abutments were used to support the masonry arch barrels, which were bolted into the reinforced concrete strong floor of the laboratory to avoid movement at the supports. Material properties were obtained from a series of sample tests. These encompass tests to determine compressive strength and density of bricks and mortar and tests on masonry prisms to obtain the strength of masonry in compression. The results of the material tests are reported in Table 4-1.

Regarding the loading arrangement, vertical loads referred to as dead loads (*DL*) were applied near the quarter and the three quarter span of the arches either by steel weights or hydraulic jacks to represent the weight of the backfill above the arches of typical masonry bridges. A further load (live load - *LL*) was then applied near the quarter span in quasi-static increments of 1kN up to the collapse of the arch. Both horizontal and vertical displacements were measured near the quarter and the three quarter span using linear variable displacement transducers (LDVTs).

Table 4-1: Properties of mortar, bricks and masonry (Melbourne et al., 2007)

	Compressive strength $\sigma_{c,m}$ (MPa)	Density ρ (kN/m^3)
Strong bricks	154	23.7
Weak bricks	18.9	16.2
Mortar	1.86	15.5
Masonry prisms with strong bricks	24.5	22.0
Masonry prisms with weak bricks	9.1	16.0

Among the experimental specimens, two masonry arches are considered here for numerical-experimental comparisons. These correspond to a 3m span arch named *Arch G* (Melbourne et al., 2007) which was constructed using strong bricks and to a 5m span arch called *Arch T* (Melbourne et al., 2007) built with weak bricks. These two specimens showed different cracks patterns and failure modes in the tests; thus the numerical simulations of their response allows for an effective validation of the proposed mesoscale modelling approach.

4.2.2 Arch G

The specimen *Arch G* is a two-ring arch with strong bricks made up of 47 courses of bricks for the lower ring and 49 courses for the top ring. Its geometrical characteristics are reported in Table 4-2 and displayed together with the loading arrangement in Figure 4-1.

Table 4-2: Principal dimensions for *Arch G* (Melbourne et al., 2007)

Span (mm)	Rise (mm)	Span-to-rise ratio	Thickness (mm)	Width (mm)	Brickwork courses	Skew
3000	750	4:1	215	455	47/49	0°

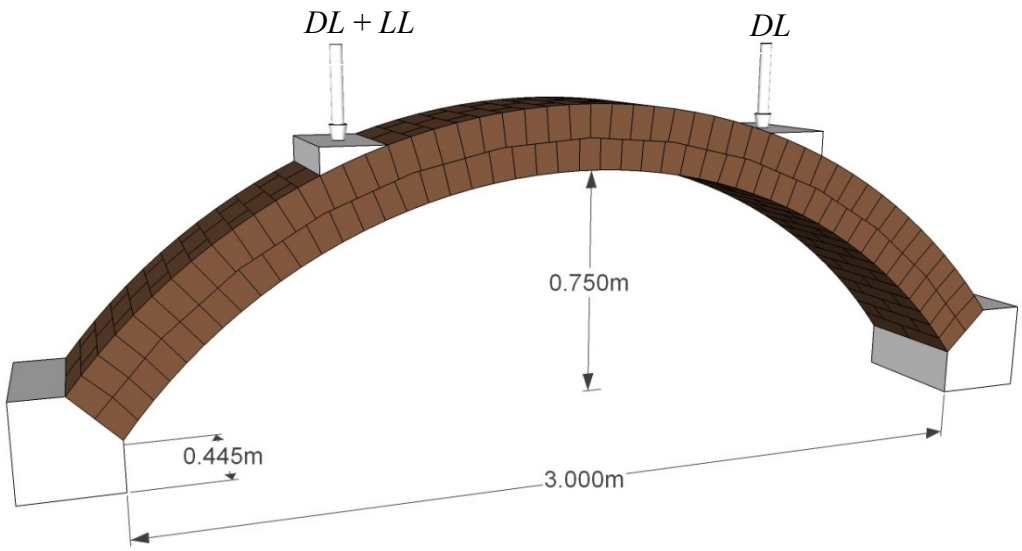

Figure 4-1: Geometric characteristics and loading arrangement for *Arch G*

In the test, the arch was initially loaded by two vertical dead loads applied at the quarter and the three quarter span equal to *DL* = 10kN, while a vertical live load *LL* was increased up to collapse under force control.

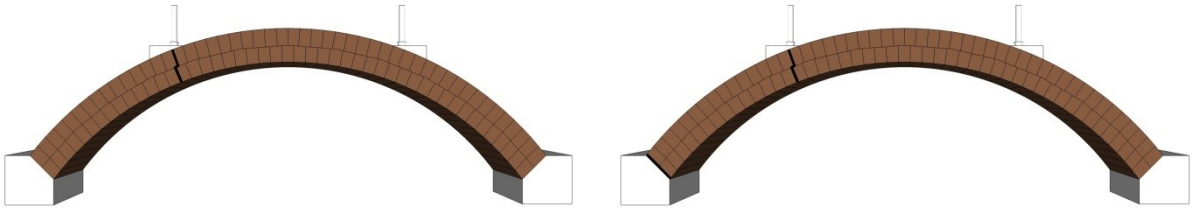

(a) 1st radial crack at quarter span (b) Radial cracks at left and right abutments

(c) Cracks at failure

Figure 4-2: Experimental crack patterns at different load levels: (a) 1st radial crack at quarter span, (b) radial cracks at left and right abutments and (c) cracks at failure

The experimental crack patterns at different live load levels are shown in Figure 4-2, which illustrates the progressive formation of four radial crack lines extending through the whole width of the arch. The first radial crack was found near quarter span, while the positions of the following two cracks were located at the left and right abutments, but their sequence was not reported in the test report (Melbourne et al., 2007). The arch became unstable after the opening of further cracks near the three quarter span, thus failing due to the formation of a mechanism (four-hinge mechanism) at about $LL_{u,exp}$ = 28kN. As the test was conducted under force control, after the attainment of the maximum load the test was terminated without investigating the post-peak response.

4.2.2.1 Model description

According to the adopted mesoscale approach for brick-masonry, the arch barrel is modelled accounting for the actual arrangement of bricks and mortar joints along the arch length, through the thickness of the arch and along its width. Only one simplification is introduced into the detailed model, as mortar radial bed joints for the two rings are considered continuous along the radial direction even though some small deviations from this condition can be seen in the actual masonry bond of the arch specimen (Figure 4-1). On the basis of this modelling assumption, 48 solid elements are used for representing the two brick courses of the bottom and the top ring. The employed finite element mesh in ADAPTIC is shown in Figure 4-3a,b where the elastic solid elements (Figure 4-3a) and the 2D nonlinear interface elements (Figure 4-3b) are displayed. In the proposed mesh, each half brick arranged along the y direction (Figure 4-3a) is represented by one 20-noded solid element, thus nonlinear interface elements (Figure 4-3b) are utilised not only to model circumferential bed and head mortar joints and radial head joints, but also potential fracture surfaces at the mid-plane of each brick. In total the FE mesh encompasses 48×4×2 solid elements, 48×4 interface elements for circumferential mortar bed joints, 47×4×2 and 48×3×2 interface elements for head joints along the span and the width of the arch.

Concerning the boundary conditions, the two reinforced concrete abutments which support the masonry arch barrel in the physical test are not explicitly included in the FE description. On the other hand the three degrees of freedom of all the nodes at the two end surfaces S1 and S2 are restrained to represent fixed-end supports.

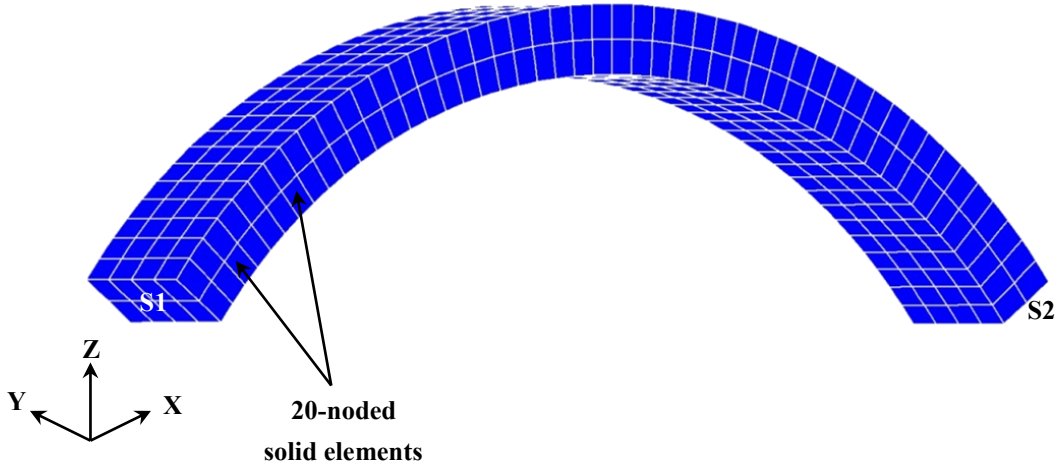

(a) FE mesh with solid elements

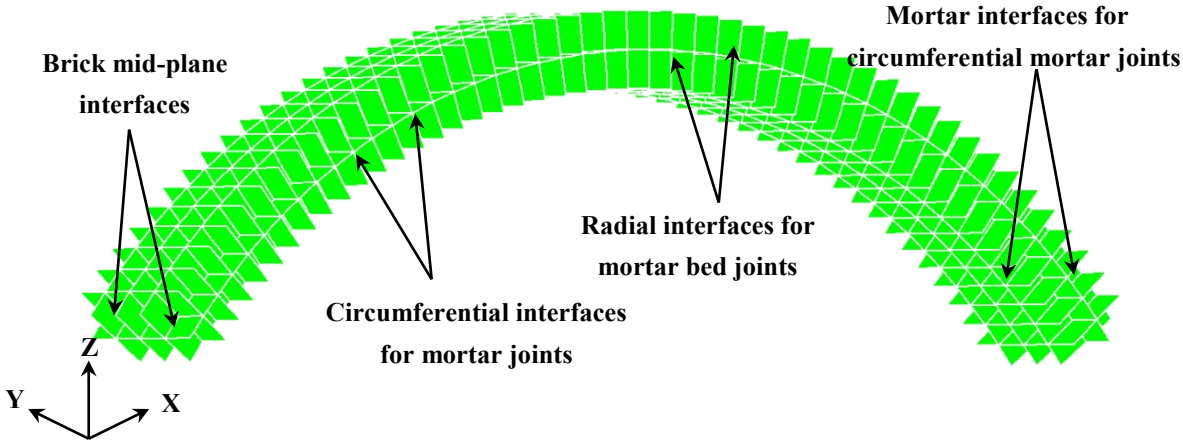

(b) FE mesh with interface elements

Figure 4-3: Mesh in ADAPTIC for Arch *G*: (a) FE mesh with solid elements and (b) FE mesh with interface elements

As the material properties for masonry components determined in the experimental program (Melbourne et al., 2007) comprise only compressive strength of bricks, mortar and masonry (Table 4-1) the complete set of elastic and nonlinear material parameters used in the mesoscale model for bricks and brick-mortar joints, as shown in Table 4-3, 4-4 and 4-5, have

been selected among the values used in previous research to represent high quality brickwork (Macorini & Izzuddin, 2011; Rots, 1997; Hodgson, 1996) so as to obtain a good correlation with the experimental response of the arch.

Table 4-3: Elastic properties for solid elements

	Elastic modulus E_b (N/mm^2)	**Poisson's ratio ν**
Brick unit	1.6×10^4	0.15

Table 4-4: Elastic properties for interface elements

	Normal stiffness K_n (N/mm^3)	**Tangent stiffness K_t (N/mm^3)**
Mortar interface	90	40
Brick-brick interface	1×10^5	1×10^5

Table 4-5: Inelastic properties of nonlinear interface elements

	Surface F_1	**Surface Q_1**	**Surfaces F_2, Q_2**
Mortar-brick interface	$C_0 = 0.40$N/mm^2 $\sigma_{t0} = 0.26$N/mm^2 $\tan\phi_0 = 0.5$ $G_{f1} = 0.12$N/mm $G_{f2} = 0.125$N/mm	$C_0 = 0.40$N/mm^2 $\sigma_{t0} = 0.26$N/mm^2 $\tan\psi_0 = 0.0$ $G_{f1} = 0.12$N/mm $G_{f2} = 0.125$N/mm	$D = 24.5$N/mm^2 $\sigma_{c0} = 24.5$N/mm^2 $\tan\theta_0 = 0.045$ $G_c = 5.0$N/mm
Brick-brick interface	$C_0 = 2.8$N/mm^2 $\sigma_{t0} = 2.0$N/mm^2 $\tan\phi_0 = 1.0$ $G_{f1} = 0.08$N/mm $G_{f2} = 0.5$N/mm	$C_0 = 2.8$N/mm^2 $\sigma_{t0} = 2.0$N/mm^2 $\tan\psi_0 = 1.0$ $G_{f1} = 0.08$N/mm $G_{f2} = 0.5$N/mm	

4.1.1.1 Numerical results

Experimental and numerical comparisons are presented in Figures 4-4 and 4-5, where the horizontal and the vertical displacements at quarter span and the horizontal displacement at three quarter span are displayed.

Numerical and experimental curves show a general good agreement until about LL = 15kN, when the first radial crack at quarter span is observed in the experimental test and predicted by the numerical model. At this loading level both the numerical and experimental curves diverge from the initial linear response, but all the numerical predictions show a stiffer response up to the maximum predicted load $LL_{u,num}$ = 27.8kN which is very close to the ultimate load measured in the test $LL_{u,exp}$ = 28kN. Moreover the predicted failure mechanism coincides with the experimental failure as well as the sequence of the formation of the four radial cracks (Figure 4-2) which developed because tensile stresses on large parts of some radial mortar head joints exceeded the tensile strength.

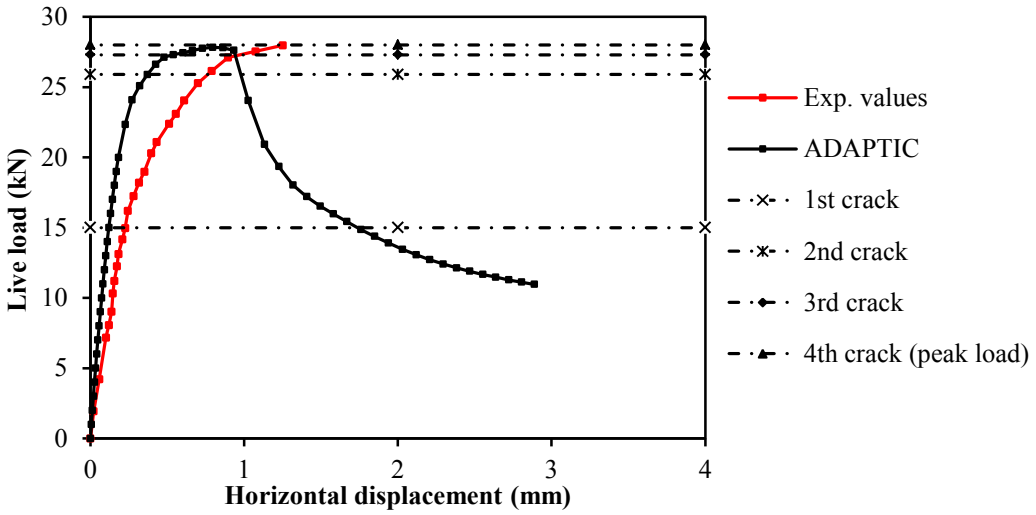

Figure 4-4: Experimental-numerical comparisons at three quarter span

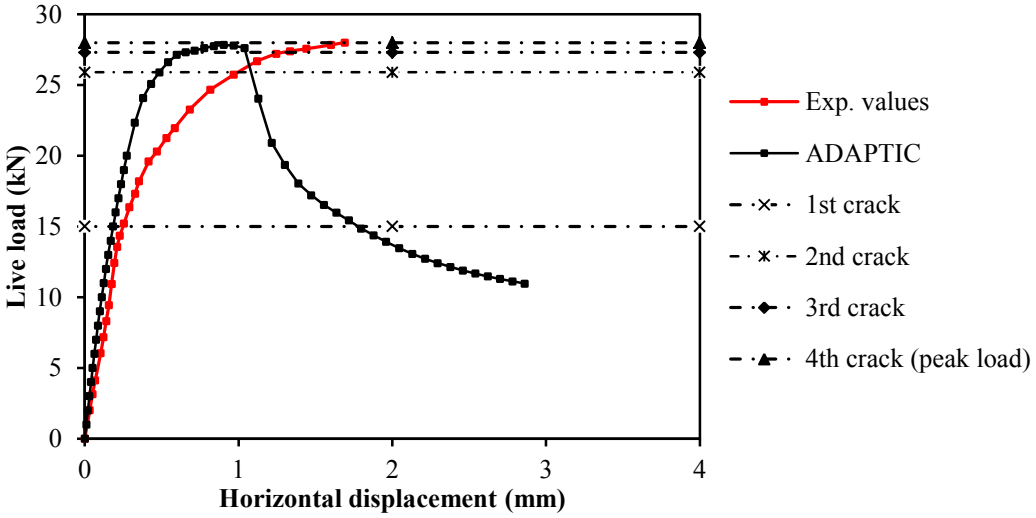

(a) Load-horizontal displacement curve

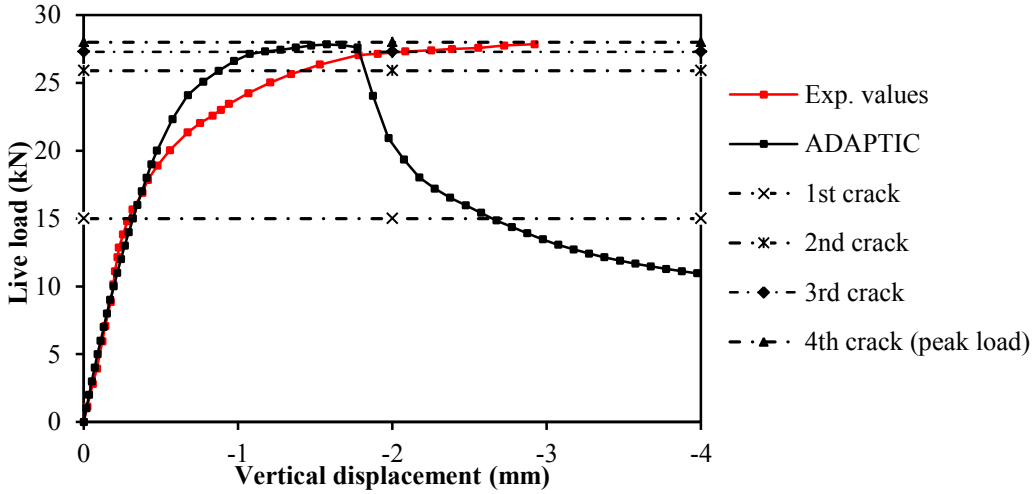

(b) Load-vertical displacement curve

Figure 4-5: Experimental-numerical comparisons at quarter span

Figure 4-6a,b,c,d,e, show the deformed shapes at different loading values corresponding to the development of the four main fracture lines and at the end of the numerical simulation. In accordance with the physical evidence, the numerical model predicts the consecutive formation of the second, third and fourth crack at loading levels which are very close, thus revealing an almost sudden transition from a stable deformation regime governed by only one main crack to an unstable failure mechanism with four radial fracture lines. As the numerical analysis was carried out using displacement control, also the post peak response has been

predicted as shown in the numerical curves in Figures 4-4 and 4-5, and in the final deformed shape in Figure 4-6e, where the full opening of the four cracks can be observed.

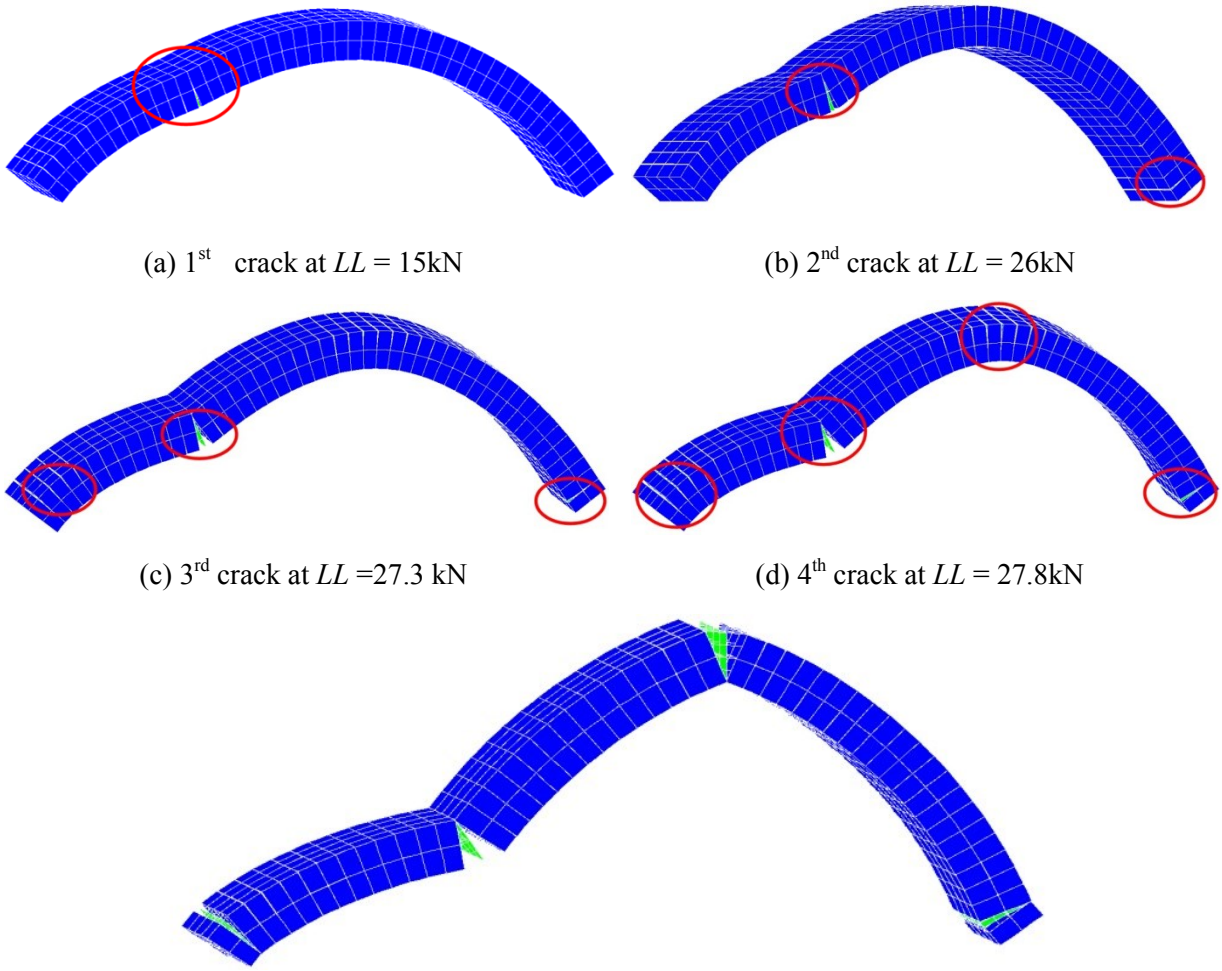

(a) 1st crack at *LL* = 15kN (b) 2nd crack at *LL* = 26kN

(c) 3rd crack at *LL* =27.3 kN (d) 4th crack at *LL* = 27.8kN

(e) Final stage

Figure 4-6: Deformed shapes: (a) 1st crack at *LL* = 15kN, (b) 2nd crack at *LL* = 26kN, (c) 3rd crack at *LL* = 27.3kN, (d) 4th crack at *LL* = 27.8kN and (e) Final stage

The numerical results provide also a quantitative description of the development of damage along the fracture lines. This is displayed in Figure 4-7a,b,c,d which show the plastic work W_{cr1} contour associated with the plastic surface F_1, where plastic work values approaching mode I fracture energy G_{f1} signifies complete degradation of the mortar resistance in tension.

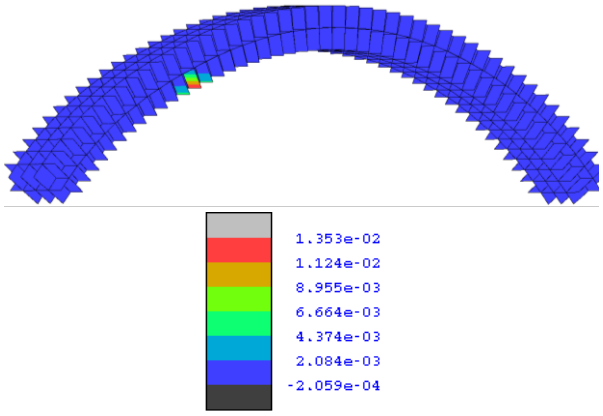

(a) 1st crack at *LL* = 15kN

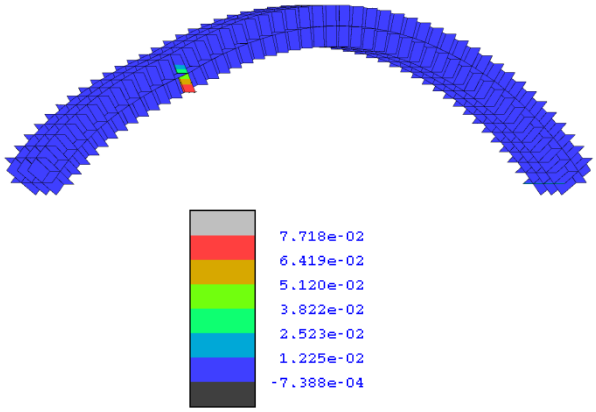

(b) 2nd crack at *LL* = 26kN

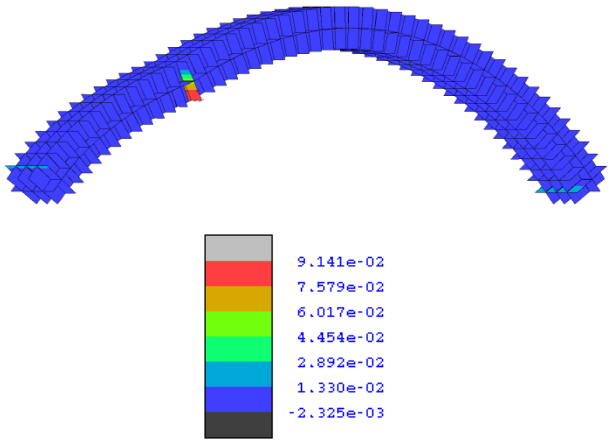

(c) 3rd crack at *LL* =27.3 kN

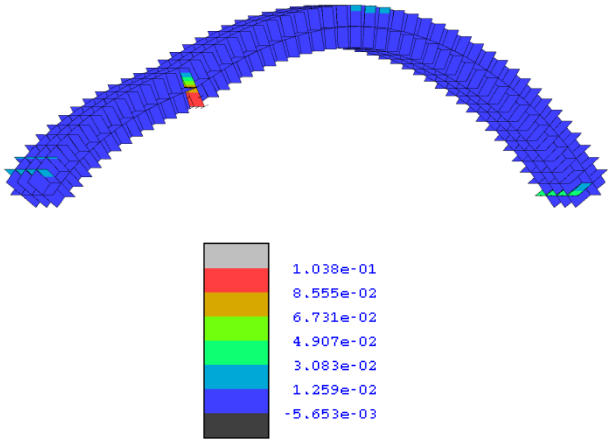

(d) 4th crack at *LL* = 27.8kN

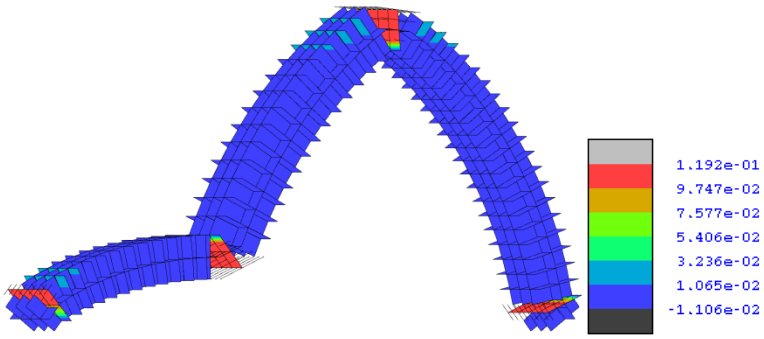

(e) Final step

Figure 4-7: Plastic work contour W_{cr1} (N/mm): (a) 1st crack at *LL* = 15kN, (b) 2nd crack at *LL* = 26kN, (c) 3rd crack at *LL* = 27.3kN, (d) 4th crack at *LL* = 27.8kN and (e) Final step

4.2.3 Arch T

The second square arch considered here for numerical-experimental comparisons corresponds to the *Arch T* specimen (Melbourne et al., 2007) which is characterised by a 5m span and three brickwork rings without interlocking headers along the span. Besides, this arch specimen is made up of weak brick units to represent deteriorated brickwork as found in many historical bridges. *Arch T* features 77, 80 and 83 courses for the bottom, the middle and the top ring respectively. The two end courses for the different rings were fixed to two reinforced concrete abutments as shown in Figure 4-8. The main dimensions of the arch are listed in Table 4-6.

Table 4-6: Principal dimensions for *Arch T* (Melbourne et al., 2007)

Span (mm)	Rise (mm)	Span-to-rise ratio	Thickness (mm)	Width (mm)	Brickwork courses	Skew
5000	1250	4:1	330	675	77/80/83	0°

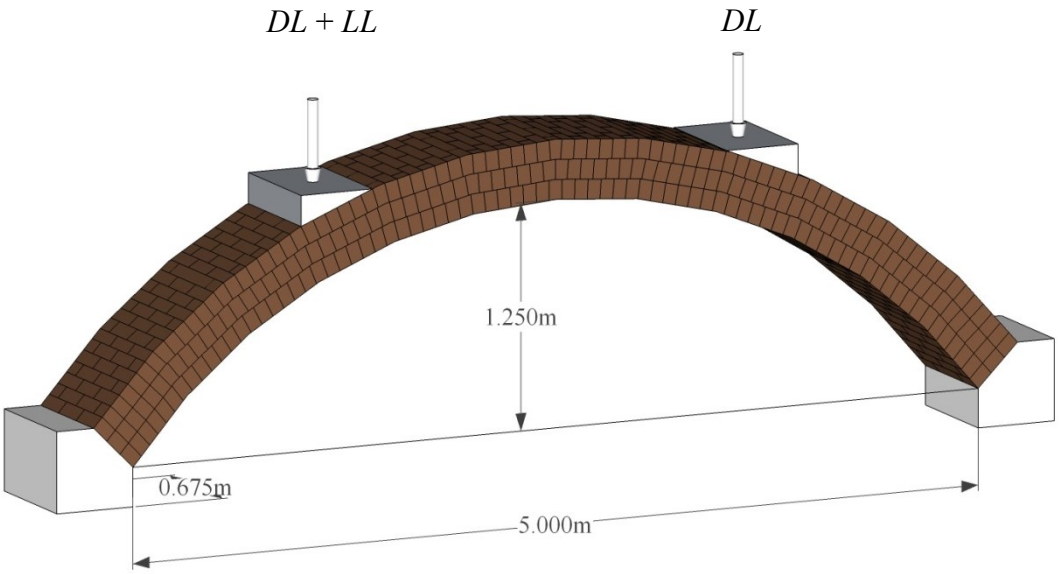

Figure 4-8: Geometric description of *Arch T*

As in the case of the *Arch G*, two equal vertical point loads *DL* = 22.5kN were applied at quarter and three quarter span and maintained constant throughout the test. Moreover, a vertical load *LL* applied at quarter span was monotonically increased up to the arch collapse.

During the test, initial radial cracks were found near the quarter span extending through the bottom two rings. Successively, ring separation developed from the quarter span to the half span at about LL = 26kN. Further load increments caused the formation of more radial cracks leading to the collapse of the masonry sample at $LL_{exp,max}$ = 31kN.

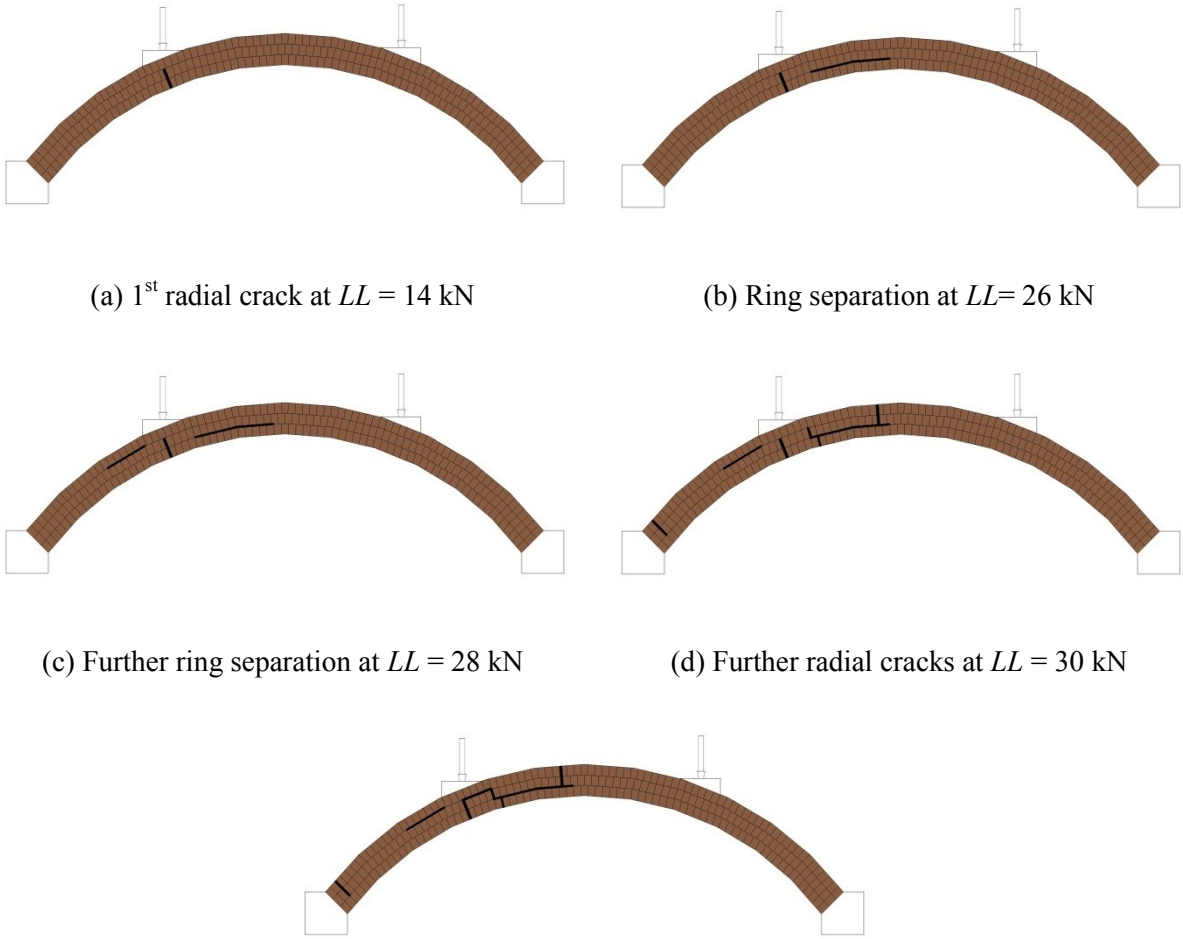

(a) 1st radial crack at LL = 14 kN

(b) Ring separation at LL= 26 kN

(c) Further ring separation at LL = 28 kN

(d) Further radial cracks at LL = 30 kN

(e) Cracks at failure at LL = 31kN

Figure 4-9: Experimental crack patterns: (a) 1st radial crack at LL = 14kN, (b) ring separation at LL = 26kN, (c) further ring separation at LL = 28kN, (d) further radial cracks at LL = 30kN and (e) cracks at failure at LL = 31kN

Figure 4-9 shows the development of radial cracks and ring separation at different load levels. As illustrated in the figure, crack propagation is mainly located between the quarter and the

middle span, where ring separation combined with radial cracks dominate the response of the whole arch up to collapse.

4.2.3.1 Model description

The same modelling technique considered in the previous example is used here to model arch *T*. As shown in Figure 4-10a,b, each half brick arranged along the y direction (Figure 4-10a) is modelled by one 20-noded solid element and nonlinear interface elements (Figure 4-10b) are utilised to represent circumferential mortar joints and radial bed joints as well as potential fracture surfaces at the mid-plane of each brick. Moreover, as before, the mortar radial joints for the three rings are considered continuous along the radial direction and 80 solid elements are adopted for the brick courses of the three rings. Thus the FE mesh for the arch consists of 80×6×3 solid elements, 80×6×2 interface elements for bed joints, 79×6×3 interface elements for bed joints along the span and 80×5×3 along the width of the arch, where the nodes at the two end surfaces S1 and S2 (Figure 4-10a) are fully restrained to represent fixed-end supports.

Material properties for solid elements and nonlinear interfaces are different from the values considered in the *Arch G* model. This is due to different type of brickwork used to build the two arches, where the *Arch T* specimen is made up of degraded brickwork with weak bricks. As no material tests have been performed in the experimental program to determine the specific material properties required for the mesoscale description, typical material parameters found in the literature (Macorini & Izzuddin, 2013b; Oliveira, 2003) to represent historical brick-masonry have been considered here for numerical-experimental comparisons. The adopted material properties are reported in Tables 4-7, 4-8 and 4-9.

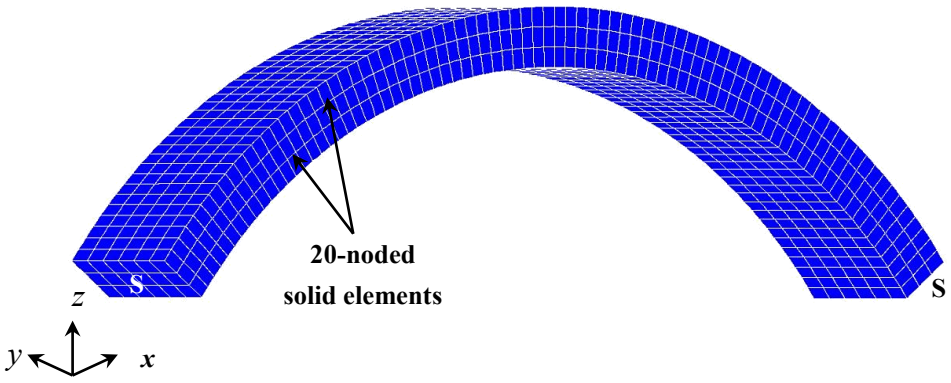

(a) FE mesh with solid elements

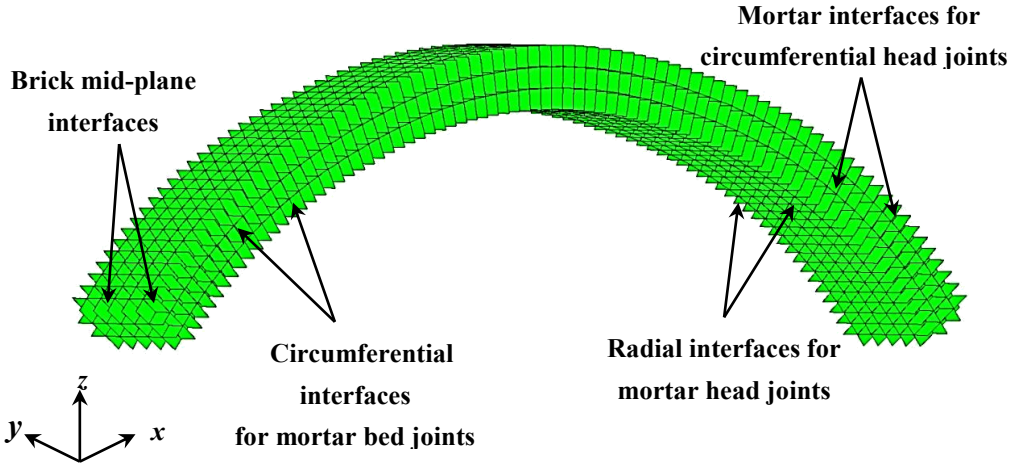

(b) FE mesh with interface elements

Figure 4-10: Mesh in ADAPTIC for *Arch T* with (a) solid elements and (b) interface elements

Table 4-7: Elastic properties for solid elements

	Elastic modulus E_b (N/mm^2)	**Poisson's ratio ν**
Brick unit	6×10^3	0.15

Table 4-8: Elastic properties for interface elements

	Normal stiffness K_n (N/mm^3)	**Tangent stiffness K_t (N/mm^3)**
Mortar interface	60	30
Brick-brick interface	1×10^5	1×10^5

Table 4-9: Inelastic properties of nonlinear interface elements

	Surface F_1	Surface Q_1	Surfaces F_2, Q_2
Mortar-brick interface	$C_0 = 0.07\text{N/mm}^2$ $\sigma_{t0} = 0.05\text{N/mm}^2$ $\tan\phi_0 = 0.5$ $G_{f1} = 0.02\text{N/mm}$ $G_{f2} = 0.125\text{N/mm}$	$C_0 = 0.07\text{N/mm}^2$ $\sigma_{t0} = 0.05\text{N/mm}^2$ $\tan\psi_0 = 0.0$ $G_{f1} = 0.02\text{N/mm}$ $G_{f2} = 0.125\text{N/mm}$	$D = 9.1\text{N/mm}^2$ $\sigma_{c0} = 9.1\text{N/mm}^2$ $\tan\theta_0 = 0.045$ $G_c = 5\text{N/mm}$
Brick-brick interface	$C_0 = 1.8\text{N/mm}^2$ $\sigma_{t0} = 1.2\text{N/mm}^2$ $\tan\phi_0 = 1.0$ $G_{f1} = 0.08\text{N/mm}$ $G_{f2} = 0.5\text{N/mm}$	$C_0 = 1.8\text{N/mm}^2$ $\sigma_{t0} = 1.2\text{N/mm}^2$ $\tan\psi_0 = 1.0$ $G_{f1} = 0.08\text{N/mm}$ $G_{f2} = 0.5\text{N/mm}$	

4.2.3.2 Numerical results

In Figures 4-11 and 4-12, the numerical results are compared against the experimental curves for the horizontal displacement at quarter span and the horizontal and the vertical displacement at three quarter span. As in the previous case, horizontal lines mark the loading values associated with the formation of the cracks observed in the experimental test. In this numerical-experimental comparison the maximum capacity is overestimated by the proposed mesoscale model, as the numerical maximum load $LL_{num,max}$ = 34.29kN exceeds the experimental ultimate load of 8.6%. On the other hand, the arch stiffness until the formation of the first crack at LL = 14kN is accurately predicted. For higher loading values, both the experimental and the numerical curves become nonlinear with a similar degradation of stiffness caused by the formation of further radial and longitudinal cracks. All the experimental curves, but the curve for the horizontal displacement at three quarter span, terminate well before the numerical curves which show a substantial final part where the displacements increase with an almost constant vertical force. This is because some of the

instruments used to measure the displacements in the test were removed to avoid damage when the arch became unstable due to the development of radial and longitudinal cracks at quarter span.

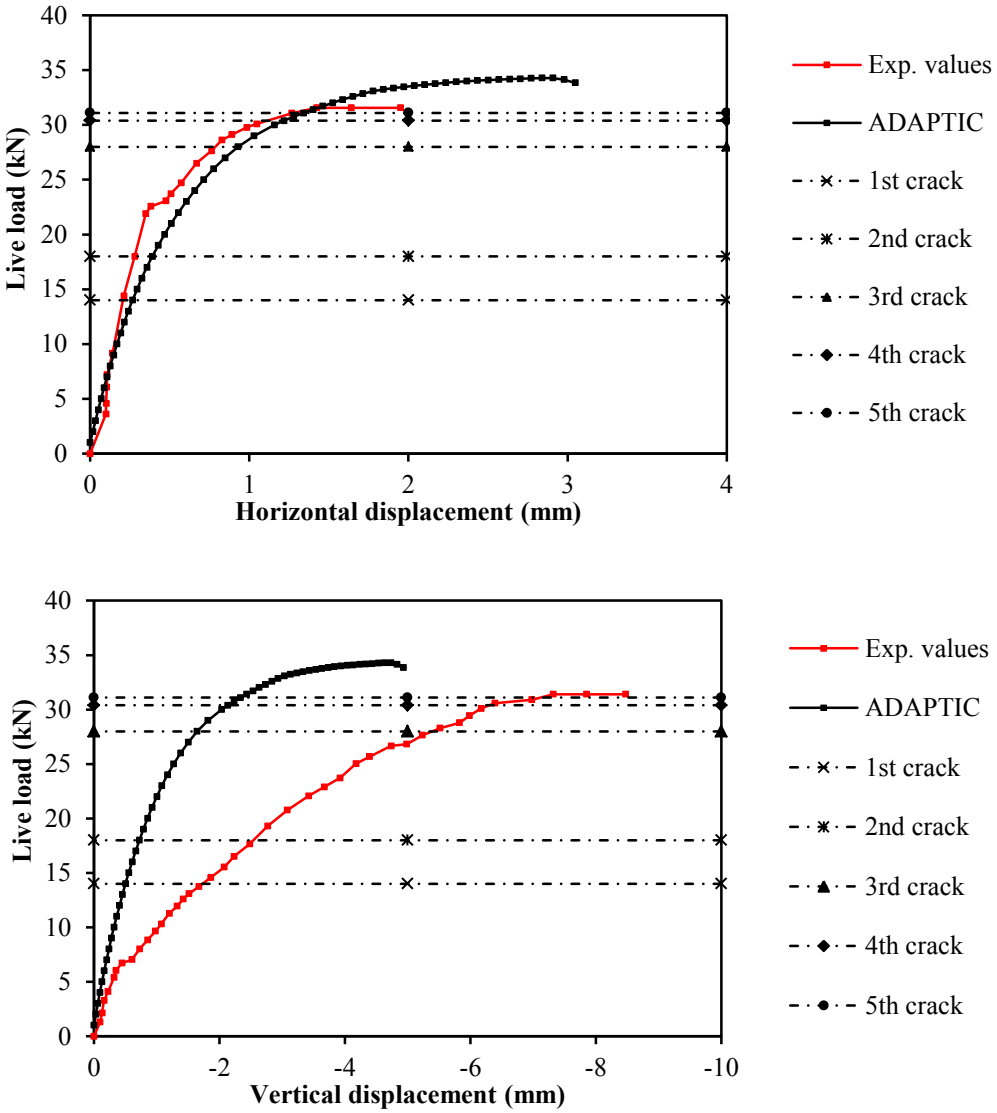

Figure 4-11: Experimental-numerical comparisons at quarter span

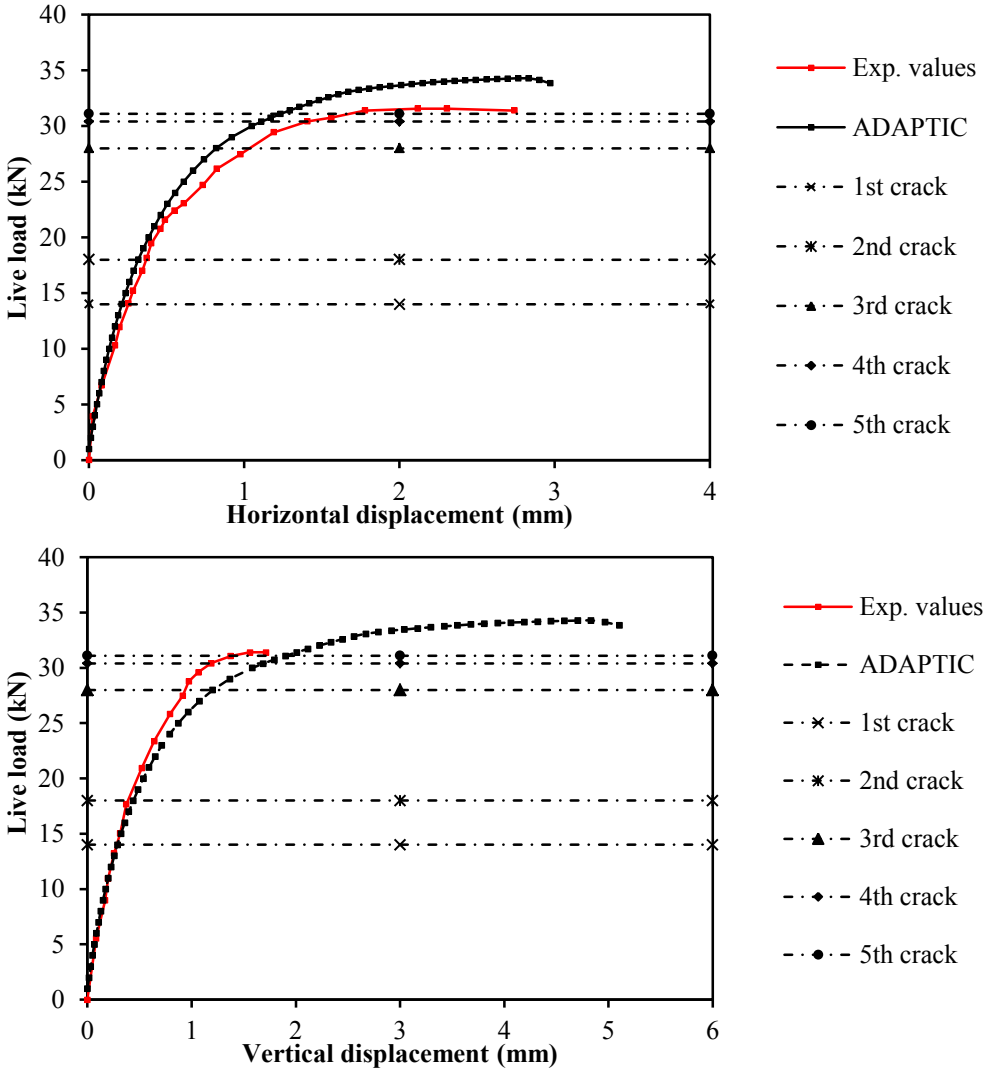

Figure 4-12: Experimental-numerical comparisons at three quarter span

The predicted position and sequence of the cracks up to the collapse of the arch (Figure 4-13) is in good agreement with what was observed in the experimental test (Figure 4-9). The onset of ring separation is predicted as in the experimental test at about LL = 26kN when a significant stiffness reduction was measured. The plastic work contour in Figure 4-14 shows that when approaching the maximum load, plastic work values at radial cracks are very large and close to the mode-I fracture energy. On the other hand plastic work values at longitudinal cracks along the circumferential mortar joints connecting adjacent rings at quarter span are not so significant and far from the mode-II fracture energy which determine the complete

cohesion exhaustion. This is not in agreement with the experimental evidence as large sliding with complete detachment of adjacent rings was observed at maximum load when the arch collapsed. This may be due to the specific material parameters used for the numerical model, as most of them were selected according to previous research and not directly determined in physical material tests within the experimental program on the masonry arches.

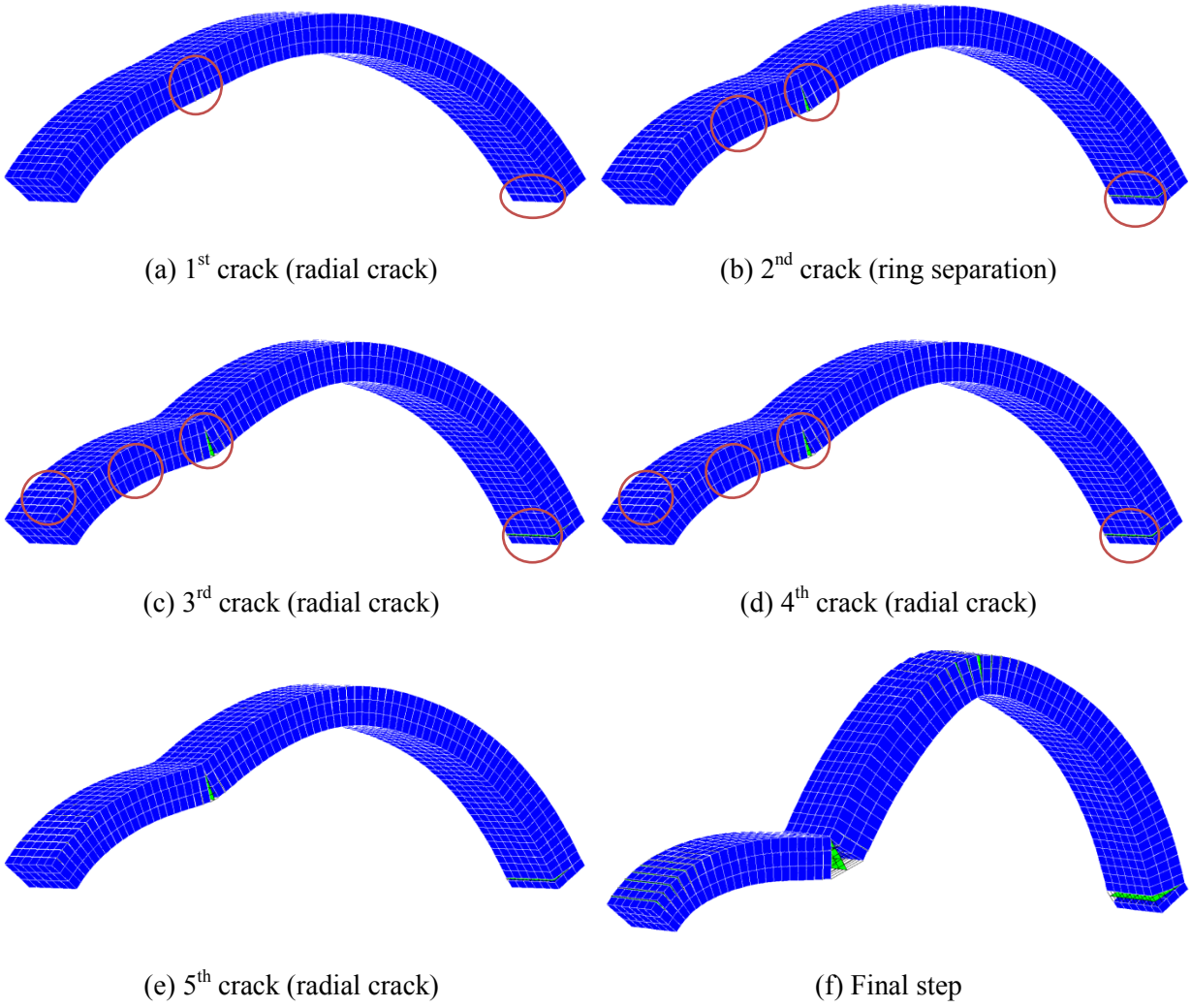

(a) 1st crack (radial crack) (b) 2nd crack (ring separation)

(c) 3rd crack (radial crack) (d) 4th crack (radial crack)

(e) 5th crack (radial crack) (f) Final step

Figure 4-13: Deformed shapes of *Arch T*: (a) 1st crack (radial crack), (b) 2nd crack (ring separation), (c) 3rd crack (radial crack), (d) 4th crack (radial crack) and (e) 5th crack (radial crack) and (f) final step

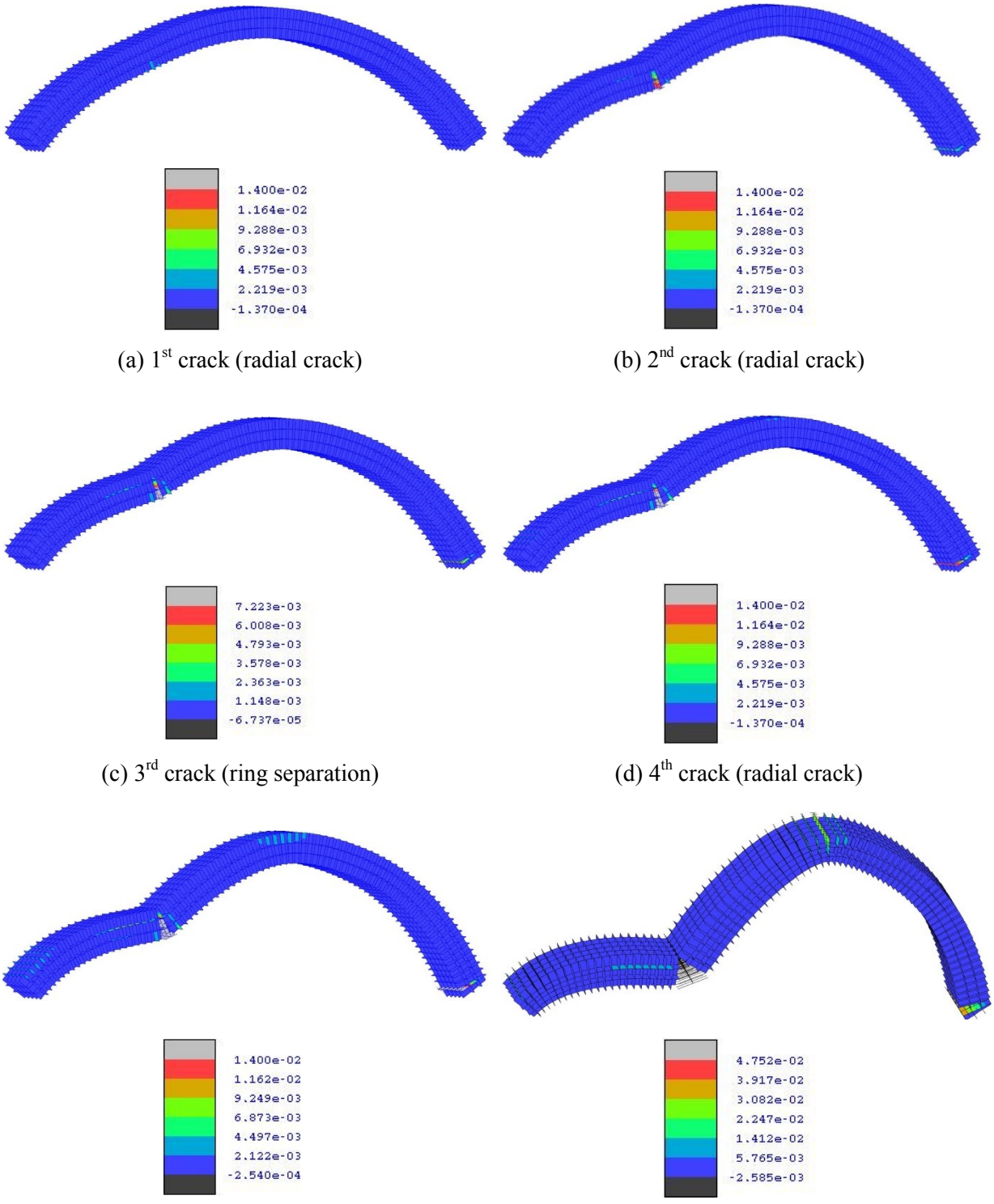

(a) 1st crack (radial crack) (b) 2nd crack (radial crack)

(c) 3rd crack (ring separation) (d) 4th crack (radial crack)

(e) 5th crack (radial crack) (f) Final step

Figure 4-14: Plastic work contour W_{cr1} (N/mm) of *Arch T*: (a) 1st crack (radial crack), (b) 2nd crack (radial crack), (c) 3rd crack (ring separation), (d) 4th crack (radial crack), (e) 5th crack (radial crack) and (f) Final step

4.2.4 Modelling considerations

Numerical analyses have been carried out to investigate the influence of some material properties on the response prediction of a square arch up to collapse and particular attention is paid to the ultimate load and the initial stiffness. Additionally, the use of less computationally demanding mesoscale descriptions is investigated. In this case the results obtained using simplified strategies, where a lower number of solid and nonlinear interface elements are employed, are compared and discussed.

4.2.4.1 Influence of material properties

Arch G is analysed considering the same loading condition as in Section 4.2.1 focusing on the effects of the most critical material properties. As discussed before, the response of the arch is governed by the development of radial cracks which are mainly associated with the normal stresses at the nonlinear interfaces for the radial mortar bed joints (Figure 4-3b, Figure 4-6). Thus the material properties considered in the parametric study comprise the Young's modulus for masonry units E_b, the normal stiffness of the nonlinear interfaces for the mortar joints K_n, the tensile strength f_t and the mode-I fracture energy G_{fI} for the mortar joints. For all the simulations the ultimate load is assumed as the peak load, while the elastic stiffness as the secant stiffness calculated at 40% of the maximum load.

Figure 4-15 shows the numerical curves and the experimental curve for the vertical displacement at quarter span determined by using the mesoscale model illustrated in Figure 4-3 and the material properties in Tables 4-3, 4-4 and 4-5 but E_b. This was varied from 3GPa to 100GPa, where the lower value represents the Young's modulus for old degraded bricks and the higher value the Young's modulus for hard stone units. Figure 4-16 and Figure 4-17 display the change of ultimate load ΔLL_u and elastic stiffness ΔK_e both calculated using the experimental values $LL_{u,exp}$ and $K_{e,exp}$ as below:

$$\Delta LL_u = \frac{LL_{u,num} - LL_{u,exp}}{LL_{u,exp}} \tag{4-1}$$

$$\Delta K_e = \frac{K_{e,num} - K_{e,exp}}{K_{e,exp}} \tag{4-2}$$

where $LL_{u,num}$ and $K_{e,num}$ are the ultimate load and the elastic stiffness obtained in the numerical simulations.

In Figure 4-15 it can be seen that an increasing of E_b leads to an increase of the maximum load and the elastic stiffness. A variation of E_b changes also the shape of the numerical curves, where the curves with low E_b are characterised by a smoother transition from the elastic response to the ultimate load. The rate of change of the ultimate load (Figure 4-16) is significant for low E_b, whereas the ultimate load change is almost negligible for high Young's modulus values (e.g. doubling E_b from 50 GPa to 100GPa leads to only about 1% increment of LL_u). The variation of the initial stiffness of the arch (Figure 4-17) is again very significant when E_b increases from low values, but the rate of change is still notable for high E_b (e.g. doubling E_b from 50 GPa to 100GPa leads to about 8% increment of K_e).

The effects of the variation of K_n are displayed in Figure 4-18, where the numerical curves obtained by changing the normal stiffness for the mortar joints from K_n = 10N/mm^3 to K_n = 500kN/mm^3 are shown together with the experimental curve. In this respect it is important to note that the most common values suggested in the literature to represent mortar joints in old brickwork are within the interval 30N/mm^3 ≤ K_n ≤ 60N/mm^3 (Oliveira, 2003) and for new masonry structures 100N/mm^3 ≤ K_n ≤ 150N/mm^3 (Macorini & Izzuddin, 2011; Lourenço & Rots, 1997). The trend of the different numerical curves shows a significant influence of K_n on both the ultimate load (Figure 4-19) and the initial stiffness (Figure 4-20). Low K_n values determine a ductile response with low ultimate load and stiffness. While increasing K_n leads to an increment of the ultimate load and the elastic stiffness, it reduces the displacement at the onset of the softening branch. Figure 4-21 displays numerical curves obtained using different f_t

values, where the tensile strength for the mortar joints varies from f_t = 0.002MPa to f_t = 1.0Mpa being the lower limit characteristic of degraded mortar joints. Comparing the different curves it can be seen that the tensile strength determines the load at first crack, the ultimate load (Figure 4-22), the initial stiffness (Figure 4-23) and the shape of the numerical response. The numerical curves with low f_t are generally smoother, while in the case of high f_t (e.g. f_t = 1.0MPa) the first cracking is followed by a sudden release of elastic energy corresponding to a softening branch which is followed by a further load increment up to the ultimate load. Moreover the rate of change of the ultimate load is still significant for high f_t values, but variation of the initial stiffness becomes less pronounced when f_t increases from 0.5MPa to 1.0MPa. Finally the influence of the mode-I fracture energy is illustrated in Figure 4-24. As expected the response of the arch becomes more ductile when G_{fI} increases, moving to the limit of elasto-plastic behaviour with no softening when G_{fI} is relatively large. Also the ultimate load is strongly affected by G_{fI} (Figure 4-25), while the influence on the stiffness is more limited. In this case an increment of the fracture energy often corresponds to a reduction of the initial stiffness (Figure 4-26). In general G_{fI} does not affect the load at first cracking which defines the linear part of the numerical response, thus all the numerical curves are almost coincident until this load level, but afterwards curves with high G_{fI} are smoother and characterised by a higher ultimate load.

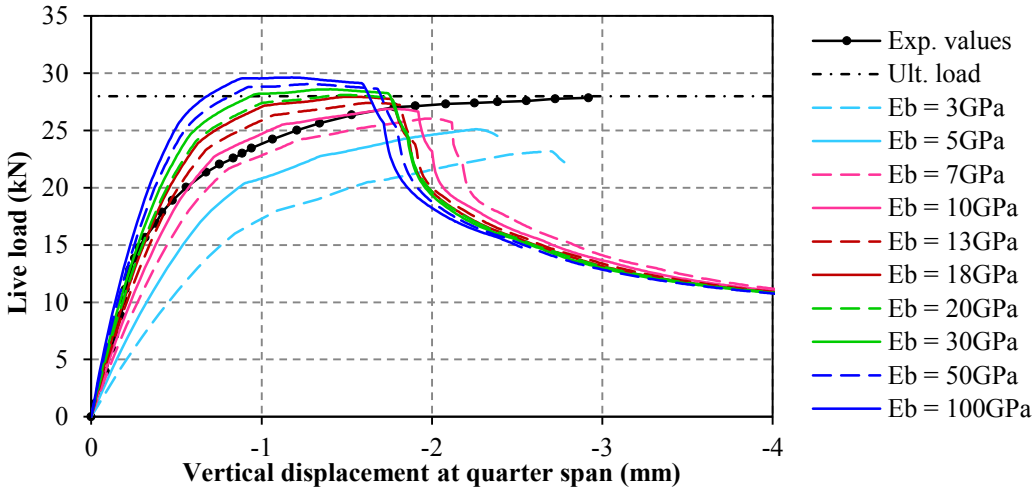

Figure 4-15: Influence of E_b on the arch response

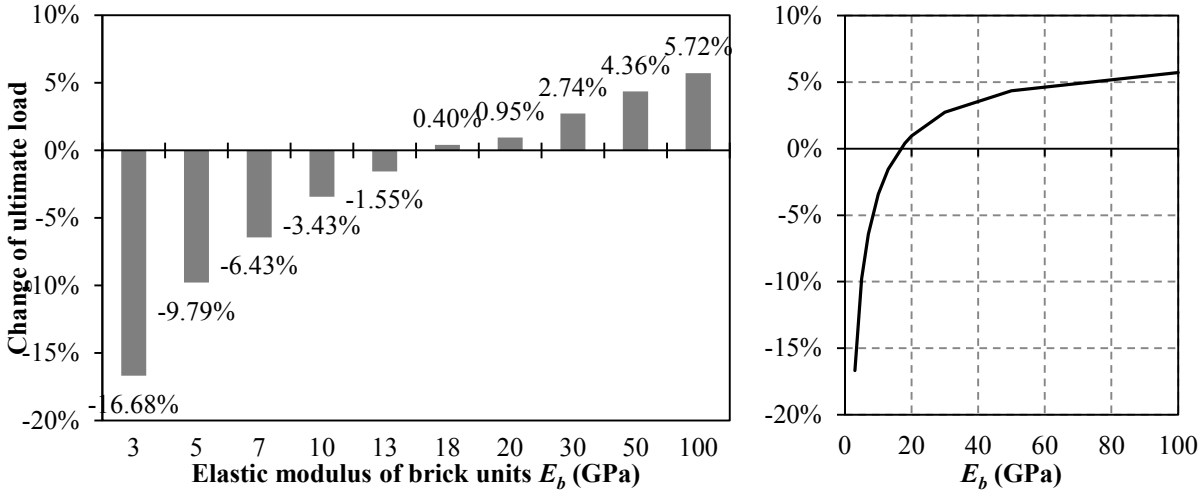

Figure 4-16: Influence of E_b on the ultimate load

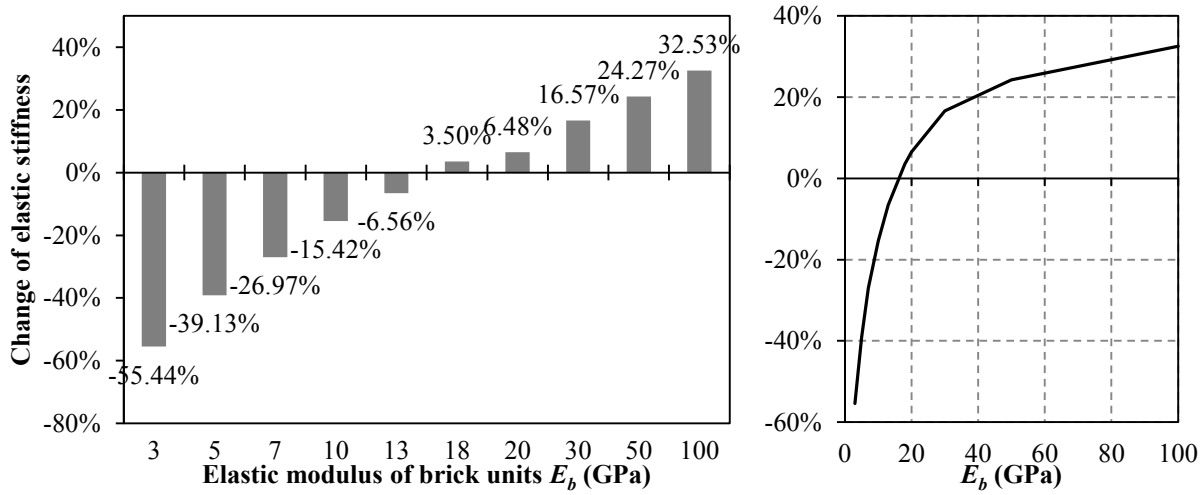

Figure 4-17: Influence of E_b on the elastic stiffness

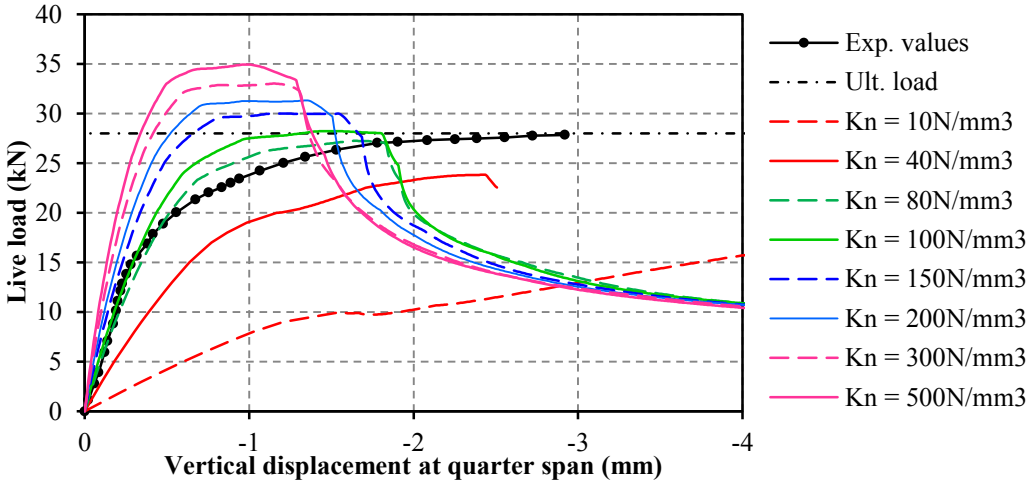

Figure 4-18: Influence of K_n on the arch response

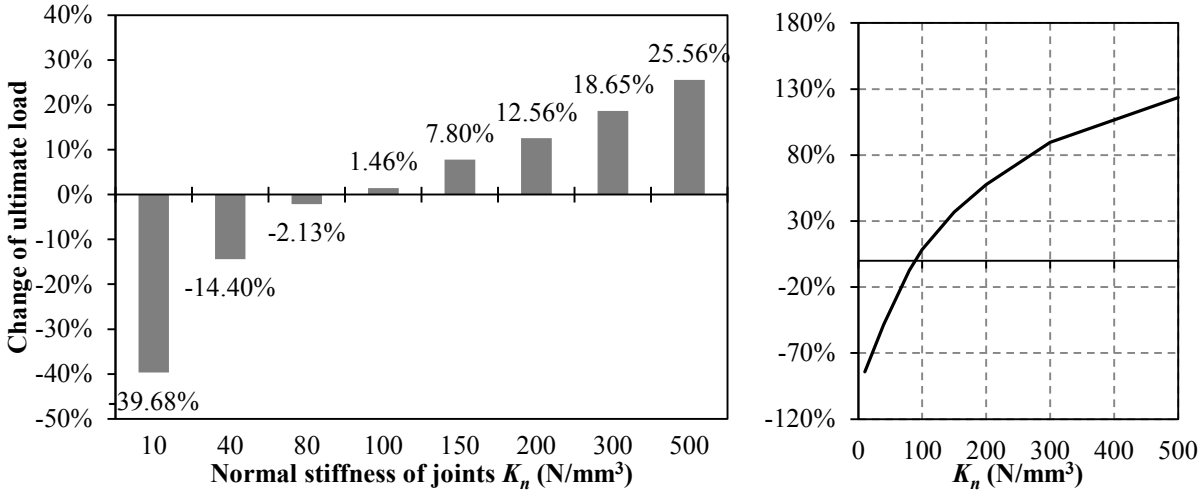

Figure 4-19: Influence of K_n on the ultimate load

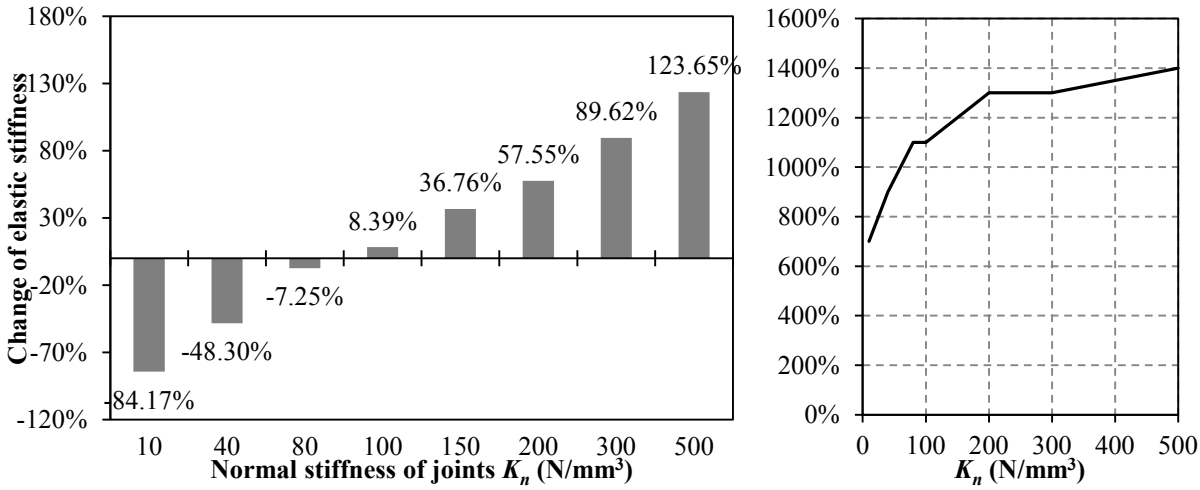

Figure 4-20: Influence of K_n on the elastic stiffness

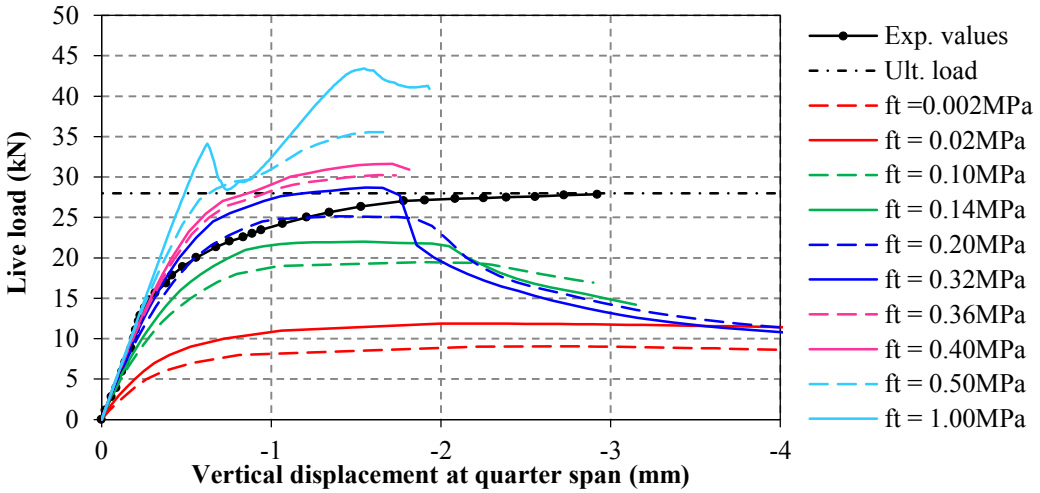

Figure 4-21: Influence of f_t on the arch response

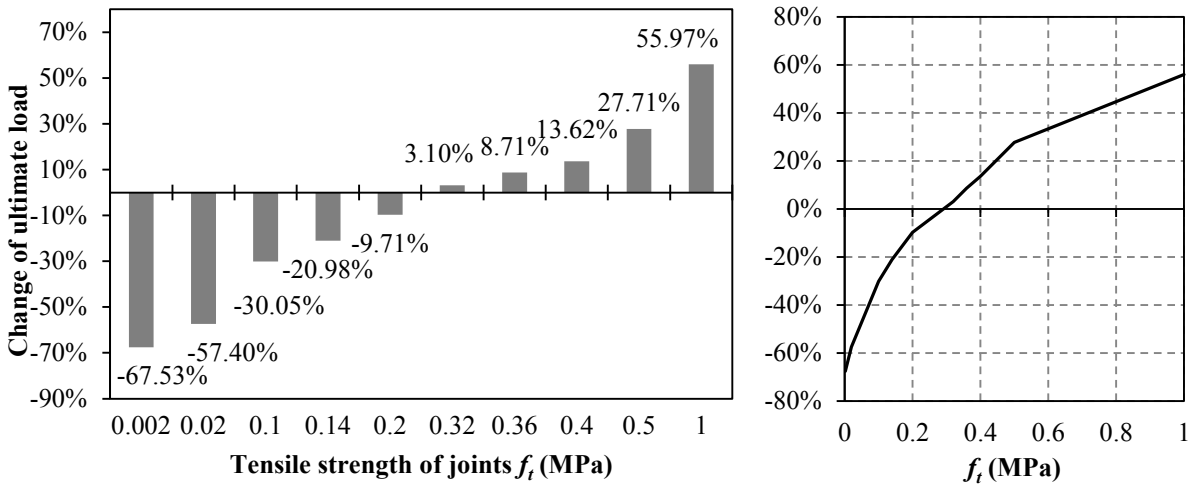

Figure 4-22: Influence of f_t on the ultimate load

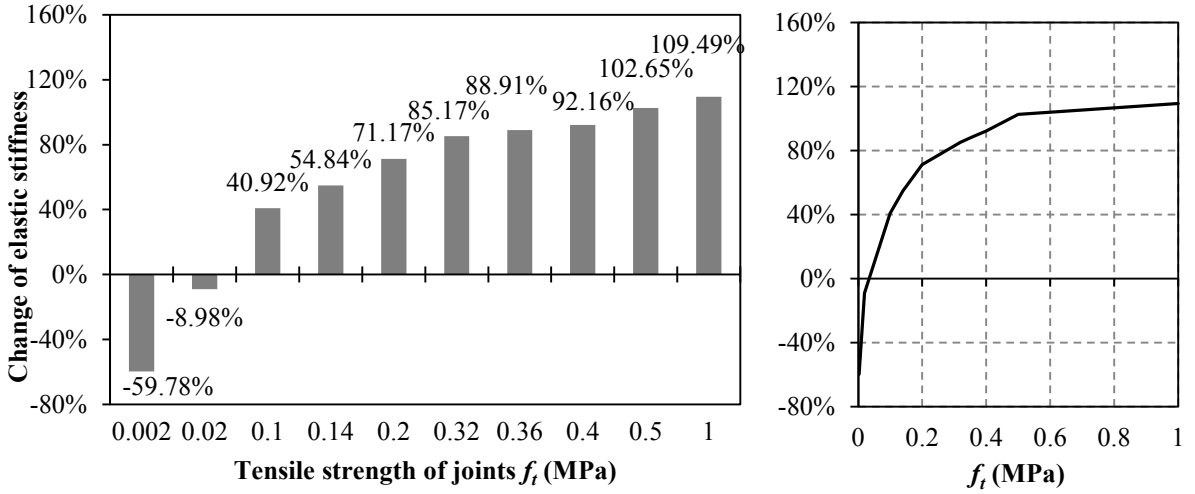

Figure 4-23: Influence of f_t on the elastic stiffness

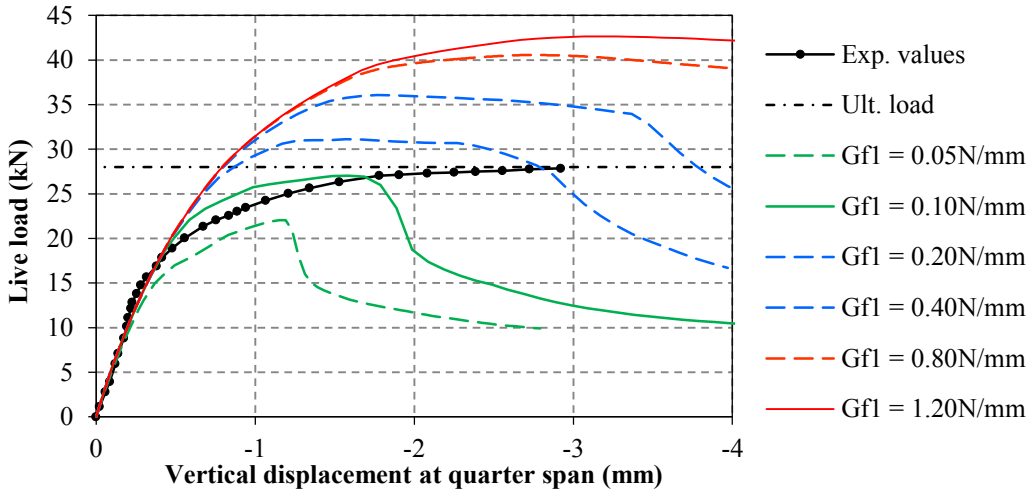

Figure 4-24: Influence of G_{fI} on arch response

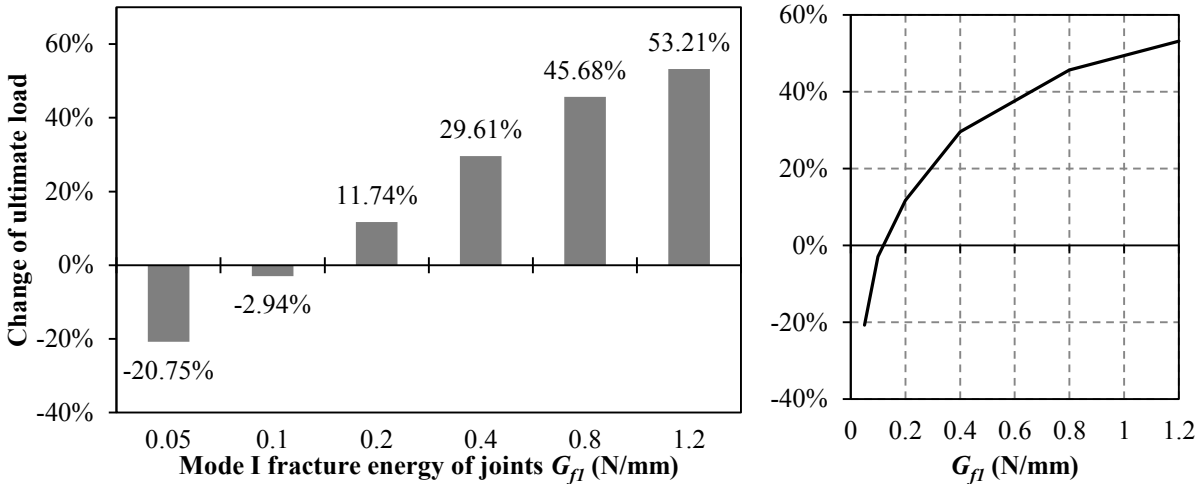

Figure 4-25: Influence of G_{fI} on the ultimate load

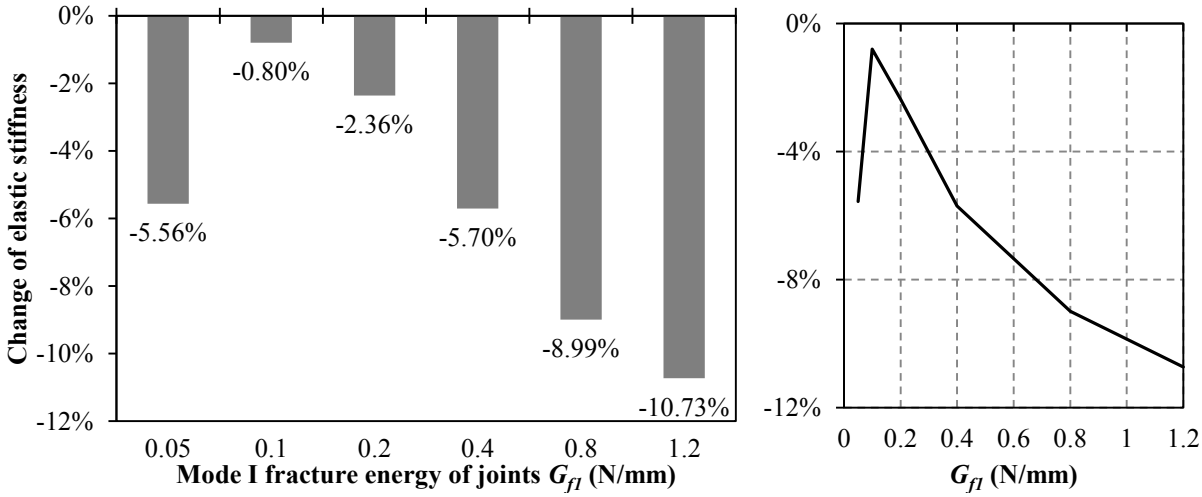

Figure 4-26: Influence of G_{fI} on the elastic stiffness

4.2.4.2 Mesoscale description

The response of the *Arch G* has been investigated using alternative mesoscale descriptions with the scope of identifying an accurate and computationally efficient strategy for predicting the response of masonry square arches under vertical static loading. In particular, the mesoscale model described in Section 4.2.2 here named *Mesoscale 1* which accounts for the actual masonry bond along the span and the width of the arch is compared against two different models. These are characterised by a reduced number of degrees of freedom (DOF) utilising a lower number of solid and nonlinear interface elements as reported in Table 4-10. In the model *Mesoscale 2* the masonry texture along the width of the arch is not taken into account ("strip" model) representing the arch with only one set of solid elements along the span for each of the two rings (Figure 4-27). Finally, in the model *Mesoscale 3* a further simplification is introduced by removing the nonlinear interface elements for the circumferential mortar joints and using only one set of solid elements along the span to model the whole arch (Figure 4-28).

Table 4-10: Number of elements and degrees of freedoms for the three mesoscale models

Model	Solid elements	Interface elements	DOF
Mesoscale 1	384	856	23040
Mesoscale 2	96	142	5760
Mesoscale 3	48	47	2880

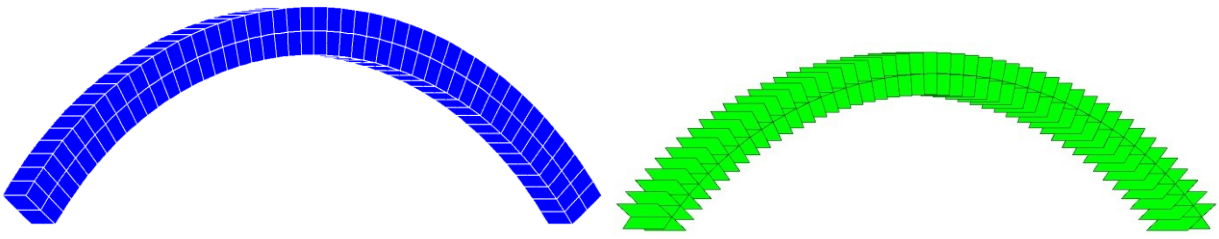

(a) Solid elements (b) Nonlinear interface elements

Figure 4-27: Model *Mesoscale 2*: (a) solid elements and (b) nonlinear interface elements

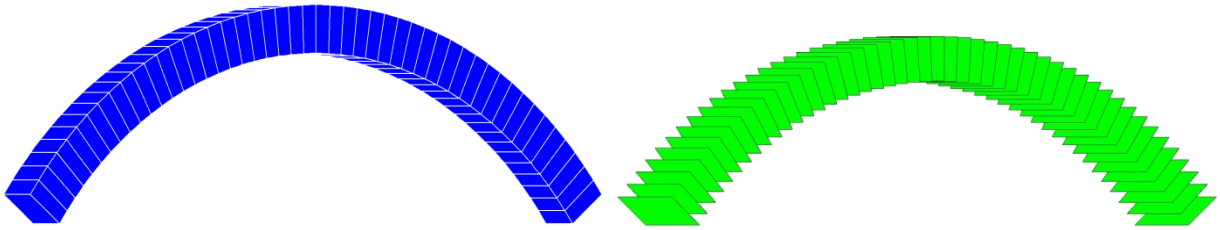

(a) Solid elements (b) Nonlinear interface elements

Figure 4-28: Model *Mesoscale 3*: (a) solid elements and (b) nonlinear interface elements

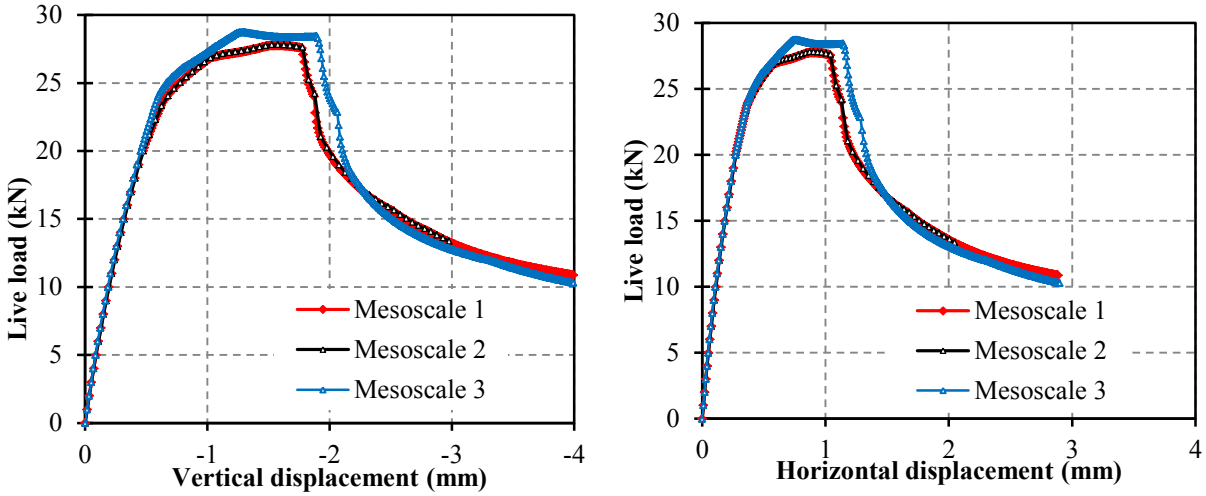

Figure 4-29: Comparisons among different models on the displacements at quarter span

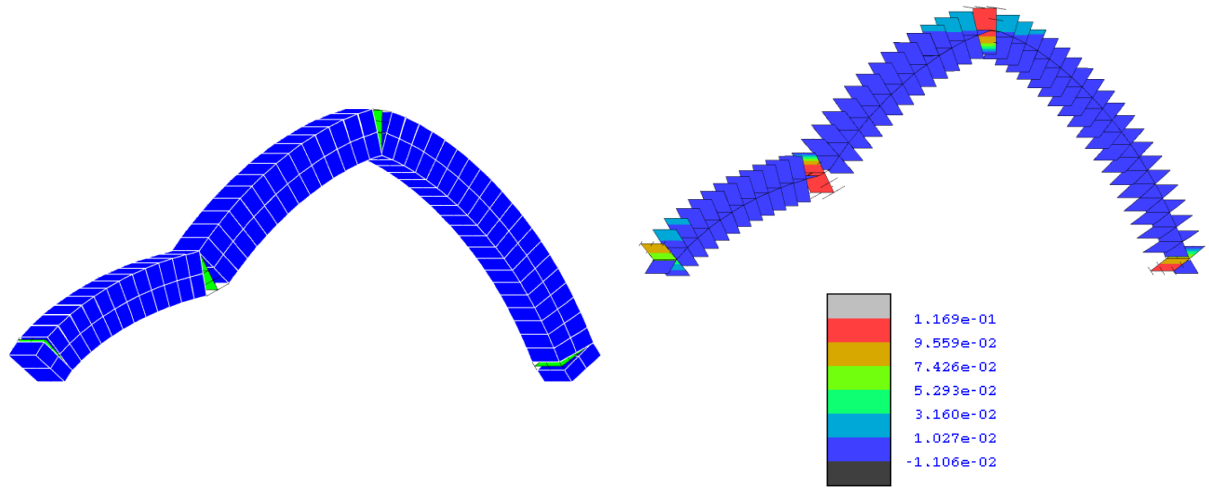

(a) Deformed shape (b) Interface plastic work W_{cr1} (N/mm) contour

Figure 4-30: Deformed shape and plastic work contour for model *Mesoscale 2* at final step

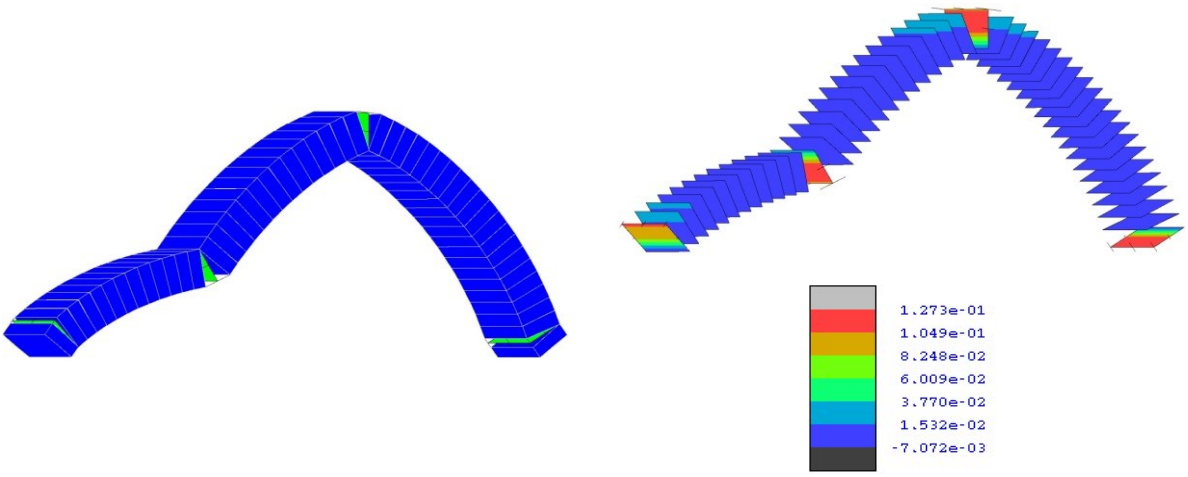

(a) Deformed shape (b) Interface plastic work W_{cr1} contour (N/mm)

Figure 4-31: Deformed shape and plastic work contour for model *Mesoscale 3* at final step

Figure 4-29 shows the numerical curves for the vertical and horizontal displacements at quarter span obtained using the three alternative descriptions. It can be noted that models *Mesoscale 1* and *Mesoscale 2* provide coincident results, while model *Mesoscale 3* leads to a minor over prediction of the ultimate load and provides a less smooth response after the formation of the first radial cracks. The good agreement between the three models can be observed also comparing Figure 4-30 with Figure 4-31 and Figure 4-6e and Figure 4-7e, where the plastic work contour at the final step of the analysis (4mm vertical displacement at quarter span) is shown. This is uniform (the same as the stress/strain distribution) along the arch width and it does not depend upon the FE mesh characteristics along the width of the arch. Thus it can be pointed out that a detailed modelling of the brick-mortar arrangement along the width of the arch is not critical when investigating square masonry arches subjected to vertical static loads uniformly applied on a strip along the whole width of the arch (strip or line loads). In this case model *Mesoscale 2* represents a good compromise between accuracy and computational efficiency. On the other hand, also the most computationally efficient *Mesoscale 3* model provides accurate results, but only when, as in this case, cracks develop along the radial bed joints. In general, this simplified modelling strategy cannot capture damage and failure due to ring separation.

4.3 Analysis of Skew Arches

Numerical simulations have been carried out to establish the effectiveness of the proposed mesoscale approach for representing the behaviour of skewed masonry arches. These are generally characterised by a complex 3D response under static loading. The results obtained in a laboratory test performed at the University of Salford (Wang, 2004) on a skewed masonry arch are considered here for numerical-experimental comparisons.

4.3.1 Experimental test

The test specimen (Figure 4-32) named *Skew2* in (Wang, 2004) consists of a masonry arch with 45° skew and 3m span. The arch is characterised by a 670mm width and 215mm thickness and it is made up of two brickwork rings connected by headers (Figure 4-32b). The arch was constructed using Class A engineering bricks on two reinforced concrete abutments representing rigid supports. The material properties obtained in the tests on bricks, mortar and masonry prisms are reported in Table 4-11.

Table 4-11: Properties of mortar, bricks and masonry for *Skew 2* (Wang, 2004)

	Compressive strength $\sigma_{c,m}$ (MPa)	**Density ρ (kN/m^3)**
Class A bricks	154	23.7
Mortar	2.0	14.7
Masonry prisms with strong bricks	25.2	22.5

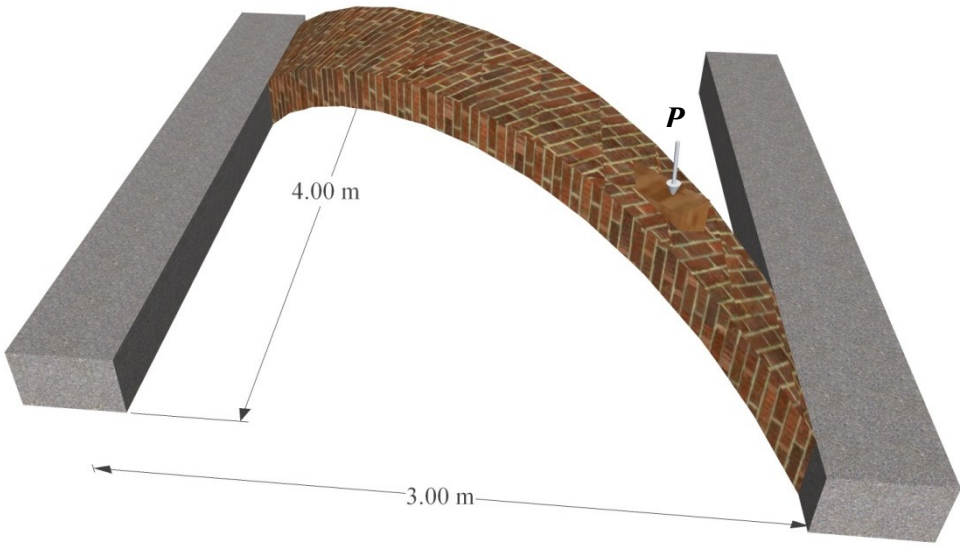

(a) Geometric characteristics and loading arrangement for the arch *Skew2*

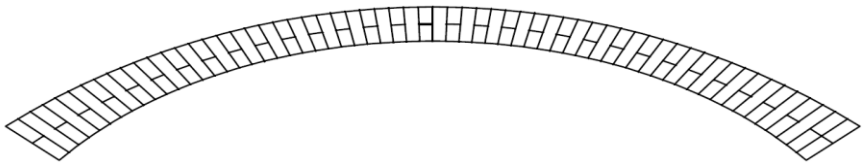

(b) Lateral view showing headers bond between adjacent rings

Figure 4-32: Description of arch *Skew 2*: (a) geometric characteristics and loading arrangement for arch *Skew2* and (b) lateral view showing headers bond between adjacent rings

In the test, a concentrated load P was applied under force control through a hydraulic jack on a wedge shaped wooden pad set at the three quarter span mid-width of the arch barrel as schematically shown in Figure 4-32a. The load was monotonically increased up to $P_{u,exp}$ = 17.4kN when collapse occurred because of the formation of five cracks extending in the mortar joints through the whole width of the arch. These divided the arch into four blocks of brickwork rotating about the lines of fracture. The cracks were not parallel due to the specific geometry of the arch and the orientation of the mortar joints giving rise to a 3D failure mode typical of skewed masonry arches.

4.3.2 Model description

The skewed arch was modelled using the proposed mesoscale description. As for the square arch mesoscale model presented before, one 20-noded solid element was utilised to represent each half brick along the width of the arch and 2D nonlinear interface elements to model mortar joints and potential fracture planes in the mid-plane of each brick. In this case, the main difficulty in defining the mesoscale mesh is due to the specific position of each brick which determines the geometry of the skew arch. To this end the expressions (Table 3-1), which were derived from the rules of descriptive geometry used in the past to build real arch bridges (George, 1880), have been employed to calculate the nodal coordinates for each solid element. The resulting 3D mesh composed of solid elements is shown in Figure 4-33a,b, while the arrangement of nonlinear interface elements connecting the different solid elements is displayed in Figure 4-33c.

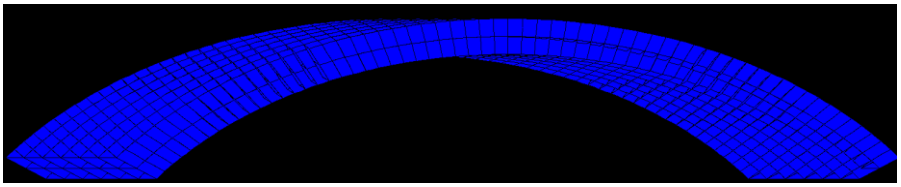

(a) Solid elements (elevation view)

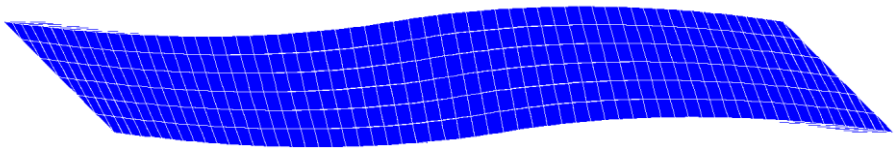

(b) Solid elements (plan view)

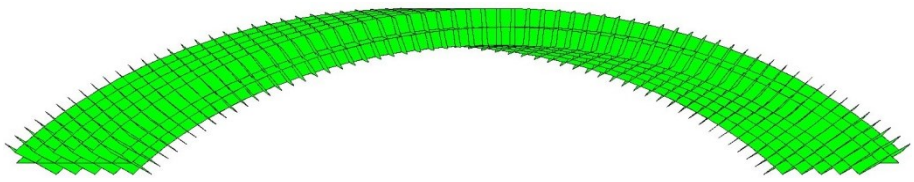

(c) Nonlinear interface elements (elevation view)

Figure 4-33: Mesoscale description for the arch *Skew 2*: (a) solid elements (elevation view), (b) Solid elements (plan view) and (c) nonlinear interface elements (elevation view)

The material properties used in the numerical analysis and presented in Tables 4-12, 4-13 and 4-14 were selected considering the material parameters reported in Table 4-11 and the typical values found in the literature for brick-masonry mesoscale descriptions (Macorini & Izzuddin, 2011; Oliveira, 2003; Rots, 1997). Among these parameters, the material properties leading to a good correlation between the experimental data and the numerical prediction of the arch response were chosen.

Table 4-12: Elastic properties for solid elements

	Elastic modulus E (N/mm^2)	**Poisson's ratio ν**
Brick unit	1.6×10^4	0.15

Table 4-13: Elastic properties for interface elements

	Normal stiffness K_n (N/mm^3)	**Tangent stiffness K_t (N/mm^3)**
Mortar interface	36	20
Brick-brick interface	1×10^5	1×10^5

Table 4-14: Inelastic properties of nonlinear interface elements

	Surface F_1	**Surface Q_1**	**Surfaces F_2, Q_2**
Mortar-brick interface	$C_0 = 0.14$N/mm^2 $\sigma_{t0} = 0.10$N/mm^2 $\tan\phi_0 = 0.6$ $G_{f1} = 0.12$N/mm $G_{f2} = 0.15$N/mm	$C_0 = 0.14$N/mm^2 $\sigma_{t0} = 0.10$N/mm^2 $\tan\psi_0 = 0.0$ $G_{f1} = 0.12$N/mm $G_{f2} = 0.15$N/mm	$D = 25.3$N/mm^2 $\sigma_{c0} = 25.3$N/mm^2 $\tan\theta_0 = 1.0$ $G_c = 5.0$ N/mm
Brick-brick interface	$C_0 = 2.8$N/mm^2 $\sigma_{t0} = 2.0$N/mm^2 $\tan\phi_0 = 1.0$ $G_{f1} = 0.08$N/mm $G_{f2} = 0.5$N/mm	$C_0 = 2.8$N/mm^2 $\sigma_{t0} = 2.0$N/mm^2 $\tan\psi_0 = 1.0$ $G_{f1} = 0.08$N/mm $G_{f2} = 0.5$N/mm	

Fixed boundary conditions were assumed at the two ends of the arch to model the rigid abutments, while a vertical patch load was applied incrementally under displacement control to represent the load applied in the test by the hydraulic jack.

4.3.3 Numerical results

In the experimental test, vertical displacements were measured at 8 different points along the arch. Their position is marked with T3, T4, T5, T6, T7, T8, T9 and T10 in Figure 4-34.

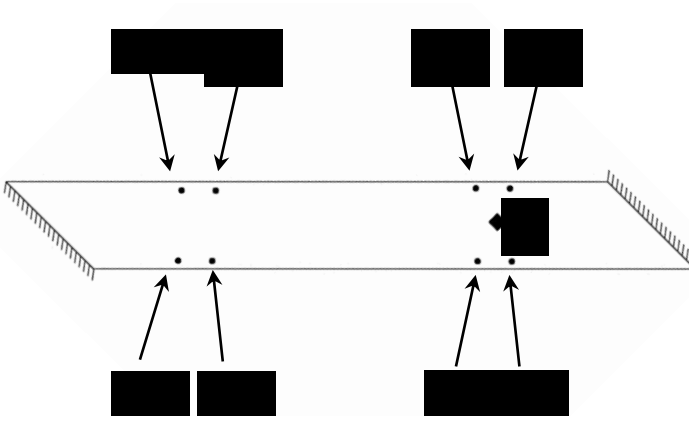

Figure 4-34: Position of the markers for vertical displacements on arch *Skew 2*

Load-displacement curves for the 8 vertical displacements are shown in Figure 4-35, where numerical predictions are compared against experimental results. The predicted maximum load is $P_{u,num}$ = 17.65kN which is very close to the experimental ultimate load $P_{u,exp}$. Numerical curves for the displacements at T3, T7 and T9 are very close to the experimental results, whereas the numerical model predicts a stiffer response at T4, T8 and T10.

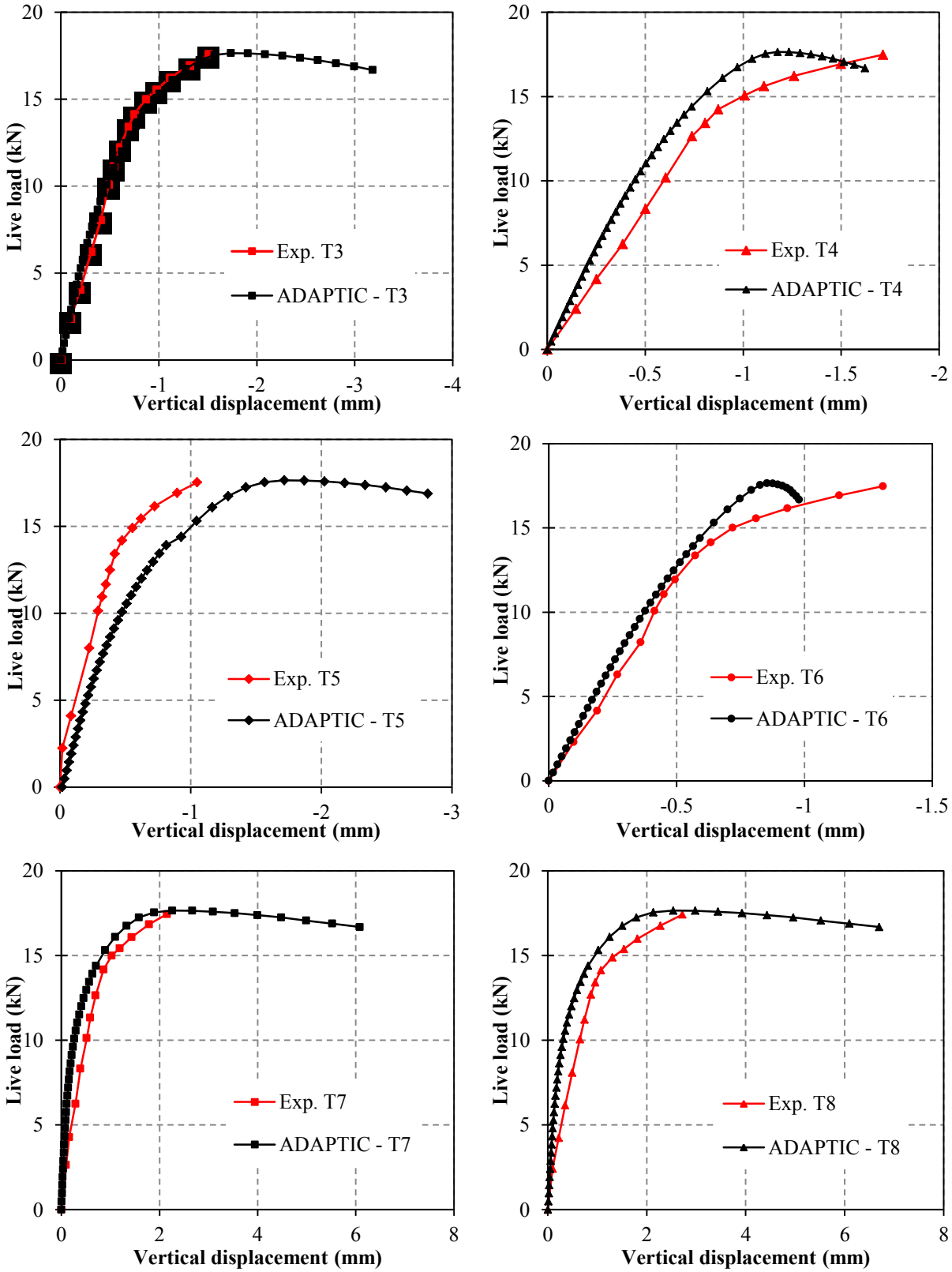

Figure 4-35: Vertical displacements at different positions on arch *Skew 2* (Cont'd …)

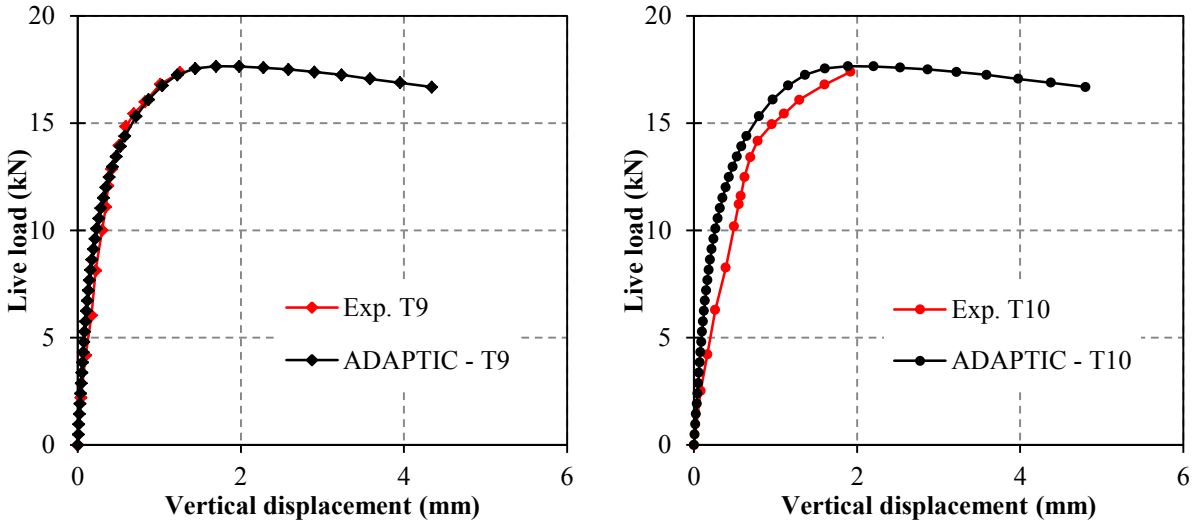

Figure 4-35: Vertical displacements at different positions on arch *Skew 2*

In the test the first large crack was found by visual inspection at about 16kN and was followed in rapid succession by other four cracks. Conversely as shown in Figure 4-36 where the plastic work contour for yield function F_1 is displayed at different loading levels, the numerical model predicts the first cracks along the mortar joints at the right abutment and underneath the applied load at P = 5.8kN. For higher loads two more cracks in mortar joints close to the left abutment and at the quarter span form as in the experimental test. The predicted failure mode is depicted also in Figure 4-37, where the deformed shape at the final step of the analysis is shown. In the figure the four different parts of brickwork divided by five fracture lines can be can be noted.

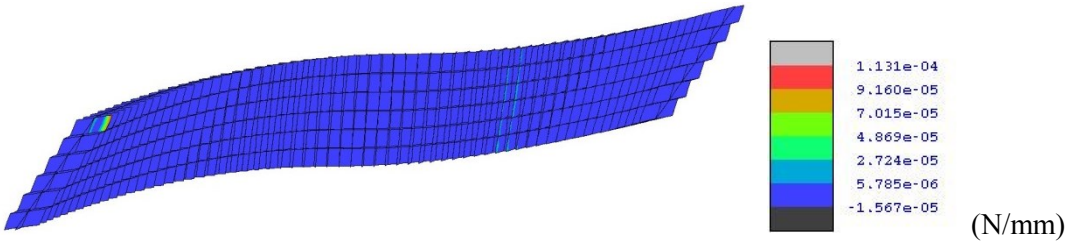

(a) P = 5.8kN

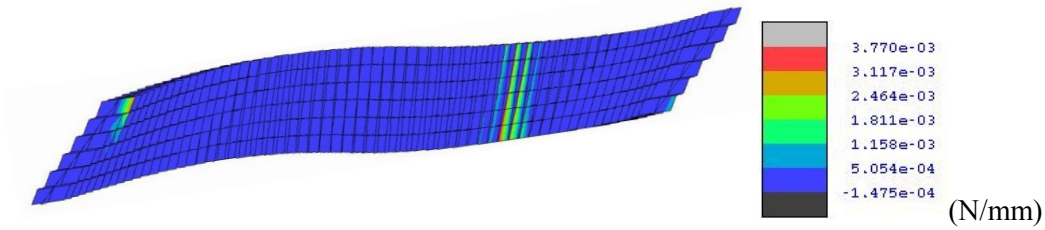

(b) P = 9.6kN

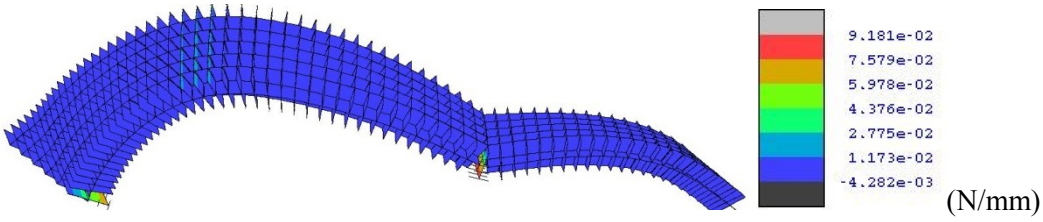

(c) P = 16.1kN

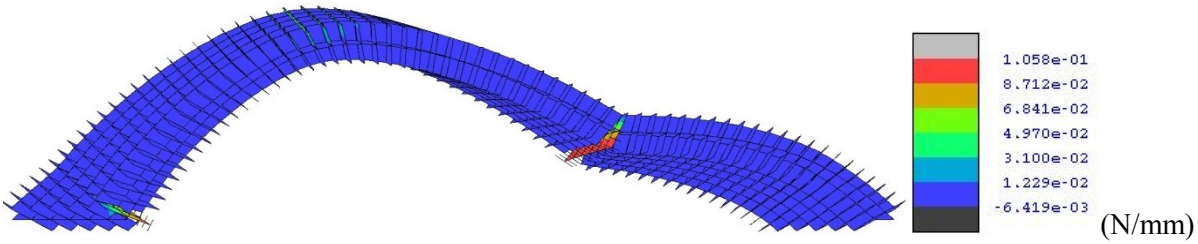

(d) P = 17.65kN (failure mode-elevation view)

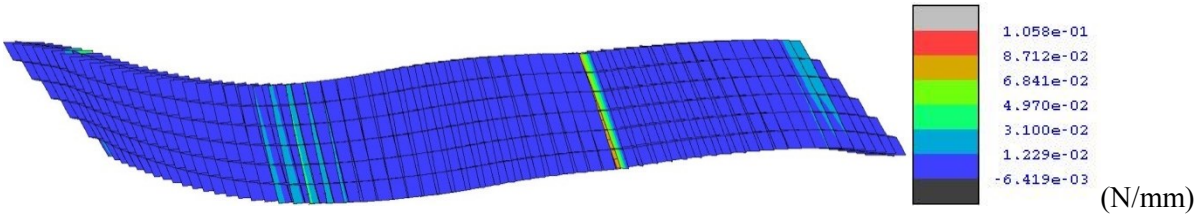

(e) P = 17.65kN (failure mode-plan view)

Figure 4-36: Plastic work W_{cr1} contour for *Skew 2* arch at (a) P = 5.8kN, (b) P = 9.6kN, (c) P = 16.1kN, (d) P = 17.65kN (failure mode-elevation view) and (e) P = 17.65kN (failure mode-plan view)

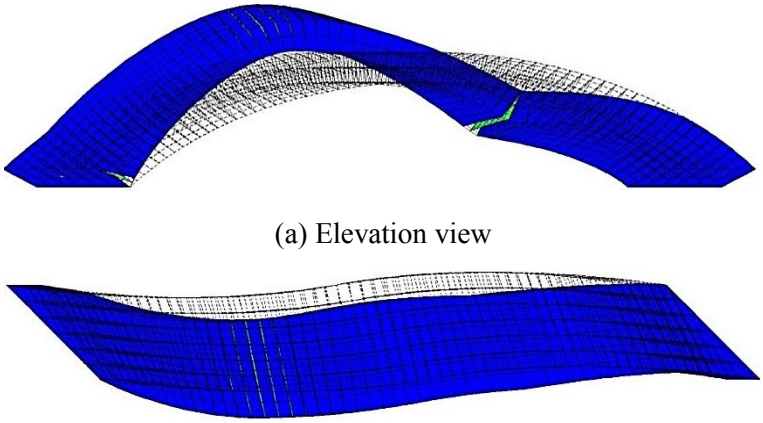

(a) Elevation view

(b) Plan view

Figure 4-37: Deformed shape of arch *Skew 2* at the final step of load: (a) elevation view and (b) plan view

4.3.4 Modelling considerations

As shown in the numerical-experimental comparison, the adopted mesoscale modelling approach for brick-masonry allows an accurate prediction of the 3D response of skew arches. However in the case of large skew arches it may require an excessive computational effort. Thus alternative strategies developed by using simplified mesoscale descriptions with a reduced number of elements, as discussed in 4.2.3 for square arches, should be explored to define an accurate and effective modelling strategy. In the following, three alternative simplified models are compared against the detailed mesoscale model described in Section 4.3.2 in the analysis of the skew arch *Skew 2* loaded by a line load parallel to the abutment and applied at three quarter span. This loading condition is more realistic than a patch load in the case of arches of masonry bridges, as the backfill above the arch usually spreads any concentrated load applied on the road/rail supported by the arch. The same material properties and support conditions adopted in section 4.3.2 for the numerical experimental comparisons are considered. The three simplified FE meshes, which do not allow for the actual masonry bond, are displayed in Figure 4-38, Figure 4-39 and Figure 4-40. In the first model named *Model Sk1* the two rings of the arch are modelled separately and connected by interface elements as in full mesoscale description (Figure 4-33), while only one solid element is utilised along the width of the arch thus forming a strip model as shown in Figure

4-38. The second FE description called *Model Sk2* considers the actual masonry texture along the arch width but utilises only one solid element along the arch thickness neglecting the circumferential mortar bed joints (Figure 4-39). Finally in the last simplified model referred to as *Model Sk3*, the arch barrel is modelled using a series of solid elements along the oblique span of the arch which are connected by interface elements representing mortar joins as displayed in Figure 4-40. This is the most computationally efficient description as only 65 solid elements and 64 nonlinear interface elements are employed.

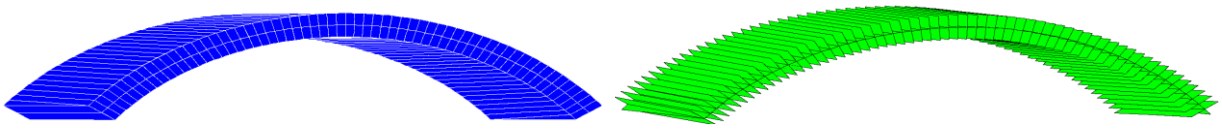

(a) 20-noded solid elements (b) 2D interface elements

Figure 4-38: *Model Sk1* for the arch *Skew 1*: (a) 20-noded solid elements; (b) 2D interface elements

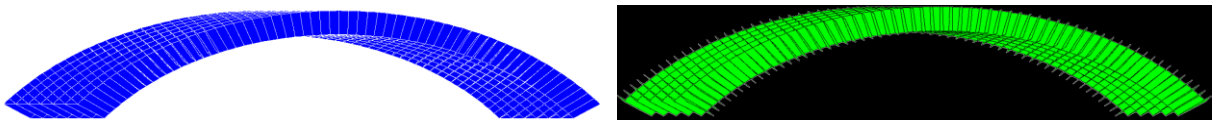

(a) 20-noded solid elements (b) 2D interface elements

Figure 4-39: *Model Sk2* for the arch *Skew 2*: (a) 20-noded solid elements; (b) 2D interface elements

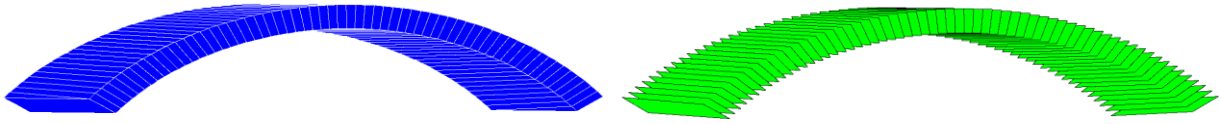

(a) 20-noded solid elements (b) 2D interface elements

Figure 4-40: *Model Sk3* for the arch *Skew 3*: (a) 20-noded solid elements; (b) 2D interface elements

Figure 4-41a,b,c,d show the contour of the plastic work W_{cr1} for the three simplified models and the full mesoscale model at the final step of the analysis. All the models predict the same failure mechanism where large cracks develop along the whole width of the arch dividing the arch barrel into large blocks of brickwork rotating about the fracture lines. The position of the fracture lines and the plastic work distribution are also very similar in all the models.

However as shown in Figure 4-42, where the vertical displacements at the central line of the quarter and the three quarter span are compared, only the *Model Sk2* provides a numerical response very close to that calculated by the full mesoscale model. This highlights that in the case of arch barrels built using the header bond method a detailed representation of the different rings does not enhance the accuracy but it only increases the computational burden. On the other hand, the use of a simplified representation for the arch along its width as in *Model Sk1* and *Model Sk3* leads to an overestimation of the load capacity, as the ultimate loads for *Model Sk1* and *Model Sk3* are 22% higher than that calculated using the full mesoscale model.

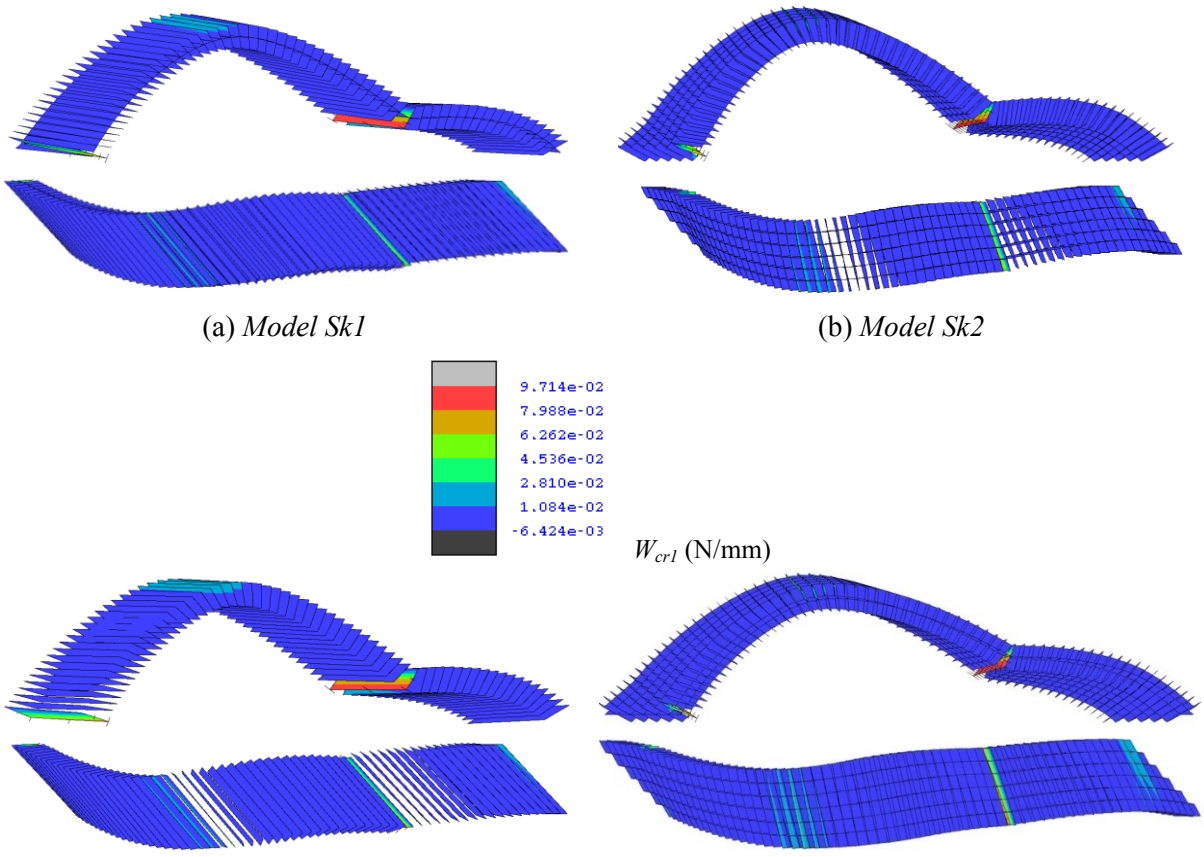

(a) *Model Sk1* (b) *Model Sk2*

(c) *Model Sk3* (d) Mesoscale model

Figure 4-41: Plastic work W_{cr1} contour at the interface elements: (a) Model *Sk1*, (b) Model *Sk2*, (c) Model *Sk3* and (d) Mesoscale model

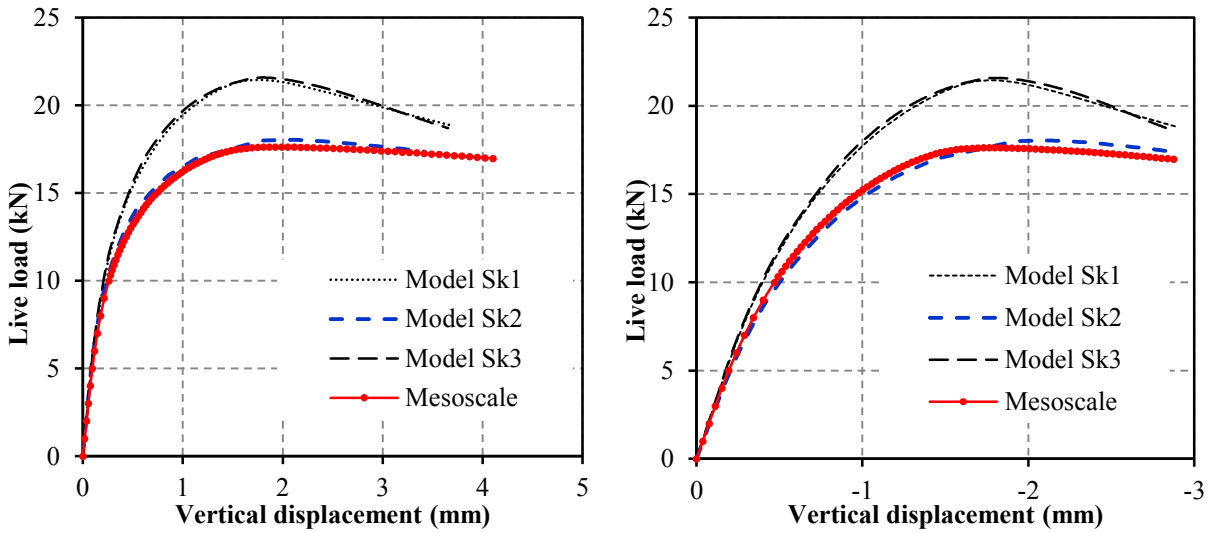

(a) Load displacement curve at quarter span (b) Load displacement curve at three quarter span

Figure 4-42: Numerical comparisons between full mesoscale and simplified models for arch *Skew 2*

In the final numerical comparisons other simplified models named *Square1, Square2, Square3* and *Square4* are considered. In particular, following current practice (McKibbins et al., 2006) which suggests the use of simple 2D square arch models to assess the response of real masonry arch bridges with a limited skew angle, square arch strip models as the *Mesoscale2* and *Mesoscale3* model discussed in Section 4.2.4.2 are employed to represent the behaviour of the arch *Skew 2* subjected to a line load. The models *Square1* and *Square2* allow for the actual connection between the two rings of the arch using circumferential interfaces elements, while *Square3* and *Square4* are single ring models. The models *Square1* and *Square3* are characterised by a span equal to the oblique span of the arch *Skew 2*, whereas the spans for the models *Square2* and *Square4* correspond to the direct span of *Skew 2*.

Figure 4-43 shows the plastic work contour at the final step of analysis for the square arch models (all the analyses terminate at the same level of vertical displacement at three quarter span). For all the models radial cracks develop at the abutments, at quarter and three quarter span with distribution similar to those found by simplified skew arch models and the full mesoscale model (Figure 4-41).

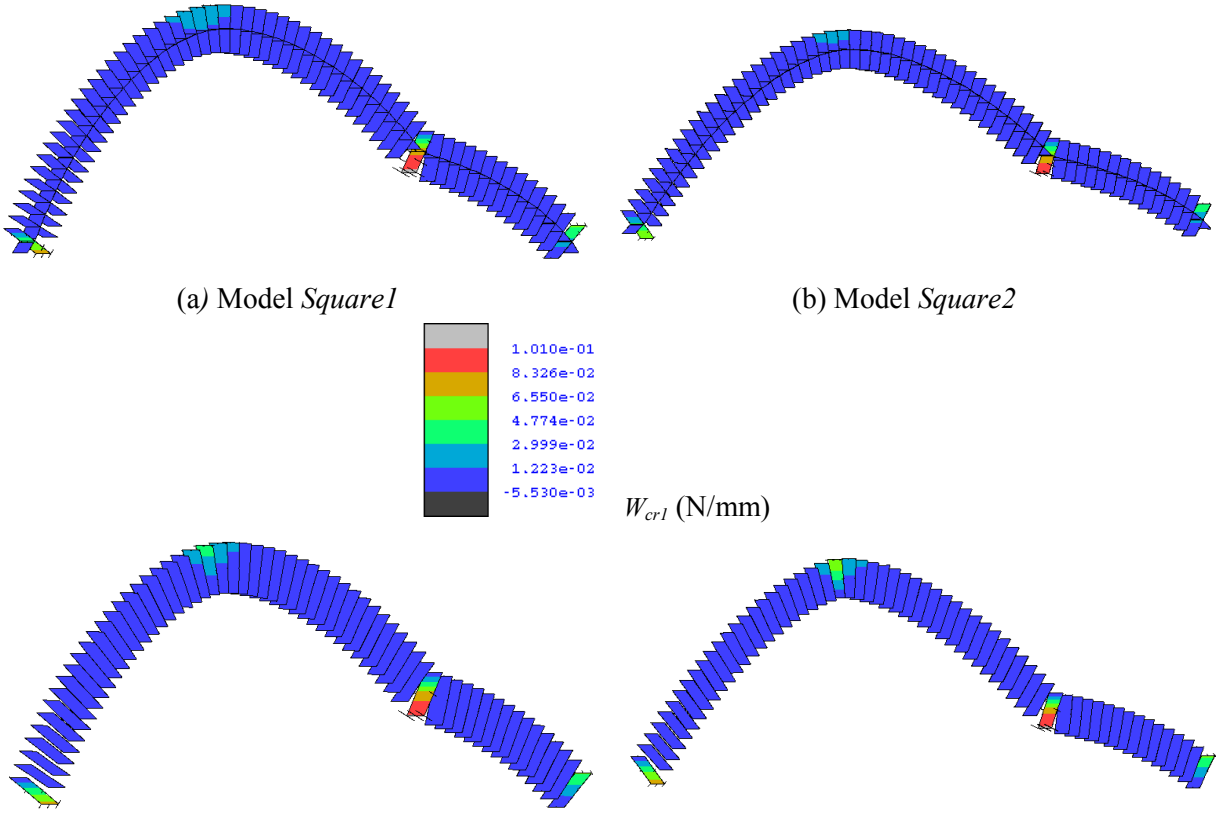

(a) Model *Square1* (b) Model *Square2*

(c) Model *Square3* (d) Model *Square4*

Figure 4-43: Interface plastic work W_{cr1} contour for (a) Model *Square1*, (b) Model *Square2*, (c) Model *Square3* and (d) Model *Square4*

On the other hand, as displayed in Figure 4-44 where the numerical curves for the vertical displacements and quarter and three quarter span are compared, the two simplified models with the same oblique span of the skew arch provide a too conservative prediction of the arch loading capacity and a reduced initial stiffness. Conversely the use of square arch models with the direct span of the skew arch allows a more realistic prediction of the arch capacity but an overestimation of the initial stiffness.

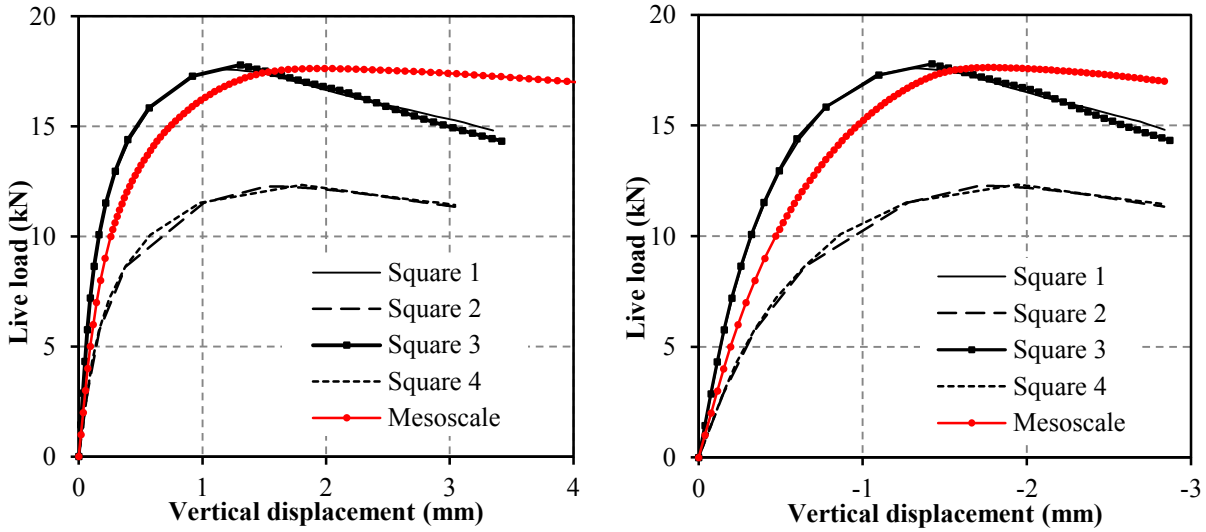

(a) Load displacement curve at quarter span (b) Load displacement curve at three quarter span

Figure 4-44: Numerical comparisons between full mesoscale and simplified square arch models

4.4 Analysis of Large arches

In the previous examples, the detailed mesoscale description for masonry has been applied to the analysis of relatively narrow masonry arches, which require the use of a limited number of solid and nonlinear interface elements also when using the full mesoscale description accounting for the actual masonry bond. As pointed out in previous research (Macorini & Izzuddin, 2013b), this detailed modelling strategy may necessitate an excessive computational effort when applied to the analysis of large structure as in the analysis of wide multi-ring brick-masonry arches. In this case to guarantee computational efficiency, the full mesoscale description can be combined with the partitioning approach allowing for parallel computation previously developed at Imperial College (Jokhio & Izzuddin, 2011), thus providing an accurate and efficient numerical strategy.

In the following, a wide brick-masonry square arch is analysed comparing the numerical predictions obtained using different partitioning strategies (Macorini & Izzuddin, 2013a) against experimental results. The analysed structure corresponds to the arch barrel *Arch1* tested at the University of Salford (Wang, 2004). In the test the masonry arch specimen was

investigated under two different support conditions. Initially, point loads were applied to the arch supported only at its springings by two rigid concrete abutments which were fixed to the strong floor of the laboratory; afterwards the support conditions were changed adding point supports to represent longitudinal supporting diaphragms and the load was increased up to collapse (Wang, 2004). In the numerical simulations only the first support condition was considered, focusing on the response of the arch loaded by a centre point load P incrementally applied at three quarter span up to P = 24kN (Figure 4-45).

Table 4-15: Principal dimensions for *Arch 1* (Wang, 2004)

Span (mm)	Rise (mm)	Span-to-rise ratio	Thickness (mm)	Width (mm)	Brickwork courses	Skew
5000	1250	4:1	215	4000	78/81	0°

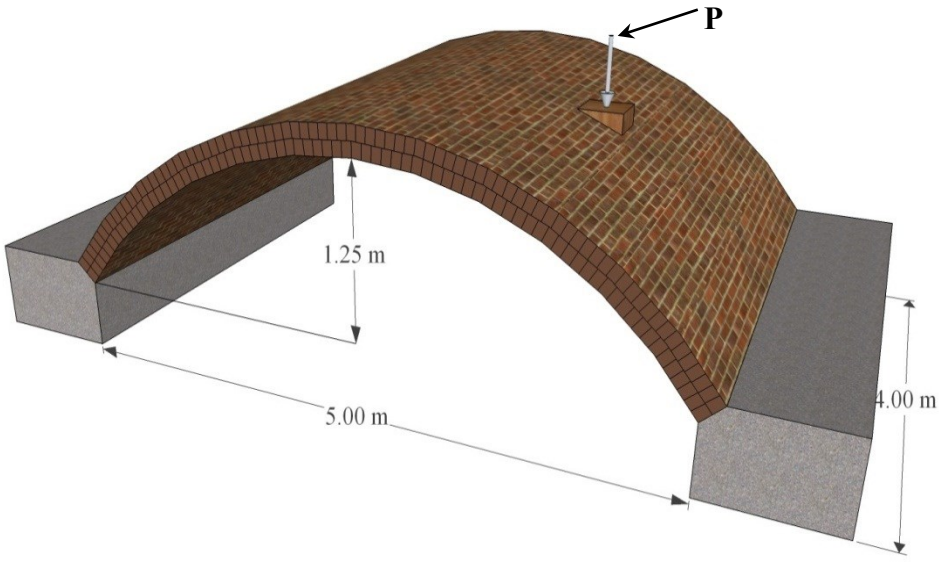

Figure 4-45: Geometric characteristics and loading arrangement for *Arch 1*

The masonry specimen is a two-ring arch characterised by a 4m width, 5m span and 215mm thickness and made up of engineering class A brick units 215×102×65 mm^3 large and 1:2:9 (cement:lime:sand) mortar joints. The stretcher bond method is used, thus the two rings are connected only by (circumferential) mortar joints. The main dimensions of the arch are

reported in Table 4-15 and displayed together with the loading arrangement in Figure 4-45, while the mechanical properties of brick, mortar and brickwork used to build the specimen are presented in Table 4-16.

Table 4-16: Properties of mortar, bricks and masonry for *Arch 1* (Wang, 2004)

	Compressive strength $\sigma_{c,m}$ (MPa)	**Density ρ (kN/m^3)**
Bricks	154	23.7
Mortar	1.81	15.8
Masonry prisms with strong bricks	24.5	22.0

4.4.1 Model description

The same mesoscale strategy adopted for describing the square arch specimens *Arch G* and *Arch T* is followed; thus one 20-noded solid element is employed to model each half brick unit and 16-noded interface elements are used for mortar joints and to represent potential fracture in the mid-plane of each brick. The FE mesh is displayed in Figure 4-46a,b and it consists of 80×36×2 solid elements, 80×36 interface elements for mortar joints connecting the two rings, 79×36×2 for radial bed joints and 80×35×2 for circumferential mortar head joints and potential fracture planes in the bricks. Fixed supports are assumed at the two springings to account for the rigid abutments. Moreover, as the component materials of *Arch1* have about the same mechanical characteristics of the *Arch G* constituents as shown in Table 4-1 and 4-16, the material parameters reported in Table 4-3, 4-4 and 4-5 have been considered for the mesoscale description of *Arch 1*.

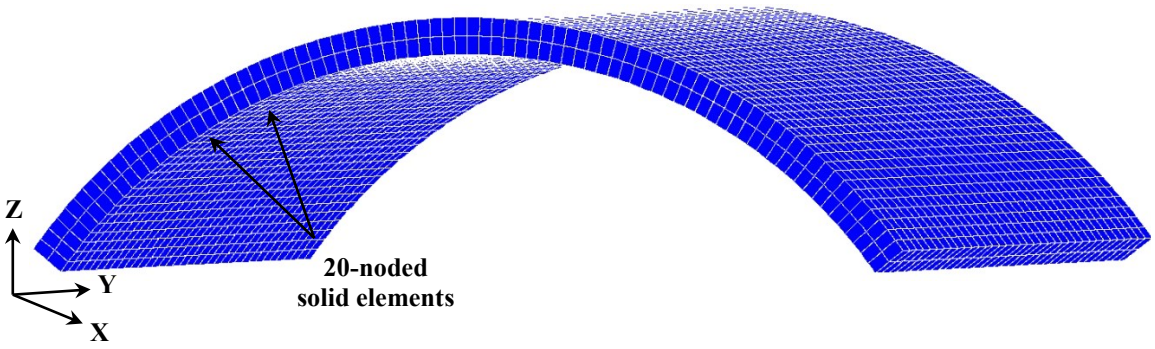

(a) FE mesh with solid elements

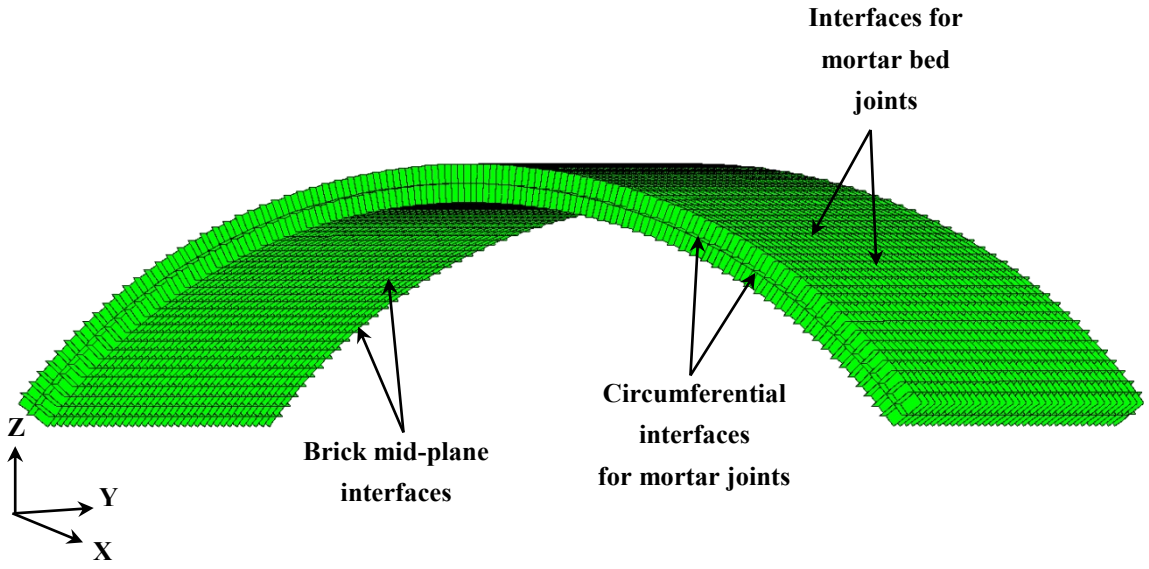

(b) FE mesh with interface elements

Figure 4-46: Mesh in ADAPTIC for *Arch 1*: (a) FE mesh with solid elements and (b) FE mesh with interface elements

4.4.2 Partitioning strategies

The computational efficiency provided by the use of the partitioning approach developed previously at Imperial College (Jokhio, 2012) and applied here to the analysis of a large brick-masonry arch is investigated. The computational cost associated with different partitioning strategies has been analysed in the case of elastic analysis, where a patch load P = 20kN was applied onto the arch in five steps. The computational performance was assessed in terms of speed-up *S*, which is given by the ratio between the wall-clock time required by a

monolithic simulation where the FE problem is solved using a serial code and that required by a partitioned model. This it is an objective measure of computational efficiency (e.g. the most efficient model is characterised by the highest speed-up).

In modelling the arch, both flat and hierarchic partitioning techniques (Jokhio & Izzuddin, 2013) are considered. The former strategy is a single level partitioning approach, where the masonry arch is represented by a parent structure consisting of super-elements which model partitioned subdomains. Conversely, hierarchic partitioning implies the use of a multi-level scheme where original child partitions are further subdivided in higher level super-elements. Thus partitions at one level are children to those at the upper level and parent to those at the lower level. Furthermore in some models to reduce the size of the parent structures, specific constraints in the mesoscale description at the boundary of each partition were adopted. In particular as suggested in Macorini & Izzuddin (Macorini & Izzuddin, 2013a) for the analysis of large masonry walls, hard coupling using a master-slave approach (Jokhio, 2012) was utilised, where the nodes of one face of a solid or a 2D interface element at the partition boundary are connected to a single node (master node).

Figure 4-47 shows the elevation of the subdivision in super-elements at the lowest hierarchical level for some of the models. Table 4-17 reports the characteristics of all the numerical descriptions in term of number of partition levels (e.g. 1 for flat partitioning, > 1 for hierarchic partitioning), number of processesses (e.g. total number of child partitions and parent files) and the number of processors employed in the numerical simulations. These were performed using 2.66 GHz Intel Xeon Processors X5650 cores. Each partitioned model is named as P-*n*-*flat/hier/mslc/hiermslc*, where *n* stands for the number of child partitions, *flat* for single level partitioning method, *hier* means multi-level hierarchic paritioning, *mslc* means single level partitioning with multi-dimensional master-slave coupling at partition boundary and *hiermslc* multi-level hierarchic paritioning with master-slave coupling. Finally, the descriptors X, Y, Z indicate the number of subdivisions in partitions of the analysed arch along the circunferential, the radial and the transverse direction.

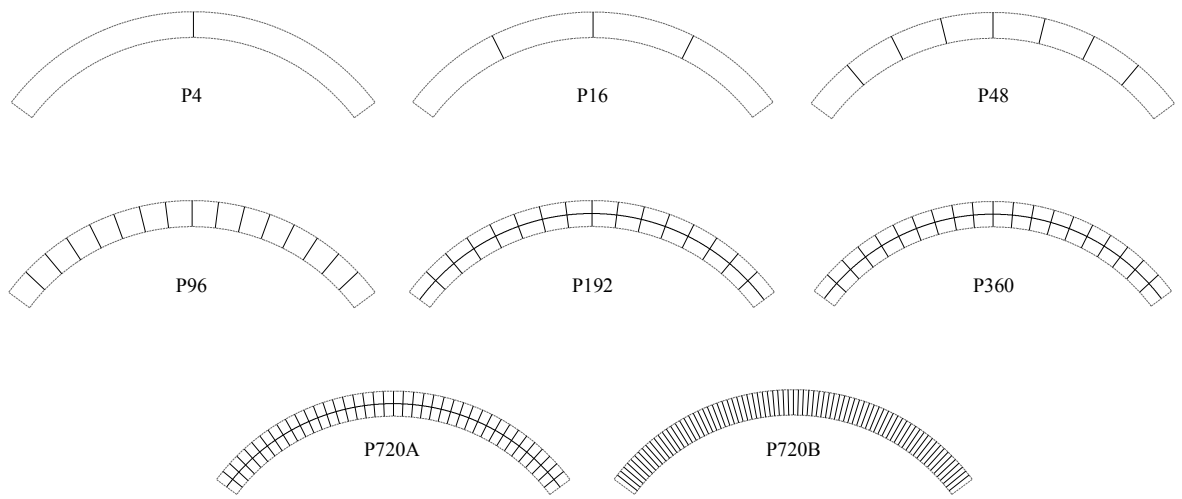

Figure 4-47: Child structures at lowest hierarchical level used for the different partitioned models

The speed-ups achieved by the different models were calculated considering the wall-clock time for the monolithic simulation T_m = 18856s. The speed-up values are reported in Table 4-17 and plotted against the number of processes in Figure 4-48. It is important to note that the maximum number of processors employed is equal to 48, thus when the number of processes exceeds 48 means that more that 1 process is run on same processor reducing computational efficiency.

In general the results show that the use of a large number of flat partitions leads to a significant increase in the size of the parent structure and subesequently to a speed-up reduction (Figure 4-48a). However, this limitation is overcome by hierarchic partitioning and multi-dimensional coupling as shown in Figure 4-48b. In this case the speed-up increases also when using a number of processes larger than the number of processors as for the model P-180-hiermslc which deployes 288 processes obtaining the maximum speed-up S_{max} = 47.55 (Table 4-17).

Table 4-17: Characteristics of partitioned models and speed-up values

	X	Y	Z	No. Levels	No. Processors	No. Processes	*S*
Monolithic	1	1	1	1	1	1	-
P-4-flat	2	1	2	1	5	5	1.65
P-4-mslc							1.79
P-16-flat	4	1	4	1	17	17	1.83
P-16-mslc							3.47
P-16-hier				2	21	21	3.60
P-16-hiermslc							4.94
P-48-flat	8	1	6	1	48	49	1.57
P-48-mslc							17.40
P-48-hier				3	48	63	4.90
P-48-hiermslc							17.35
P-96-flat	16	1	6	1	48	97	1.15
P-96-mslc							26.67
P-96-hier				4	48	127	4.00
P-96-hiermslc							33.07
P-192-hier	16	2	6	4	48	223	1.62
P-192-hiermslc							27.20
P-180-hier	20	1	9	3	48	216	2.17
P-180-hiermslc							**47.55**
P-360-hier	20	2	9	3	48	396	1.03
P-360-hiermslc							42.13
P-720I-hier	40	2	9	4	48	796	0.68
P-720I-hiermslc							33.89
P-720II-hier	80	1	9	5	48	876	0.344
P-720II-hiermslc							19.10

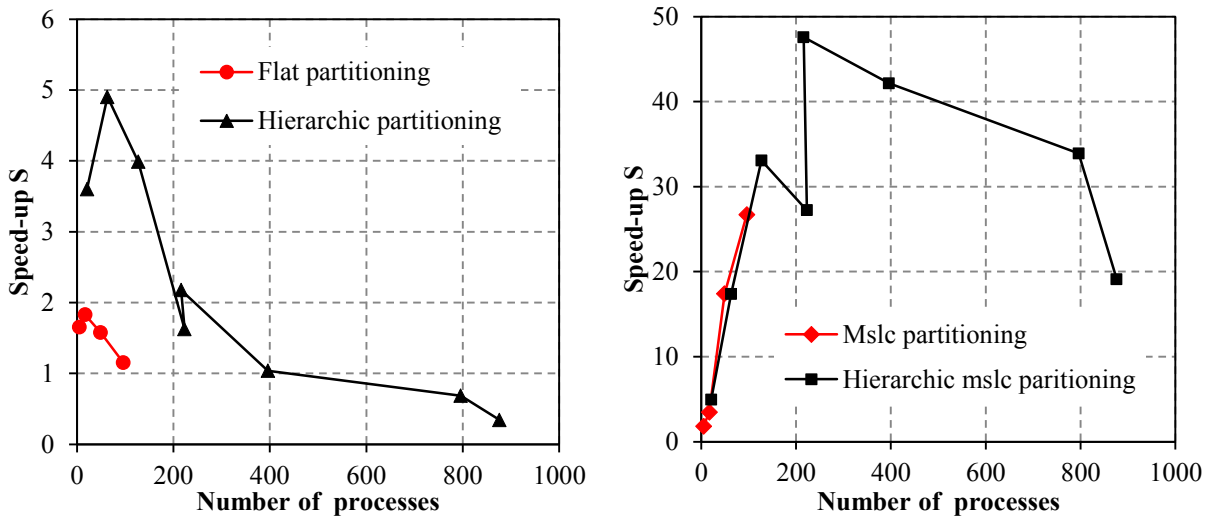

(a) Flat and hierarchic partitioning

(b) Flat and hierarchic partitioning with master-slave coupling

Figure 4-48: Speed-up vs. the number of processes using (a) flat and hierarchic partitioning and (b) flat and hierarchic partitioning with master-slave coupling

Finally it is important to note that a critical role is played also by the arrangement of the partitions. In particular, a subdivision in partitions along the radial direction (e.g. partition boundaries on the surface between the two rings of the arch, Y > 1) significantly increases the nodes at the partition boundary thus reducing S. This can be seen in Figure 4-48b and comparing the computational efficiency of model P-180-hiermslc with S = 47.55 an model P-192-hiermslcwith S = 27.20. Both models deploy a similar number of processes but a different partition arrangement, where the model with lower speed-up is assembled with partitions along the radial direction.

4.4.3 Numerical-experimental comparisons

The accuracy provided by the proposed partitioned mesoscale model for brick-masonry arches is assessed in numerical experimental comparisions. The numerical results for the vertical displacements at quarter and three quarter span obtained using the monolithic model and the most efficient partitioned mesoscale model are compared against the experimental data.

Figure 4-49 shows the numerical and experimental curves, where the displacements along the arch width at P = 16kN are plotted.

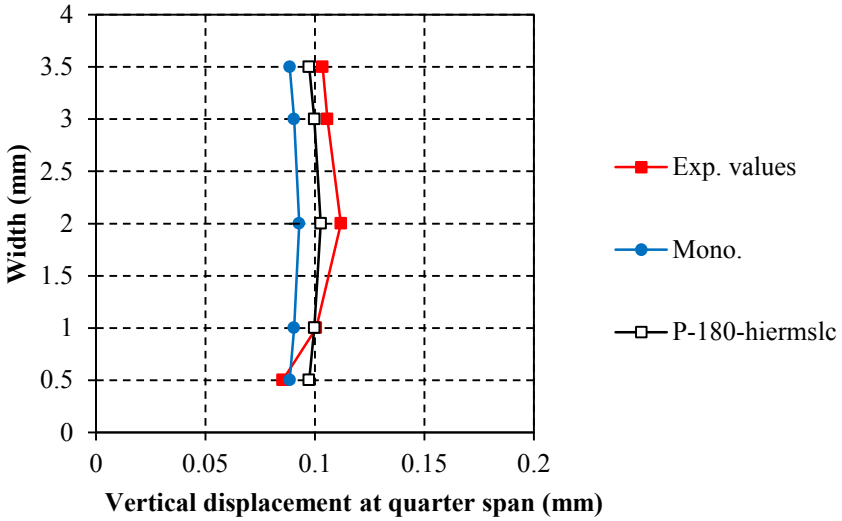

(a) Load-displacements at quarter span

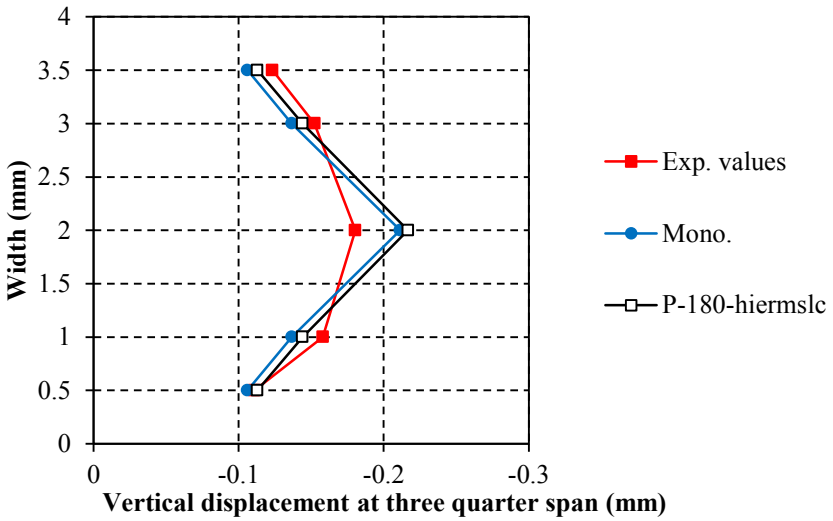

(b) Load-displacements at three quarter span

Figure 4-49: Vertical displacements along the arch width at P = 16kN

It can be seen that the two numerical curves are quite close, where the minor differences are due to the unrealistic rigid constrains adopted in the model with master-slave coupling at the partition boudary to reduce the number of freedoms of the parent files at different hierarchical

levels. Previous reseach on numerical analysis of large masonry walls (Macorini & Izzuddin, 2013a) has found that, while this modelling approach allows for a significat improvement of the computational performace (high speed-up), it introduces some minor errors especially in the local stress/strain distribution around the partition boudaries where the master-slave (hard) coupling is applied. However these local errors, which can also be seen in Figure 4-50, where the normal stress distributions obtained at P = 16kN using the monolithic and the P-180-hiermslc model are depicted, do not significantly influence the global response and the prediction of the displacements along the arch. Moreover comparing the numerical curves with the experimental values, it can be noted that the trends of the numerical predictions along the arch width (0 < z < 4m) both at quarter and three quarter span are similar to the experimental displacement variation. In general, it is envisaged that a better agreement could be achieved adopting material parameters for the mesoscale model directly derived from specific material tests instead of using material parameters found in the literature and associated with similar brickwork.

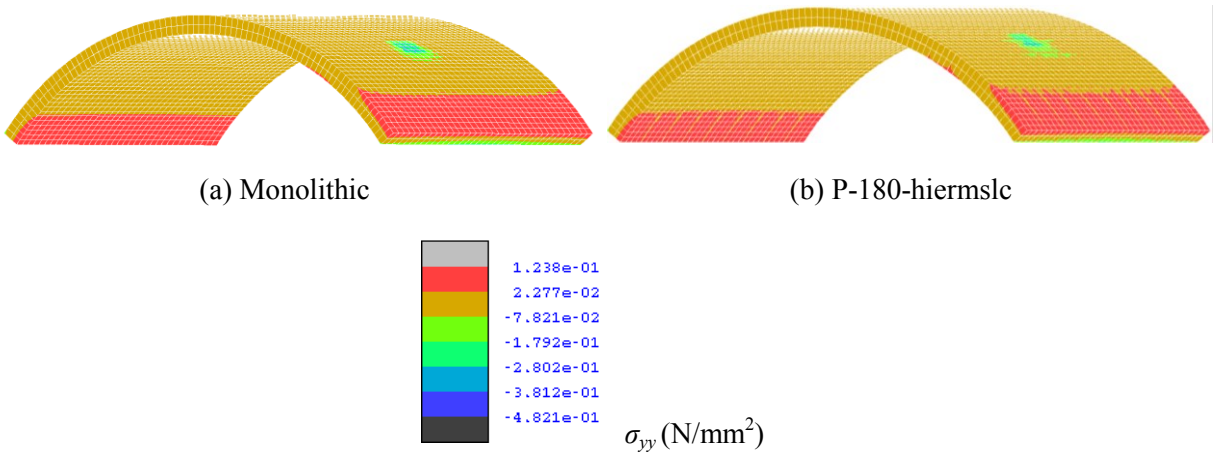

(a) Monolithic (b) P-180-hiermslc

Figure 4-50: Contour of normal stresses at P = 16kN: (a) Monolithic and (b) P-180-hiermslc

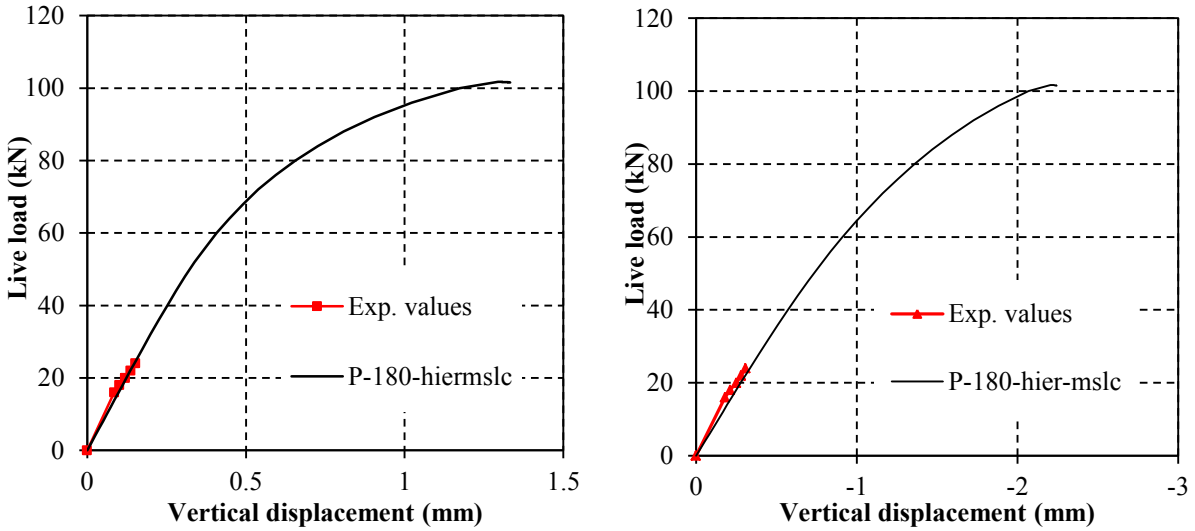

(a) Load-displacement curves at quarter span (b) Load-displacement curves at three quarter span

Figure 4-51: Experimental-numerical comparisons

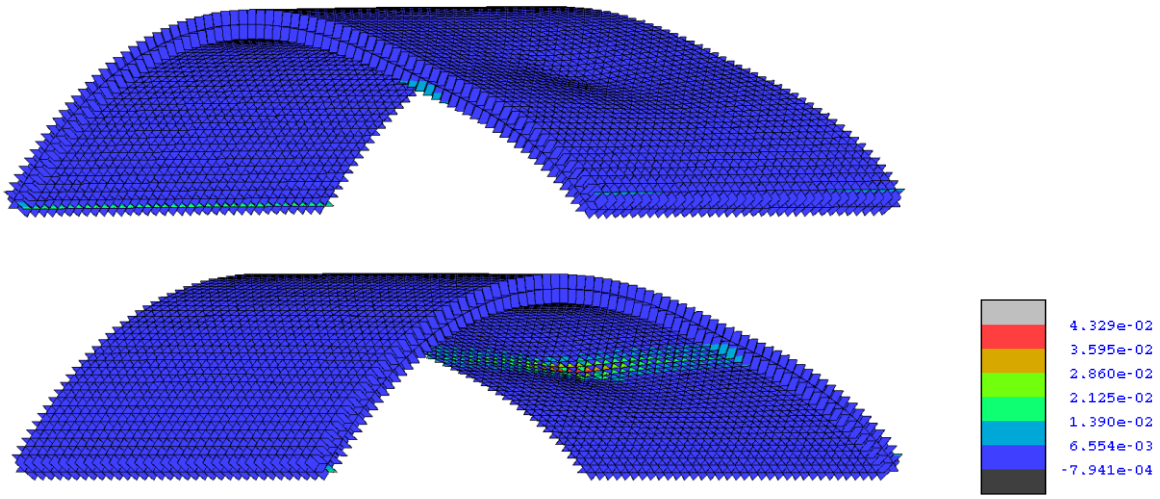

(a) Plastic work W_{cr1} at nonlinear interface elements (N/mm)

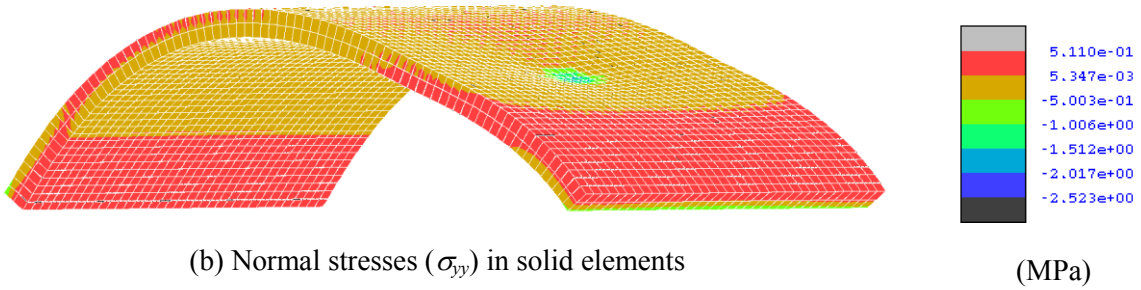

(b) Normal stresses (σ_{yy}) in solid elements (MPa)

Figure 4-52: Plastic work contour at nonlinear interfaces and normal stresses in the solid elements at the final step of the numerical simulation

4.5 Conclusions

The accuracy and the effectiveness of the adopted mesoscale modelling approach for brick-masonry arches have been investigated. Experimental-numerical comparisons have been carried showing that the proposed numerical description allows for a realistic response prediction up to collapse. The development of damage and the most critical failure mechanisms of multi-ring square and skew arches can be predicted with good accuracy.

A parametric study has been conducted analysing the influence of the different material parameters on the numerical response of a square arch. It was found that the most critical parameters are associated with the nonlinear interfaces for the mortar joints. Concerning the normal stiffness K_n, the use of the analytical expressions (3-3) provides excessively high stiffness values leading to overestimating the ultimate load capacity and the initial stiffness of the arch. Moreover the interface stiffness values suggested in the literature for different type of masonry are not uniform which renders their selection as well as the choice of the other parameters for mortar joints (e.g. tensile strength, fracture energy) quite problematic.

As the inherent drawback of the proposed detailed mesoscale modelling strategy is due to the high computational cost, alterative numerical descriptions adopting a reduced number of elements for modelling the 3D domain of a brick-masonry arch have been investigated. It was found than in the case of multi ring arches constructed by using the headers bond method, a simplified description where the arch is modelled by a series of solid and interface elements extending throughout the whole thickness of the arch provides accurate results, almost identical to those obtained employing the more demanding full mesoscale description. Moreover in the case of square arch loaded by line loads, good results can be achieved reducing the 3D numerical description into a “strip” model, where only one solid element is arranged along the width of the arch. On the other hand when analysing skew arches which are characterised by a more complex 3D failure mode, the use of a strip model may lead to overestimating the ultimate capacity, while adopting a simple square arch model with a

reduced span seems to provide better results at least in term of loading capacity. However as only one skew arch has been analysed in this chapter, further investigations and a more systematic parametric study are required to draw final conclusions and suggest simple but accurate representations for skew arches.

Finally, the effectiveness in coupling the mesoscale model with a domain partitioning approach allowing for parallel computation has been studied analysing the response of a large square arch. In the numerical simulations different partitioning approaches have been employed. These encompass flat partitioning, multi-level hierarchic partitioning and partitioning with master-slave coupling at the partition boundaries to reduce the size of the parent structures (Jokhio & Izzuddin, 2013). As found in previous research on large masonry wall structures (Macorini & Izzuddin, 2013a), the most effective computational strategy relies on the use of master-slave coupling and a large number of partitions. This way a significant speed-up can be achieved but some local errors in the stress/strain distribution at the partition boundaries are introduced. However the distribution of damage and the displacement up to collapse are very close to the predictions obtained using a monolithic model, which is impractical in the case of nonlinear analysis of large arches.

CHAPTER 5

Mesoscale Analysis of Masonry Arches

5.1 Introduction

In Chapter 4, the proposed mesoscale modelling strategy for masonry arches has been validated and calibrated against a series of experimental tests carried out at the University of Salford (Melbourne et al., 2007; Wang, 2004). In the present chapter, the validated numerical description is employed in nonlinear numerical simulations to provide a deep insight into the response up to collapse of square and skew masonry arches characterised by different geometrical and material characteristics, and subjected to different static loading and boundary conditions.

To investigate the effects of the geometry of the arch, multi-ring arches with segmental circular shape built using the stretcher and the header bond method, and characterised by different rise-to-span ratios are analysed. In this respect, the geometrical characteristics of typical arches found in a statistical survey on old masonry bridges (Brencich & Morbiducci, 2007) are considered. According to this study, 50% of the brick-masonry bridges within the Italian railway network built between 1830 and 1940 are formed by arches with 0.5 rise-to-span ratio (deep arches). The remaining bridges are shallow arch bridges with a rise-to-span ratio included in the interval 0.1-0.4. The material properties utilised in the analysis of square arches correspond to the values reported in Tables 4-3, 4-4 and 4-5, and used in Section 4.2.2 to validate the mesoscale description against the experimental response

of a square arch with good quality brickwork. On the other hand in the analysis of skew arches, the material properties adopted in Section 4.3 and reported in Tables 4-12, 4-13 and 4-14 are employed.

To study the influence of defects in the brickwork, the response of defective arches with weak circumferential mortar joints connecting adjacent rings are compared to that of arches with uniform (strong) mortar joints. Previous studies pointed out that "defective" mortar joints in multi-ring arches without headers may facilitate ring separation. In real bridges, imperfection in mortar joints may be caused by mortar wash out or due to the use of poor material which leads, in time, to "ring delamination". Beare (Beare, 1993) highlighted that ring debonding is the most common defect in multi-ring arches with stretcher bond. Besides, according to Sunley (Sunley, 1990) all existing brick-masonry bridges with insufficient interconnecting headers are defective, whether or not they are weakened by existing cracks or ring separation. To explore the behaviour of masonry arch bridges prone to ring separation, Melbourne and Gilbert (Melbourne & Gilbert, 1995) performed physical tests on models of arch bridges, where damp sand was used rather that standard mortar to bond arch rings so as to promote ring separation. The results of this study confirmed that ring separation strongly influences the response up to collapse, reducing the loading capacity. Moreover it was found that ring debonding may occur not only in arches with weak joints connecting adjacent rings, but also in arches with mortar joints of good quality.

Additional numerical simulations have been carried out to study the effects of the abutment stiffness and movements at the supports. In this respect, the failure modes induced by differential vertical settlements and inward and outward horizontal displacements at the abutments are investigated, and the influence of these movements on the arch load capacity is analysed. Considering the layout of this chapter, in the first part the results obtained for square arches are presented and discussed, while the second part reports the numerical studies on skew arches.

5.2 Mesoscale analysis of square arches

The static response of square arches is investigated using the simplified mesoscale "strip" model introduced in Section 4.2.4.2. As discussed before, in the case of square arches subject to line loads, the effects of the masonry bond along the arch width are negligible. Thus square arches can be modelled using a computationally efficient description utilising only one set of solid elements along the span for each arch ring (see model *Mesoscale 2* in the Section 4.2.4.2). Under these assumptions, the specific width of the arch does not influence its qualitative response characteristics. Therefore for convenience, square arches with unit width (1m) are considered hereinafter.

5.2.1 Effects of rise-to-span ratio

As mentioned before, the response up to collapse of segmental arches characterised by the most common rise-to-span ratios as found in a number of existing masonry arch bridges (Brencich & Morbiducci, 2007) are analysed. These include eight arches with two or five rings connected by good quality mortar. The main geometrical properties of the arches are reported in Table 5-1, while Figure 5-1 shows the mesoscale FE mesh for the arches with 3m span.

Table 5-1: Geometry of the arches with different rise-to-span ratio

Model	Rise - H (mm)	Span - L (mm)	No. of Rings	Thickness (mm)	Rise-to-span ratio
Arch 1	1500	3000	2	215	1:2
Arch 2	750	3000	2	215	1:4
Arch 3	375	3000	2	215	1:8
Arch 4	300	3000	2	215	1:10
Arch 5	4000	8000	5	537.5	1:2
Arch 6	2000	8000	5	537.5	1:4
Arch 7	1000	8000	5	537.5	1:8
Arch 8	800	8000	5	537.5	1:10

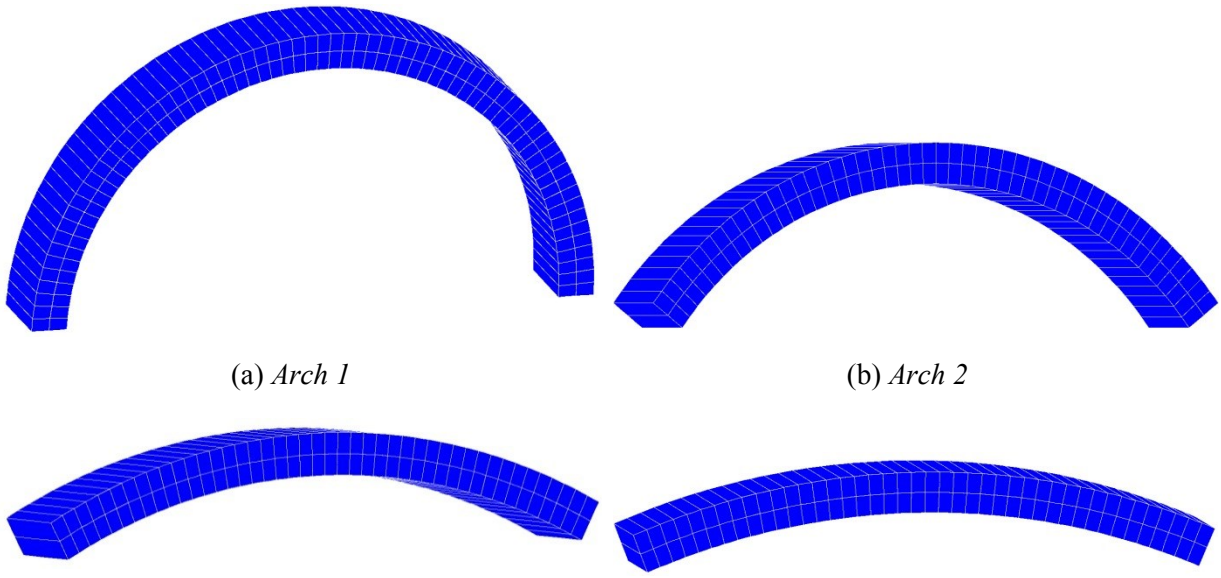

(a) *Arch 1* (b) *Arch 2*

(c) *Arch 3* (d) *Arch 4*

Figure 5-1: Mesoscale strip models for square arches with different rise-to-span ratio

As for the square arches analysed in Section 4.2, the loading arrangement encompasses two initial vertical (dead) loads. These are applied at the quarter and three quarter span to represent the weight of the backfill above the arch as in typical masonry bridges. More specifically, the two identical dead loads are equal to 22.5kN/m for the arches with 3m span and to 100kN/m for the 8m span arches. In the nonlinear numerical simulations, an additional line load (live load) is then applied at quarter span up to collapse under displacement control.

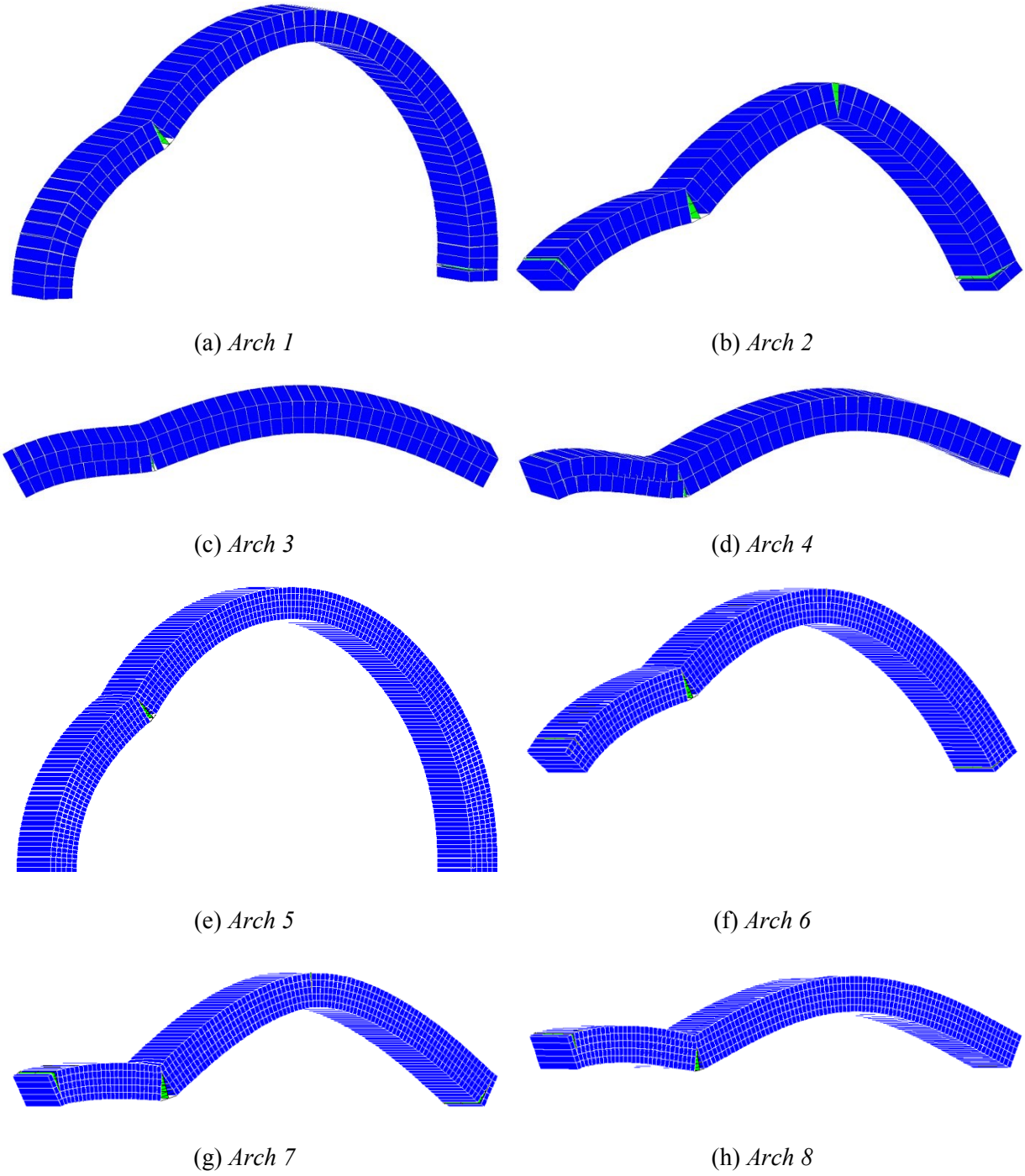

(a) *Arch 1* (b) *Arch 2*

(c) *Arch 3* (d) *Arch 4*

(e) *Arch 5* (f) *Arch 6*

(g) *Arch 7* (h) *Arch 8*

Figure 5-2: Deformed shapes at the last step of the analysis

Similar results have been found for arches with different span length. The deformed shapes and the plastic work W_{cr1} contours at the end of the numerical simulations are shown in Figure 5-2 and 5-3. In particular it can be seen that in the case of deep arches and arches with 1:4 rise-to-span ratio the failure mechanism is a typical “hinge mechanism”, which is

governed by the development of four radial cracks at the opposite haunches and at about the quarter and the three quarter span. Conversely in the case of the two arches with 1:8 and 1:10 rise-to-span ratio, radial cracks are combined with ring separation, which takes place at the arch haunch close to the live load. This is mainly caused by the shear forces in the arch which generally increase when the rise-to-span ratio reduces, becoming relatively large for very shallow arches (Dym & Williams, 2011).

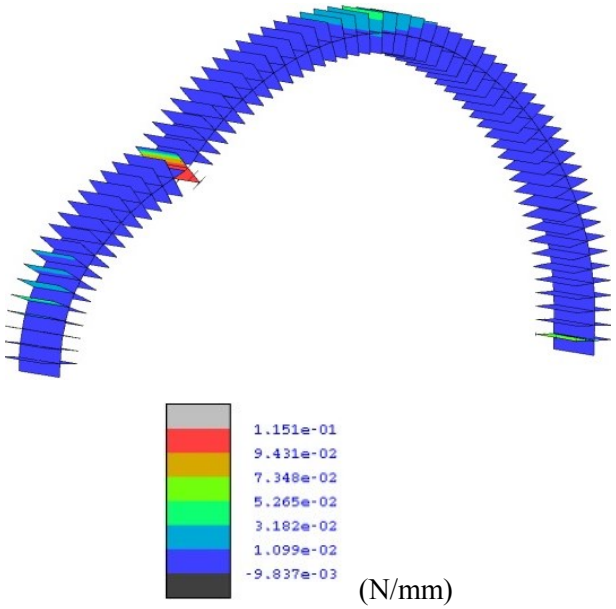

(a) *Arch 1*

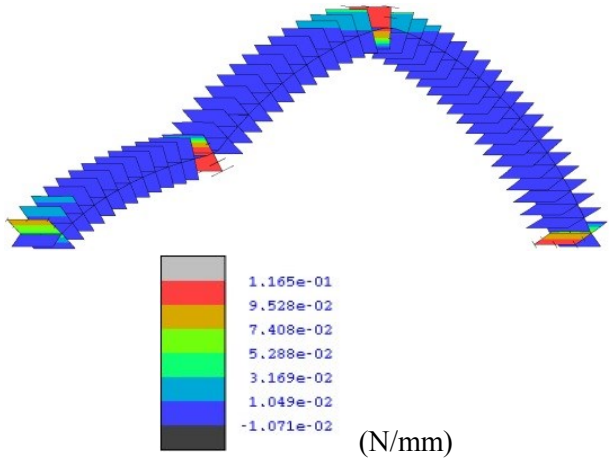

(b) *Arch 2*

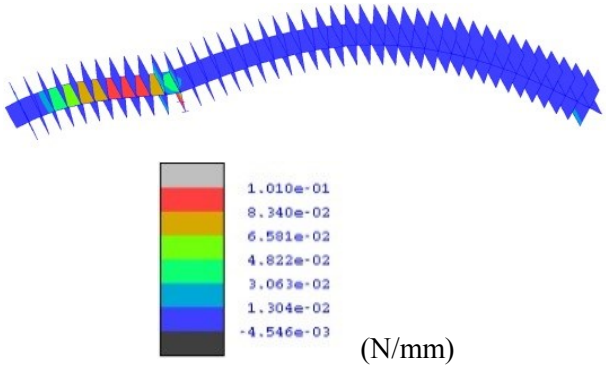

(c) *Arch 3*

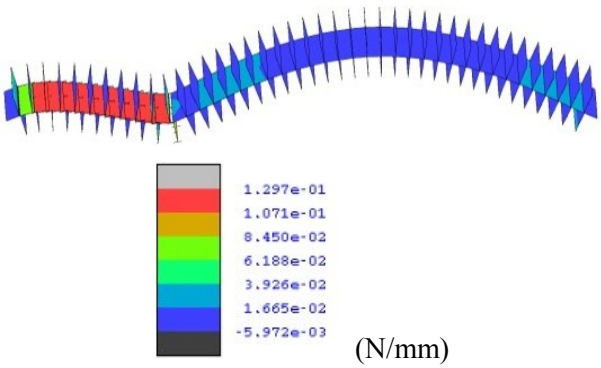

(d) *Arch 4*

Figure 5-3: Plastic work W_{cr1} contour at the last step of analysis (Cont'd …)

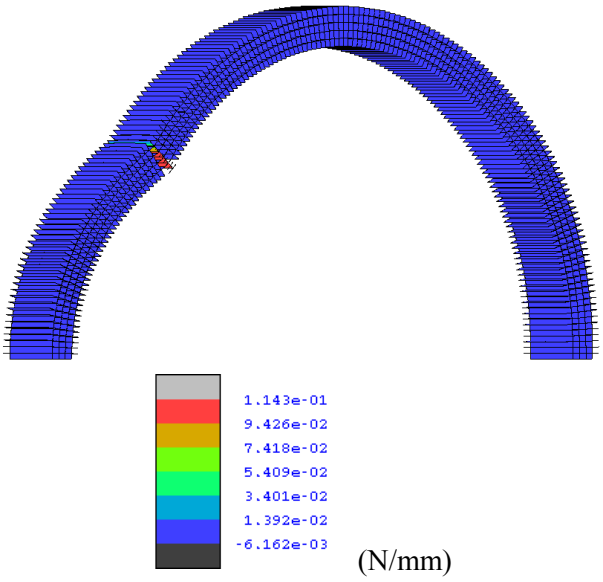

(e) *Arch 5*

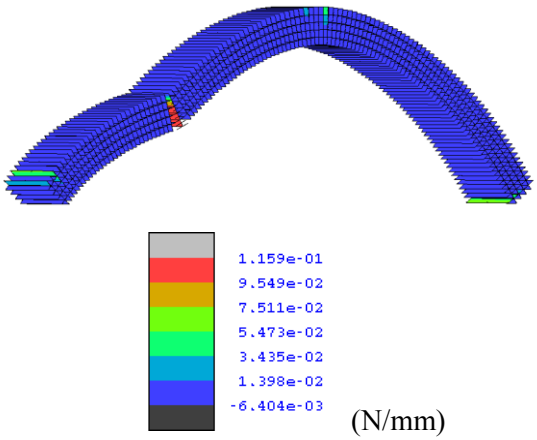

(f) *Arch 6*

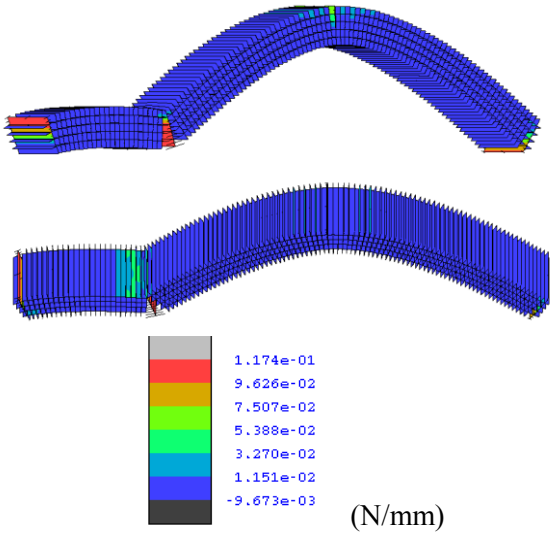

(g) *Arch 7*

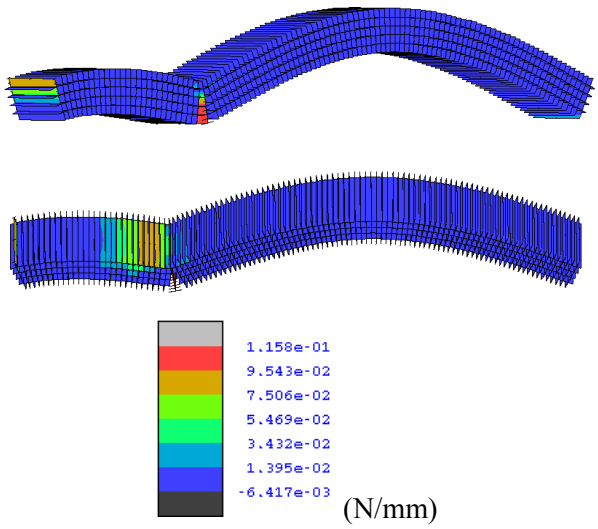

(h) *Arch 8*

Figure 5-3: Interface plastic work W_{cr1} contour at the last step of analysis

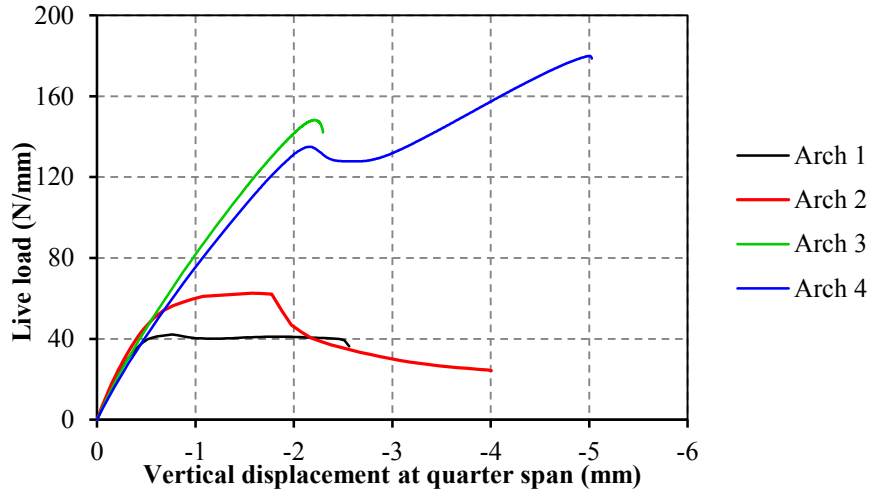

(a) 3m span

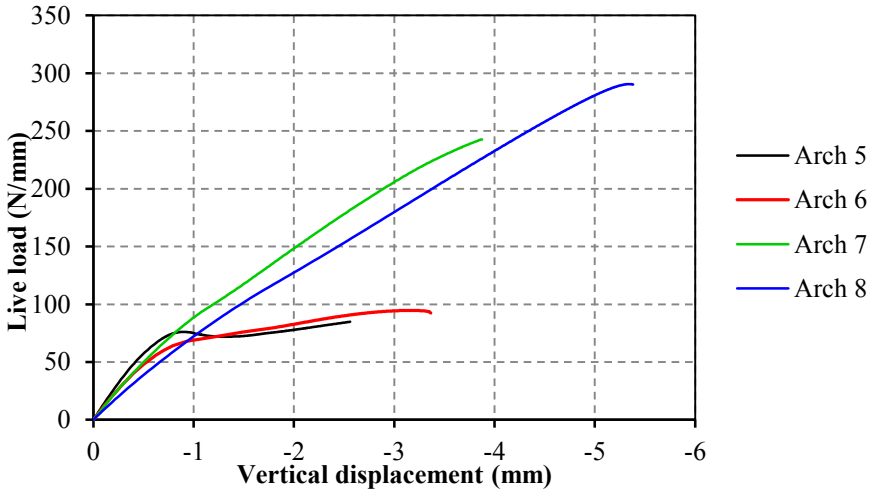

(b) 8m span

Figure 5-4: Load displacement curves for arches with different rise-to-span ratios

Figure 5-4a,b display the load-displacement curves at quarter span for the arches with 3m and 8m span. A significant change in the response for different rise-to-span ratio values can be observed. The deep arch is characterised by the lowest loading capacity but a notable ductility, as after reaching the maximum load the displacements significantly increase while the load remains almost constant. The ultimate load rises for arches with low rise-to-span ratio (Figure 5-5), but the response up to the maximum load becomes less smooth especially for the very shallow arch (1:10 rise-to-span ratio). In this case while three radial cracks around the two springings and at about the quarter span develop gradually, ring separation

occurs suddenly producing a rapid realise of elastic energy and causing an abrupt softening in the load-displacement curve. After a short almost flat branch, where the displacement increases while the live load remains constant, the load-displacement curve rises again up the ultimate load. This is reached when the fourth radial crack forms at about three quarter span. A similar behaviour is expected also for the *Arch 3* whose response is also governed by ring separation. However in this case, convergence problems occurred just after the sudden development of ring separation at the left haunch (Figure 5-3c). This prevented an accurate prediction of the maximum load; thus the ultimate load value for the *Arch 3* reported in Figure 5-5 should be considered only as a conservative estimate.

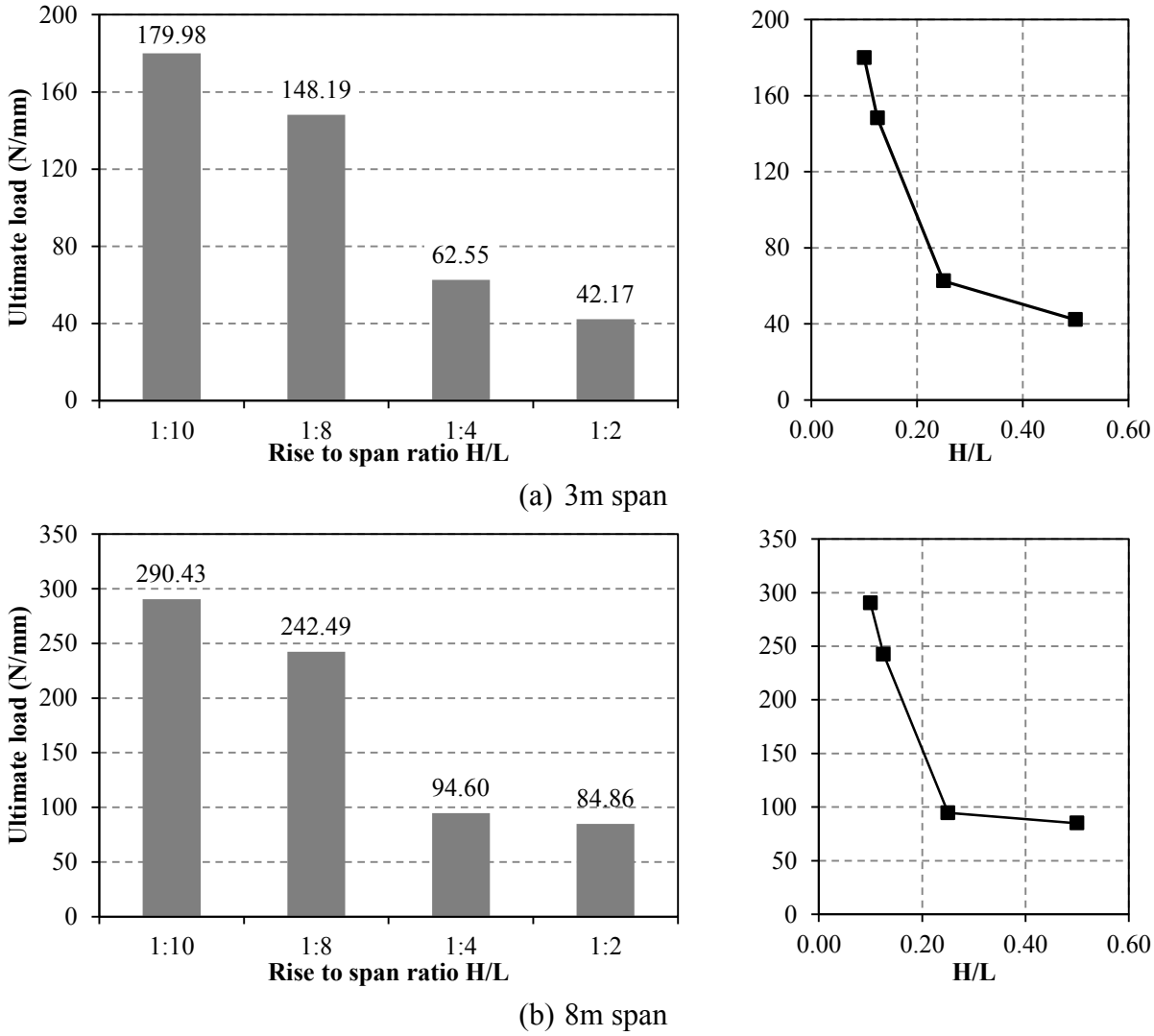

Figure 5-5: Ultimate load for different rise-to-span ratio

5.2.2 Effects of brickwork defects

Four defective arches prone to ring separation have been investigated. These are characterised by geometrical features identical to those of the *Arch 1*, *Arch 2*, *Arch 3* and *Arch 4* analysed in the previous section, but are constructed with weak circumferential mortar joints. In this respect, the material properties reported in Table 5-2 are employed for the interface elements representing the joints which connect the two rings. These include reduced cohesion, tensile strength and friction angle values. In the following the four defective arches are referred to as *Arch 1m*, *Arch 2m*, *Arch 3m* and *Arch 4m*.

Table 5-2: Inelastic properties of the interface elements for weak mortar joints

	Surface F_1	**Surface Q_1**	**Surfaces F_2, Q_2**
Mortar-brick interface	$C_0 = 0.004\text{N/mm}^2$ $\sigma_{t0} = 0.002\text{N/mm}^2$ $\tan\phi_0 = 0.3$ $G_{f1} = 0.02\text{N/mm}$ $G_{f2} = 0.125\text{N/mm}$	$C_0 = 0.004\text{N/mm}^2$ $\sigma_{t0} = 0.002\text{N/mm}^2$ $\tan\psi_0 = 0.0$ $G_{f1} = 0.02\text{N/mm}$ $G_{f2} = 0.125\text{N/mm}$	$D = 24.5\ \text{N/mm}^2$ $\sigma_{c0} = 24.5\text{N/mm}^2$ $\tan\theta_0 = 0.045$ $G_c = 5.0\text{N/mm}$
	$G_{f1} = 0.08\text{N/mm}$ $G_{f2} = 0.5\text{N/mm}$	$G_{f1} = 0.08\text{N/mm}$ $G_{f2} = 0.5\text{N/mm}$	

In Figures 5-6 and 5-7 the deformed shapes and the plastic work contours at the last step of the numerical simulations are displayed, whereas in Figure 5-8 the load-displacement curves are shown. In all the cases ring separation characterises the response at collapse and the failure modes. Comparing the curves plotted in Figures 5-4 and 5-8, it can be seen that the poor connection between the two rings significantly influences the load-displacement response of the four arches. Ring separation starts at very low load levels, and its development is gradual leading to progressive stiffness degradation up to the ultimate load,

but not to a sudden force reduction as for the very shallow arches with good quality mortar (e.g. *Arch 3* and *Arch 4* in Section 5.2.1).

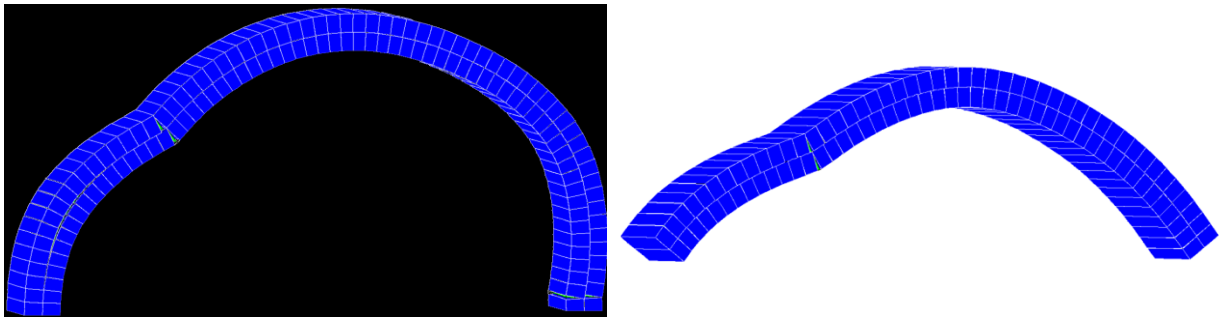

(a) Rise-to-span ratio = 1:2 (b) Rise-to-span ratio = 1:4

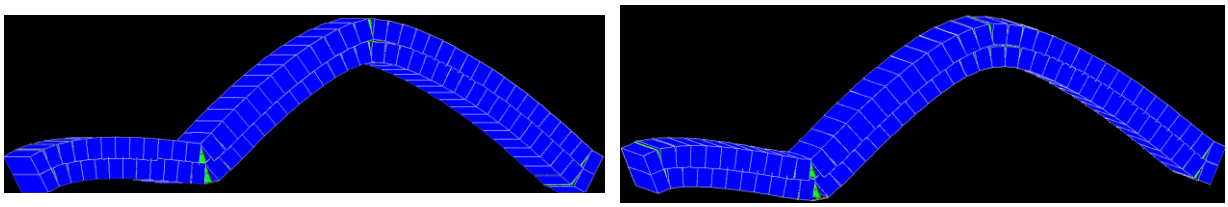

(c) Rise-to-span ratio = 1:8 (d) Rise-to-span ratio = 1:10

Figure 5-6: Deformed shapes at the last step of analysis for defective arches

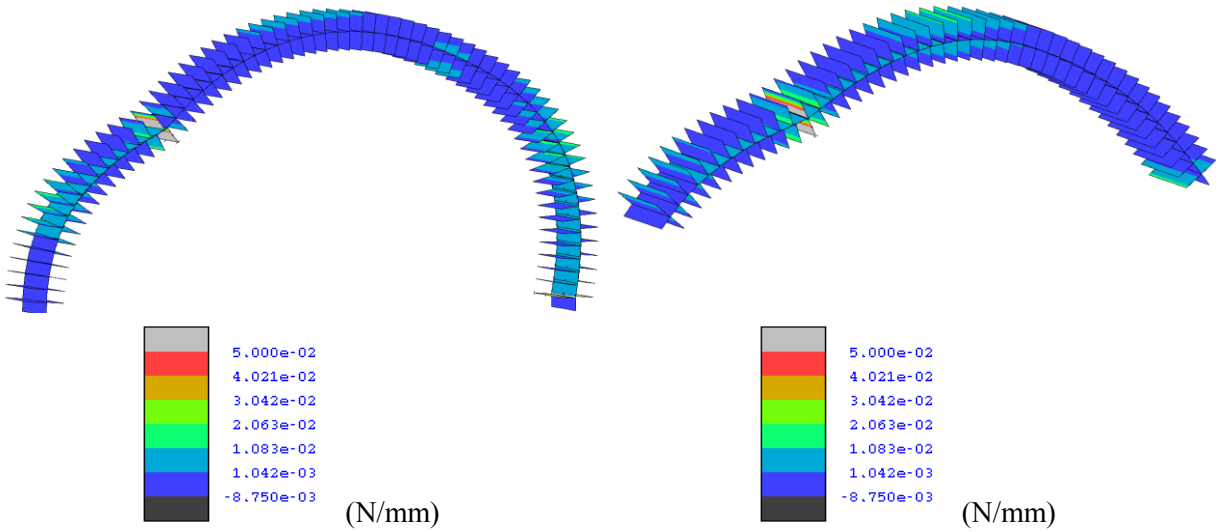

(a) Rise-to-span ratio = 1:2 (b) Rise-to-span ratio = 1:4

Figure 5-7: Plastic work W_{cr1} contour at the last step of analysis for defective arches (Cont'd …)

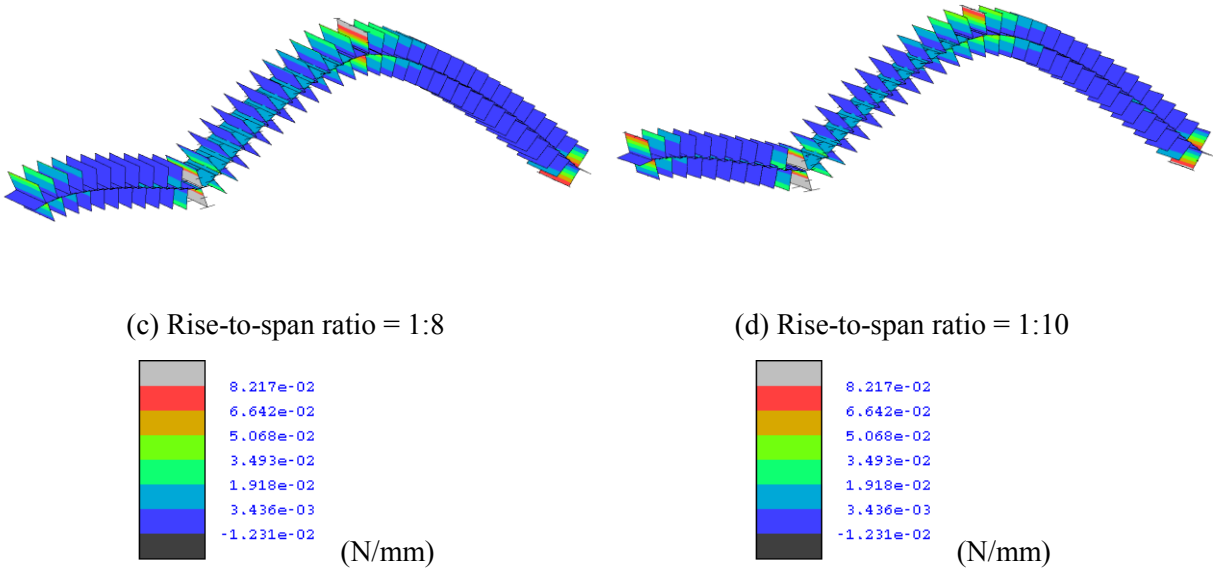

Figure 5-7: Plastic work W_{cr1} contour at the last step of analysis for defective arches

Finally, Figure 5-9 and 5-10 compare ultimate load and initial stiffness values for arches with good quality masonry against those for arches with poor circumferential mortar joints. More than 50% strength and stiffness reduction can be observed for all the analysed arches. This highlights the critical role played by the connections between adjacent rings and the importance of a correct evaluation of the mechanical characteristics of the mortar joint for an accurate response prediction of existing masonry arches.

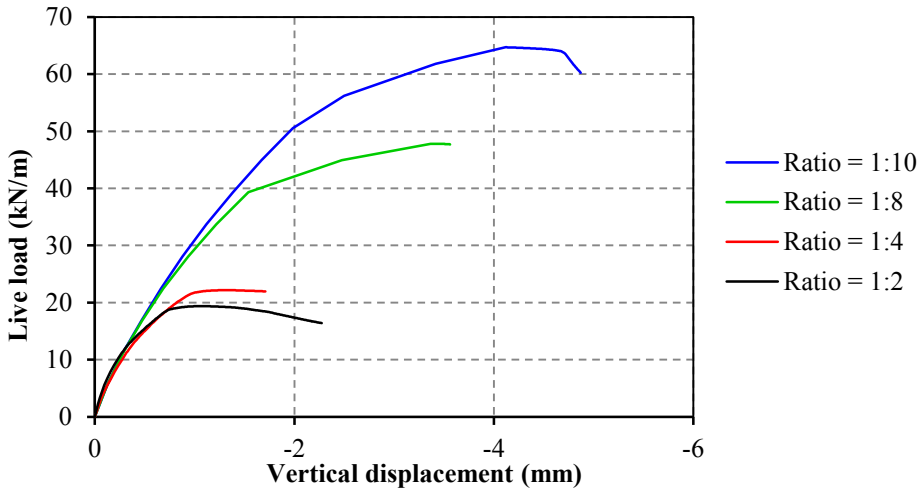

Figure 5-8: Load displacement curves for defective arches with different rise-to-span ratios

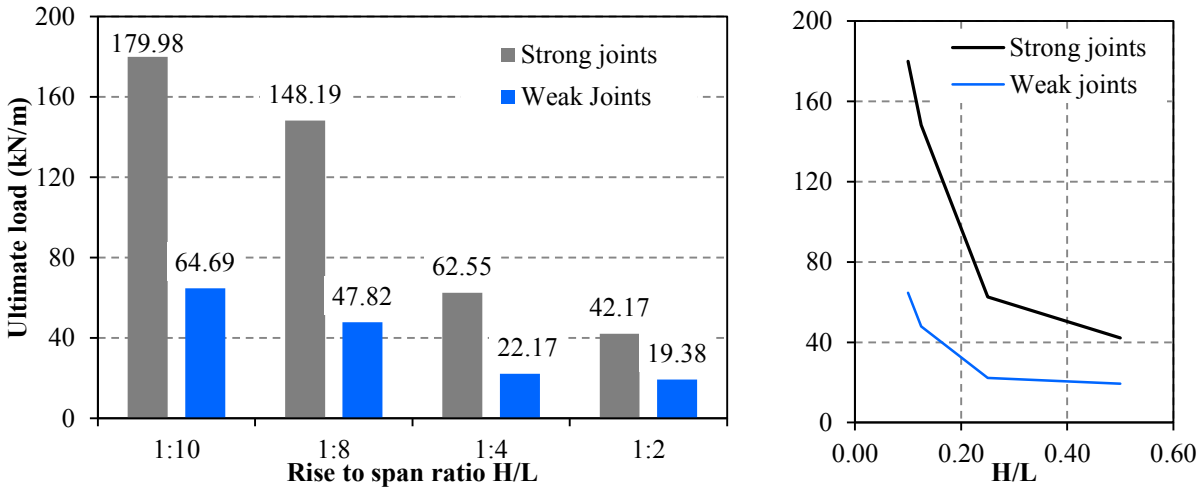

Figure 5-9: Ultimate load for different rise-to-span ratios and different circumferential mortar joints

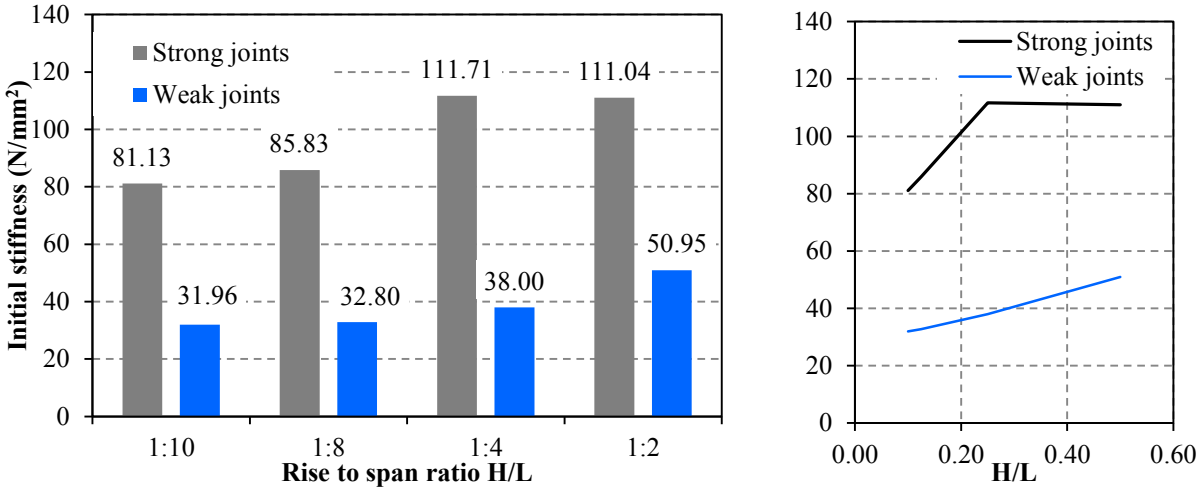

Figure 5-10: Initial stiffness for different rise-to-span ratios and different circumferential mortar joints

5.2.3 Effects of loading position

The two-ring arches with 3m span considered in Section 5.2.1, are analysed here to study the influence of the loading position on the response up to collapse. Particular attention is given to the ultimate capacity and the type of failure mechanism. As shown in Figure 5-11, two dead loads (22.5 kN/m) are applied at quarter and three quarter span, while a live load is placed at four different positions: close to the left springing (Case 1), at 1/8 span (Case 2), at quarter span (Case 3) and at mid-span (Case 4), and then increased up to collapse.

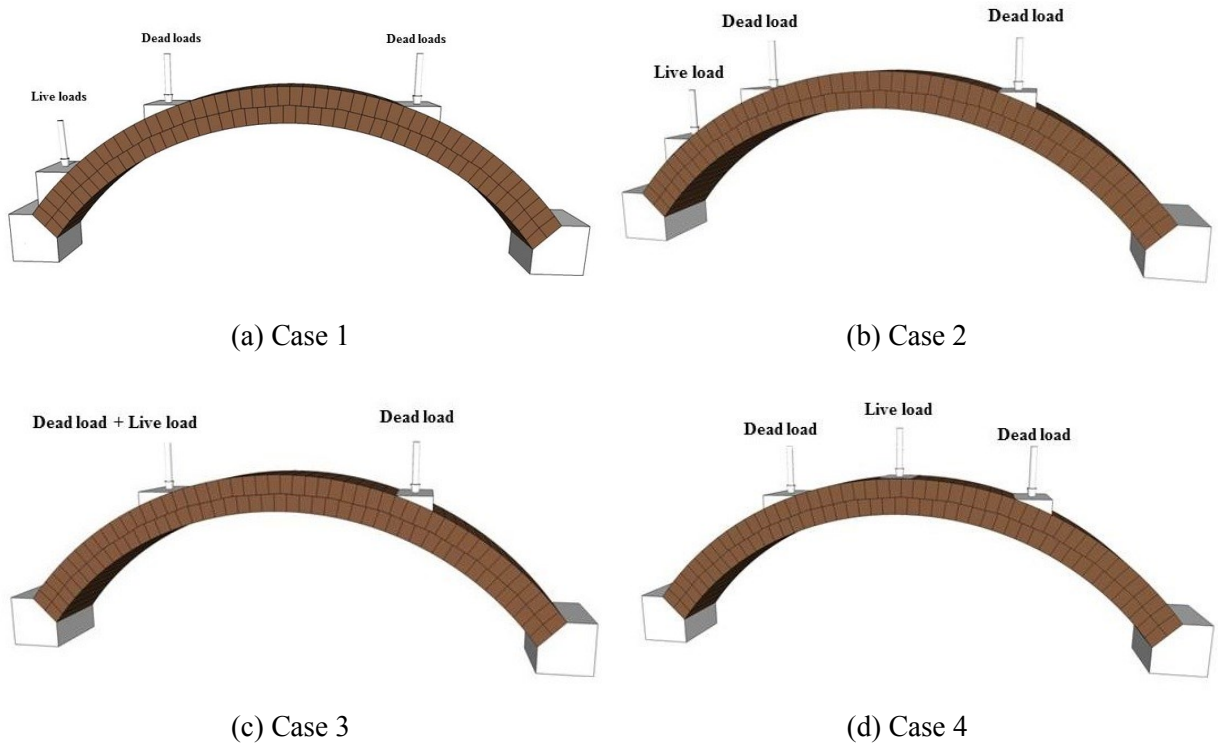

(a) Case 1 (b) Case 2

(c) Case 3 (d) Case 4

Figure 5-11: Loading positions

Deformed shapes at the final step of the numerical simulations for the arch with 1:4 rise-to-span ratio (*Arch 2*) are shown in Figures5-12a,b,c,d, while the plastic work contours at collapse for the same arch are displayed in Figures 5-13a,b,c,d. Different failure mechanisms can be clearly noticed. In Case 1 the load near the left support induces a local failure mode; this is due to shear sliding at the radial bed joint close to where the load is applied. In Case 3 only radial cracks form (high mechanism), while in Case 2 and Case 4 radial cracks are accompanied by ring separation. This develops at the left haunch close to the live load in Case 3, and symmetrically at both haunches when the live load is applied at mid-span.

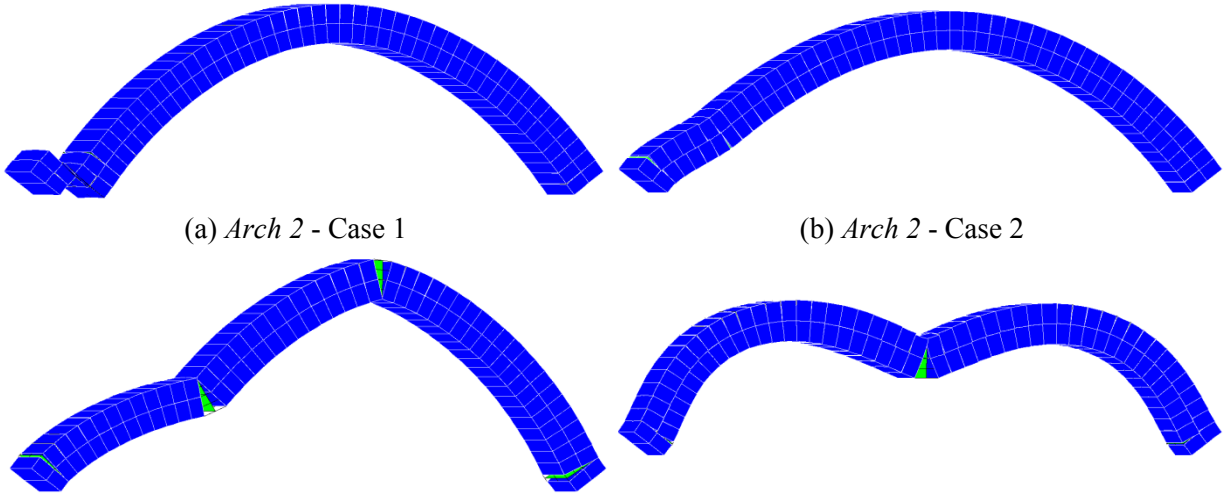

(a) *Arch 2* - Case 1 (b) *Arch 2* - Case 2

(c) *Arch 2* - Case 3 (d) *Arch 2* - Case 4

Figure 5-12: *Arch 2* deformed shapes at the last step of the numerical simulation for different live load positions

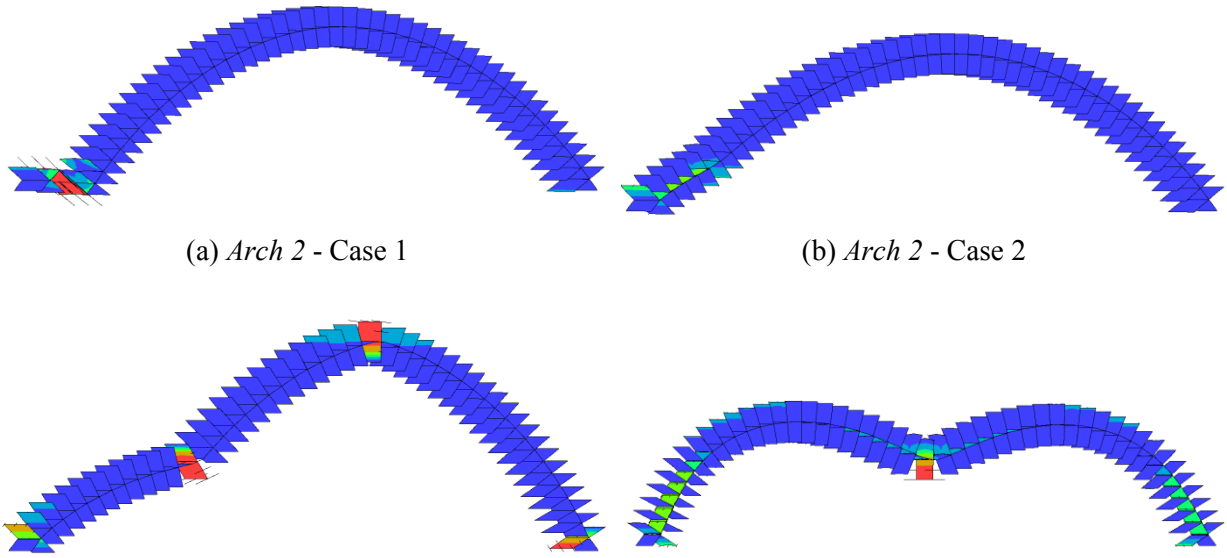

(a) *Arch 2* - Case 1 (b) *Arch 2* - Case 2

(c) *Arch 2* - Case 3 (c) *Arch 2* - Case 4

Figure 5-13: Interface plastic work W_{cr1} of *Arch 2* at the last step of analysis for different live load positions

In Figure 5-14, the displacements at the live load position for the four different cases are plotted against the live load. It can be seen how the response characteristics including the ultimate load, the initial stiffness and the arch ductility strongly depend upon the location of the live load. When the load is applied near the support, the load capacity of the arch is influenced by its ability to resist shear forces. These may cause plastic shear sliding at radial

bed joints as in Case 1, or ring separation associated with local failure as in Case 2. In both cases shear failure prevents an adequate redistribution of internal forces limiting the arch ductility. On the other hand the response of *Arch 2* under a live load applied at quarter span is very ductile, being governed by the formation of radial cracks (Figure 5-13c) leading to a four-hinge mechanism without ring separation.

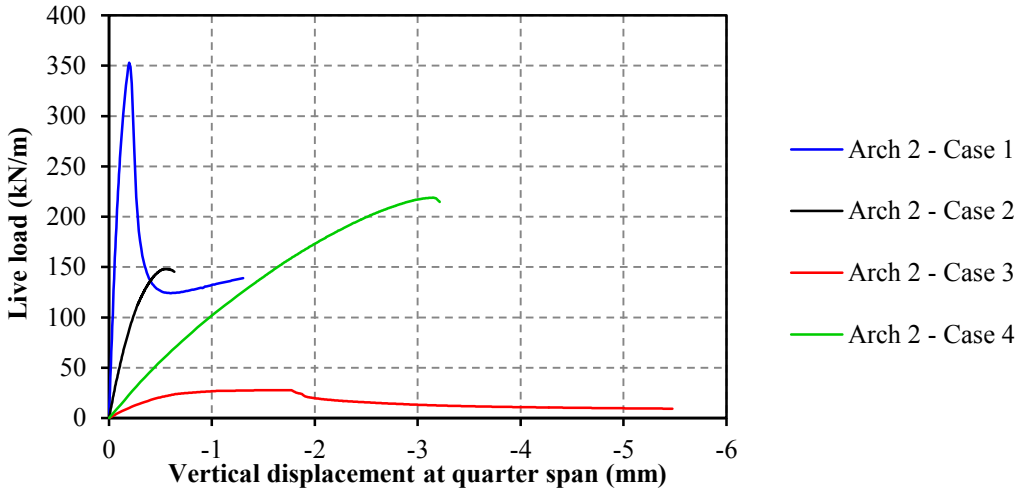

Figure 5-14: Load-displacement curves for different positions of the live load

Figure 5-15 presents the ultimate load values for arches with different rise-to-span ratios (e.g. *Arch 1*, *Arch 2*, *Arch 3* and *Arch 4* in Section 5.2.1) loaded at different positions. The results show that the condition with loads close to the supports is the most critical for very shallow arches, while the lowest load capacity for the deep arch and the arch with intermediate 1:4 rise-to-span ratio is achieved when the live load is applied at quarter span.

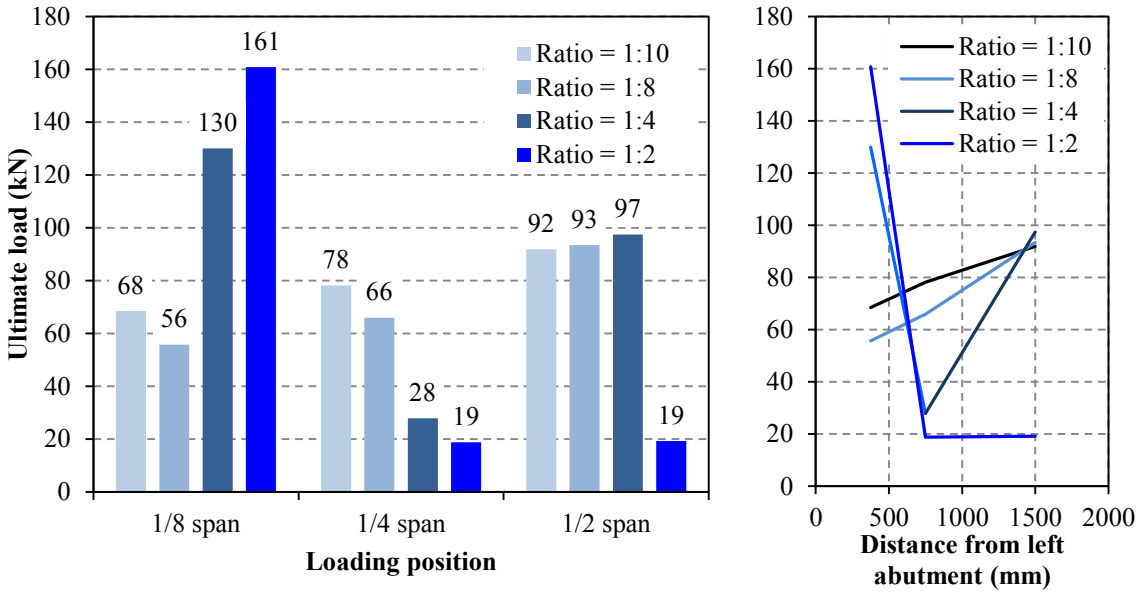

Figure 5-15: Influence of the loading position on the ultimate load for arches with different rise-to-span ratios

5.2.4 Effects of abutment stiffness

In the previous numerical simulations, square arches have been modelled assuming that the supports at the springings are perfectly rigid. In this section, the effects of potential deformations at the abutments are investigated. These may develop in real arch bridges under the forces transferred by the masonry arch to the foundations (Davey, 1953). To analyse the effects of the abutment stiffness, elastic interface elements are used to connect the arch springings to fixed supports so as to represent elastic abutments. In particular, the 3m span arches presented in Section 5.2.1 have been analysed employing the five pairs of elastic normal and tangent stiffness values reported in Table 5-3.

Figures 5-16a,b,c,d,e show the plastic work contours at the end of the numerical analyses for *Arch 2*. It can be seen that the failure mechanism does not change by varying the stiffness at the lateral supports, and in all the cases arch failure is reached when a hinge mechanism with four radial cracks forms.

Table 5-3: Elastic stiffness values for the interface elements at the arch springings

Model	Normal stiffness K_n (N/mm^3)	Tangent stiffness K_t (N/mm^3)
K_{ab1}	1.0×10^0	1.0×10^0
K_{ab2}	1.0×10^1	1.0×10^1
K_{ab3}	1.0×10^2	1.0×10^2
K_{ab4}	1.0×10^4	1.0×10^4
Rigid	-	-

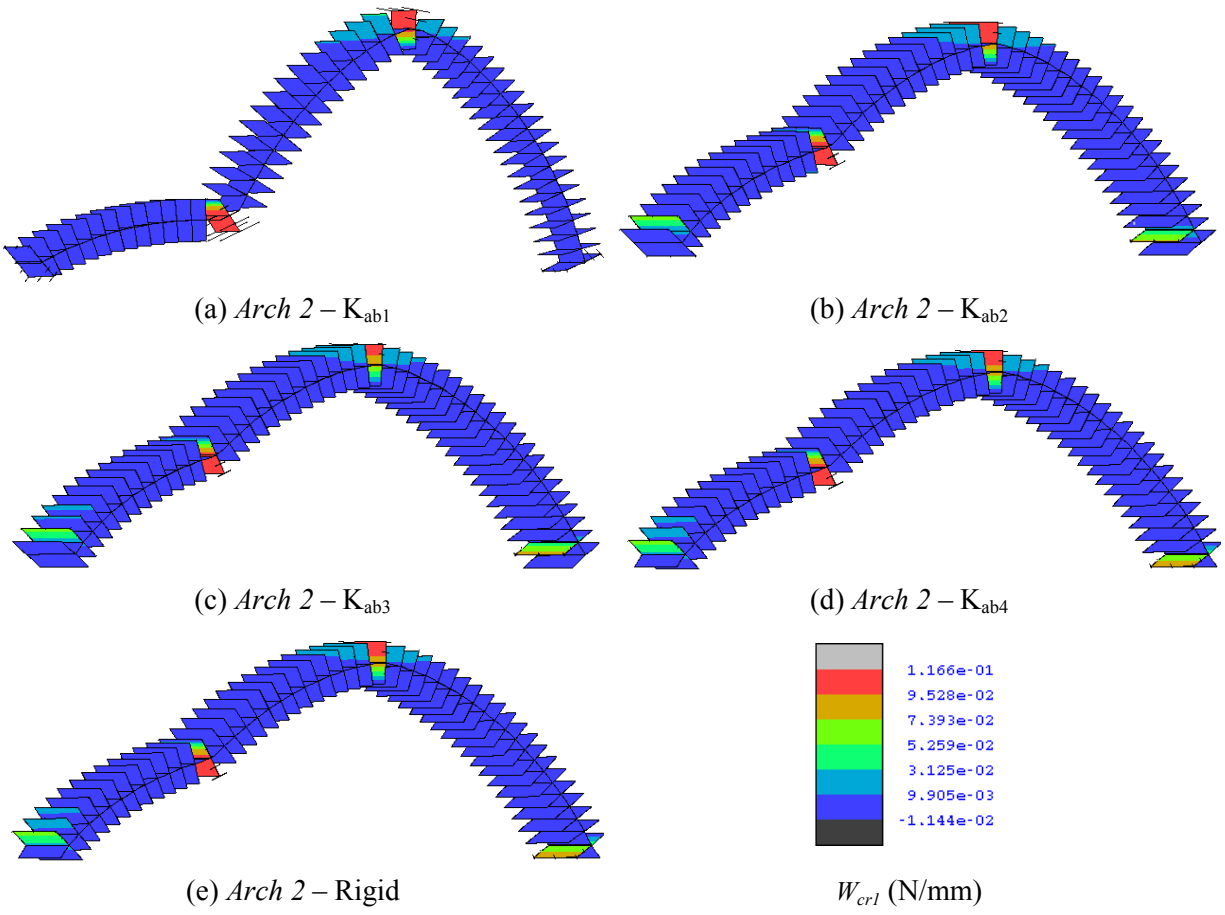

(a) *Arch 2* – K_{ab1} (b) *Arch 2* – K_{ab2}

(c) *Arch 2* – K_{ab3} (d) *Arch 2* – K_{ab4}

(e) *Arch 2* – Rigid W_{cr1} (N/mm)

Figure 5-16: Plastic work W_{cr1} contour for *Arch 2* with different abutment stiffness values

The load-displacement curves showing the response of *Arch 2* are plotted in Figure 5-17. The variation of the ultimate load and the initial stiffness of the arch with the abutment stiffness are displayed in Figures 5-18 and 5-19. Ultimate load and initial stiffness do not change significantly for large stiffness values, but they both notably reduce for a normal and tangential stiffness at the abutments of 1N/mm^3. In this case, a reduction of 46% for the ultimate load and 60% for the initial stiffness compared to the arch with perfectly rigid supports can be observed. As shown in Figure 5-20, when arches with different rise-to-span ratios are analysed, different variations of stiffness and strength can be noticed. In particular, for very shallow arches (e.g. 1:10 and 1:8 rise-to-span ratios) only a marginal reduction of the load capacity can be observed, but the stiffness variation is remarkable.

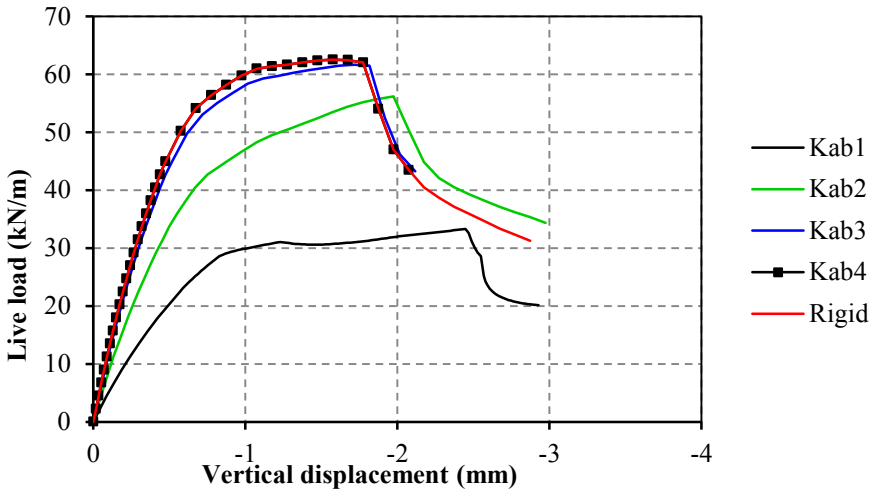

Figure 5-17: Load-displacement curves for *Arch 2* width different abutment stiffness values

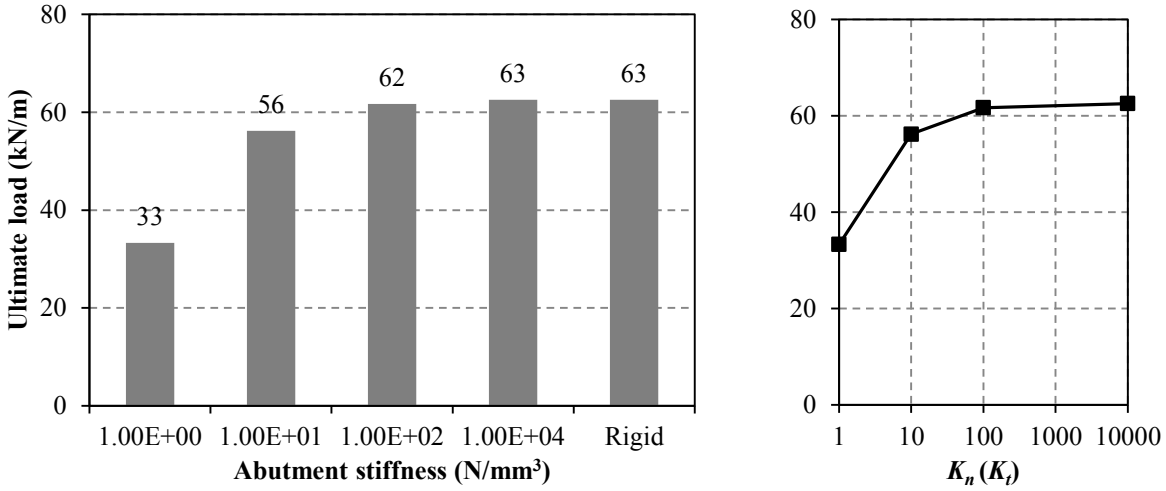

Figure 5-18: Influence of abutment stiffness on the load capacity of the arch

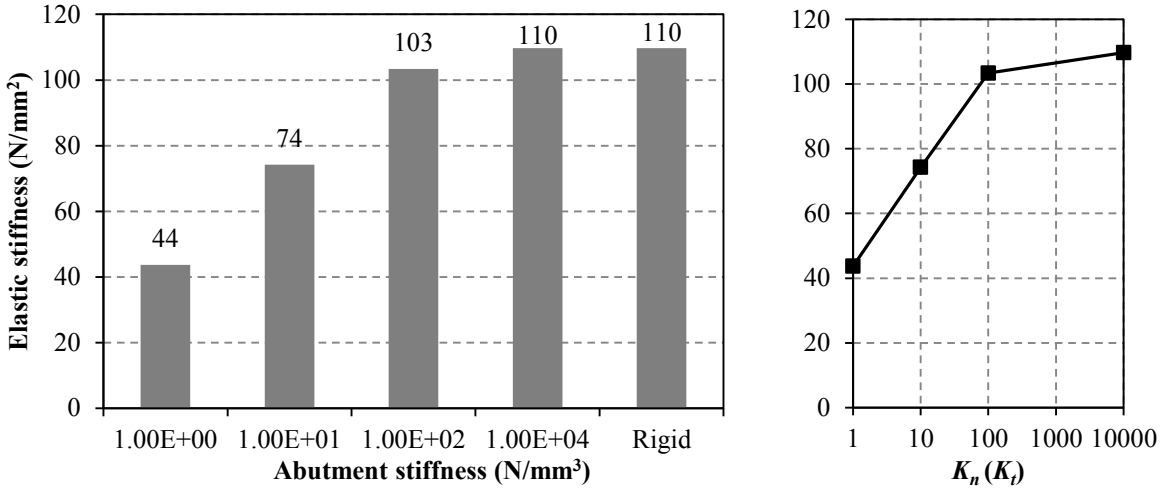

Figure 5-19: Influence of abutment stiffness on the initial stiffness of the arch response

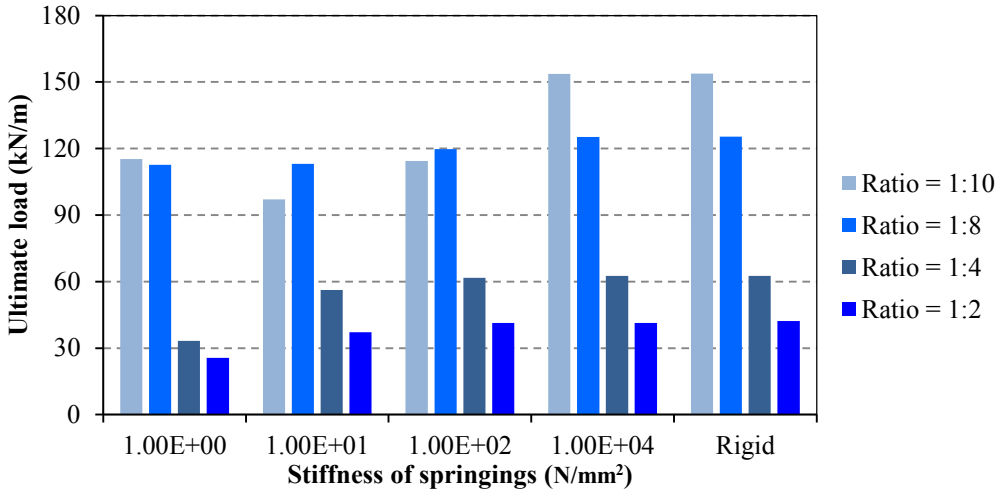

(a)

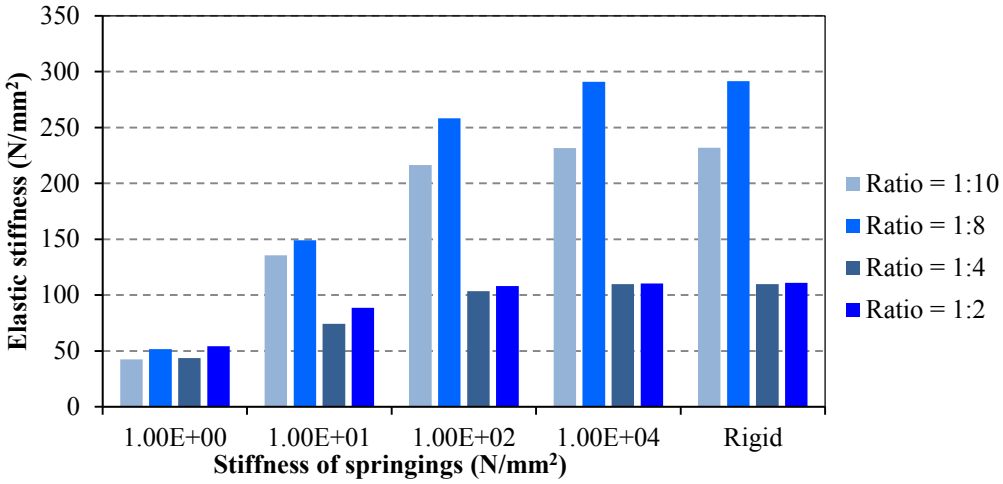

(b)

Figure 5-20: Influence of the abutment stiffness on (a) the ultimate load and (b) the initial stiffness for arches with different rise-to-span ratios

5.2.5 Effects of abutment movement

Movement at the abutments and piers resulting from the instability of the foundations is one of the most common causes of deterioration for masonry arch bridges. In general, the performance of masonry arch barrels, which are the most critical structural components in masonry bridges, is highly affected by differential settlements (McKibbins et al., 2006). Support movements may occur during the bridge construction or may be caused by extreme events (e.g. earthquakes) or due to a change in the soil conditions below the foundations.

Moreover if the bridge is built on waterways, water flow may induce scour at the footings of piers and abutments, often leading to the collapse of the bridge. In practical assessment of masonry arch bridges, the formation of three hinges caused by vertical or horizontal differential movements at the supports represents a failure mechanism, and indicates that the arch should be immediately repaired (McKibbins et al., 2006).

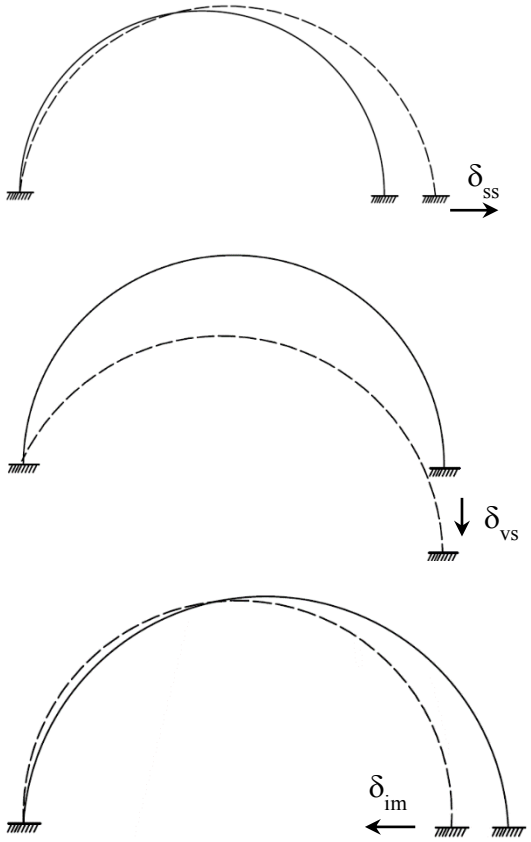

Horizontal spread of support δ_{ss}

Vertical differential settlement δ_{vs}

Horizontal inward movement δ_{im}

Figure 5-21: Settlement modes

In this section, the possible consequences and effects of different types of support movements are investigated. To this end, the square arches with 3m span considered before (*Arch 1*, *Arch 2*, *Arch 3*, *Arch 4*, *Arch 5* and *Arch 6* in Section 5.2.1) are analysed considering the settlement modes shown in Figure 5-21. Afterwards, different levels of support displacements are applied before increasing the live load at quarter span up to collapse.

Moreover, as in Section 5.2.2, the influence of defects in masonry is investigated comparing the response of arches with good quality brickwork (strong joints) against that of arches with weak mortar joints connecting the two rings (weak joints).

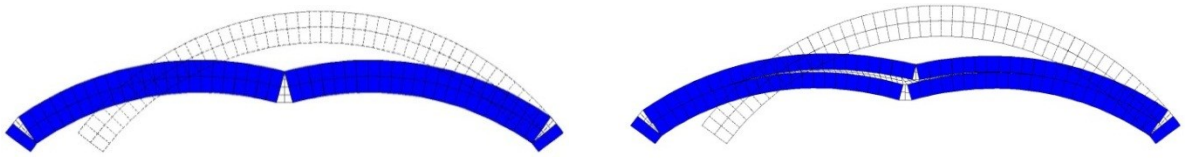

Strong joints Weak joints

(a) Horizontal spread of support

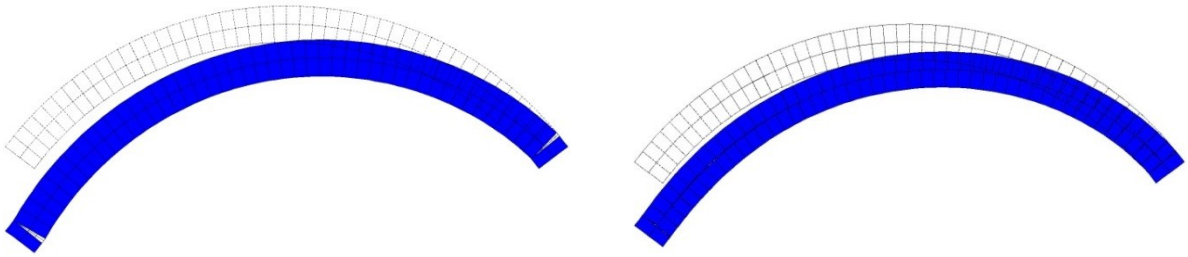

Strong joints Weak Joints

(b) Vertical differential settlement

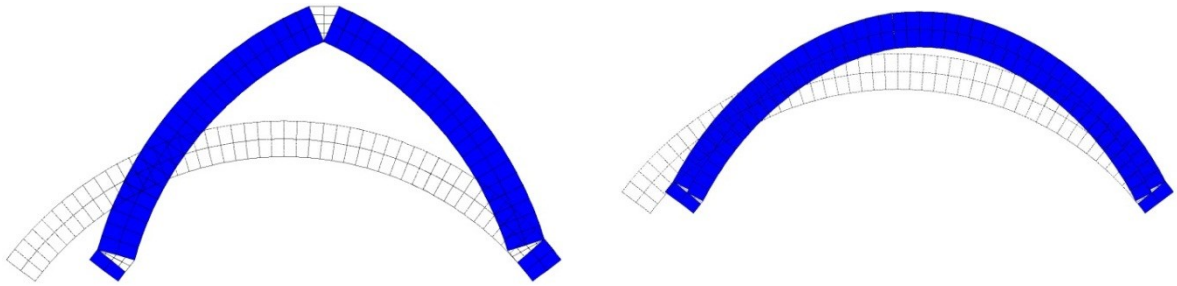

Strong joints Weak joints

(c) Horizontal inward movement

Figure 5-22: Deformed shapes at the last step of the numerical simulations considering different settlement modes for *Arch 2* with different brickwork

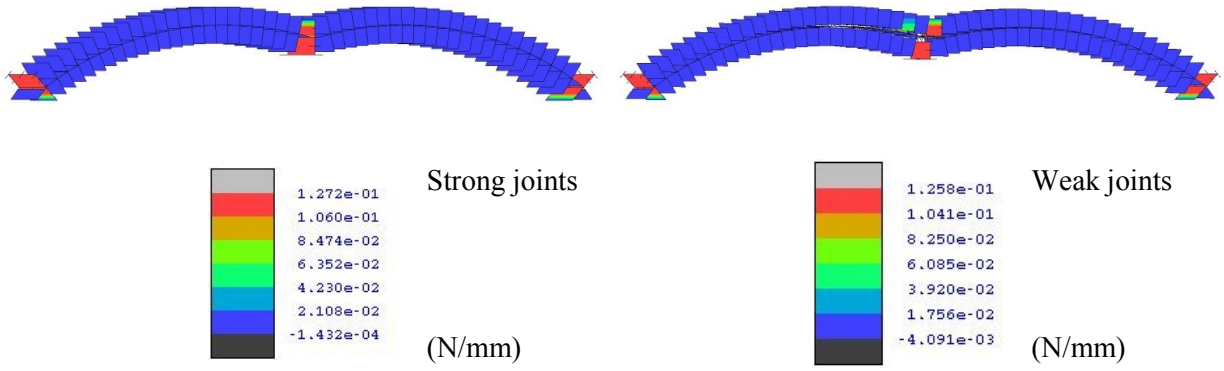

(a) Horizontal spread of support

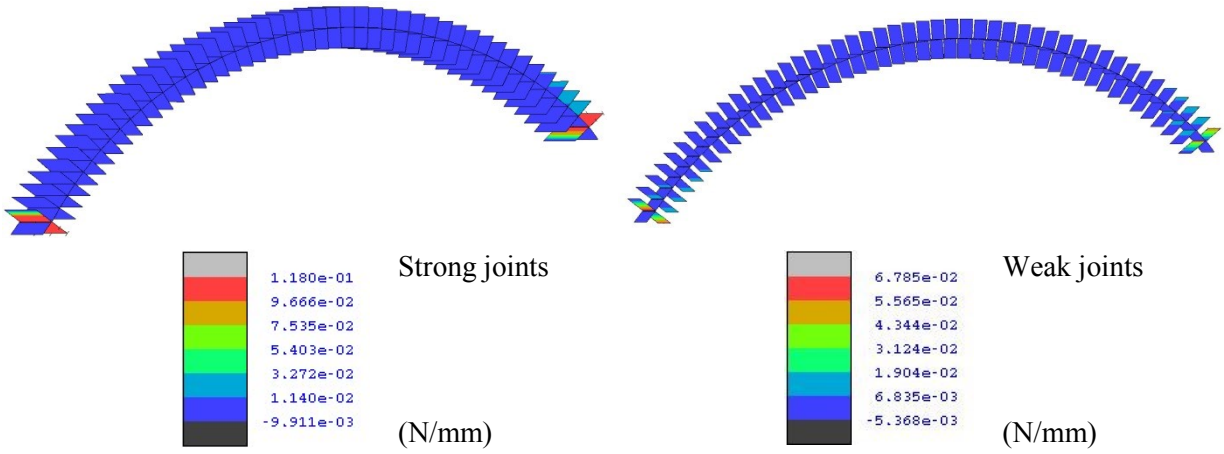

(b) Vertical differential settlement

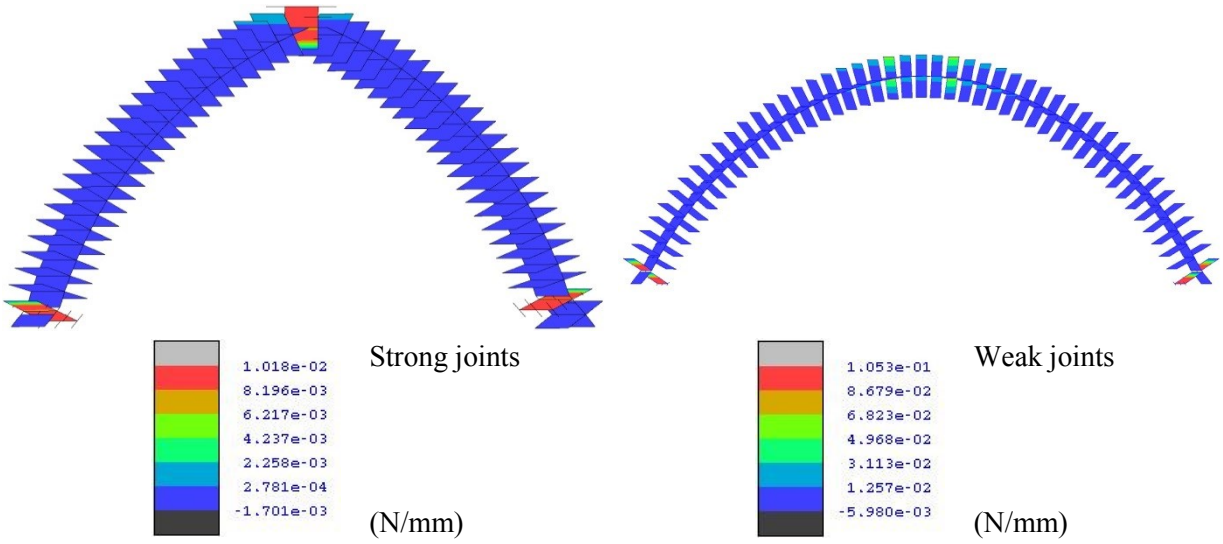

(c) Horizontal inward movement

Figure 5-23: Plastic work W_{cr1} contour at the last step of the numerical simulations considering different settlement modes for *Arch 2* with different brickwork

Figure 5-22 displays the deformed shapes for *Arch 2* subjected to the three settlement modes and Figure 5-23 shows the plastic work W_{cr1} contour for the different cases. All these figures refer to the last step of the numerical simulations at the failure of the arch. The failure mode depends not only on the specific type of settlement but also on the brickwork characteristics and does not always involve the formation of three main radial cracks (hinges). In the case of horizontal spread of support and horizontal inward movement, three radial cracks develop in the arch with good quality joints, but in the arch with weak mortar joints radial cracks occur with ring separation, which extends from the arch crown to the left support moving laterally. On the other hand, when vertical differential settlements are applied only two main radial cracks form at the springings of the arch.

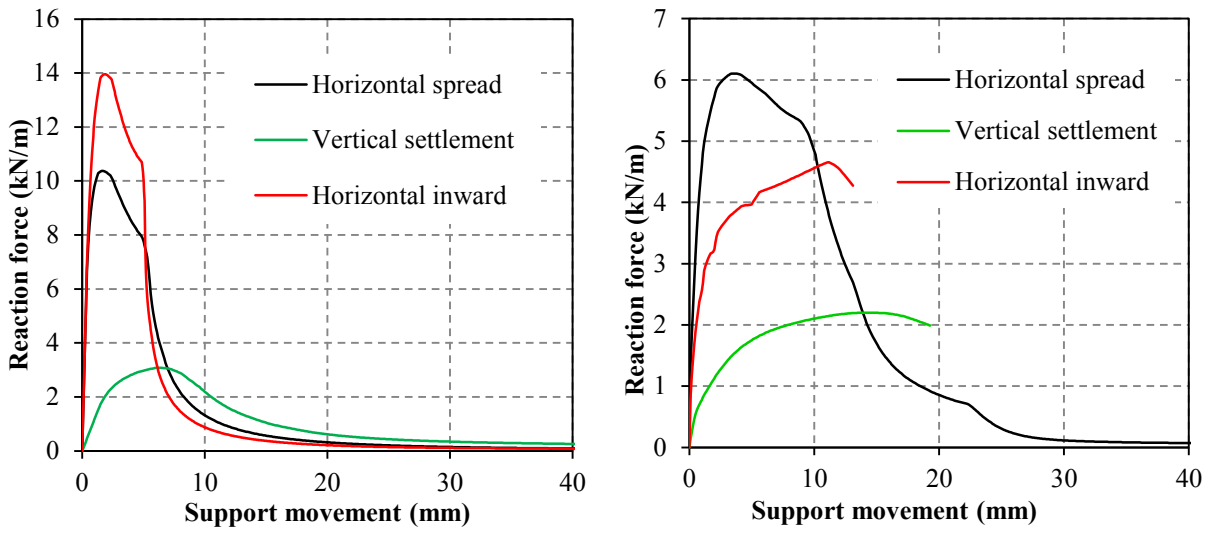

(a) Strong joints (b) Weak joints

Figure 5-24: Reaction force-support displacement curves for *Arch 2* with different brick work

The imposed displacements at the left support are plotted against the associated reaction forces in Figure 5-24. It can be seen that when the failure mechanism due to a specific settlement mode develops, the associated reaction force decreases showing a post-peak softening response which is steeper for the arch with strong joints. Finally Figure 5-25 summarises the results of the numerical simulations for *Arch 2* in term of maximum reaction forces and the corresponding support displacements, indicating the settlement level at which

a mechanism starts to develop. In general, it can be noticed that the support displacement required to form a mechanism is notably lower for arches with good quality mortar joints especially in the case of horizontal inward displacements.

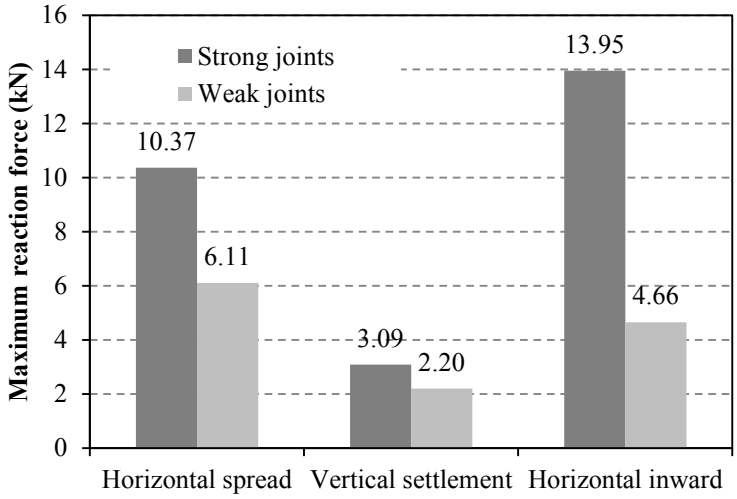

(a) Maximum reaction force R_{max} (kN)

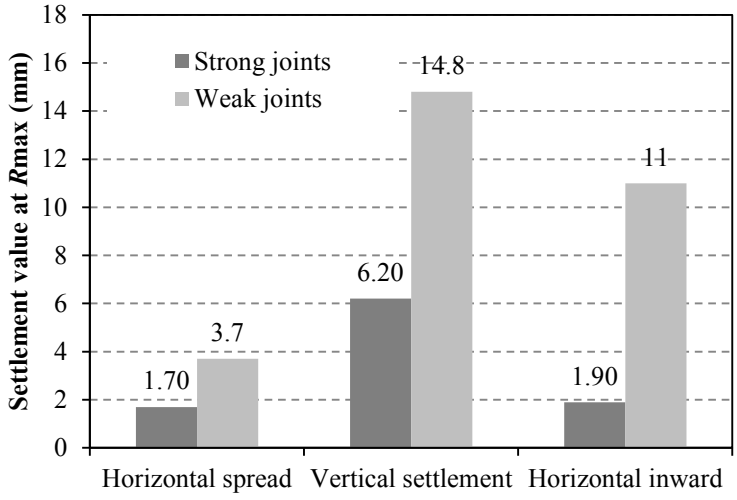

(b) Displacement at R_{max} (mm)

Figure 5-25: Reaction forces and displacements at maximum reactions under different settlement modes for *Arch 2* with different brick work

5.2.5.1 Horizontal spread of support

Numerical simulations were carried out to investigate the response of the 3m span arches subjected to different levels of prescribed horizontal displacements followed by the

application of a line load at quarter span. In particular, static time-history analyses were performed considering two phases, where two loading conditions were applied in sequence. In the initial phase, a specific horizontal outward displacement δ_{ss} was exerted at the left springing of the arch incrementally; afterwards the line load was increased up to collapse. Six δ_{ss} values were considered within the interval $1\text{mm} \leq \delta_{ss} \leq 6\text{mm}$, where the upper limit is higher than the horizontal spread of support at which a mechanism starts to develop (see Figures 5-24 and 5-25). The numerical responses were calculated under force control, thus the nonlinear analyses terminated when the maximum loads were reached without representing the post-peak behaviour.

Figures 5-26a,b display the numerical curves for *Arch 2* with strong and weak mortar joints, where the line load is plotted against the vertical displacements at quarter span, while Figures 5-27a,b present the results of the six numerical simulations for *Arch 2* in term of ultimate load ratios. These correspond to the ratios between the ultimate loads P_{ult} calculated for different δ_{ss} values and the maximum load for the arch with fixed supports. It can be seen that the load capacity of the arch with good quality mortar joints significantly decreases when δ_{ss} rises, and about 60% reduction is calculated for the 6mm horizontal support displacement. On the other hand, in the case of defective brickwork (weak joints), the reduction in load capacity is less pronounced reaching about 18% for the 6mm horizontal displacement. This is due to the characteristics of the response under horizontal spread of support (Figures 5-26a,b), where the arch with weak joints shows a more ductile behaviour.

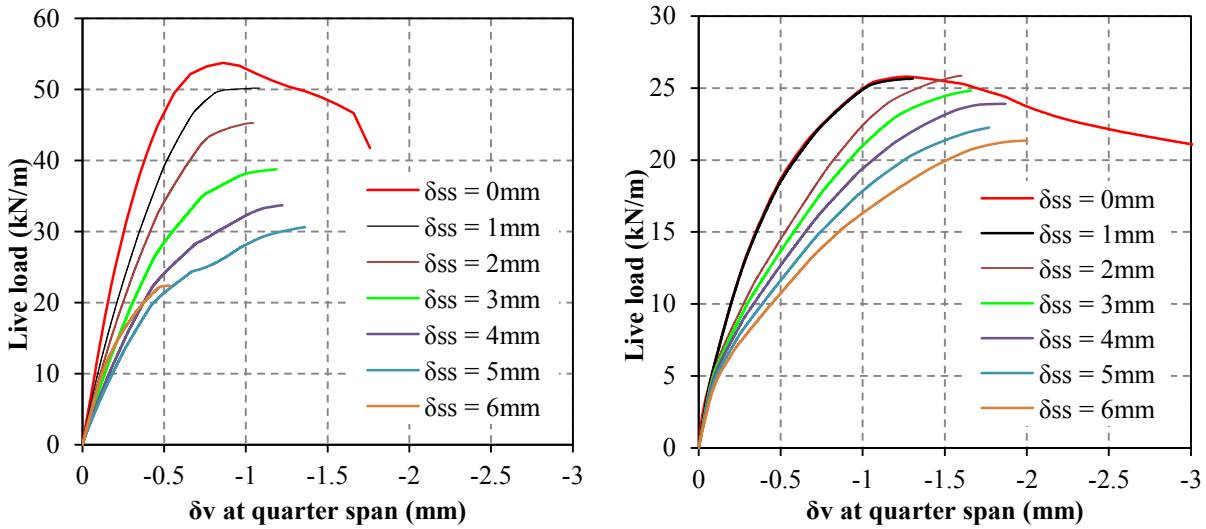

(a) Strong joints (b) Weak joints

Figure 5-26: Load-displacement curves for different levels of horizontal spread of support

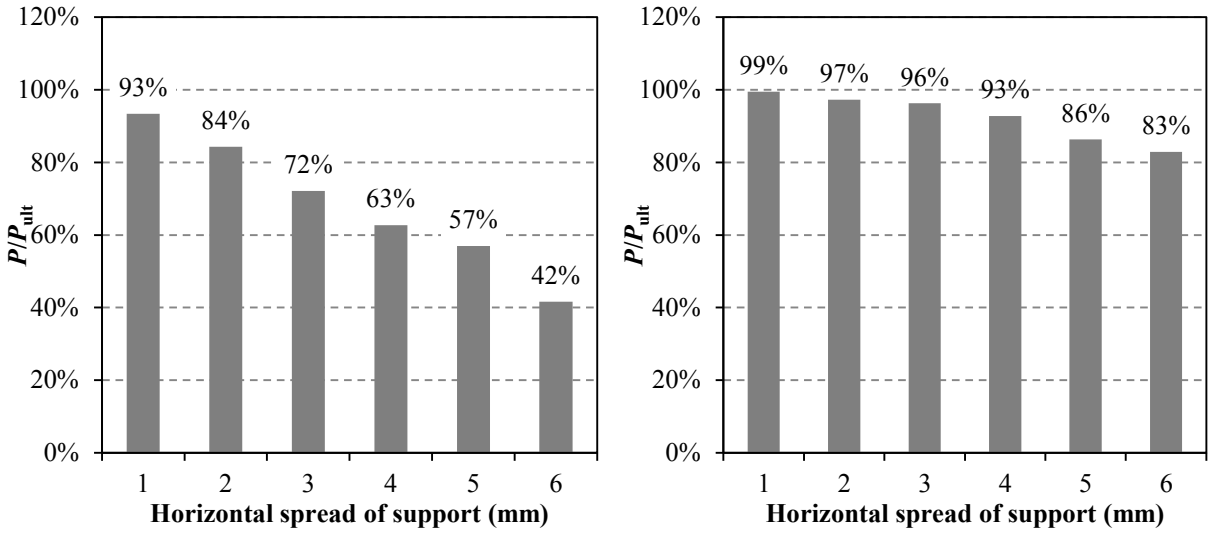

(a) Strong joints (b) Weak joints

Figure 5-27: Effect of horizontal spread of support

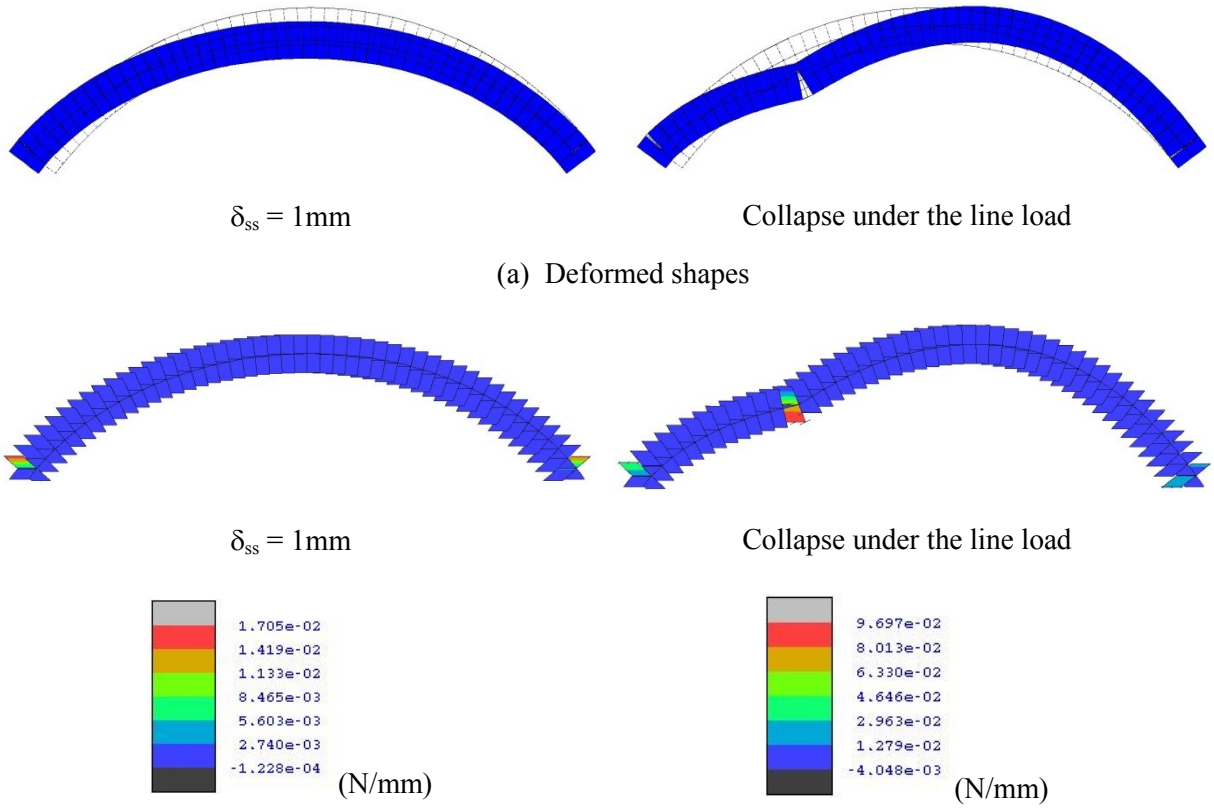

Figure 5-28: Deformed shapes and plastic work contours for *Arch 2* and δ_{ss} = 1mm

Figures 5-28 and 5-29 show some results for the arch with strong joints and subject to 1mm and 6mm spread of support. In the two figures the deformed shapes and the contours of the plastic work W_{cr1} after the application of the two support movements and at collapse are displayed. It can be observed that the lower prescribed displacement induces the formation of two cracks at the opposite springings, while at collapse a third crack forms close to where the line load is applied. When a higher displacement is exerted, even though the mechanism associated with the support prescribed displacement forms, the arch can still carry additional live load and the collapse is attained only when a further crack develops below the load.

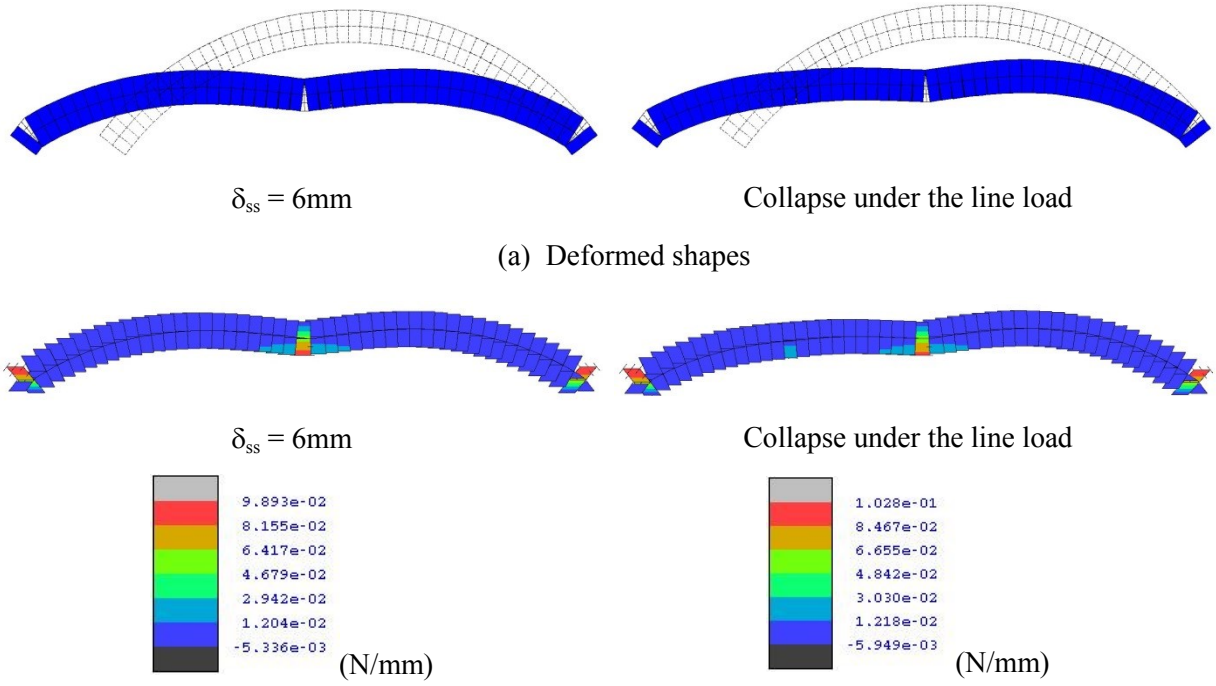

Figure 5-29: Deformed shapes and plastic work contours for *Arch 2* and δ_{ss} = 6mm

The influence of the horizontal spread of abutments on the load capacity of masonry arches with strong mortar joints and different rise-to-span ratios is shown in Figure 5-30. The ratio between the ultimate load achieved after the application of different horizontal outward displacements at the left support and the ultimate load calculated with fixed supports for the arches *Arch1*, *Arch2*, *Arch3* and *Arch4* (see Section 5.2.1) is plotted against the prescribed displacement values. A similar variation of the ultimate capacity can be observed for the first three arches, with a maximum reduction of 46% for the arch with 1:8 rise-to-span ratio under a 5mm horizontal support displacement.

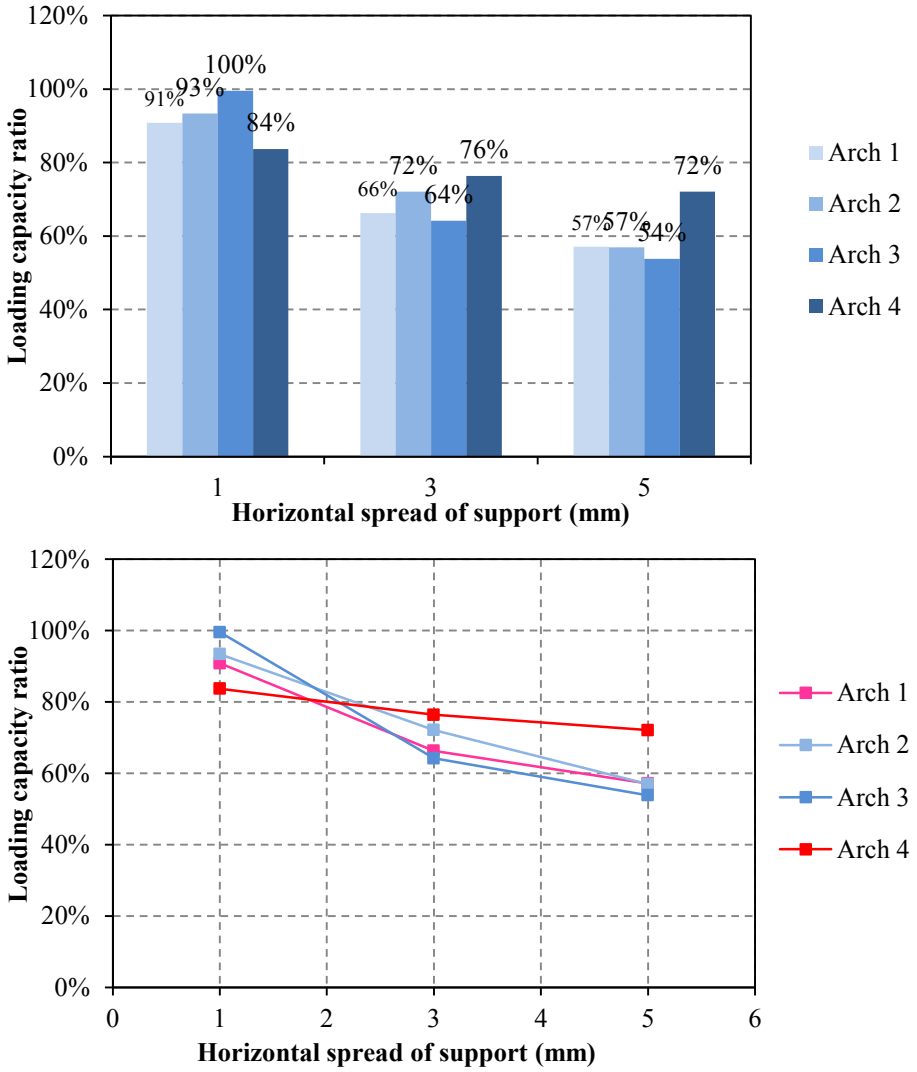

Figure 5-30: Load capacity ratio for different values of horizontal spread of abutment for arches with different rise-to-span ratio

5.2.5.2 Vertical settlement of support

As for the case of horizontal spread of support, the influence of differential vertical settlements on the arch load capacity was investigated performing time-history analyses, where different levels of vertical displacements δ_{vs} were imposed on the left abutment before loading the arch at the quarter span up to collapse. Six δ_{vs} values were considered within the interval $1mm \leq \delta_{ss} \leq 6mm$, where the upper limit is about the vertical settlement at which a mechanism starts to develop for *Arch 2* with strong circumferential mortar joints. Also in this

case the numerical responses were calculated under force control, thus the nonlinear analyses terminated when the maximum loads were reached without representing the post-peak behaviour.

Figures 5-31a,b show the load-displacement curves for *Arch 2* with strong and weak mortar joints, while Figures 5-32a,b display the ratio between the ultimate load calculated in the six two-phase time-history analyses and the ultimate load achieved considering fixed supports.

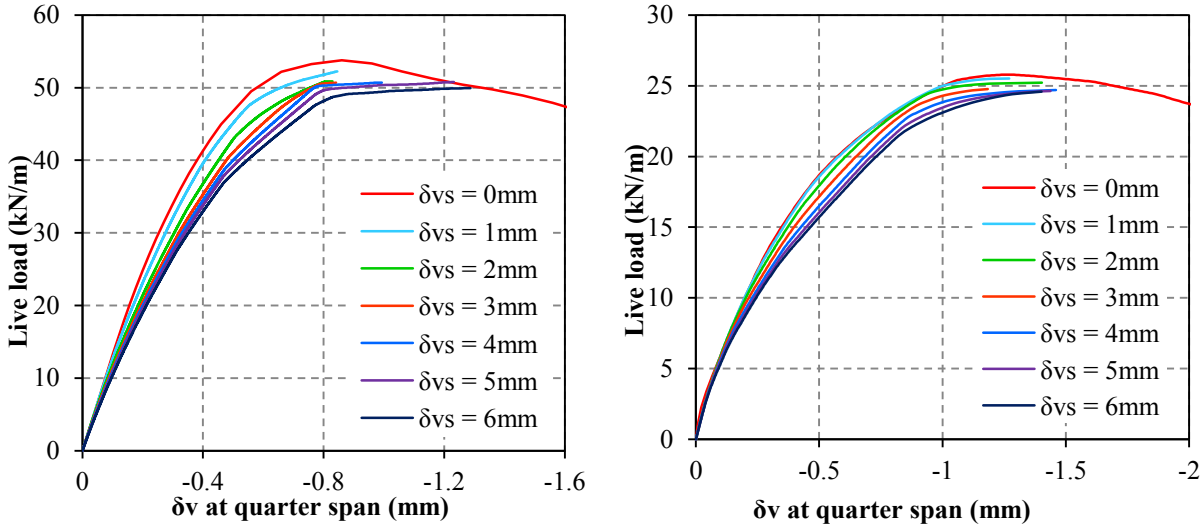

(a) Normal joints (b) Weak joints

Figure 5-31: Load-displacement curves for different levels of vertical settlement of support

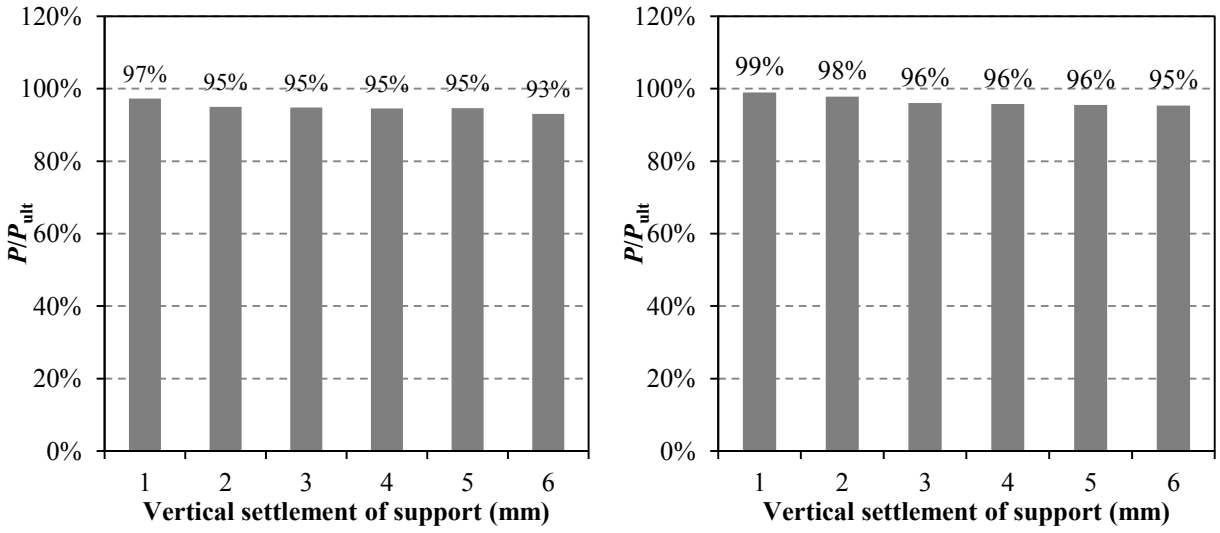

(a) Strong joints (b) Weak joints

Figure 5-32: Effect of vertical settlement

Examining the results, it can be seen that a vertical support movement does not significantly influence the arch load capacity for the arches with strong mortar joints and those with weak mortar joints. In this case the considered prescribed displacements are not sufficiently large to notably reduce the load bearing capacity of the arch, especially in the case weak mortar joints, where the maximum vertical settlement is smaller than the displacement level at which a mechanism starts to develop (see Figures 5-24 and 5-25). This is confirmed also by Figures 5-33 and 5-34, where the deformed shapes and the contours of the plastic work W_{cr1} for the smallest and the largest vertical settlements are displayed. The figures show that the support displacement does not influence the collapse mechanism, which corresponds to that of the arch with fixed supports showing four radial cracks at the two springings and at the quarter and three quarter span.

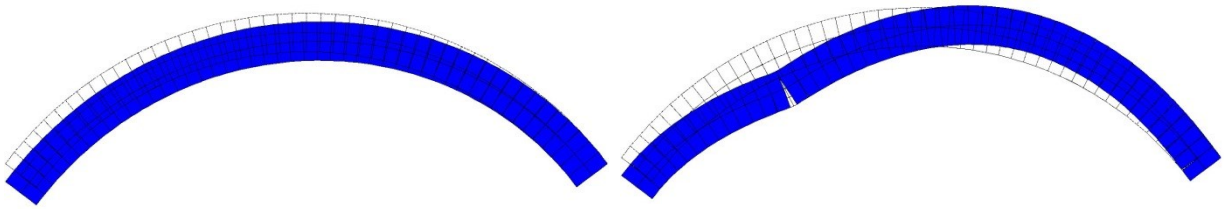

δ_{vs} = 1mm Collapse under line load

(a) Deformed shapes

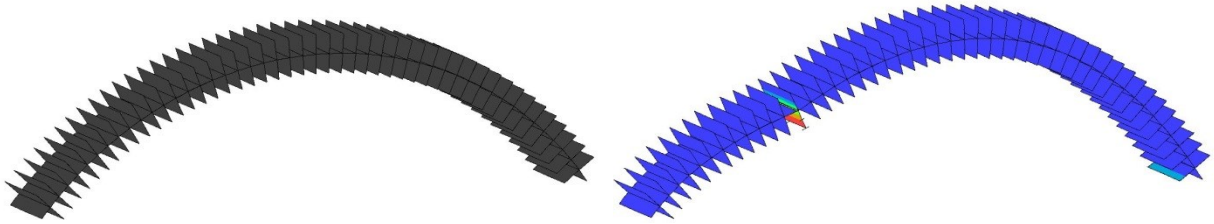

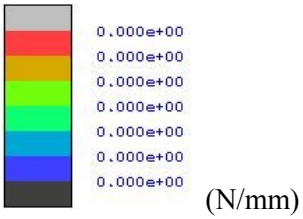

(N/mm)

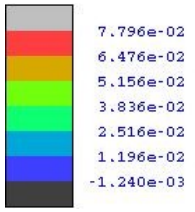

(N/mm)

δ_{vs} = 1mm Collapse under line load

(b) Contour of plastic work W_{cr1}

Figure 5-33: Deformed shapes and plastic work contours for *Arch 2* and δ_{vs} = 1mm

Finally, investigating the response of arches with different rise-to-span ratios (Figure 5-35), it has been found that the support vertical movement may induce a strain/stress state in the arch which mitigates the effects of the live load, thus increasing the load capacity as for the arch with 1:8 rise-to-span ratio (*Arch 3*). Evidently the settlement level should be lower than the limit leading to a mechanism.

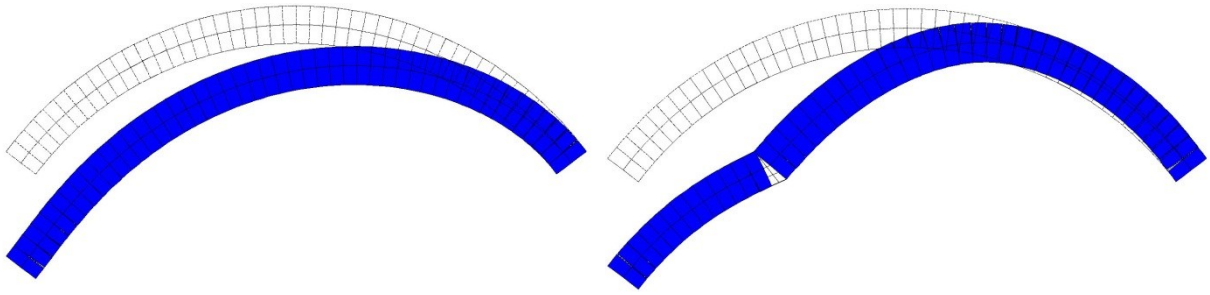

δ_{vs} = 6mm Collapse under line load

(a) Deformed shapes

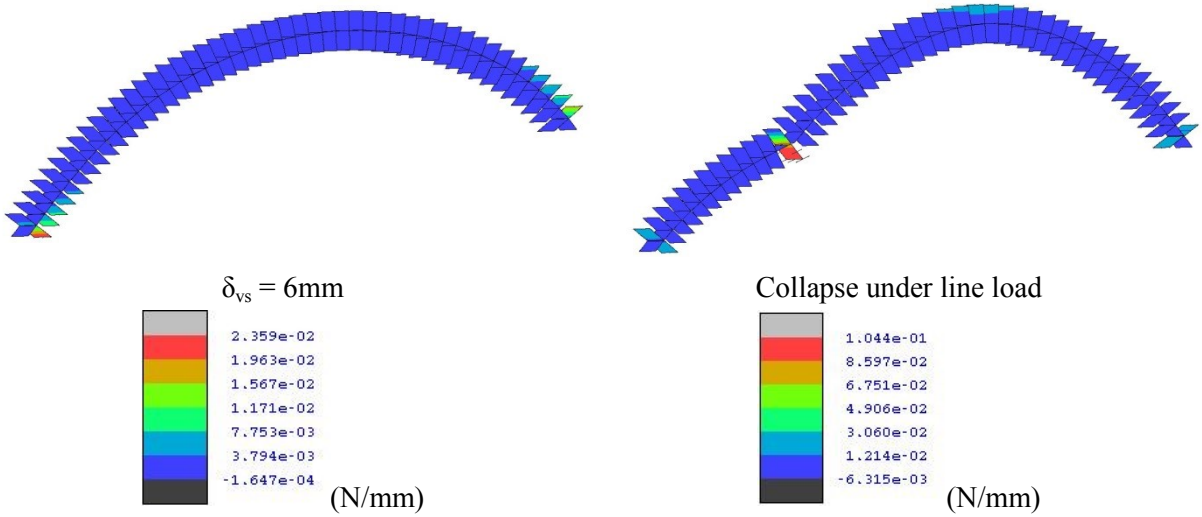

δ_{vs} = 6mm Collapse under line load

(b) Contour of plastic work W_{cr1}

Figure 5-34: Deformed shapes and plastic work for *Arch 2* and δ_{vs} = 6mm

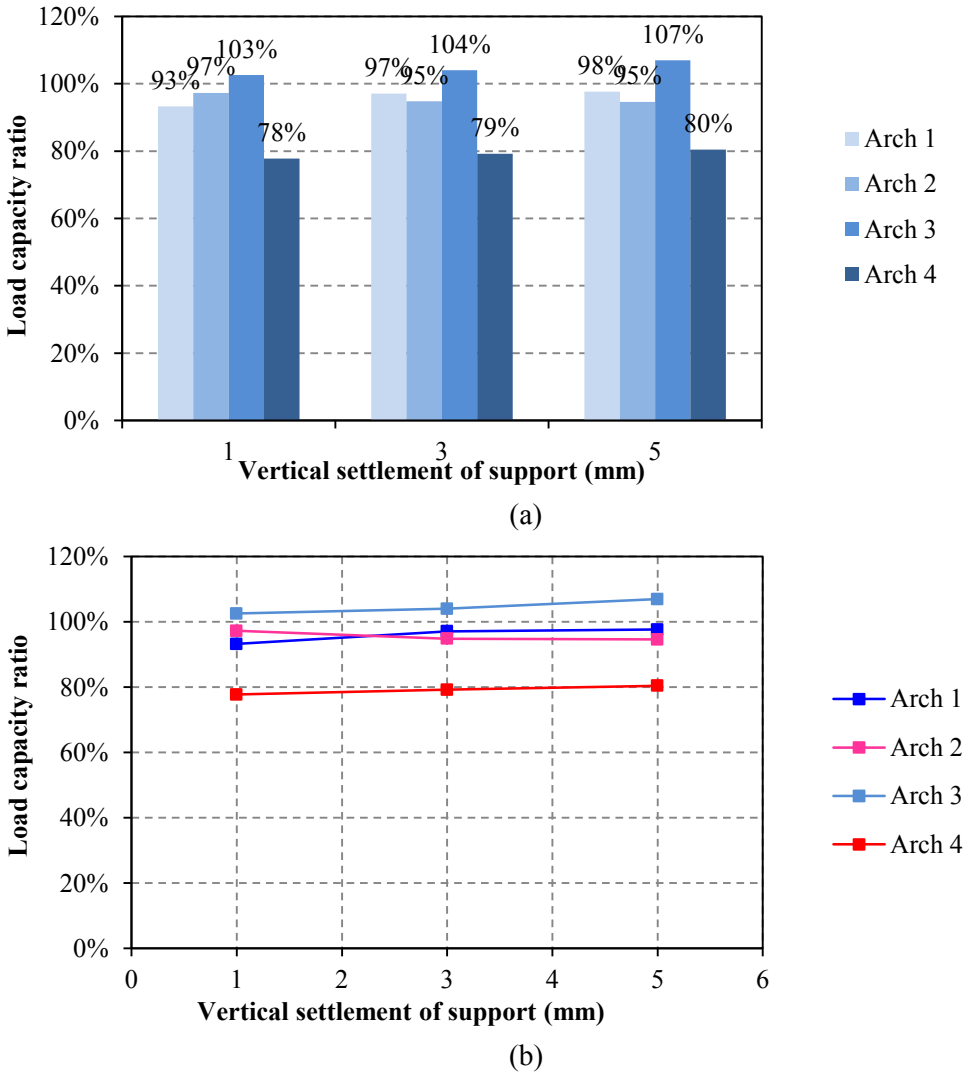

Figure 5-35: Load capacity ratio for different values of vertical settlement for arches with different rise-to-span ratio

5.2.5.3 Horizontal inward support displacement

Similar numerical simulations have been carried out to study the effects of horizontal inward movements at the left support. As before, six horizontal inward displacements values δ_{im} were considered within the interval $1\text{mm} \leq \delta_{ss} \leq 6\text{mm}$, where the upper limit is significantly higher than the horizontal inward movement leading to a mechanism for *Arch 2* with strong mortar joints, but lower than the same displacement limit for *Arch 2* with weak mortar joints (see Figures 5-24 and 5-25). The load-displacement curves in Figure 5-36 and the ultimate

load ratios in Figure 5-37 confirm the significant influence of the horizontal inward movement on the arch response. This is critical not only for the arch with strong mortar, where a notable maximum reduction of 46% have been calculated, but also for the arch with weak circumferential joints. Moreover it can be observed than the prescribed support displacements give rise to a strain/stress state which opposes the live load which, for relatively small inward movements, may lead to an increment in the load capacity (see curves δ_{im} = 1mm in Figures 5-36a,b).

Concerning the failure mechanisms due to the line load at quarter span applied after the horizontal inward support movement, Figure 5-38 shows that, in the case of relatively small support displacements, the failure mode corresponds to that of the arch with fixed supports. Conversely Figure 5-39 highlights that, by increasing the support movement, a different crack pattern forms in the arch. This is similar to that shown in Figure 5-23c and due to inward support displacements alone, but with a more diffuse cracking at the crown.

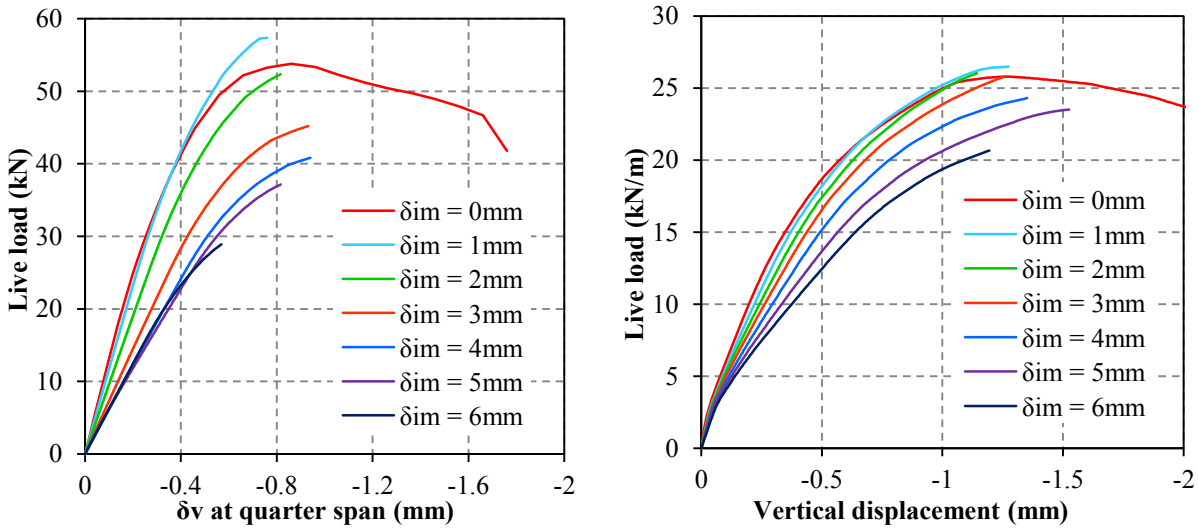

(a) Strong joints (b) Weak joints

Figure 5-36: Results for different level of horizontal inward support displacement

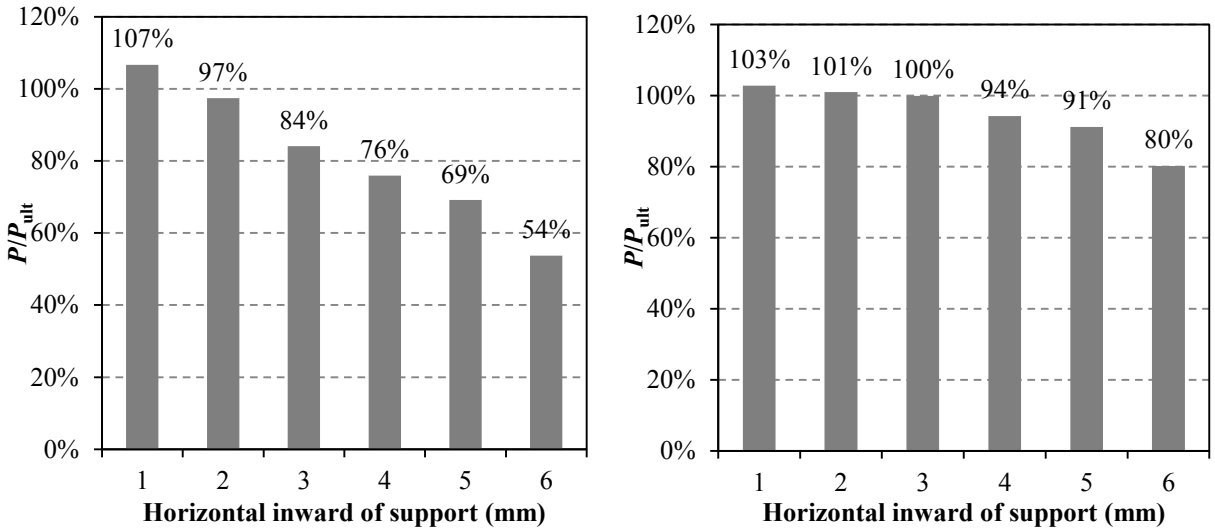

(a) Strong joints (b) Weak joints

Figure 5-37: Effect of horizontal inward support displacement

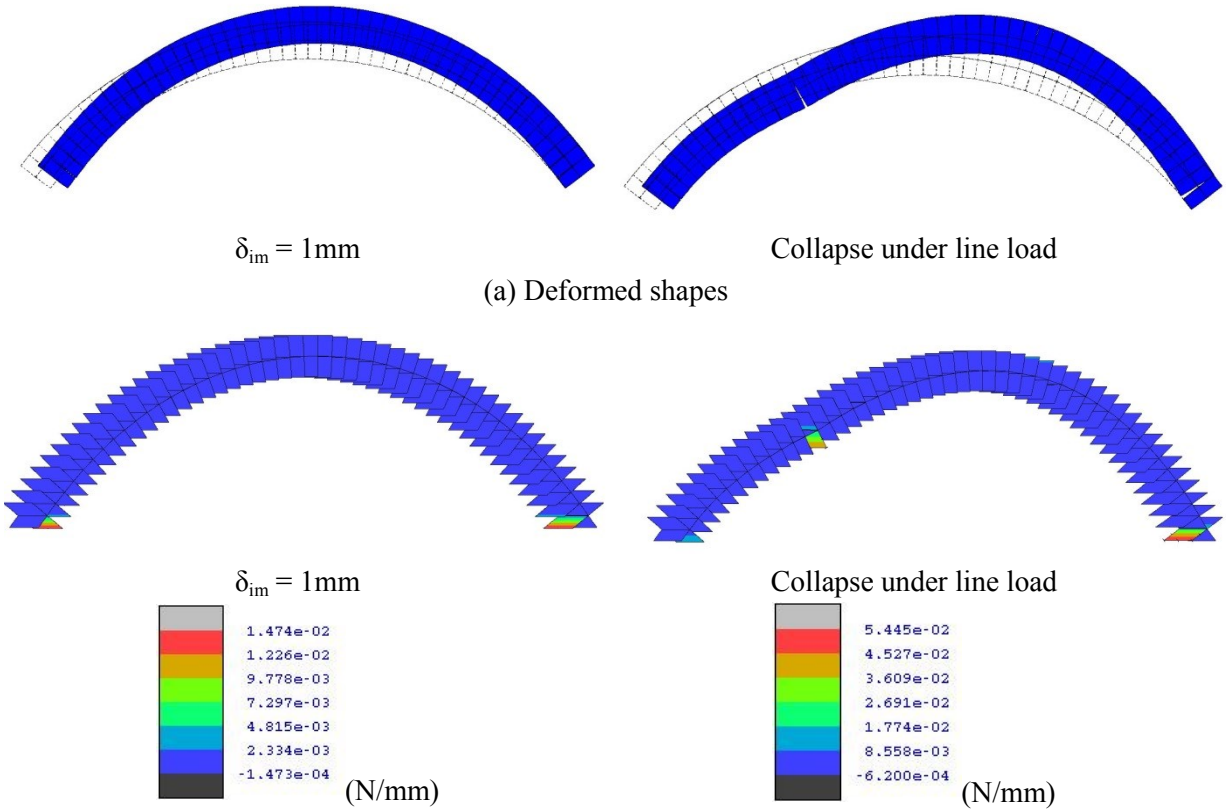

(a) Deformed shapes

(b) Contour of plastic work W_{cr1}

Figure 5-38: Deformed shapes and plastic work contours for *Arch 2* and δ_{im} = 1mm

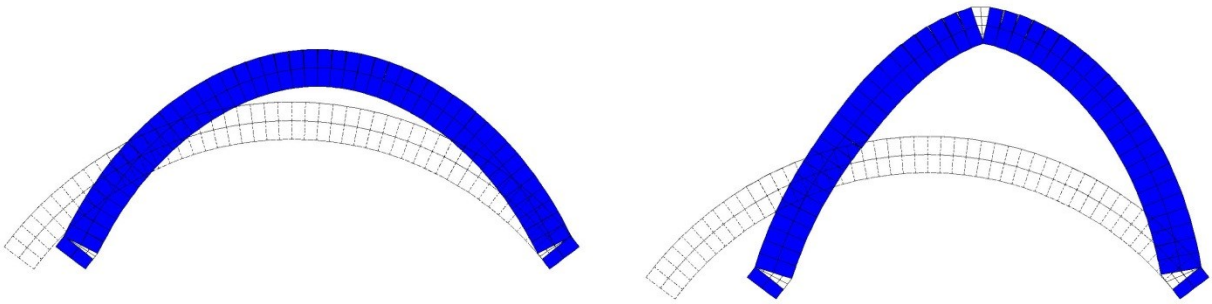

δ_{im} = 6mm Collapse under line load

(a) Deformed shapes

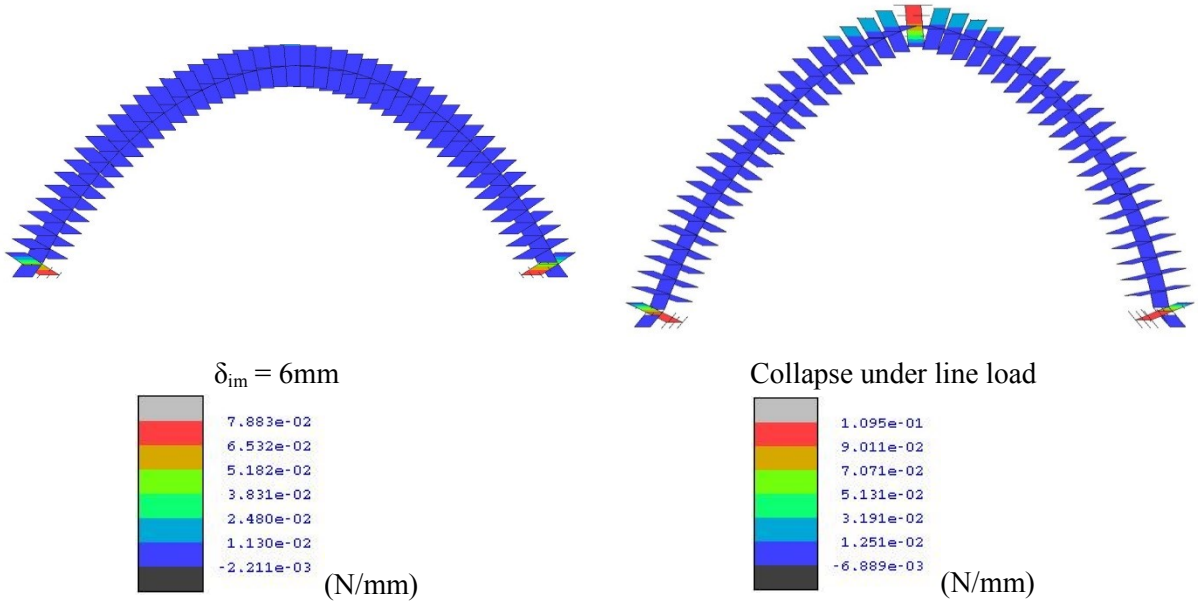

δ_{im} = 6mm Collapse under line load

(b) Contour of plastic work W_{crl}

Figure 5-39: Deformed shapes and plastic work contours for *Arch 2* and δ_{im} = 6mm

Finally the influence of the horizontal inward support movements on the load capacities of arches with different rise-to-span ratios is shown in Figure 5-40. It can be seen that the effect of support movement is more critical for shallow arches with 1:8 and 1:10 rise-to-span ratios (e.g. *Arch 3* and *Arch 4*). However in these cases, convergence problems allowed only an approximate estimate of the ultimate load for 5mm inward displacement. Thus the calculated 70% and 83% reductions in loading capacity should be considered as conservative predictions.

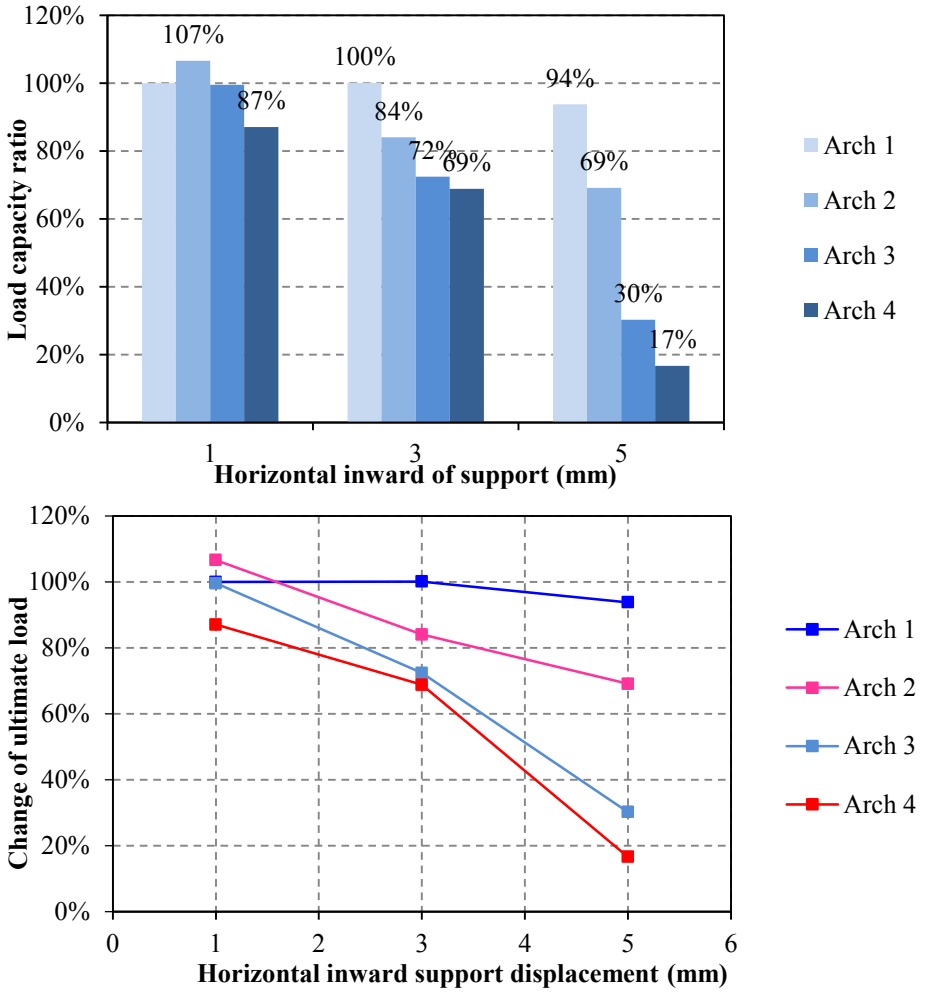

Figure 5-40: Load capacity ratio for different values of horizontal support displacement for arches with different rise-to-span ratio

5.2.5.4 Modelling considerations

A parametric study has been conducted to identify the most critical material properties which determine the qualitative response under the combinations of the prescribed support displacements and the live loads considered before. Not surprisingly, it has been found that the fracture energy values (especially Mode-I fracture energy G_{fI}) strongly affect the numerical predictions. In particular using unrealistically large fracture energy values (e.g. two orders of magnitude larger than the values in Table 4-5), the response prediction under the live load seems to be almost independent of the level of support displacement, as well as the ultimate load capacity. This is shown in Figure 5-41, where the live load is plotted against the

vertical displacement at quarter span for the three types of support displacement. The results obtained confirm what was pointed out in Chapter 4, where it was shown that the use of large fracture energy values, which disregard the actual quasi-brittle nature of the mortar joints and the fracture in the masonry units, usually moves the numerical response towards the elastic-plastic limit, where the solution does not depend upon potential support movements.

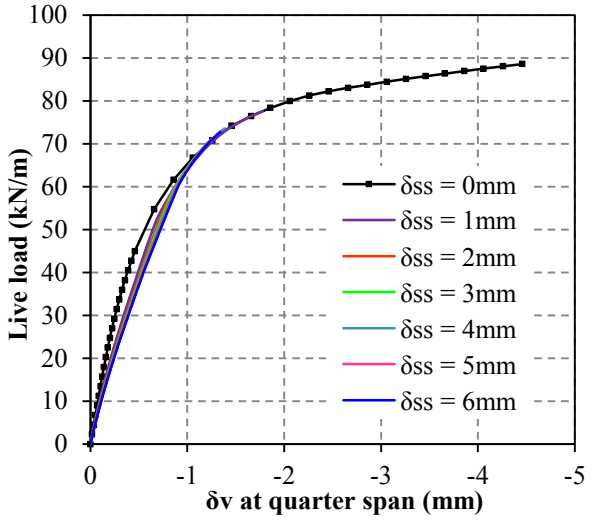

(a) Arch with horizontal spread of support

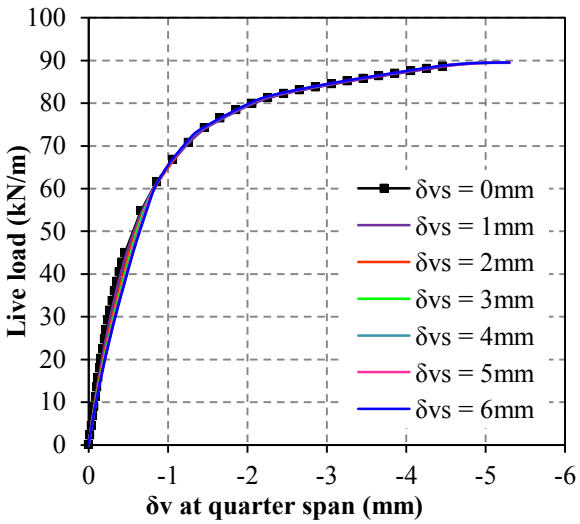

(b) Arch with vertical support settlement

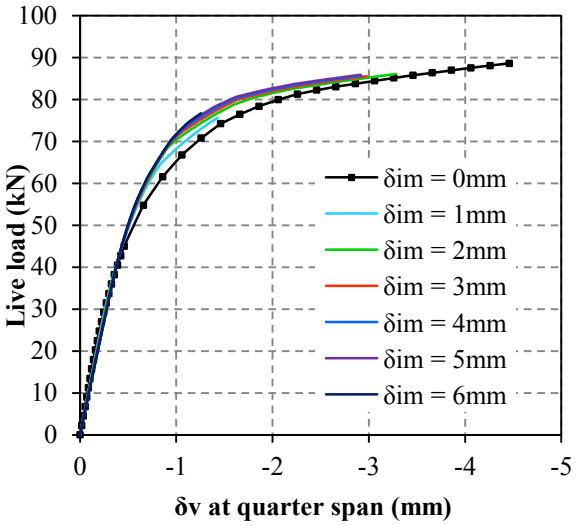

(c) Arch with horizontal inward support displacement

Figure 5-41: Load-displacement curve analysis for different settlement of left support

5.3 Mesoscale analysis of skew arches

In Chapter 4, it has been shown that for an accurate analysis of skew masonry arches a full 3D mesoscale description accounting for the actual 3D masonry bond should be considered. In this case the use of a more efficient strip model may lead to unrealistic results.

In the following, the detailed 3D mesoscale strategy for skew arches presented in Chapter 4 is adopted to investigate the response of brick-masonry skew arches considering the effects of (i) rise to span ratio, (ii) masonry bond and defects in the brickwork , (iii) abutment stiffness and (iv) support movements. The two-ring skew arch with header bond investigated in Section 4.3 is considered here as the reference model. Thus all the analysed arches are characterised by a 3m direct span, 670mm width, 215mm thickness and 45° skew angle.

5.3.1 Effects of rise-to-span ratio

The effects of the skew arch geometry have been analysed by comparing the numerical responses of three arches with different rise-to-span ratios. The main geometrical properties are reported in Table 5-4, while Figure 5-42 shows the three FE mesoscale meshes.

Table 5-4: Geometry of the skew arches with different rise-to-span ratio

Model	Rise - H (mm)	Direct span - L_d (mm)	No. of Rings	Thickness (mm)	Rise-to-span ratio
Skew 1	1500	3000	2	215	1:2
Skew 2	750	3000	2	215	1:4
Skew 3	375	3000	2	215	1:8

In the numerical simulations, a line load was applied near the three quarter span perpendicularly to the oblique span. Figure 5-43 and 5-44 show the deformed shapes and the plastic work W_{cr1} contours at the end of the numerical simulations. In all the cases failure occurred because of the development of five main cracks along the mortar bed joints forming the typical 3D mechanism with five “hinges” (see Section 4.3).

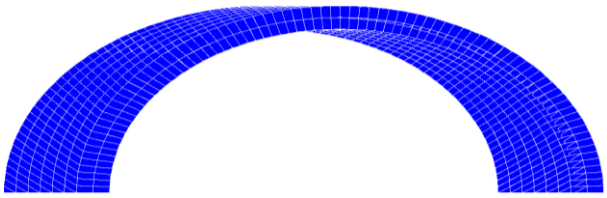

(a) *Skew 1*- Ratio = 1:2

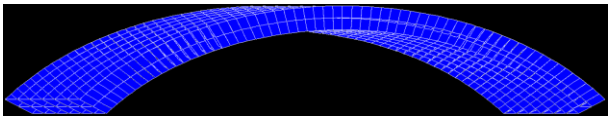

(b) *Skew 2*- Ratio = 1:4

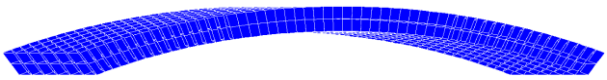

(c) *Skew 3* - Ratio = 1:8

Figure 5-42: 3D mesoscale meshes for skew arches with different rise-to-span ratios

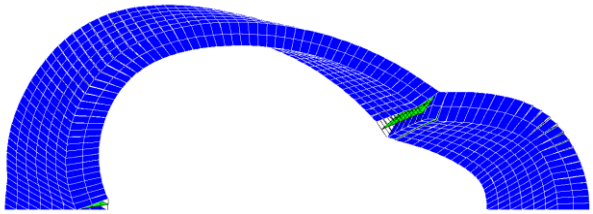

(a) *Skew 1*- Ratio = 1:2

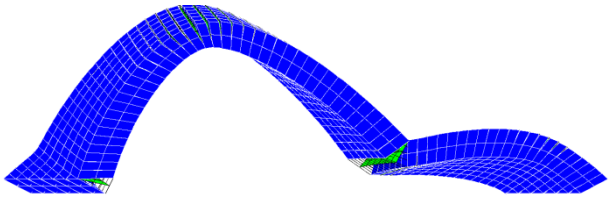

(b) *Skew 2*- Ratio = 1:4

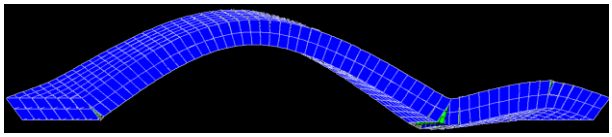

(c) *Skew 3* - Ratio = 1:8

Figure 5-43: Deformed shapes at the last step of the analysis

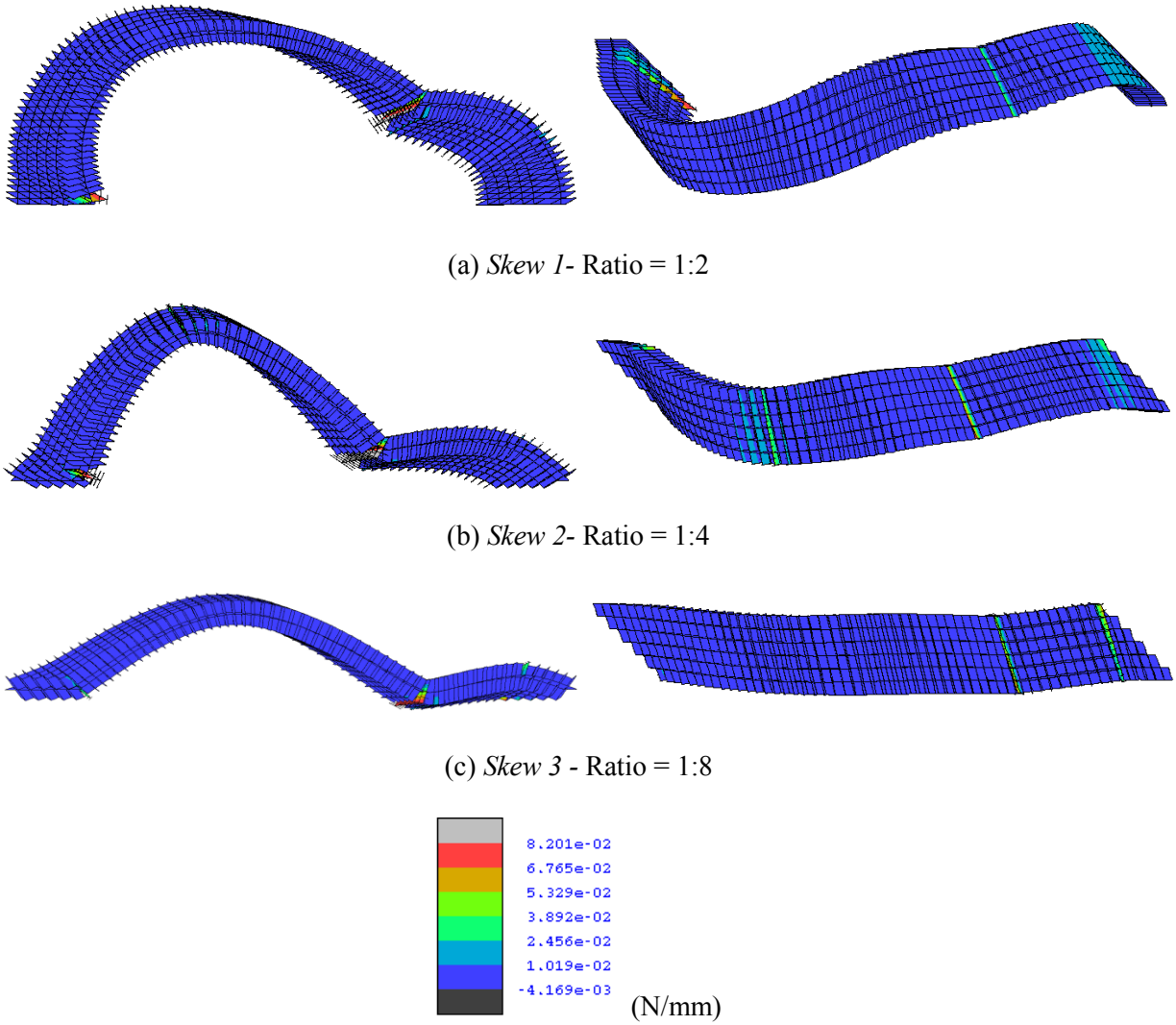

(a) *Skew 1*- Ratio = 1:2

(b) *Skew 2*- Ratio = 1:4

(c) *Skew 3* - Ratio = 1:8

Figure 5-44: Plastic work W_{cr1} contours at the last step of the analysis

In Figures 5-45a,b the numerical load-displacement curves measured at quarter and three quarter span are plotted. The deep arch features the highest load capacity but a limited ductility, as it shows a softening behaviour just after reaching the maximum load. The arch *Skew 2* is characterised by the lowest load capacity but a notable ductility. Finally, the arch with a 1:8 rise-to-span ratio shows an intermediate response. In this case the analysis stopped because of convergence problems probably before reaching the maximum load.

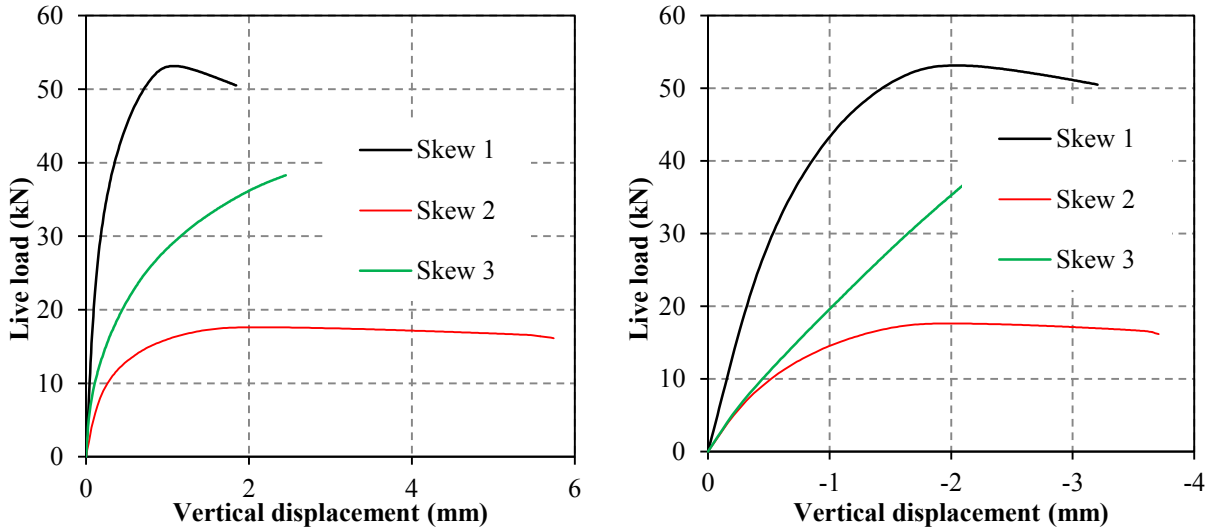

(a) Quarter span (b) Three quarter span

Figure 5-45: Load displacement curves at (a) quarter span and (b) three quarter span for arches with different rise-to-span ratios

5.3.2 Influence of masonry bond and defects in brickwork

The three arches with different rise-to-span ratios presented in the previous section, has been analysed considering different masonry bonds and defective brickwork. In particular, the responses of arches built with the stretcher or the header method (Figure 5-46) to connect the adjacent rings have been compared. Moreover the effects of defective mortar joints at the interface between the two brickwork rings have been taken into account. In this case, very small tensile strength and cohesion values for the nonlinear interface elements representing the circumferential mortar joints have been employed (Table 5-2).

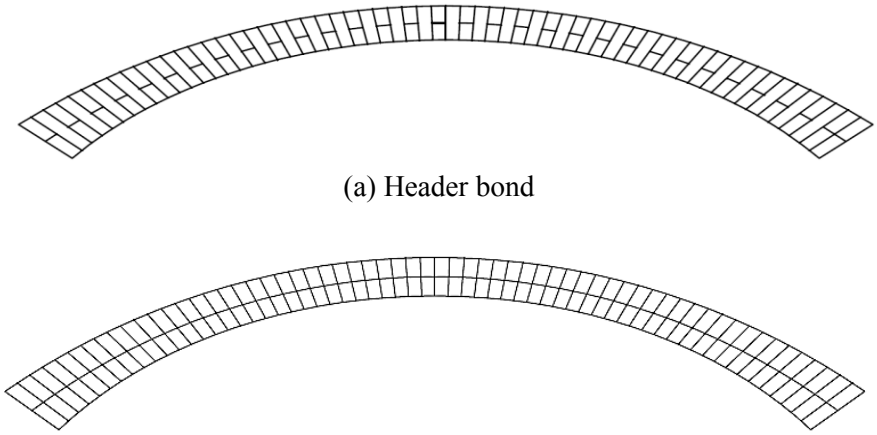

(a) Header bond

(b) Stretcher bond

Figure 5-46: Lateral view showing the two alternative bond methods to connect adjacent rings

Figure 5-47 displays the load-displacement curves for the arches with 1:4 rise-to-span ratio (*Skew2*), while the deformed shapes obtained from the different models and the corresponding plastic work contours are illustrated in Figures 5-48 and 5-49. Ring separation occurs only in the arch built according to the stretcher method and with defective circumferential mortar joints (weak joints). This arch is also characterised by the lowest load capacity, but it shows a significant ductility as depicted in Figure 5-47. All the other numerical curves are very close, being characterised by practically identical initial stiffness, ultimate load and alike post-peak response. This is reflected into very similar failure modes with cracks along the mortar bed joints without ring separation.

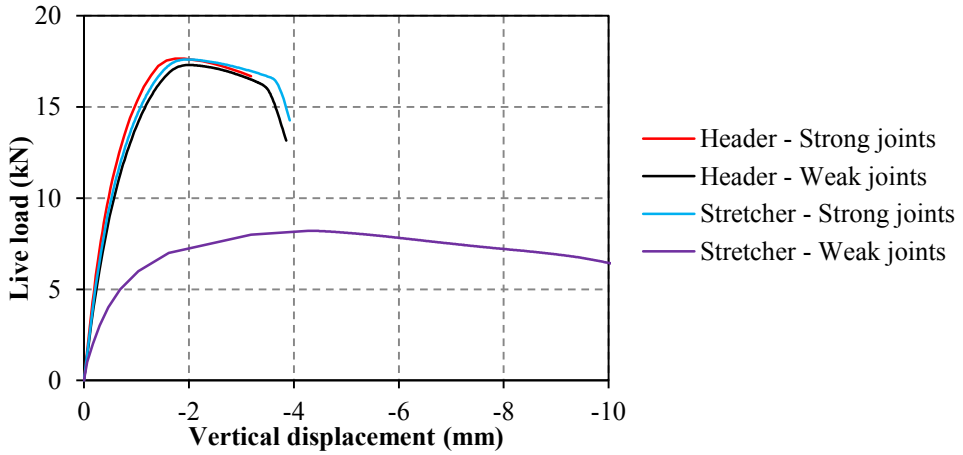

(a) Load-displacement curves at quarter span

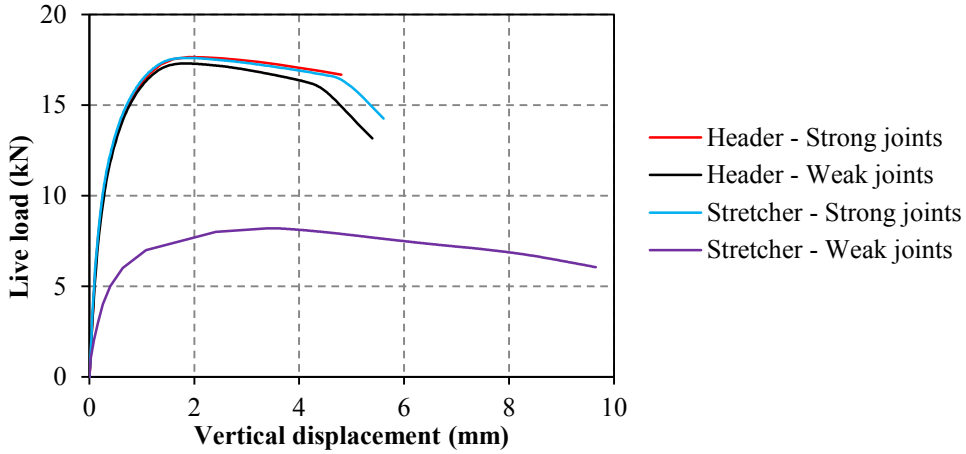

(b) Load-displacement curves at three quarter span

Figure 5-47: Numerical results for arches with 1:4 rise-to-span ratio and different circumferential joints

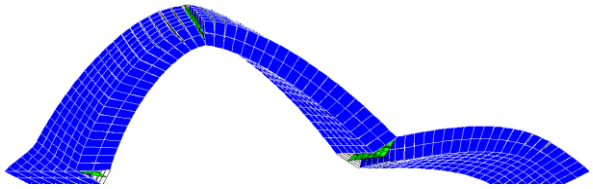

(a) Header bond – weak joints

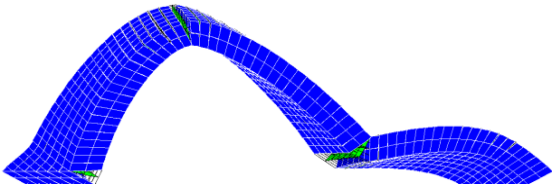

(b) Stretcher bond– strong joints

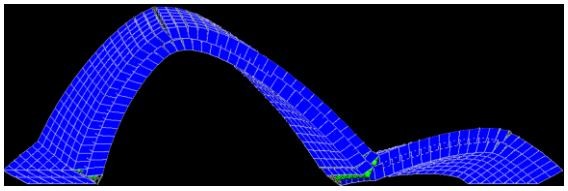

(c) Stretcher bond – weak joints

Figure 5-48: Failure mode for arches with 1:4 rise-to-span ratio and different circumferential joints

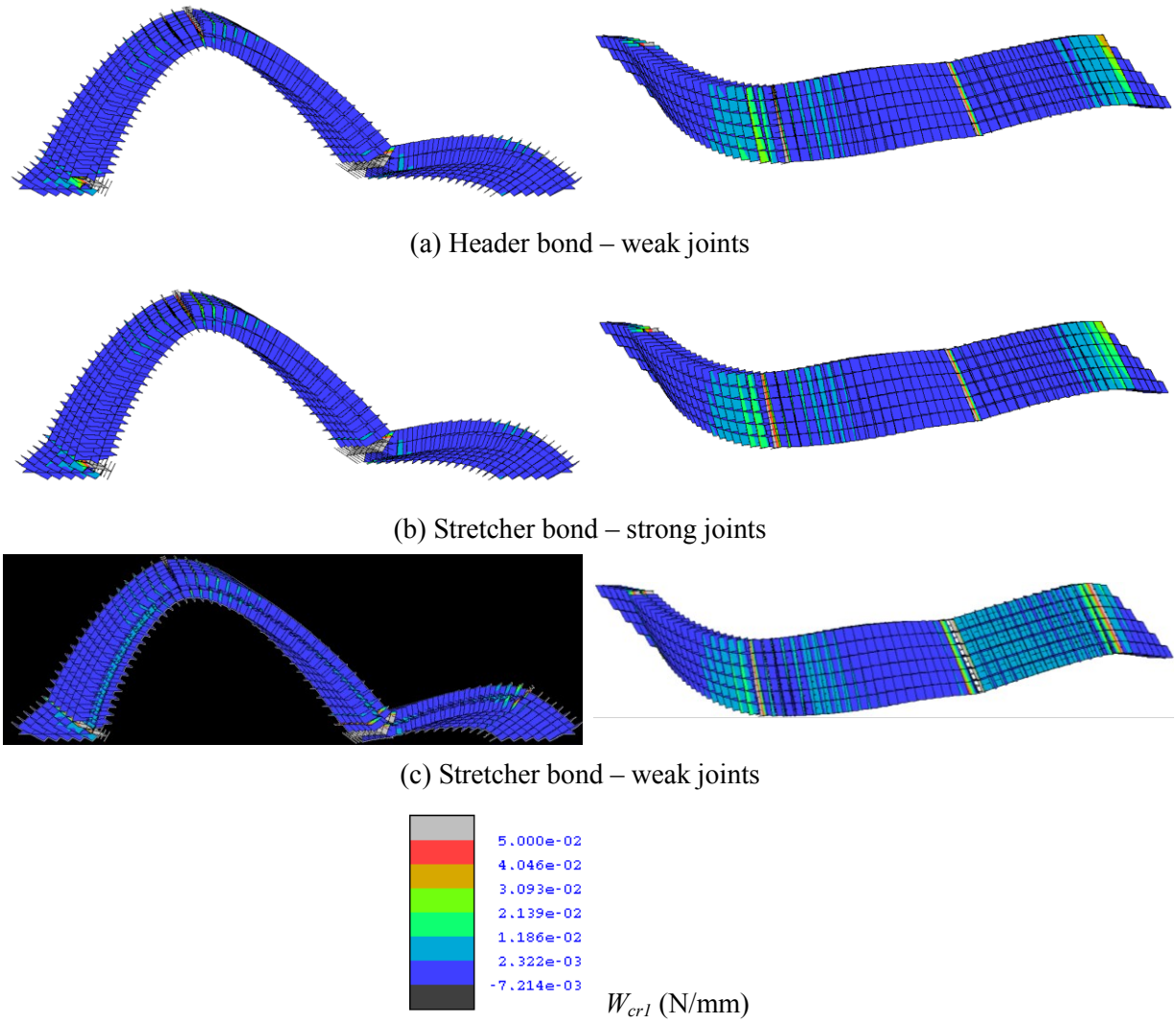

(a) Header bond – weak joints

(b) Stretcher bond – strong joints

(c) Stretcher bond – weak joints

Figure 5-49: Interface plastic work contour for arches with 1:4 rise-to-span ratio and different circumferential joints

Besides, the influence of defective brickwork on the behaviour of skew arches with different rise-to-span ratio has been investigated. Numerical analyses have been carried out for the arches *Skew 1*, *Skew 2* and *Skew 3* with stretcher bond. In all the cases, weak circumferential mortar joints have been considered.

Figure 5-50 displays the load-displacement curves. As for the arches with header bond and strong joints (Figure 5-45), the deep arch is characterised by the highest load capacity, the arch *Skew 2* by the lowest peak load, while the arch *Skew 3* shows an intermediate behaviour. However when compared against the numerical responses in Figure 5-45, all the curves for

arches with stretcher bond and defective brickwork show higher ductility. This is associated with the development of ring separation which is coupled with cracks in the mortar bed joints.

The influence of mortar defects is summarised in Figure 5-51, where the ultimate loads and the initial stiffness values obtained in the analysis of arches with weak and strong joints are compared. It has been found that defective brickwork leading to ring separation significantly reduces both initial stiffness and load capacity, where the maximum reduction of stiffness (60%) and ultimate load (68%) have been calculated for the arch with 1:8 rise-to-span ratio.

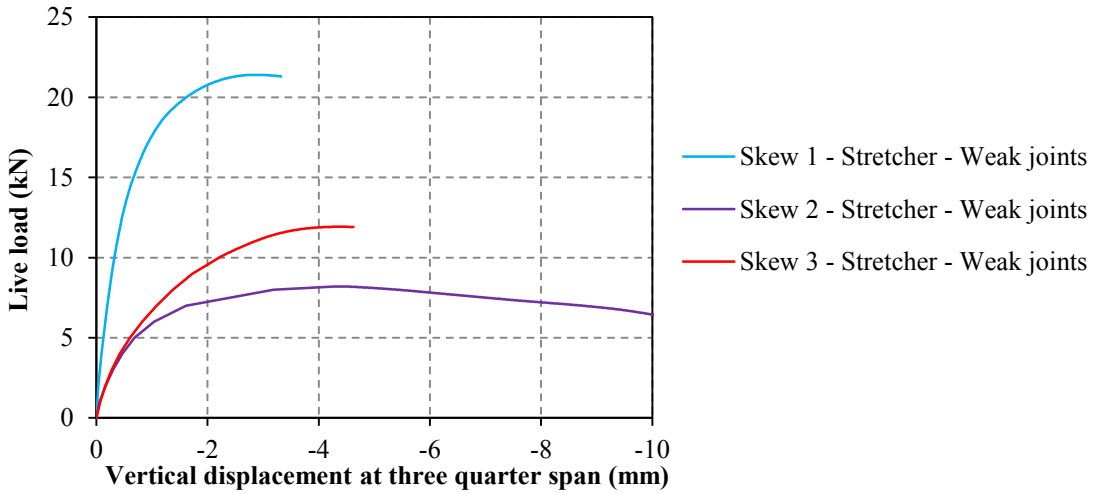

Figure 5-50: Load-displacement curves for skew arches with weak joints

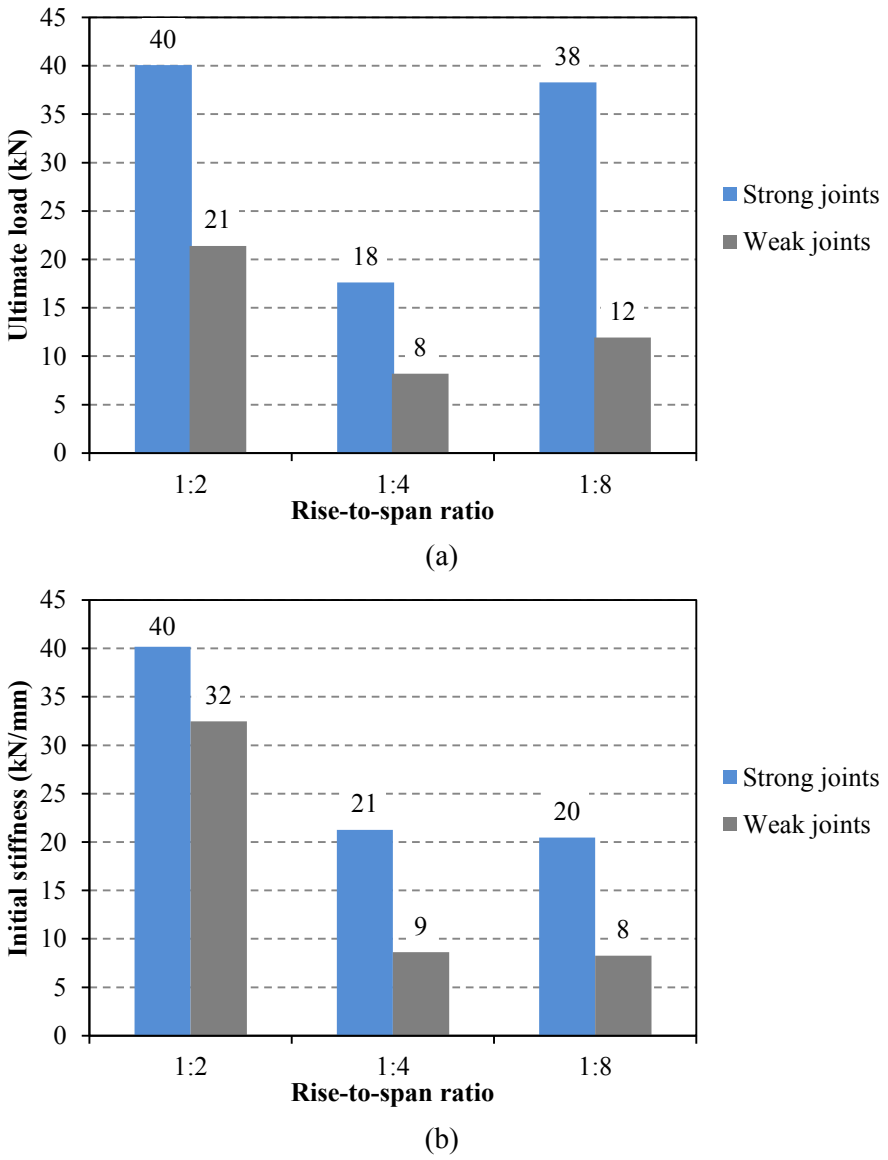

Figure 5-51: Influence of bond and defects on skew arches with different rise-to-span ratio on (a) ultimate load and (b) initial stiffness

5.3.3 Effects of the abutment stiffness

In Section 5.2.4, the influence of the abutment stiffness on the response of square arches was examined. In this section, the effects of potential deformations at the abutments on the response of an arch with 45° skew angle are investigated. Also in this case, elastic interface elements are used to connect the arch springings to fixed supports so as to represent elastic abutments. Again, the reference skew arch (e.g. arch *Skew 2* with header bond) is analysed

considering the five pairs of elastic normal and tangent stiffness values reported in Table 5-3. As for the square arches, the failure mechanism does not change by varying the stiffness at the lateral supports, and in all the cases arch failure is reached when a 3D hinge mechanism with five main cracks forms.

The load-displacement curves showing the response of the arch *Skew 2* with header bond are plotted in Figure 5-52, where the displacement was measured at the centre line of the arch barrel at three quarter span. The variation of the ultimate load and the initial stiffness of the arch with the abutment stiffness are displayed in Figures 5-53 and 5-54. As for the square arches (see Section 5.2.4), only the case with the lowest support stiffness (K_{ab} = 1N/mm^3) shows a significant change in the response, where an ultimate load (Figure 5-53) and initial stiffness (Figure 5-54) reduction can be observed. Moreover when compared to the responses of the arches with fixed supports or higher abutment stiffness, the skew arch with K_{ab} = 1N/mm^3 shows a more ductile behaviour with no softening.

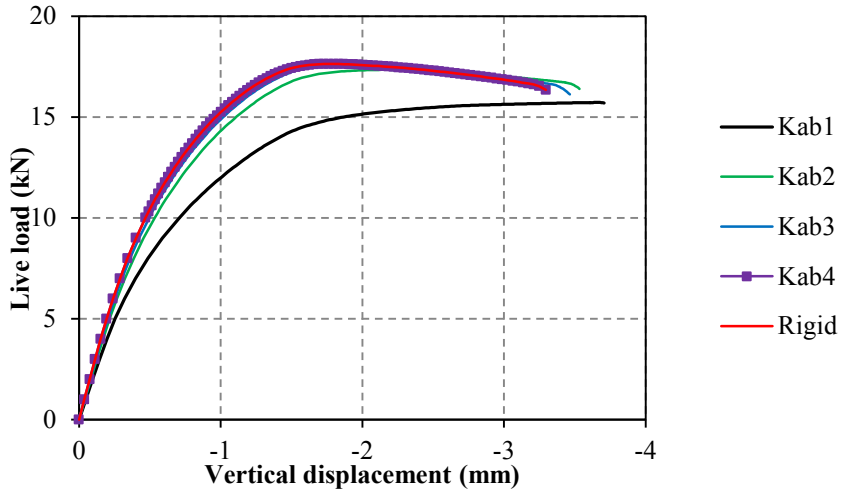

Figure 5-52: Load-displacement curves for arch *Skew 2* with different abutment stiffness

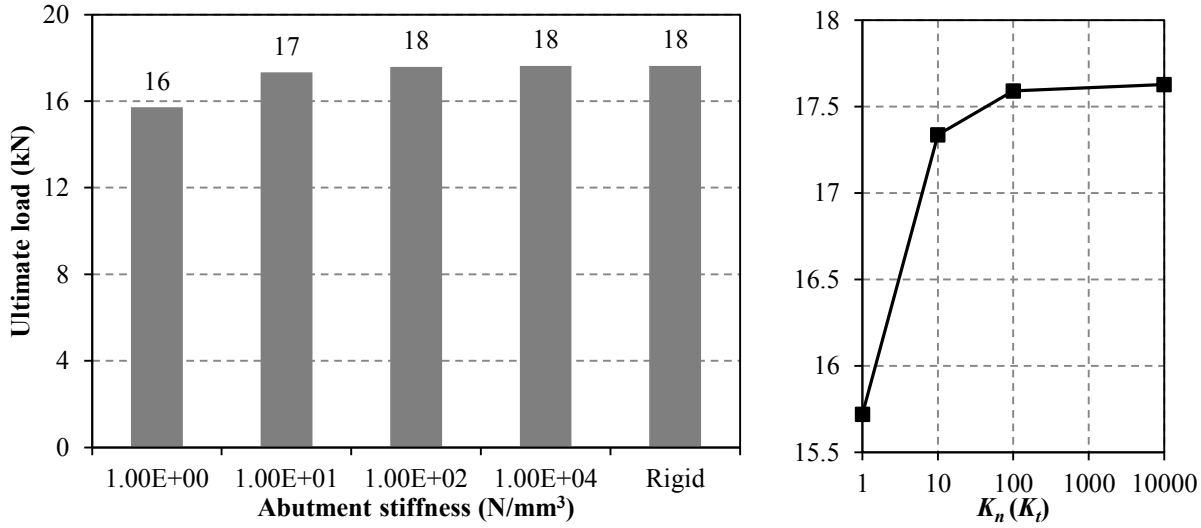

Figure 5-53: Influence of abutment stiffness on the load capacity of the skew arch

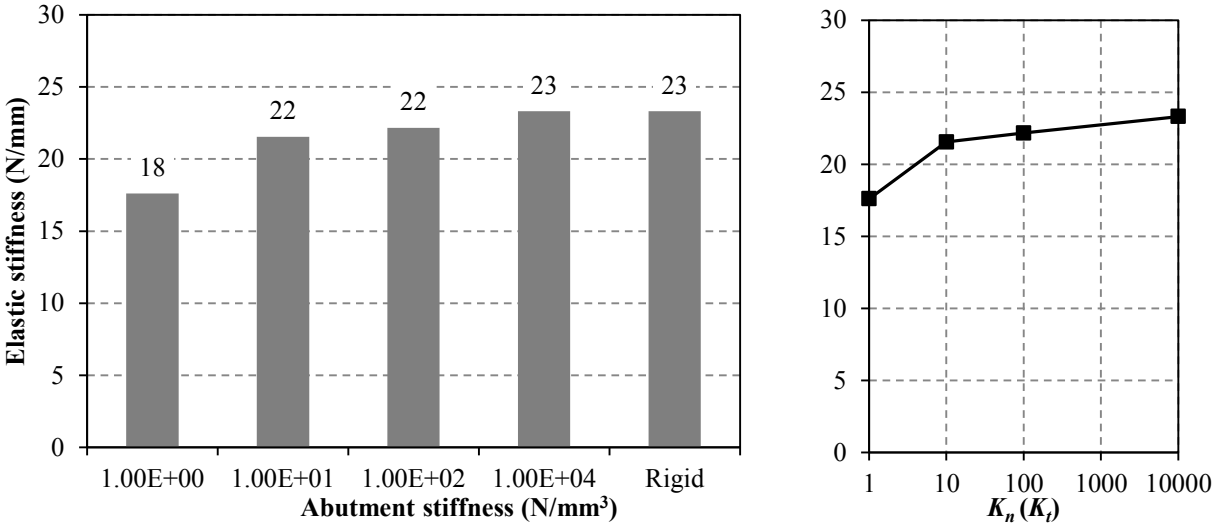

Figure 5-54: Influence of abutment stiffness on the initial stiffness of the skew arch

5.3.4 Effects of abutment movement

The skew arch collapse mechanisms due to support movements have been investigated considering the response of the reference arch (arch *Skew 2* with header bond) subject to the three support displacement modes considered in Section 5.2.5 and shown in 5-21. The imposed displacements at the left support are plotted against the associated reaction forces in Figure 5-55. When the failure mechanisms due to horizontal support displacements develop,

the associated reaction forces decrease showing a post-peak softening response. Conversely, in the case of differential vertical support movements, the reaction force remains almost constant for relative large displacement values. Figure 5-56 displays the deformed shapes for skew arch subjected to the three settlement modes, and Figure 5-57 shows the plastic work W_{cr1} contour for the different cases. All these figures refer to the last step of the numerical simulations at the failure of the arch. It can be noticed that the three failure modes are associated with the formation of cracks close to the two springings but not at the crown as in the case of square arches (see Figure 5-22).

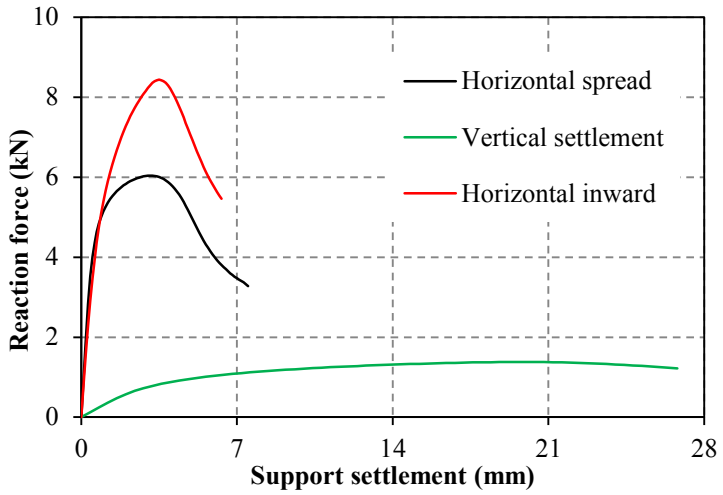

Figure 5-55: Reaction force-support displacement curves for arch *Skew 2*

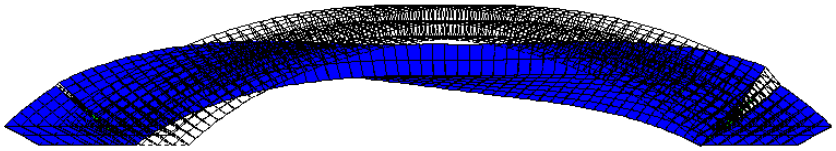

(a) Horizontal spread of support

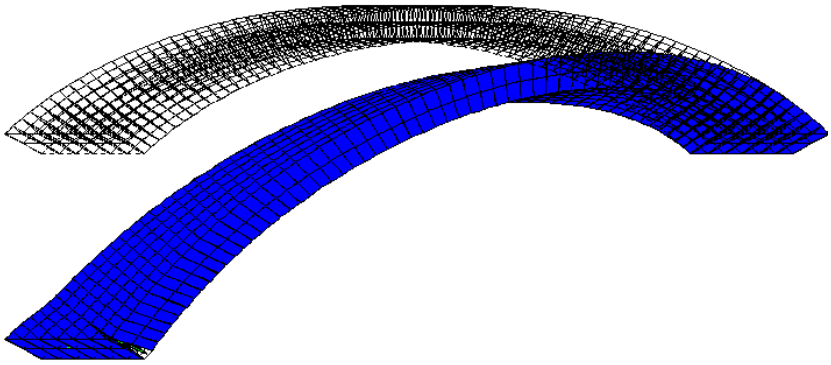

(b) Vertical differential settlement

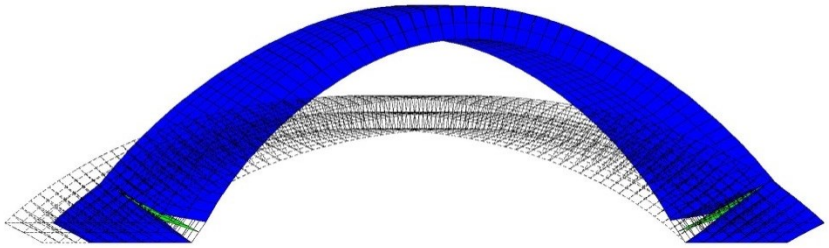

(c) Horizontal inward movement

Figure 5-56: Deformed shape for the arch *Skew 2* subject to different support displacement

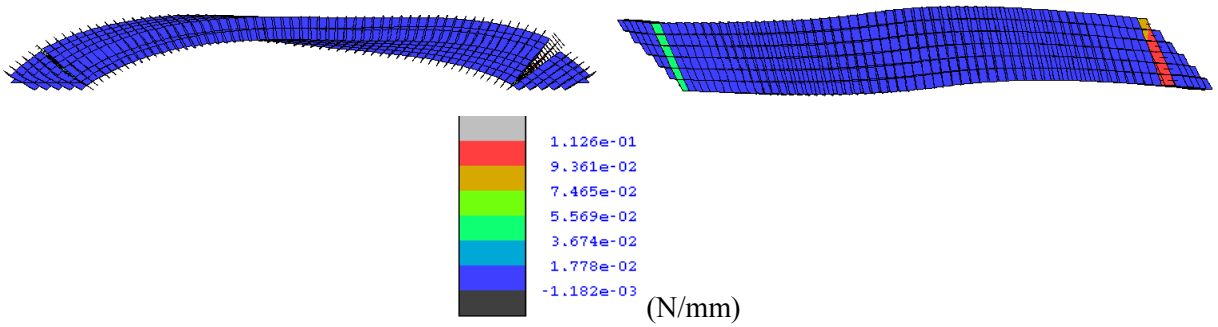

(a) Horizontal spread of support

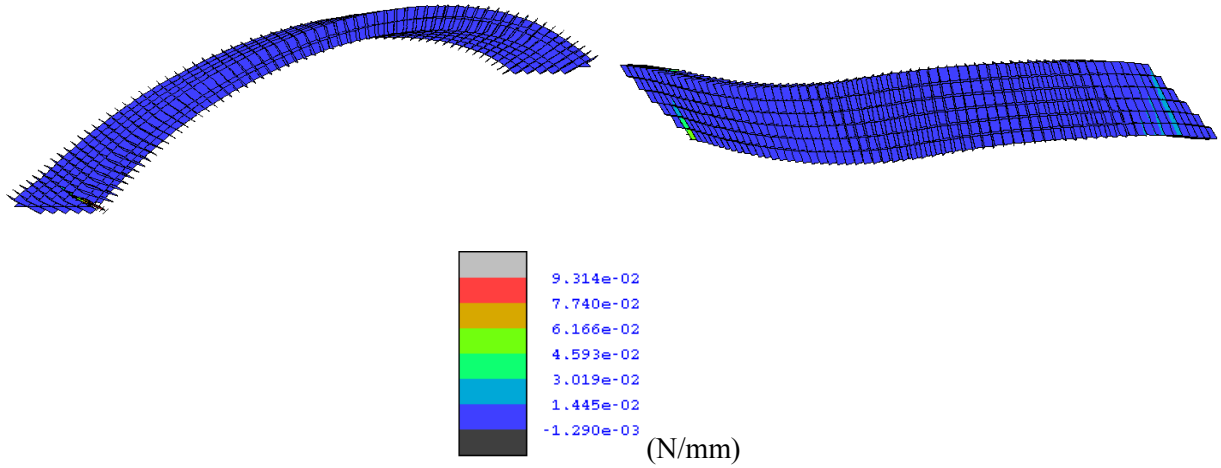

(b) Vertical differential settlement

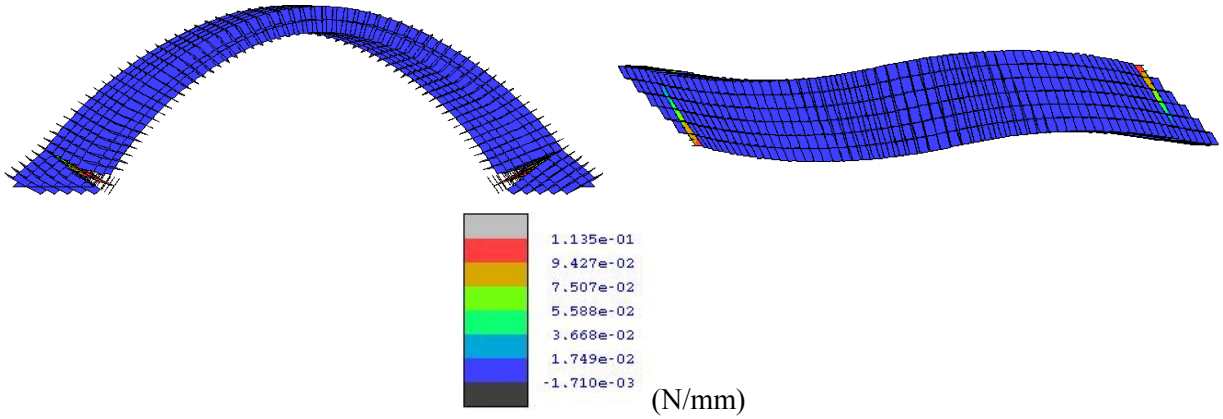

(c) Horizontal inward movement

Figure 5-57: Plastic work W_{cr1} contour for the arch *Skew 2* subject to different support displacement

5.4 Conclusions

The response up to collapse of square and skew brick-masonry arches has been investigated using the validated mesoscale strategy described in Chapter 4. The effects of (i) rise-to-span ratio, (ii) loading position, (iii) masonry bond and defects in the brickwork, (iv) abutment stiffness and (iv) support movements have been considered in the numerical study.

In the case of square arches it has been found that the rise-to-span ratio significantly influences the arch response and failure mode, but similar results have been obtained for arches with different span lengths. Deep arches or arches with intermediate rise-to-span ratio generally show a typical four hinge mechanisms, where cracks form in the mortar bed joints. On the other hand, shallow arches may fail by a combination of radial cracks and ring separation, where the later usually develops abruptly, leading to a sudden release of elastic energy. Moreover the arch failure mode strongly depends upon the load position, as line loads close to the springings may induce a brittle collapse, also for arches with high rise-to-span ratio. This may occur because of ring reparation at the arch haunch close to the load, or shear sliding at a radial mortar joint. In the case of multi-ring square arches built according to the stretcher method and with weak circumferential mortar joints, the response is governed by ring separation, which develops gradually causing a progressive stiffness reduction but leading to a more ductile behaviour. The numerical study on the effects of support stiffness has shown that the abutment deformability may significantly reduce the arch stiffness and the load capacity, but it seems that it does not modify the failure mode characteristics. Finally, the numerical simulations on the effects of abutment movements revealed that brick-masonry arches can support live loads also after the formation of a mechanism due to differential support movements. This additional load bearing capacity depends on the level of abutment displacement. Moreover it has been shown that the accuracy of these predictions is associated with the ability of the numerical description in representing the quasi-brittle nature of masonry. In fact, the use of a material model which disregards de-cohesion and potential friction reduction (e.g. an elastic-plastic approximation with high fracture energy values)

generally leads to unrealistic response predictions, where the arch capacity is insensitive to potential abutment movements.

As opposed to the analyses on square arches which were conducted using efficient strip models, full 3D mesoscale descriptions have been adopted in the numerical studies for skew arches. In has been found that arches with different rise-to-span ratio are characterised by a different response, where the deep arch shows the highest load capacity, but the same failure mode with five cracks in the mortar bed joints. On the other hand, arches built according to the stretcher method, and made up of defective brickwork with weak circumferential mortar bed joints, may also experience ring reparation. As for square arches, this reduces the initial stiffness but improves arch ductility. The response up to collapse of skew arches subject to abutment movements has been also analysed. It has been found that the failure modes under differential horizontal and vertical support displacements are characterised by the development of cracks at the two springing regions but not at the crown.

CHAPTER 6

Mesoscale Partitioned Analysis of Masonry Bridges

6.1 Introduction

Masonry arch bridges are heterogeneous systems whose behaviour is determined by the interaction between different structural and non-structural components, including the arch barrel, the backfill and the lateral walls.

In Chapters 4 and 5 a mesoscale approach for masonry (Macorini & Izzuddin, 2011) has been adopted to investigate the response of masonry arches. It has been shown that this advanced modelling strategy allows for an accurate response prediction, as it takes into account the actual masonry bond, including potential defects in the brickwork.

In this chapter the interaction between the arch and the backfill is accounted for in the analysis of masonry bridges. Because of the significant computational cost, in all the numerical simulations the proposed modelling strategy with solid and nonlinear interface elements is coupled with the partitioning approach allowing for parallel computation which has been developed previously at Imperial College (Jokhio, 2012; Jokhio & Izzuddin, 2013).

Initially, the assumption of rigid spandrel walls is considered which, in the case of square arch bridges, enables the use of an efficient description where the arch and the backfill are represented by a strip model. This implies employing a FE mesh with only one set of solid elements for the arch and the soil domain along the width of the bridge, and restraining the

transverse displacements to allow for the confinement provided to the backfill by the two rigid lateral walls. Using this simplified modelling strategy, numerical simulations have been performed on a multi-ring arch bridge, which was previously tested at the Bolton Institute (Gilbert & Melbourne, 1998). In the following the numerical predictions are firstly compared against the test results, and then the results of parametric studies are presented and discussed. These have been conducted to investigate the influence of the backfill and the arch characteristics, the loading position, the arch shape and the effects of abutment movements on the bridge response. Subsequently the results of full 3D mesoscale analyses carried out to investigate the contribution of the spandrel walls are shown.

In the final part of this chapter, the computational performance associated with the use of the mesoscale partitioning approach for the full 3D analysis of a realistic stone masonry bridge is investigated. The efficiency and the accuracy provided by using alternative strategies with flat partitioning, hierarchic partitioning and master-slave coupling at the partitioned boundaries (Jokhio, 2012) is also analysed.

6.2 Analysis of a brick-masonry arch bridge

A brick-masonry arch bridge previously tested at the Bolton Institute (Melbourne & Gilbert, 1995) is analysed using the proposed mesoscale partitioned modelling strategy for masonry arch bridges. The characteristic of the analysed bridge and a description of the experimental test are provided below. Then the results obtained using a strip model and a full 3D description are presented and discussed.

6.2.1 Experimental test

In 1995 an experimental programme including tests on four masonry arch barrels and seven single span masonry arch bridges was conducted at the Bolton Institute (Melbourne & Gilbert, 1995). In particular masonry bridges with 3m and 5m span and 2.88m width were subject to vertical line loads up to collapse.

Hereinafter the response of the bridge specimen named *Bridge 3-3* in (Melbourne & Gilbert, 1995) is investigated. The bridge geometry is sketched in Figure 6-1 and indicated in Table 6-1. The 3m span two-ring arch barrel was built according with the stretcher method in a segmental circular shape on massive concrete foundations. The arch is 215mm thick and is characterised by a 4:1 span-to-rise ratio with a springing angle of 37°. The spandrel and the wing walls are made up of English bond brick-masonry. Full size class A engineering bricks and a 1:2:9 (cement:lime:sand) mortar were used for all the brickwork, while 50mm graded crushed limestone was adopted for the backfill, filling the space above the arch and between the two lateral walls (spandrel and wing walls).

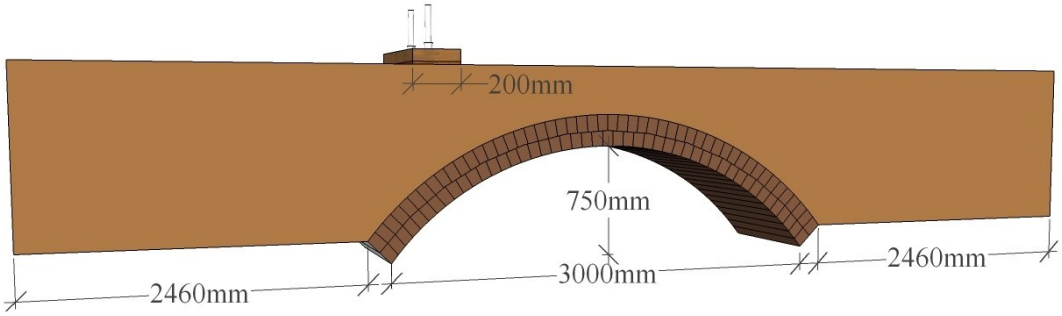

Figure 6-1: Geometric characteristics and loading arrangement for *Bridge 3-3*

Table 6-1: Principal dimensions for *Bridge 3-3* (Melbourne & Gilbert, 1995)

Arch	**Span (mm)**	**Rise (mm)**	**Ring thickness (mm)**	**Width (mm)**	**Number of bricks**
	3000	750	215	2880	48
Backfill	**Depth at crown (mm)**		**Width (mm)**	**Length (mm)**	
	300		2880	2460×2+3000	
Spandrel walls	**Depth at crown (mm)**		**Width (mm)**	**Length (mm)**	
	300		330	2460×2+3000	

In the test, a vertical line load was applied at quarter span through a 2200×200mm^2 steel loading beam placed on the surface of the backfill and against a reaction frame incorporating

hollow jacks and three sets of prestressing tendons. The full width line load was increased monotonically until the failure of the bridges specimen.

Figure 6-2 depicts the failure mode of Bridge 3-3 which was due to the formation of four large radial cracks (hinges) in the arch mortar bed joints. These transformed the arch into a mechanism when the applied load reached about 600kN. The first hinge developed under the load at about the quarter span, and the other three main cracks progressively formed at about the three quarter span and at the two springings. At collapse significant separation between the arch and the lateral walls was also observed.

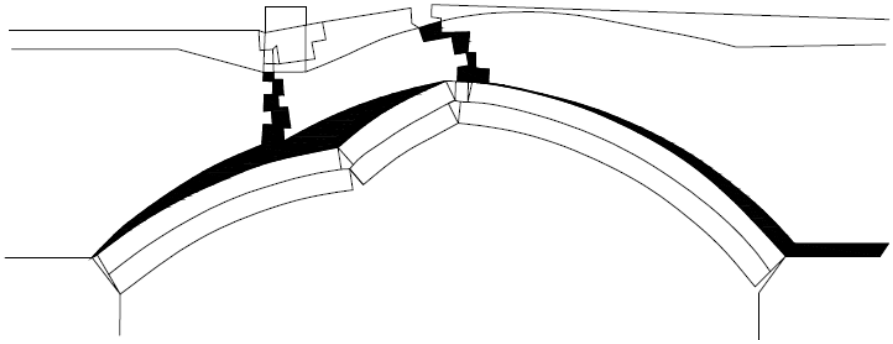

Figure 6-2: Failure mechanism of *Bridge 3-3* (Melbourne & Gilbert, 1995)

6.2.2 Strip-model analysis

As anticipated in the introduction, numerical simulations have been performed adopting a simplified strip-model.

6.2.2.1 Model description

The bridge is represented by a FE mesh with only one set of solid elements for the arch and the soil domain along the width of the bridge as shown in Figure 6-3. The actual masonry bond of the arch on the face of the bridge is accurately represented adopting one 20-noded solid element for each brick. Thus two nonlinear interface elements are used for representing each individual radial mortar joint. The adopted mesh for the backfill is not uniform and

formed by 15-noded solid elements, where a linear refinement has been considered at the abutments, and at the quarter span close to the loading area. Moreover to allow for an accurate modelling of the arch backfill interaction, the FE mesh for the backfill is constructed with the rectangular faces of the 15-noded prismatic solid elements at the bottom of the backfill coincident with the top face of the solid elements representing masonry bricks at the extrados of the arch. Coincident nodes belonging to the two domains are then connected by nonlinear interface elements to represent separation and frictional sliding at the arch-backfill interface.

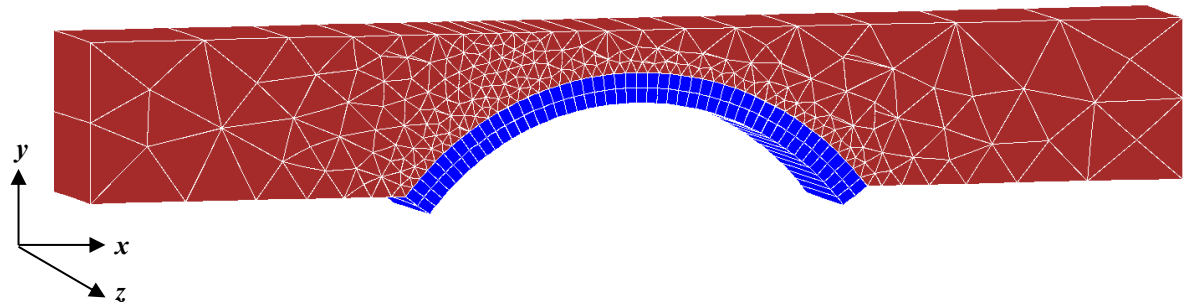

Figure 6-3: Strip model mesh for *Bridge 3-3*

Concerning the model boundary conditions, fixed supports have been assumed for the nodes on two bases of the backfill domain extending beyond the two arch springings. Additionally, the nodes on the two lateral faces of the backfill are restrained longitudinally (along x in Figure 6-3), and the node of the arch and the backfill on the two longitudinal faces of the bridges are restrained along z (Figure 6-3). This is to prevent transverse deformations within the bridge to model the contribution of rigid lateral walls.

The FE mesoscale description for the arch encompasses 96 20-noded elastic solid elements for the brick units, 94 nonlinear interface elements for the mortar bed joints, 48 nonlinear interface elements for the circumferential mortar joints connecting the two adjacent rings and 48 interface elements for representing the interaction between the arch and the fill. Moreover the backfill domain is represented by 407 15-noded elasto-plastic tetrahedral elements. Thus

the bridge is described by a strip-model employing more than 7000 degrees of freedoms. To improve computational efficiency, the model for the bridge is incorporated into an advanced partitioning strategy (Jokhio, 2012) allowing for parallel computation. Hierarchic partitioning techniques are employed for the mesoscale description of the masonry domain, while a flat partitioning strategy is adopted for the backfill. The FE mesh with partitions has been generated using *Caim*, a semi-automatic mesher developed at Imperial College (Rodriguez-Villares, 2014). More specifically, 24 child partitions have been used for the masonry domain and 11 child partitions for the backfill. According to the adopted partitioning strategy, the parent file at level 0 collects all the nodes at the interface between the arch and the backfill.

The material tests performed in the experimental program (Melbourne & Gilbert, 1995) did not provide information on the critical material parameters required by the adopted mesoscale model for brick-masonry (Macorini & Izzuddin, 2011). Thus, in the numerical simulations of *Brige3-3*, the masonry material properties reported in Tables 4-3, 4-4 and 4-5 and used in Chapter 4 to investigate *Arch G* have been employed. This is because the generic characteristics of bricks and mortar for *Arch G* (e.g. class A bricks and 1:2:9 mortar) correspond to those of the masonry components for *Brige3-3*.

The main material properties for the backfill are reported in Table 6-2. These have been used with the Hooke's law and the rounded hyperbolic Mohr-Coulomb failure criterion (Abbo & Sloan, 1995) to capture the elasto-plastic behaviour of the backfill.

Finally, the values in Tables 4-4 and 4-5 have been considered for the nonlinear interface elements representing the interaction between the arch and the backfill.

Table 6-2: Mechanical properties for backfill

Elastic modulus E_f **(N/mm^2)**	**Poisson's ratio** v_f	**Frictional angle** φ_f	**Cohesion** c_f**(N/mm^2)**	**Unit weight** ρ_f**(kN/m^3)**	a_1	θ_T
500	0.20	45°	0.01	19.1	0.05	25°

6.2.2.2 Numerical-experimental comparison

In Figure 6-4, the deformed shape of the strip model at the last step of analysis is displayed. A typical four-hinge mechanism with radial cracks below the load, at the two springings and at three quarter span can be noticed.

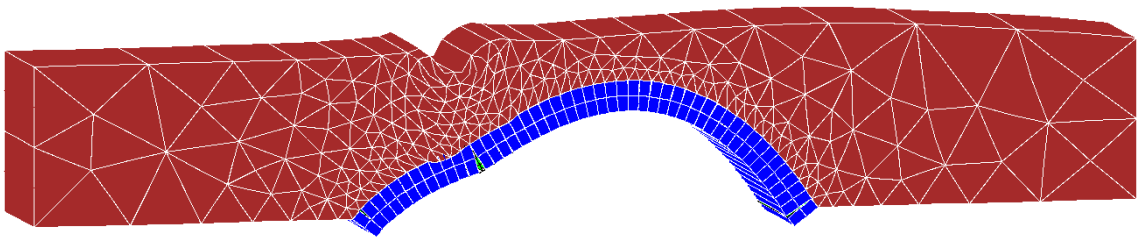

Figure 6-4: Deformed shape at the last step of the analysis for *Bridge 3-3*

Numerical-experimental comparisons in term of the applied load against the vertical displacement measured on the arch at the quarter span are shown in Figure 6-5. A generally good agreement between the experimental and the numerical curves can be observed, where the initial stiffness and load capacity measured in the test are accurately predicted by the proposed strip-model. It is important to note that the numerical simulation was stopped just after reaching the peak load at the onset of a softening branch, because the prediction of the post-peak response would have required an excessive computational time.

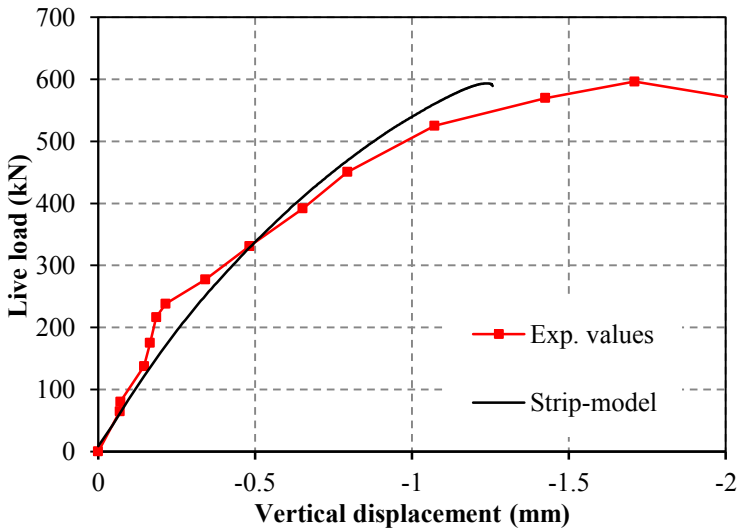

Figure 6-5: Experimental-numerical comparison for *Bridge 3-3*

Cracking in the arch barrel and damage at the interface between the arch and the backfill are shown at different loading levels in Figures 6-6a,b,c,d,e. Radial cracks first appear in the mortar bed joints at the quarter span just below the load (Figure 6-6a). Then cracking develops at the left springing (Figure 6-6b), which is almost simultaneously followed by cracking at the right springing (Figure 6-6c). Finally, the formation of the fourth radial cracks at about the three quarter span leads to a mechanism when the arch reaches the maximum load (Figures 6-6d,e). At this loading level, significant plastic work can be also noticed at the top circumferential interface elements in the area close to the quarter span. This reveals separation and plastic sliding at the interface between the arch and the backfill.

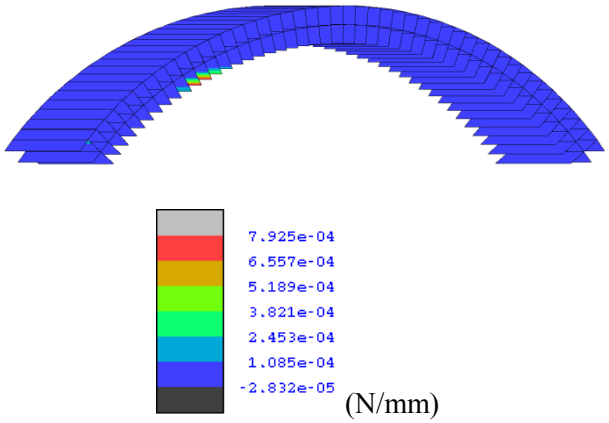

(a) 1st radial crack P = 80kN

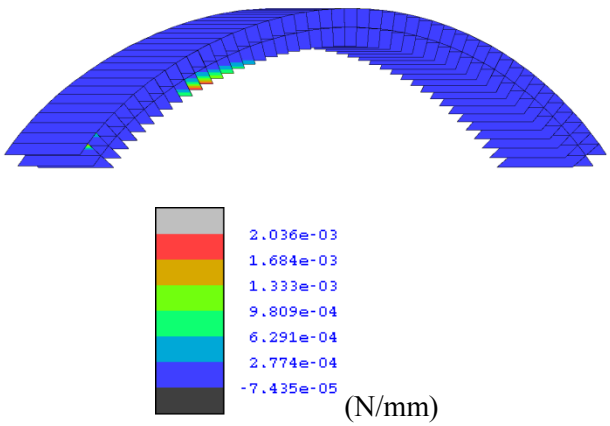

(b) 2nd radial crack P = 150kN

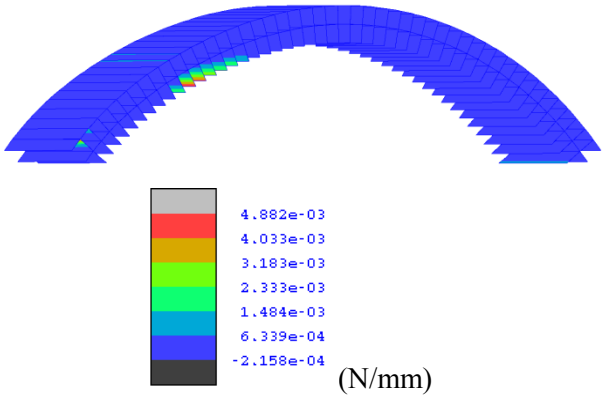

(c) 3rd radial crack P = 350kN

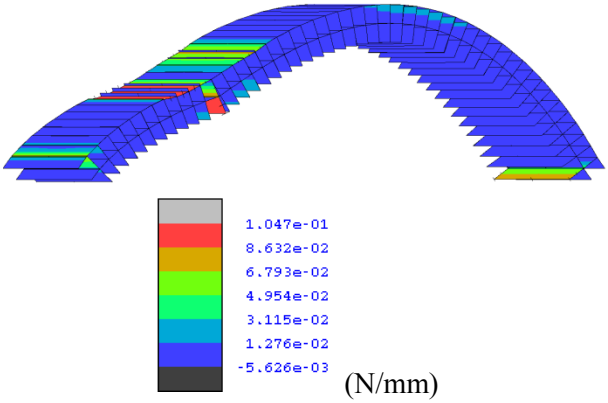

(d) 4th radial crack P = 570kN

Figure 6-6: Plastic work W_{cr1} contours at (a) 1st radial crack P = 80kN, (b) 2nd radial crack P = 150kN, (c) 3rd radial crack P = 350kN, (d) 4th radial crack P = 570kN and (e) at the final step of analysis (Cont'd …)

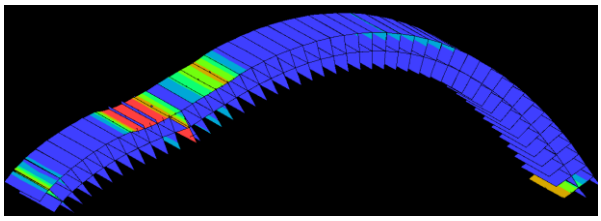

(e) Final step

Figure 6-6: Plastic work W_{cr1} contours at (a) 1st radial crack P = 80kN, (b) 2nd radial crack P = 150kN, (c) 3rd radial crack P = 350kN, (d) 4th radial crack P = 570kN and (e) at the final step of analysis

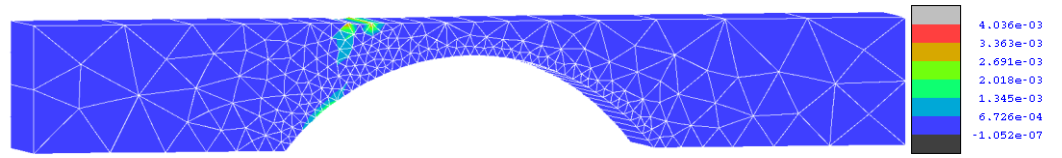

(a) P = 80kN

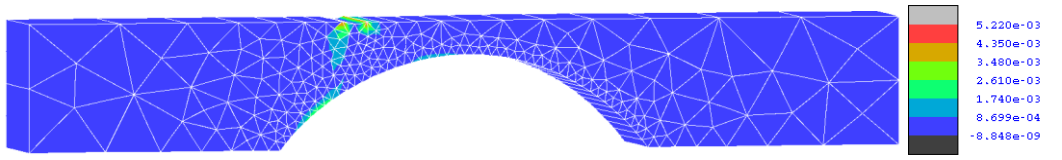

(b) P = 150kN

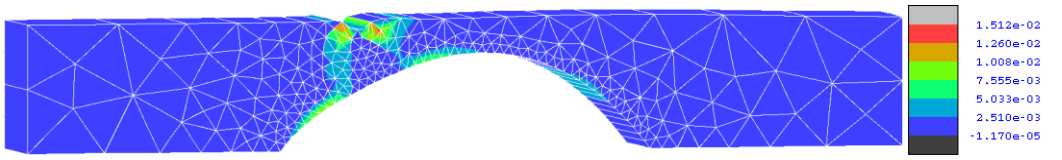

(c) P = 350kN

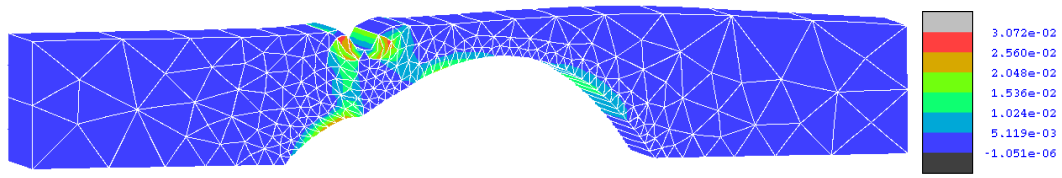

(d) P = 570kN

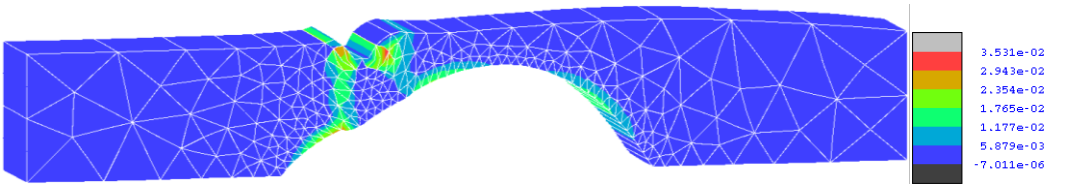

(e) Final step

Figure 6-7: Equivalent von Mises plastic deformations in the backfill at (a) P = 80kN, (b) P = 150kN, (c) P = 350kN, (d) P = 570kN and (e) at the final step of analysis

Figures 6-7a,b,c,d,e display the equivalent von Mises plastic deformations in the backfill, when the cracks progressively developed in the masonry arch. It can be seen that at low loading levels plastic deformations form below the loading area and then, by increasing the load, they develop at the bottom of the fill domain when it connects to the right haunch of the arch and close to the arch crown. Finally, plastic deformations form at the bottom of the backfill at the three quarter span of the arch. These are caused by the pressure exerted by the backfill to the arch (passive pressure) which opposes the arch sway.

6.2.2.3 Modelling arch-fill interaction

To investigate the influence of the modelling strategy adopted to represent the contribution of the backfill and the arch-fill interaction, numerical simulations have been performed comparing the results obtained by the strip-model described in the previous section and those achieved using alternative simplified strategies. These include (i) a model which disregards the backfill and considers only the contribution of the arch (*Arch-model 1)*, (ii) a numerical description where backfill contribution is represented as an additional distributed load onto the arch (*Arch-model 2)*, (iii) a model where the fill is described by a continuum elastic approach (*Strip-model elastic fill*), and (iv) a model similar to the original strip-model introduced before, but with rigid interface elements for describing the arch-fill interaction (*Strip-model rigid interface*).

Figure 6-8 compares the load-displacement responses obtained using the strip-model and the two arch models (e.g. *Arch-model 1* and *Arch-model 2)*. Significant differences, both in term of initial stiffness and load capacity, can be easily observed. In particular *Arch-model 1* predicts an ultimate load of 150kN, while *Arch-model 2* a load capacity of 180kN. Both predictions are quite far from the experimental ultimate load P = 600kN, which practically coincides with the maximum load calculated by the *Strip-model*. The difference in the response predictions of two arch models is due to the beneficial effects due to the weight of the backfill which are accounted for only in *Arch-model 2*. However, these results confirm that the most critical backfill contribution is associated with the pressure exerted by the fill

onto the arch which opposes the arch sway. This can be captured only by employing an explicit modelling for the backfill.

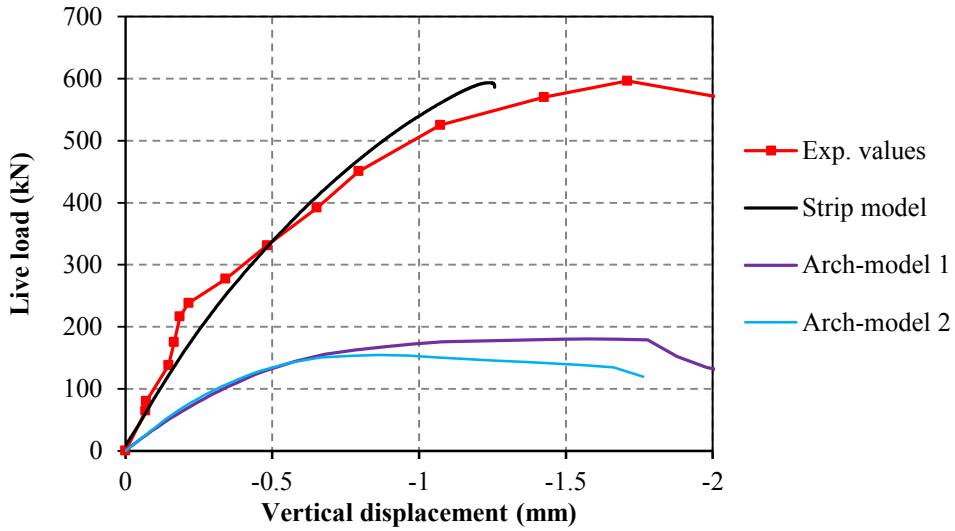

Figure 6-8: Numerical comparisons among the strip-model and models modelling only the arch contribution

In Figure 6-9, the response obtained assuming the backfill as an elastic continuum domain (*Strip-model elastic fill*) is compared against the prediction provided by the original strip-model with an elasto-plastic backfill. It can be noticed that the *Strip-model elastic fill* curve shows unrealistic high stiffness and load capacity. This points out that the use of a continuum description neglecting material nonlinearity for the backfill leads to significantly overestimating the backfill contribution. In this case, cracking in the arch is partially restrained by the backfill and it starts to develop at higher load level. This is shown in Figure 6-10, where the von Mises stresses σ_{VM} ($\sigma_{VM} = \sqrt{3/2\boldsymbol{\sigma}' : \boldsymbol{\sigma}'}$ with $\boldsymbol{\sigma}' = \boldsymbol{\sigma} - \sigma_m$) in the backfill and the plastic work W_{cr1} contour in the interface elements are depicted at a displacement equal to the displacement at maximum load measured in the test. It can be seen that only one radial crack forms in the arch, when the predicted load is about 3 times higher than the collapse load in the test.

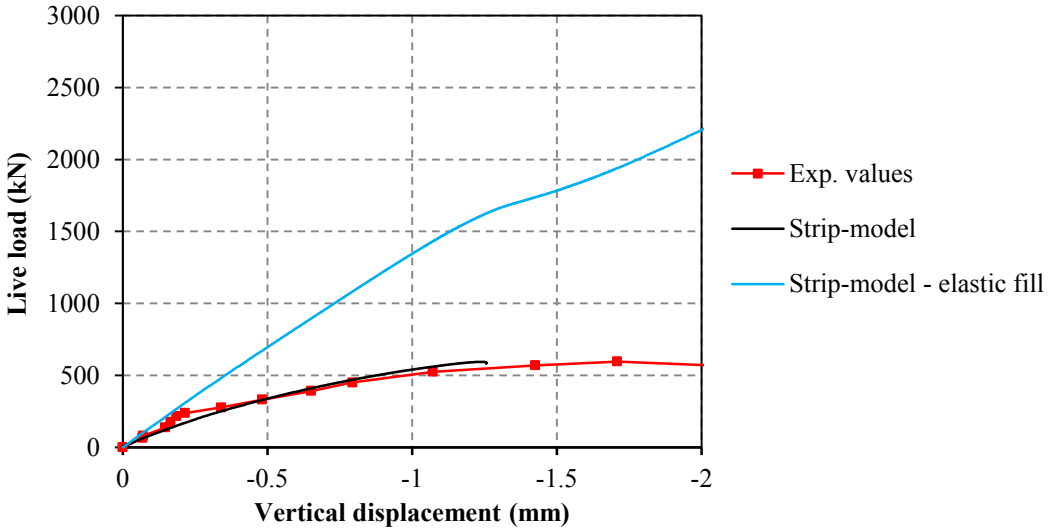

Figure 6-9: Numerical comparisons on the contribution of different modelling strategies for fill domain

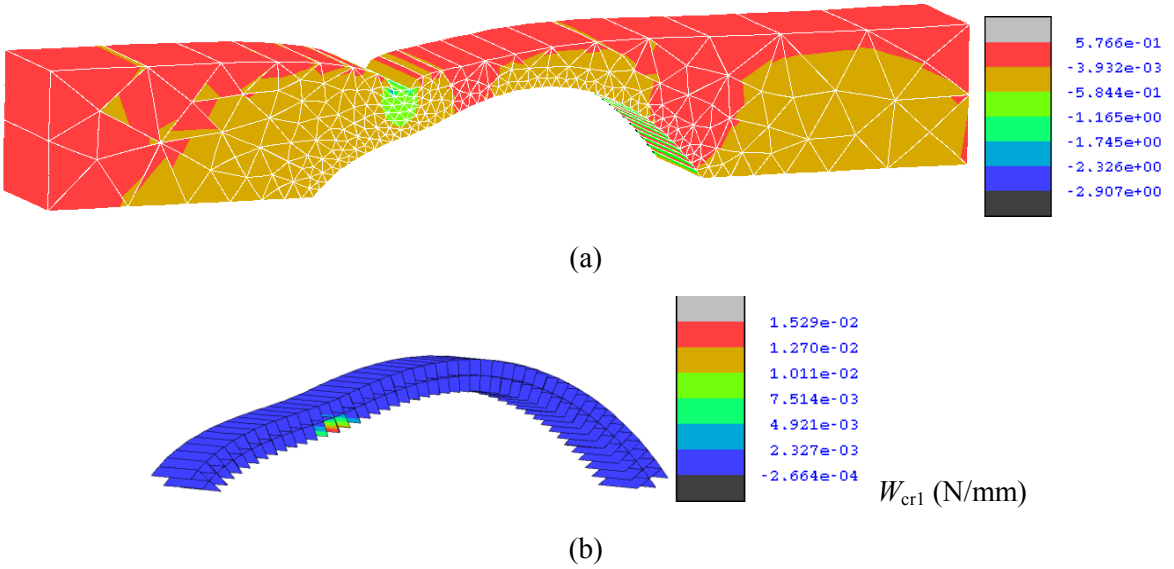

Figure 6-10: Contours of (a) equivalent von Mises stresses in the backfill and (b) plastic work in the interface elements for the strip-model with elastic fill

To investigate the influence of the mechanical properties of the interface elements modelling the arch-backfill interface, the response obtained using the original strip model, where the physical interface is represented by nonlinear interface elements with the same properties of the mortar joints (Tables 4-4 and 4-5), is compared against the numerical prediction obtained employing rigid interface elements to connect the extrados of the arch with the backfill. The two numerical curves and the experimental response are shown in Figure 6-11. It can be seen

that introducing a rigid interface between the two bridge components significantly influences the numerical prediction at different loading levels, where the maximum load is about 33% higher than that obtained using the original strip-model.

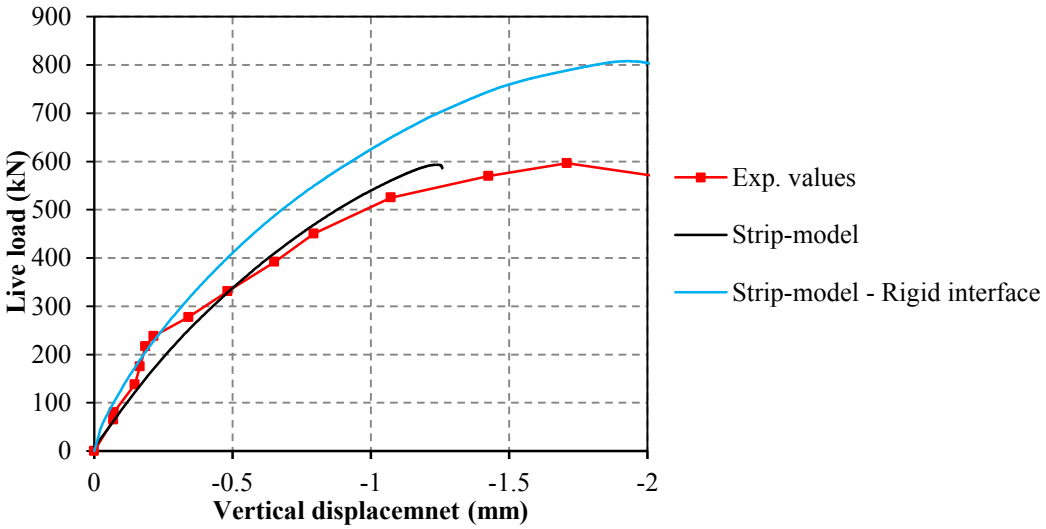

Figure 6-11: Numerical comparisons on the contribution of different modelling strategies for the interface between the arch and the fill domain

6.2.3 Parametric studies

Numerical analyses have been carried out to study the influence of material and geometric aspects on the response prediction of masonry arch bridges up to collapse. The brick-masonry bridge analysed in the previous section by adopting a strip-model is considered here as the reference structure. In the initial studies, the numerical responses obtained changing the material parameters for the backfill, and considering defective brickwork for the arch have been analysed. Then the effects due to the loading position, the arch rise-to-span ratio, and support movements have been investigated.

6.2.3.1 Influence of backfill material properties

Numerical simulations have been performed varying the most critical material parameters for the backfill one at a time. These include Young's modulus E_f, cohesion c_f and friction angle φ_f.

Then the response of *Bridge 3-3* has been analysed considering the two most common types of soil material for the backfill, namely clay and limestone.

Figure 6-12 compares the load-displacement responses determined considering three typical Young's modulus values for the backfill: E_f = 200 MPa, 500 MPa, 1000MPa, while Figure 6-13 shows the relative errors calculated assuming the experimental results as the exact values for the initial stiffness and the load capacity. It can be seen that a variation of E_f within realistic limits is more critical for the prediction of the initial stiffness with a maximum error of 26%, but the variation of strength is more limited with a maximum error of 8%.

Similar numerical analyses have been conducted assuming a change in the cohesion, considering the values c_f = 10kPa, 30kPa, 50kPa (Figure 6-14) and a variation in the friction angle φ_f =45°, 50°, 60° (Figure 6-16). Similar results have been found for the two cases, where the top values lead to overestimating maximum load and initial stiffness of about 20% (see Figures 6-15 and 6-17).

The material properties presented in Table 6-3 (Melbourne, Wang & Tomor, 2007) have been used together with a Young's modulus E_f = 500MPa to describe clay and limestone backfill.

Table 6-3: Mechanical properties for typical backfill

	Friction angle φ_f	**Cohesion c_f (N/mm^2)**	**Unit weight ρ_f (kN/m^3)**
Limestone	46.4°	0.0224	19.1
Clay	20°	0.078	22.1

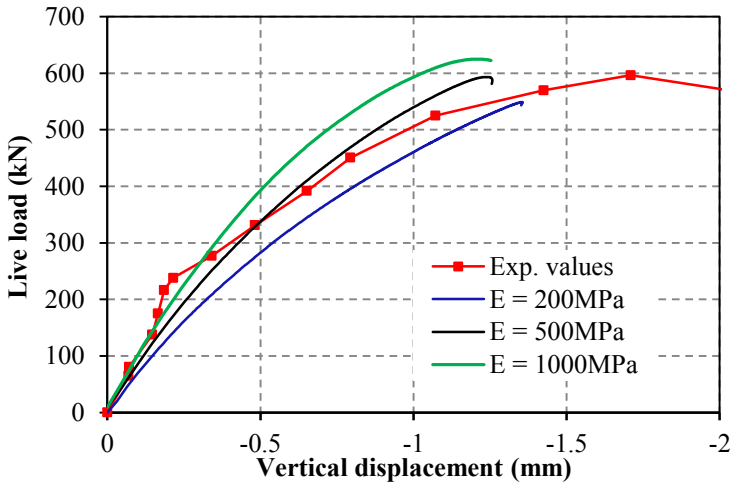

Figure 6-12: Influence of backfill Young's modulus on the bridge response

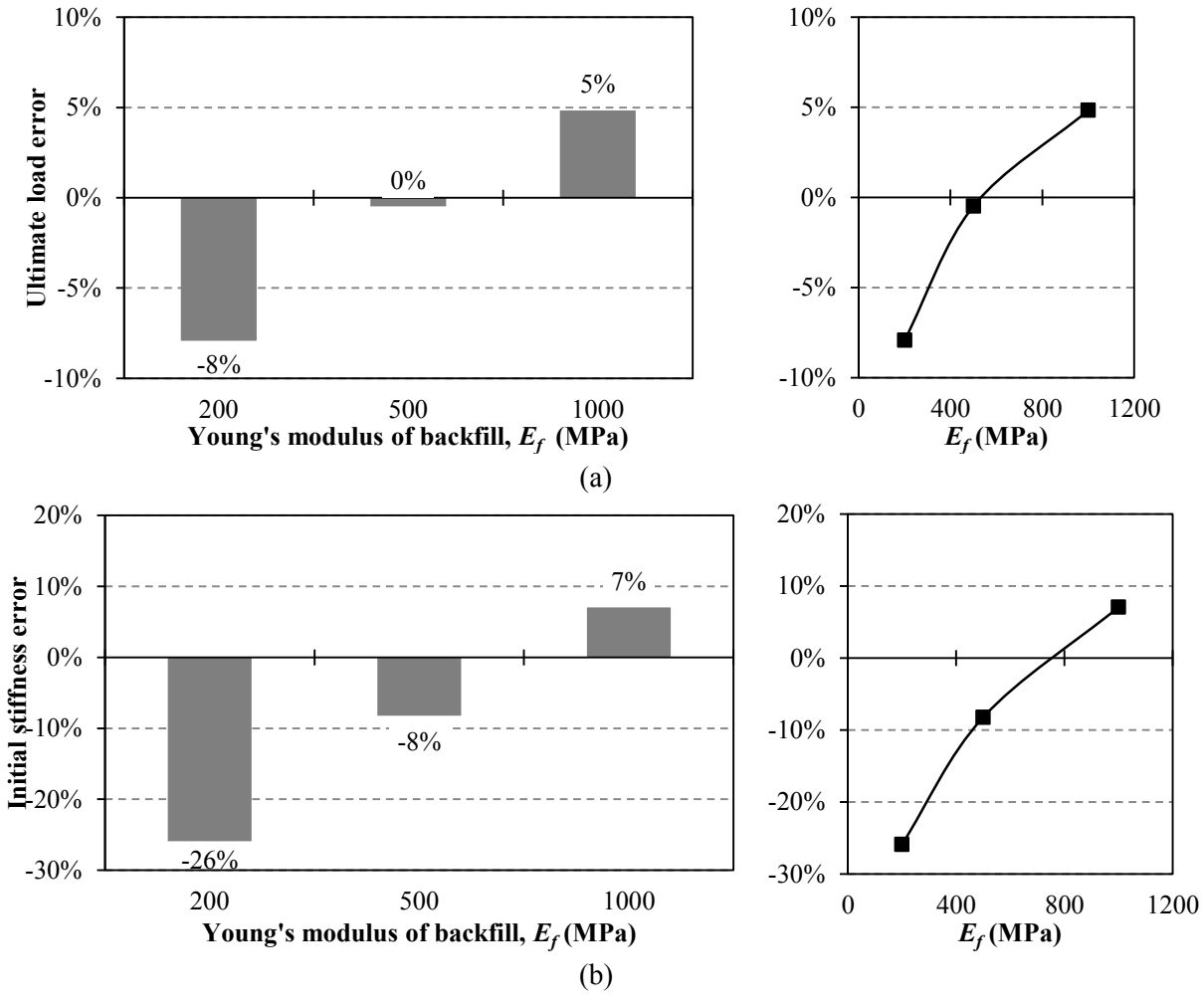

Figure 6-13: Influence of E_f on (a) ultimate load and (b) initial stiffness

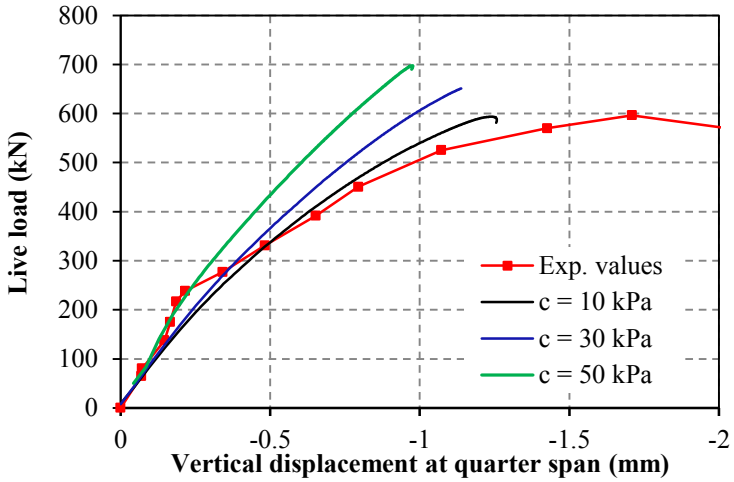

Figure 6-14: Influence of backfill cohesion on the bridge response

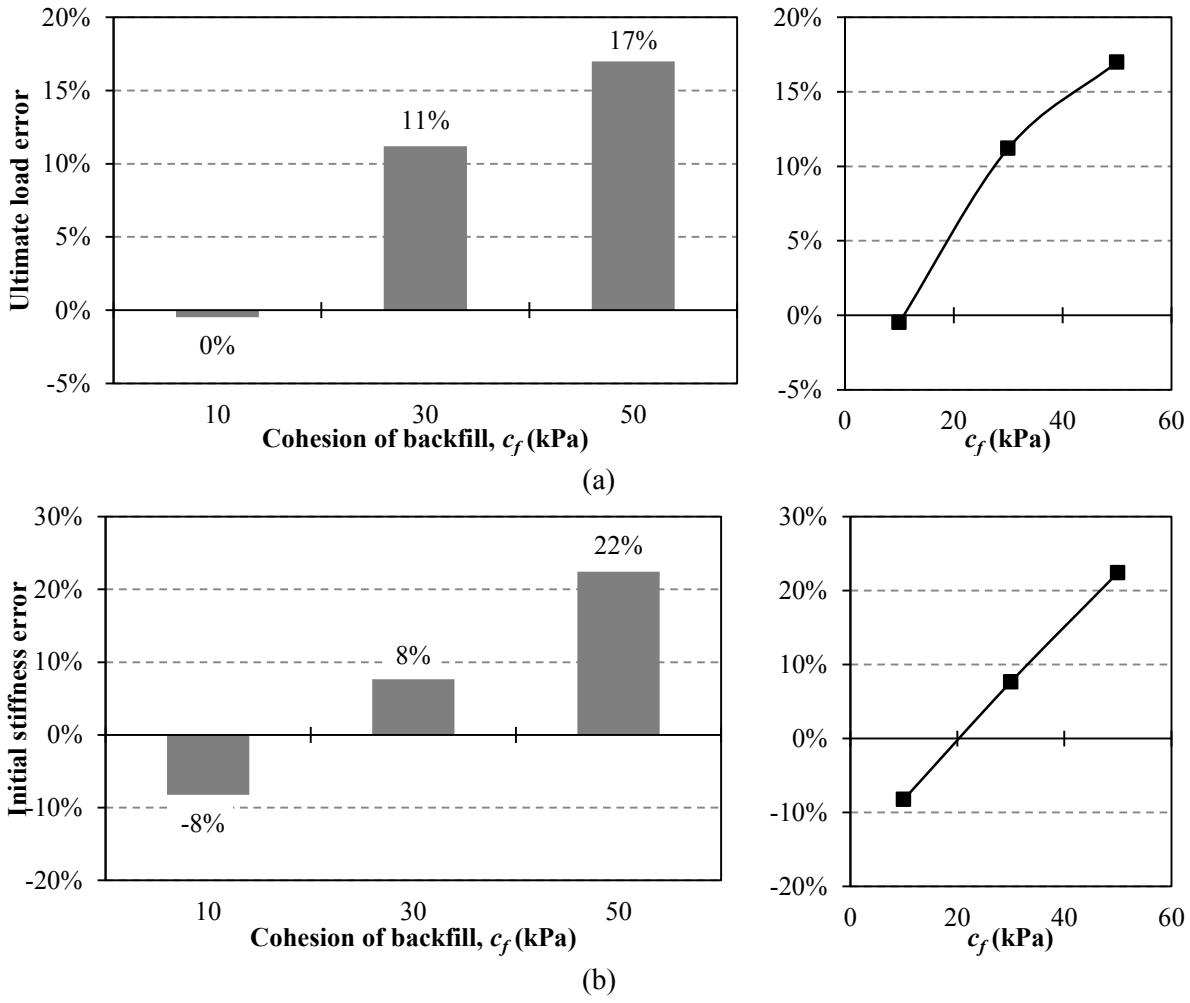

Figure 6-15: Influence of c_f on (a) ultimate load and (b) initial stiffness

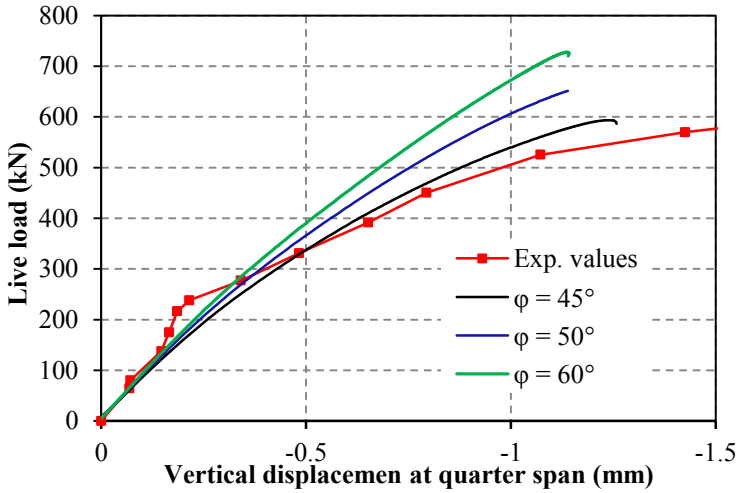

Figure 6-16: Influence of backfill frictional angle on the bridge response

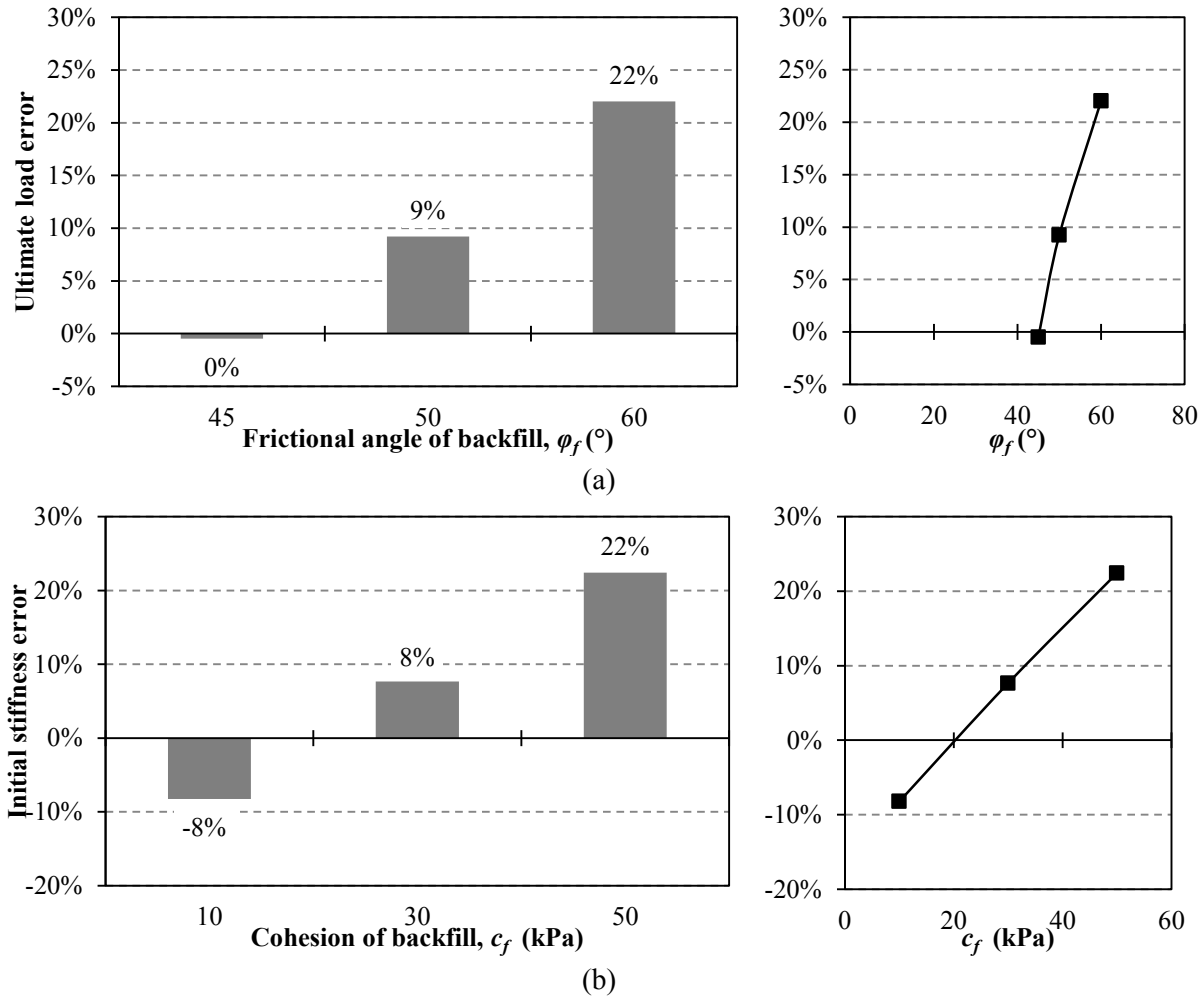

Figure 6-17: Influence of c_f on (a) ultimate load and (b) initial stiffness

The numerical results (Figure 6-18) confirm than the masonry bridge with limestone backfill is characterised by the higher load capacity. The responses of the two structures are quite similar (e.g. about the same initial stiffness) until the development of the substantial cracking. For higher loading values the bridge with limestone fill shows a stiffer behaviour up to collapse. The distribution of plastic deformations is slightly different, as plastic deformations in the limestone backfill are mainly concentrated below the load, while plastic deformations develop also above the arch crown in the bridge with clay fill (Figure 6-19). On the other hand, the plastic work contours in the interface elements (Figure 6-20) reveal a similar cracking pattern and damage at the interface between the arch and the backfill domain.

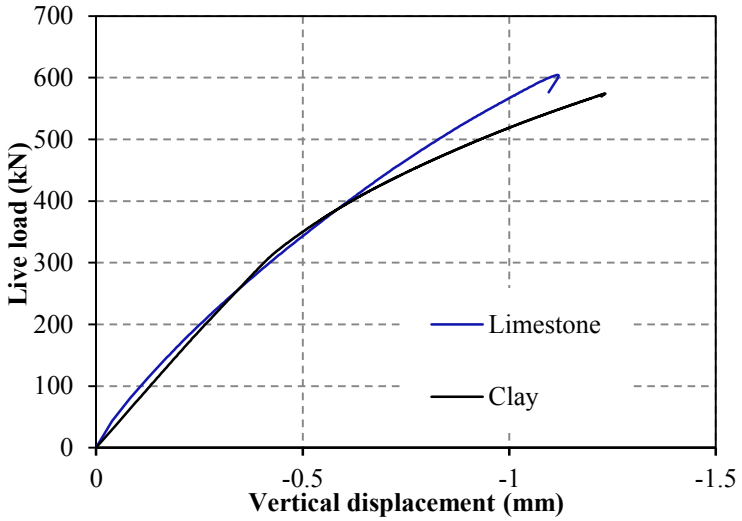

Figure 6-18: Load displacement curves for different types of backfill

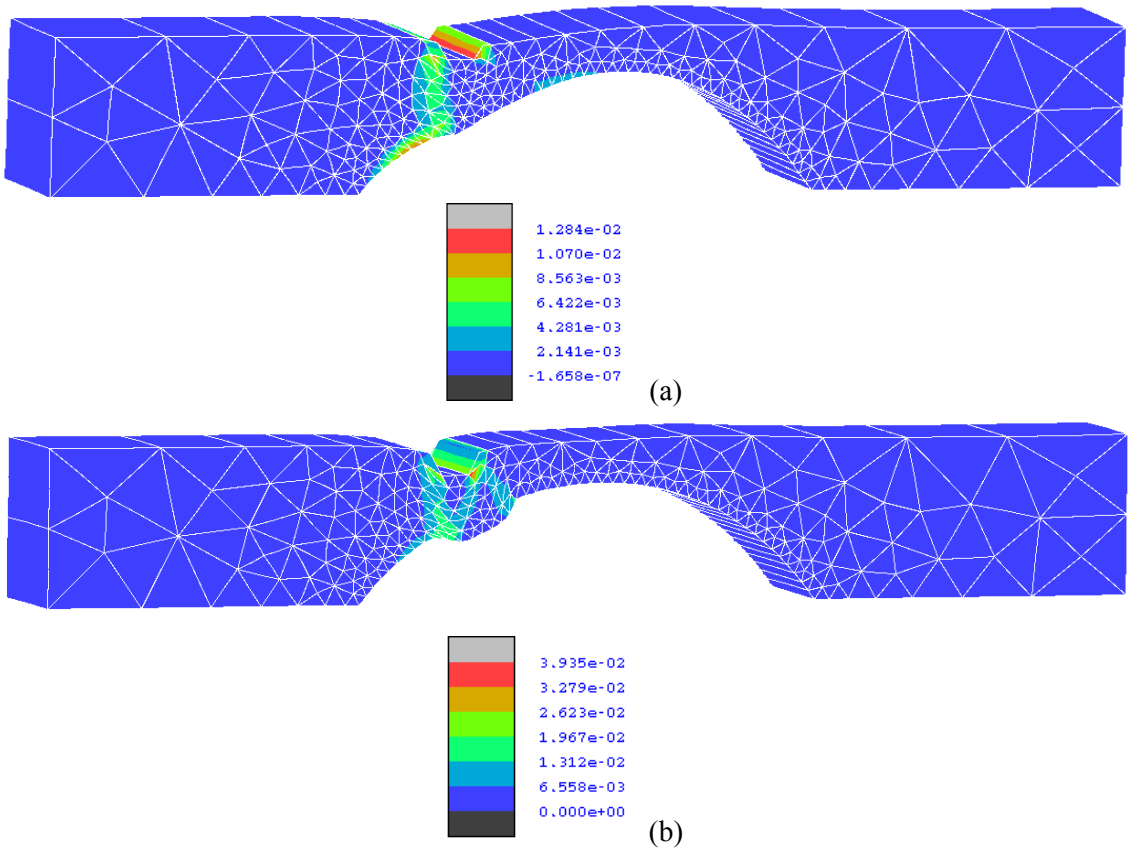

Figure 6-19: Equivalent von Mises plastic deformations for (a) limestone and (b) clay backfill

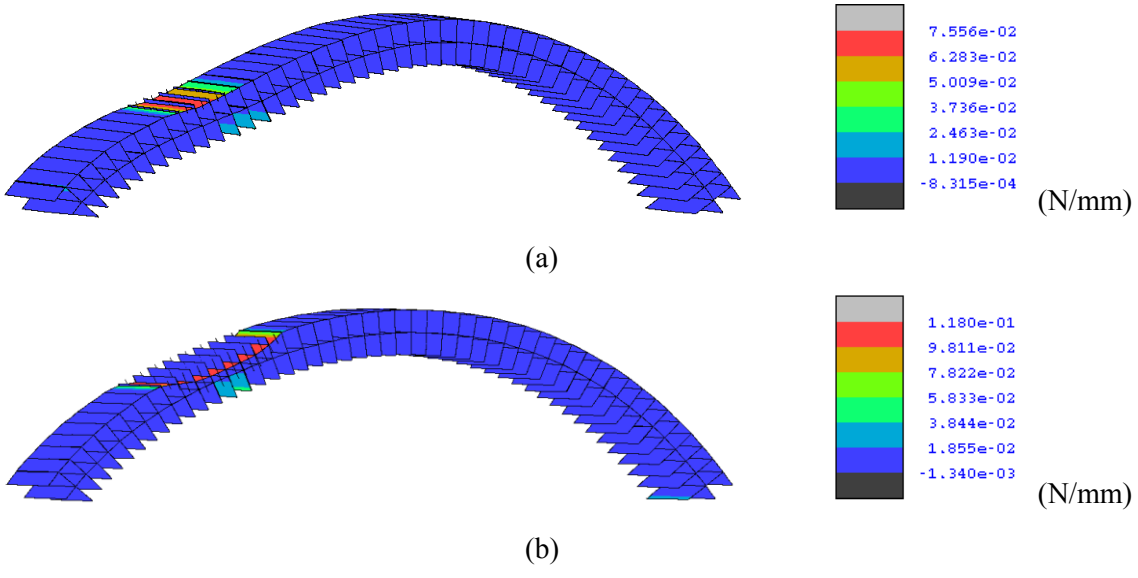

Figure 6-20: Plastic work W_{cr1} in the interface elements for (a) limestone and (b) clay backfill

6.2.3.2 Influence of brickwork defects

As in Chapter 5, the influence of defects in the brickwork has been analysed assuming a weak circumferential mortar joint to connect the two adjacent rings. The material properties for the nonlinear interface elements used to model the weak joints are reported in Table 5-2.

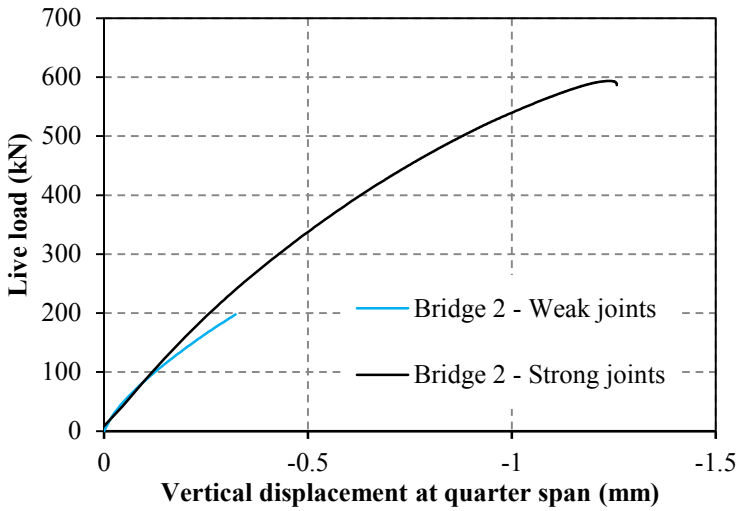

Figure 6-21: Influence of defects in the brickwork in the bridge response

Figure 6-21 compares the numerical load-displacement responses of the two models with strong and weak circumferential mortar joints, while Figure 6-22 shows the contours of plastic deformations in the backfill and the plastic work in the interface elements of the arch. As for masonry arches (see Section 5.2.2), defects in the brickwork lead to ring separation which starts at a very low loading level and develops from the left haunch up to the crown of the bridge. This strongly influences the load capacity of the bridge which is notably lower than the ultimate load for the bridge with no defects in the brickwork (strong joints).

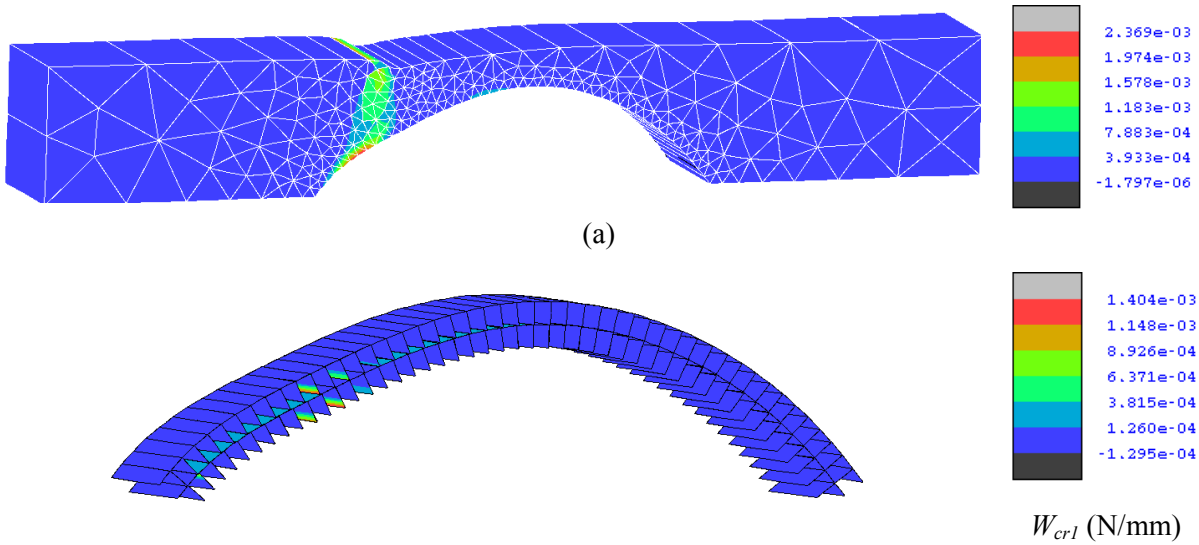

Figure 6-22: Contours at final step of the analysis for (a) equivalent von Mises plastic deformations in the backfill; (b) interface plastic work in the arch barrel for a masonry bridge with defects in the brickwork

6.2.3.3 Influence of loading position

In this section, the effects of the loading position on the structural behaviour of masonry arch bridges are analysed. The reference bridge (*Bridge 3-3*) has been investigated considering (i) a live load applied on the top surface of the backfill above the mid-span of the arch barrel (*Load 1*), (ii) a live load at the quarter span (*Load 2*) and (iii) a live load at one-eighth span (*Load 3*). Figure 6-23 displays the three FE meshes and the loading positions. Figure 6-24 shows the deformed shapes, while Figure 6-25 compares the load-displacement curves. In Figure 6-26 and 6-27, the contours of plastic deformations in the backfill and the plastic work contours in the interface elements of the arch barrel are presented.

In all the cases, radial cracks developed below the load and at the two springings. The analyses for *Load 1* and *Load 3* stopped because of convergence problems, thus the ultimate loads for these two cases should be considered as conservative predictions. The numerical curves confirm than the maximum load is reached when the load is applied at the one-eighth span. The responses of the other two cases are quite similar until the load level when the analysis for *Load 1* stopped.

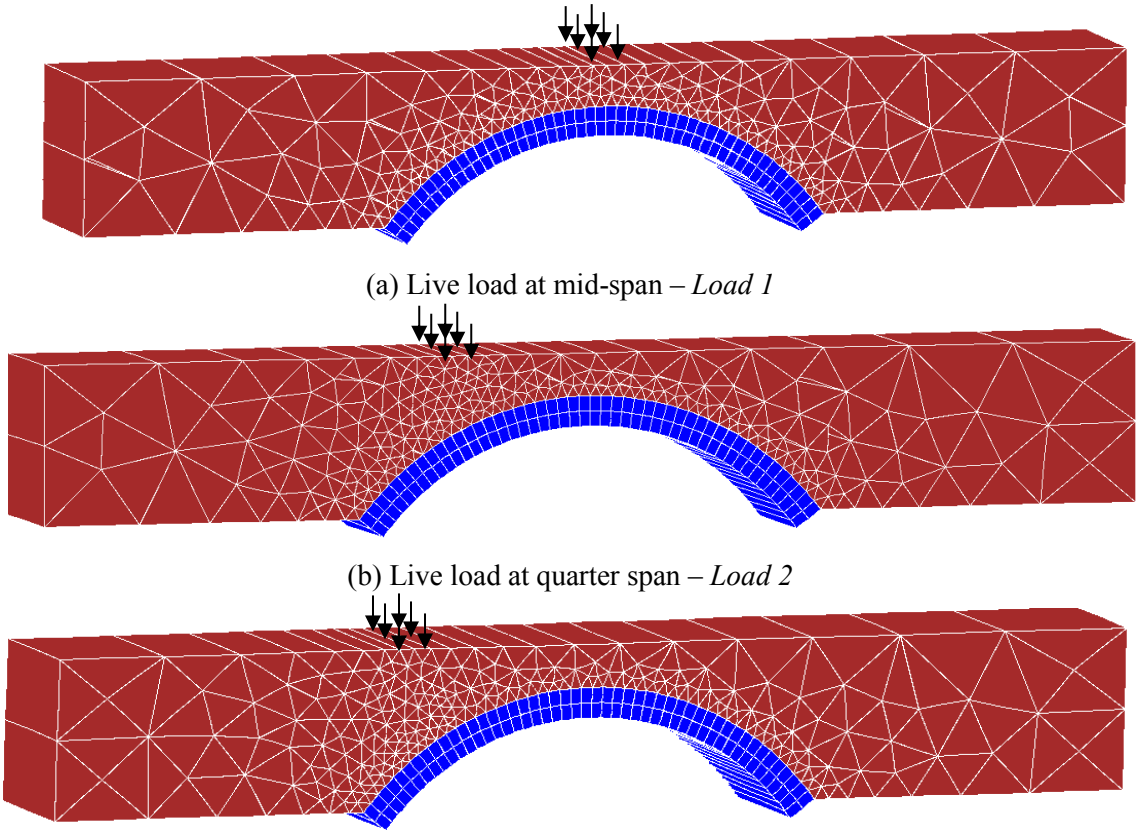

(a) Live load at mid-span – *Load 1*

(b) Live load at quarter span – *Load 2*

(c) Live load at 1/8 span – *Load 3*

Figure 6-23: FE meshes and Loading positions (a) *Load 1*, (b) *Load 2* and (c) *Load 3*

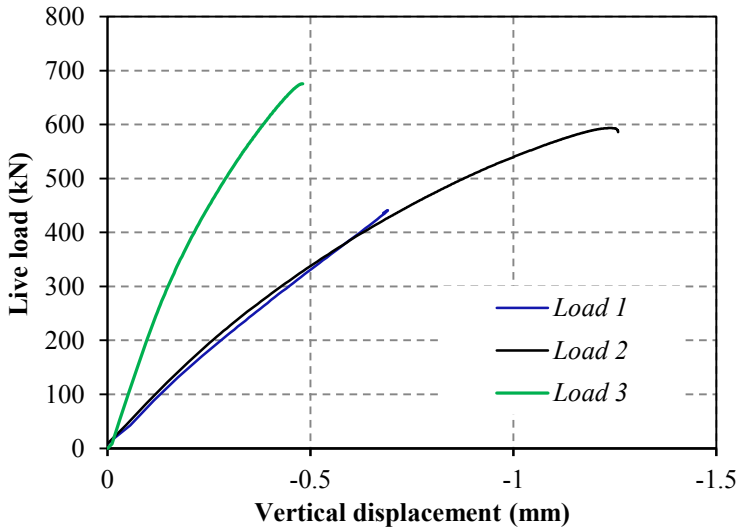

Figure 6-24: Load-displacement curves for different loading positions

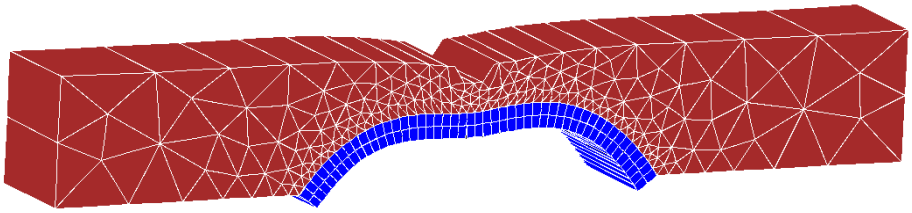

(a) *Load 1*

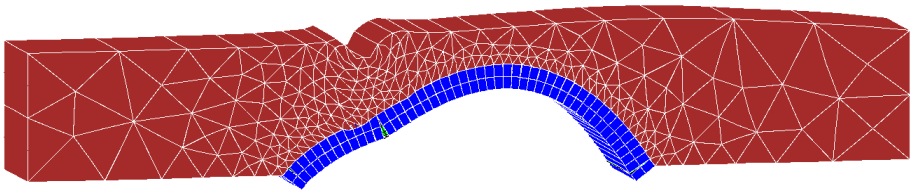

(b) *Load 2*

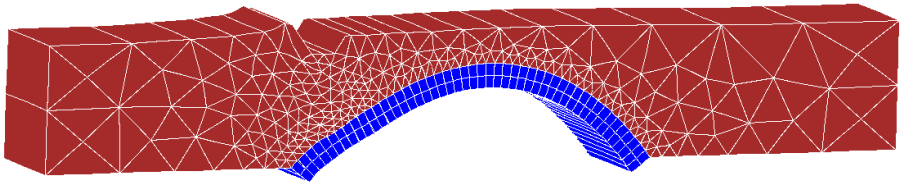

(c) *Load 3*

Figure 6-25: Deformed shapes for (a) *Load 1*, (b) *Load 2* and (c) *Load 3*

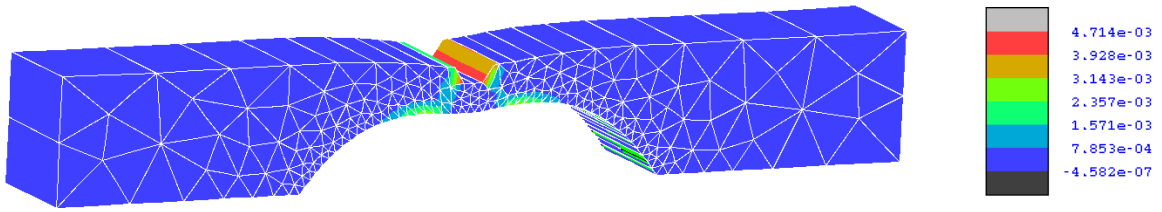

(a) *Load 1*

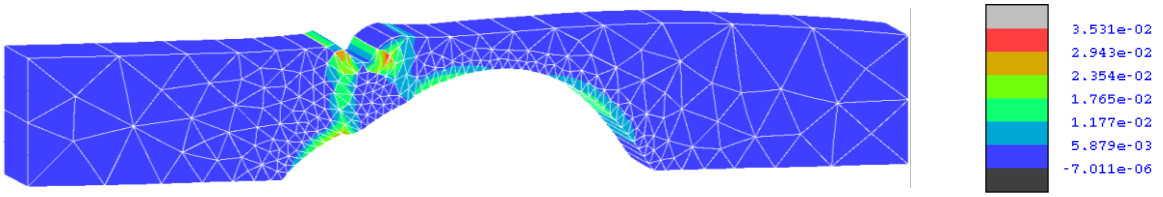

(b) *Load 2*

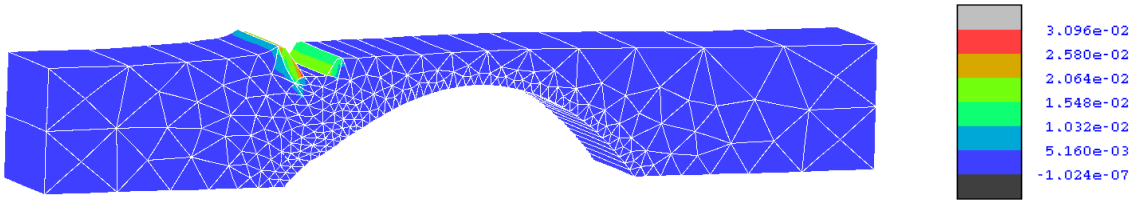

(c) *Load 3*

Figure 6-26: Plastic deformation in the backfill for (a) *Load 1*, (b) *Load 2* and (c) *Load 3*

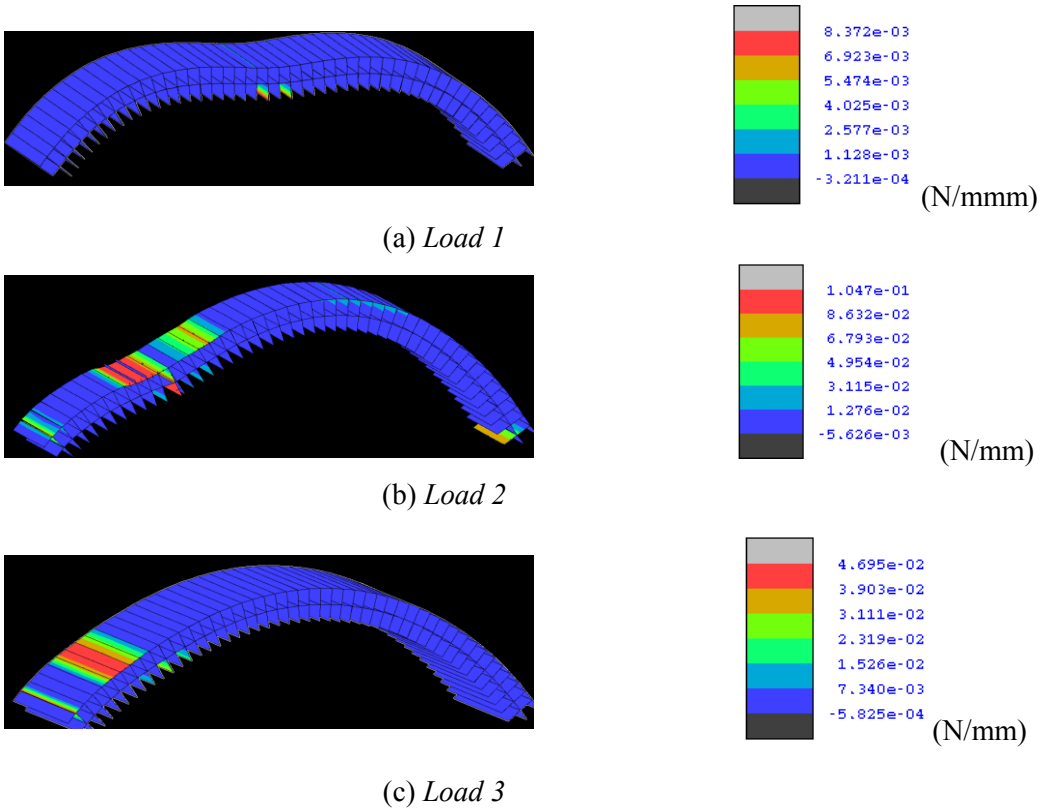

(a) *Load 1*

(b) *Load 2*

(c) *Load 3*

Figure 6-27: Interface plastic work W_{cr1} contour for (a) *Load 1*, (b) *Load 2* and (c) *Load 3*

6.2.3.4 Influence of rise-to-span ratio

Similar to the analyses on brick-masonry arches presented in Section 5.2.1, a numerical study has been conducted to analyse the response of segmental arch bridges characterised by the most common rise-to-span ratios as found in a number of existing masonry arch bridges (Brencich & Morbiducci, 2007). The main geometrical properties of the three analysed bridges are reported in Table 6-4, while the FE meshes for the three strip models are shown in Figure 6-28. In Figure 6-29 the load-displacement curves are compared, while the deformed shapes for the three bridges subject to a live load at quarter span are provided in Figure 6-30.

Table 6-4: Principal geometry for bridges with different rise-to-span ratio

	Height	Backfill depth at the crown	Rise	Ring thickness	Rise-to-span ratio
Bridge 1	1885	170	1500	215	1:2
Bridge 2	1135	170	750	215	1:4
Bridge 3	685	170	300	215	1:10

Note: all the dimensions are in mm

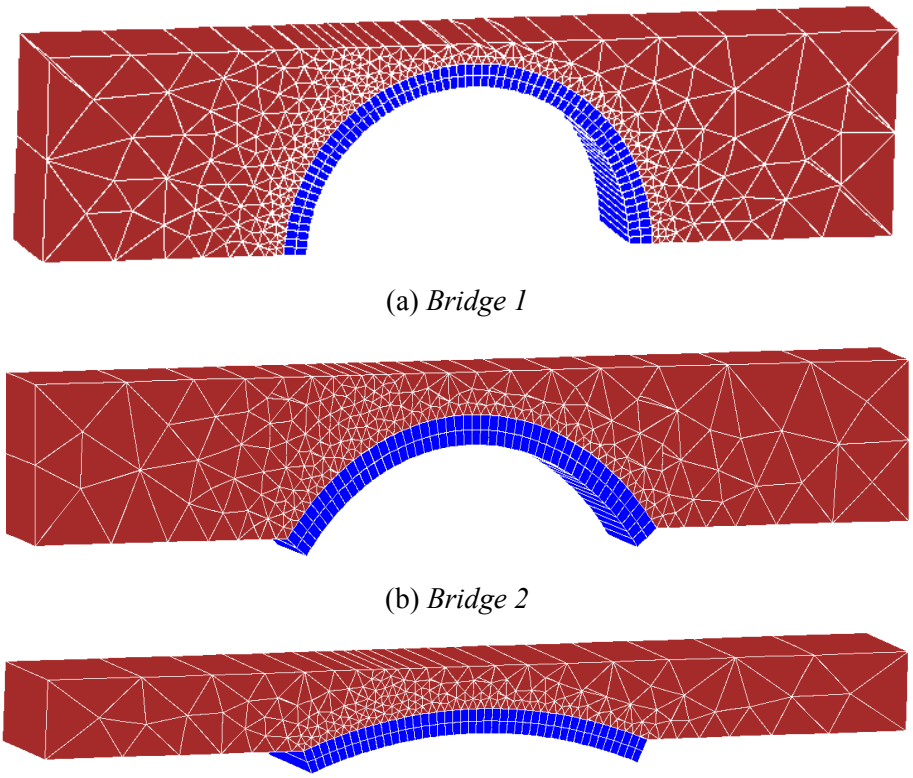

(a) *Bridge 1*

(b) *Bridge 2*

(c) *Bridge 3*

Figure 6-28: FE meshes for (a) *Bridge 1*, (b) *Bridge 2* and (c) *Bridge 3*

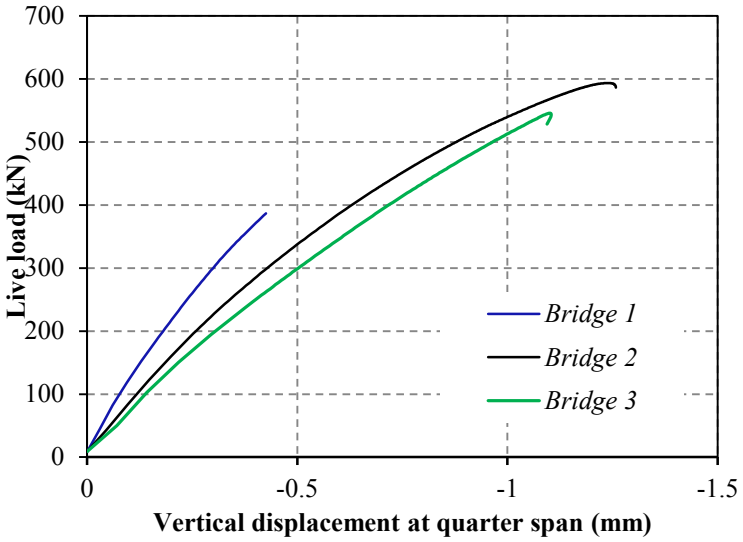

Figure 6-29: Load displacement curves for bridges with different rise-to-span ratios

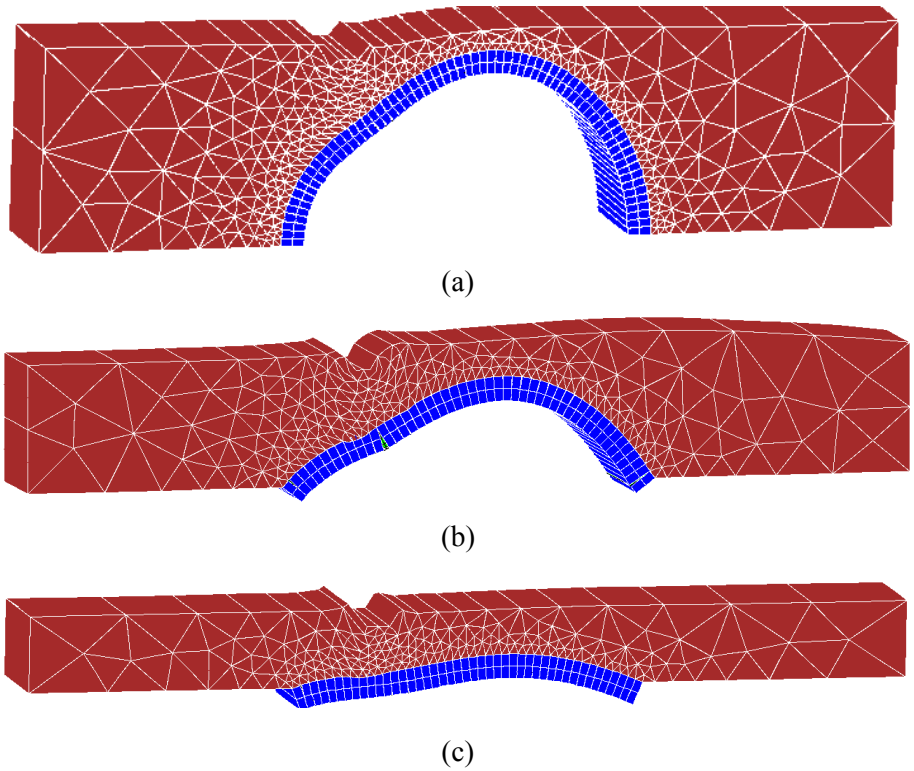

Figure 6-30: Deformed shape for (a) *Bridge 1*, (b) *Bridge 2* and (c) *Bridge 3*

Comparing the three responses (Figure 6-29) it can be seen that the bridge with a deep arch (*Bridge 1*) is characterised by the stiffest behaviour, while *Bridge 2* shows the highest

capacity. However the simulation for *Bridge 1* stopped because of convergence problems thus in this case, the maximum load is a conservative prediction. Concerning the backfill, plastic deformations (Figure 6-31) formed below the load and at the interface between the arch and the fill (Figure 6-32). These were mostly concentrated around the left haunch of the arch for *Bridge 1* and *Bridge 3*, while in the case of *Bridge 2* plastic deformations developed also above the three quarter span of the arch. Mainly radial cracks formed in the mortar bed joints below the load in *Bridge 1*; four main radial cracks transformed the arch of *Bridge 2* into a mechanism with significant plastic sliding and separation at the arch-fill interface. Finally radial cracks combined with ring separation at the left haunch characterised the nonlinear behaviour of *Bridge 3*.

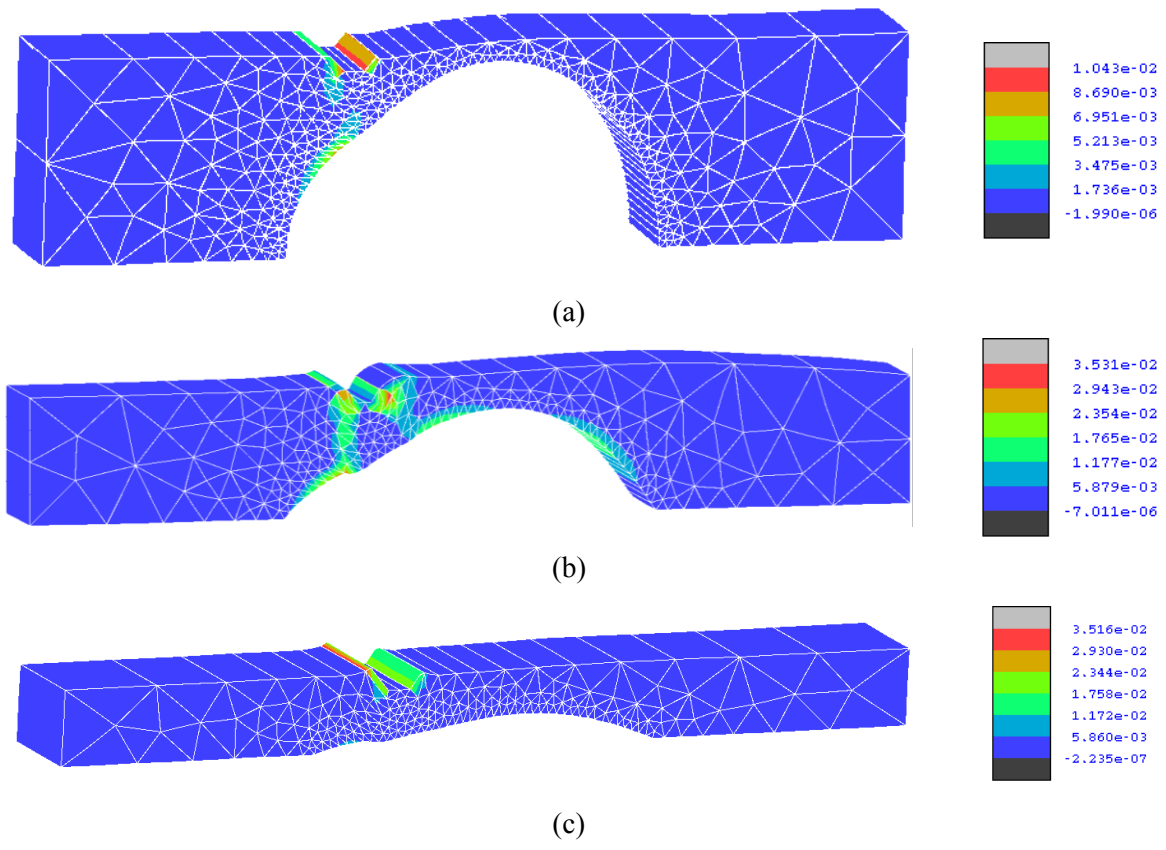

Figure 6-31: Plastic deformations contour of backfill for (a) *Bridge 1*, (b) *Bridge 2* and (c) *Bridge 3*

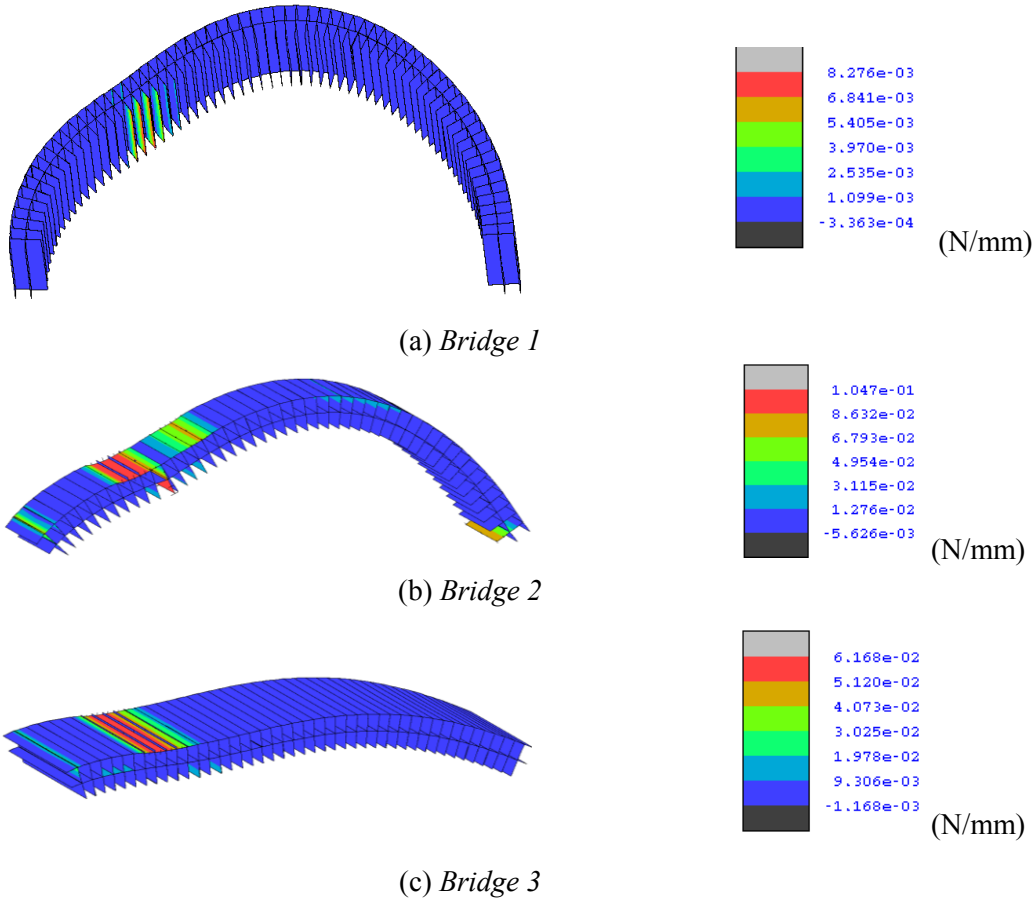

(a) *Bridge 1*

(b) *Bridge 2*

(c) *Bridge 3*

Figure 6-32: Plastic work W_{cr1} contour in the interface elements for (a) *Bridge 1*, (b) *Bridge 2* and (c) *Bridge 3*

6.2.3.5 Influence of abutment movements

In this section the effects of movements at the abutments are investigated. As pointed out by Melbourne et al. (2006), differential displacements at the abutments and the piers resulting from the instability of the foundations is one of the most common causes of deterioration for masonry arch bridges.

Three different displacement modes have been considered. These include vertical downward uniform displacements, horizontal inward and horizontal outward movements. In the numerical simulations, all the nodes of the left arch springing and at the base of the backfill extending from the arch to the left have been subject to prescribed displacements, which have been increased up to collapse. Reaction forces obtained from the left abutment bottom surface

and the arch left end surface are plotted against the support movement in Figure 6-33. The three failure modes are depicted in Figure 6-34, where Figure 6-35 shows the imposed displacement at the left abutment against the reaction forces. As in the case of masonry arches, the formation of a mechanism is associated with a softening branch. However in this case the contribution of the backfill mitigates the force reduction, especially in the case of vertical settlement.

Figure 6-36 displays the contours of plastic deformations in the backfill and Figure 6-37 the plastic work in the interface elements of the arch. It can be seen that by increasing the vertical displacement at the left abutment, two main radial cracks form in the arch barrel at about the quarter and the three quarter span. In this case, the plastic deformations in the fill form at the arch-fill interface from the crack at the quarter span to the crown of the arch and extend to the top of the backfill domain. The failure mode under horizontal inward displacements is characterised by three main radial cracks at the two springings and at the crown. Also in this case plastic deformations in the backfill develop above the cracks up to the top of the backfill. Finally when the bridge is subjected to horizontal inward displacement at the left abutment, a local failure occurs at the left springing with cracks also in the masonry bed joints at the opposite haunch and plastic deformations in the backfill at the left springing and at the arch-fill interface at about the three quarter span.

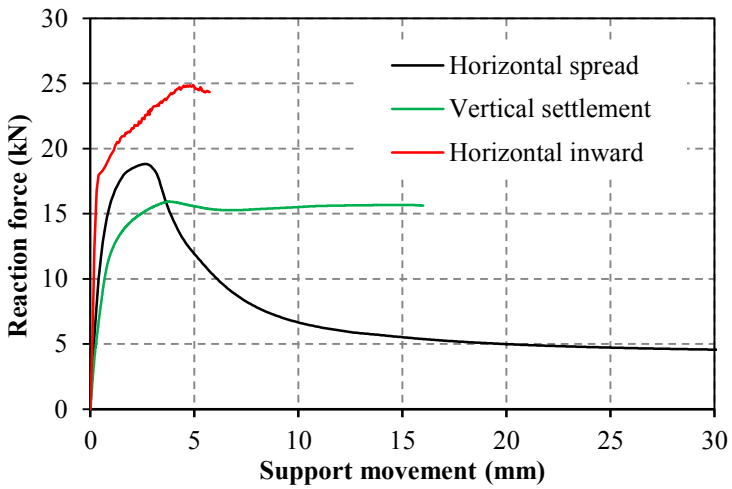

Figure 6-33: Numerical results for *Bridge 3-3* subjected to different support movement

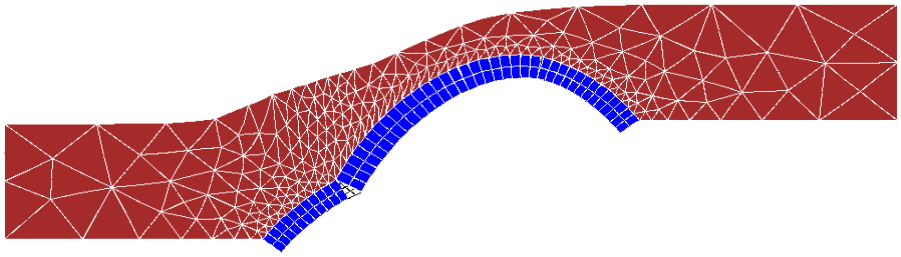

(a) Vertical differential settlement of support

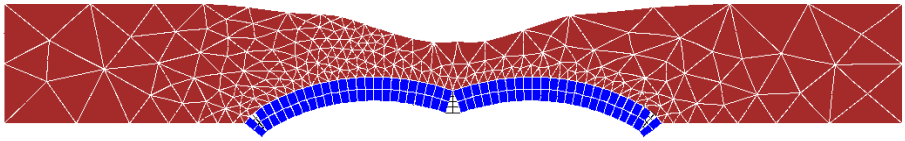

(b) Horizontal spread of support

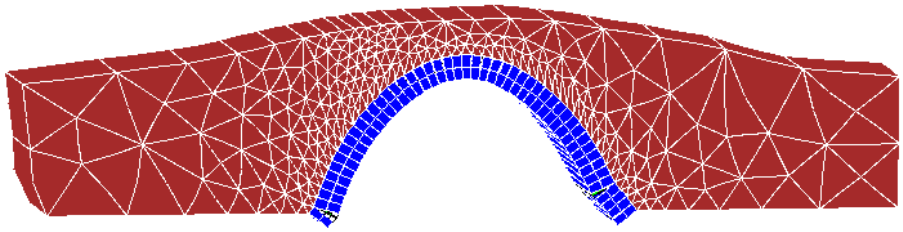

(c) Horinzontal inward displacement at the abutment

Figure 6-34: Deformed shapes for *Bridge 3-3* subject to different abutment displacements

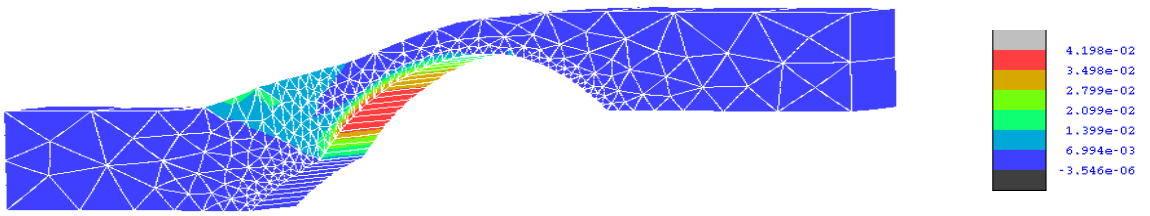

(a) Vertical settlement of support

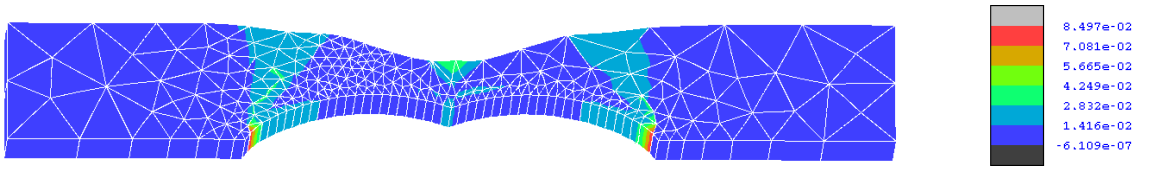

(b) Horizontal spread of support

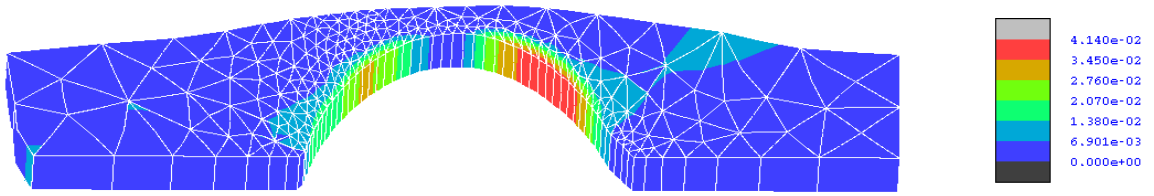

(c) Horizontal inward of support

Figure 6-35: Equivalent von Mises plastic deformations in the backfill for *Bridge 3-3* subject to different abutment displacements

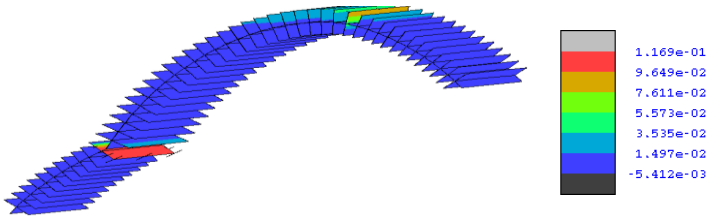

(a) Vertical differential settlement of support

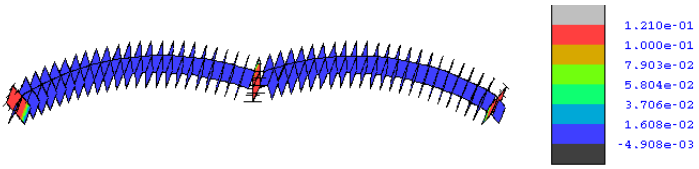

(b) Horizontal spread of support

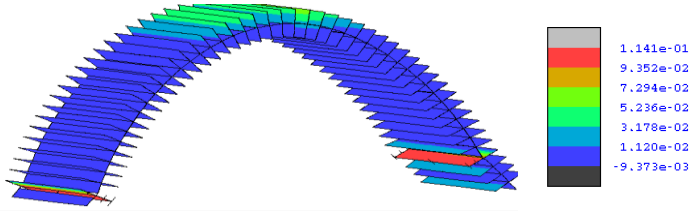

(c) Horizontal inward movement at the abutment

Figure 6-36: Plastic work W_{cr1} contour in the interface elements in the backfill for *Bridge 3-3* subject to different abutment displacements

6.2.4 Full 3D model analysis

Numerical simulations have been carried out considering a full 3D representation of *Bridge 3-3* subject to a line load uniformly distributed on the top of the backfill along the width of the bridge.

6.2.4.1 Model description

Thanks to the symmetry of the bridge response about the vertical plane at the longitudinal axis of the bridge, a FE mesh representing only half bridge has been considered (Figure 6-37). As opposed to the strip-model, five set of solid elements along the width of the arch have been utilised allowing the representation of the transverse behaviour of the bridges and a more realistic description of the contribution of the lateral walls. According to the proposed modelling strategy for masonry arch bridges (see Section 3.4) the lateral wall is modelled with 15-noded solid elements as an extension of the backfill domain. Thus in the FE mesh (Figure 6-37), one longitudinal strips of solid elements represents the lateral wall, the remaining four the backfill. The dimension of the solid elements for the lateral wall along z corresponds to the actual thickness of the wall equal to 330mm, while the same dimension for the solid elements of the backfill is 277.5mm.

Fixed supports have been assumed at the abutments (bottom of the fill domain on the left and the right of the arch), while the transverse displacements (along *z* in Figure 6-37) at the nodes on the vertical plane at the bridge longitudinal axis have been restrained to allow for symmetry condition.

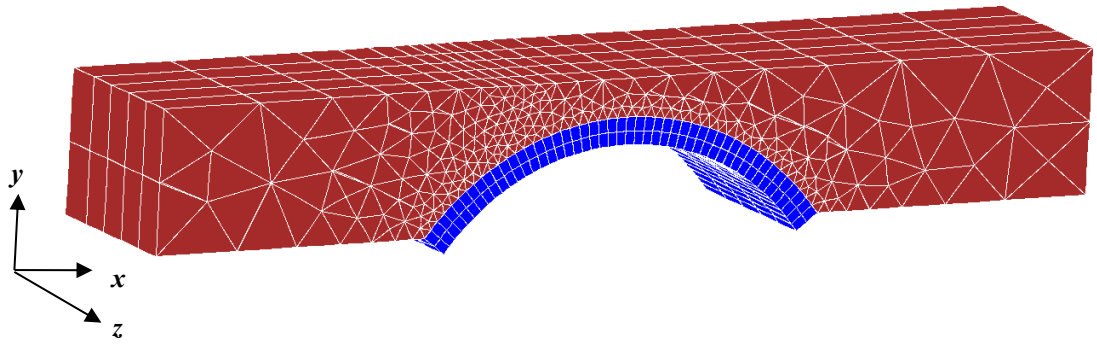

Figure 6-37: 3D FE mesh for *Bridge 3-3*

The same material properties for masonry and the backfill adopted in the strip-model (Section 6.2.2) have been adopted, while for the masonry spandrel wall, the elastic properties in Table 6-5 have been considered.

Table 6-5: Elastic properties for spandrel walls

Elastic modulus E_w (N/mm^2)	Poisson's ratio v_w	Unit weight ρ_w (kN/m^3)
16000	0.15	22.7

The 3D model comprises 480 20-noded solid elements and 1948 16-noded nonlinear interface elements for the arch, 2035 15-noded solid elements for the backfill and the lateral walls, and 240 interface elements at the boundary between the arch and the fill. This corresponds to 77,493 degrees of freedom which makes the nonlinear analysis of the bridge impractical when using conventional computational resources with a serial code.

Thus to improve computational efficiency, the partitioning scheme illustrated in Figure 6-38 has been considered. This has been generated using *Caim*, a semi-automatic mesher developed at Imperial College (Rodriguez-Villares, 2014) and includes 11 child partitions for the backfill and the lateral wall and 120 partitions for the arch, where the parent structure collects the 2747 nodes at the interface between the arch and the backfill.

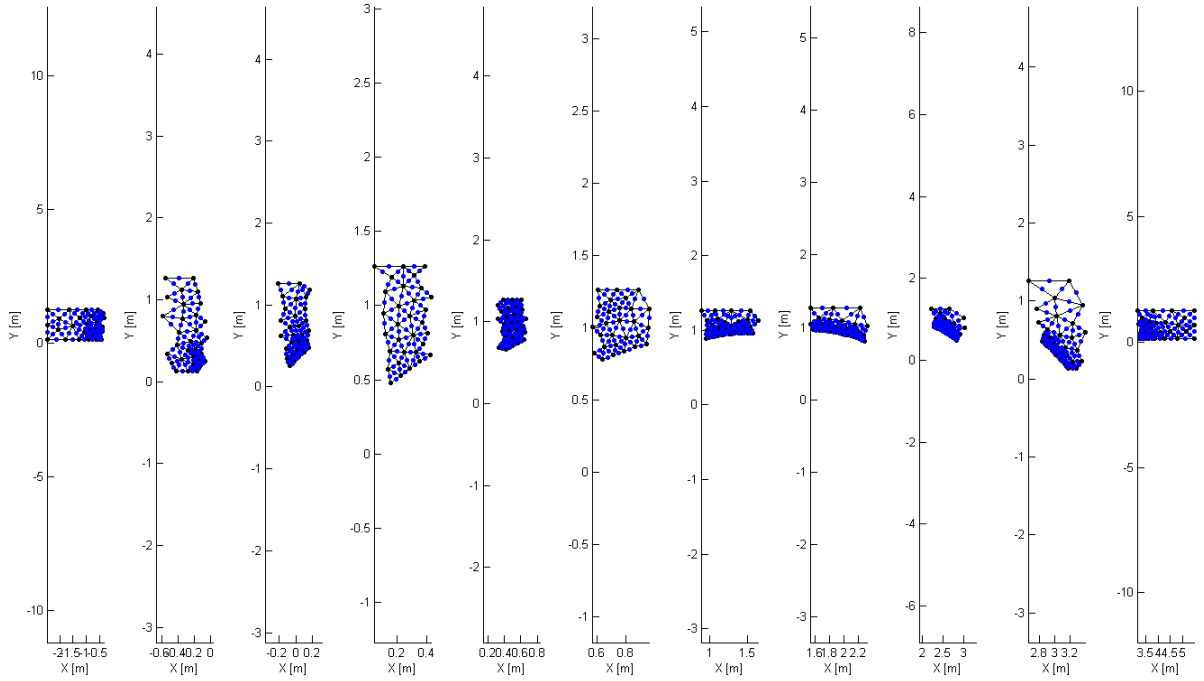

(a)

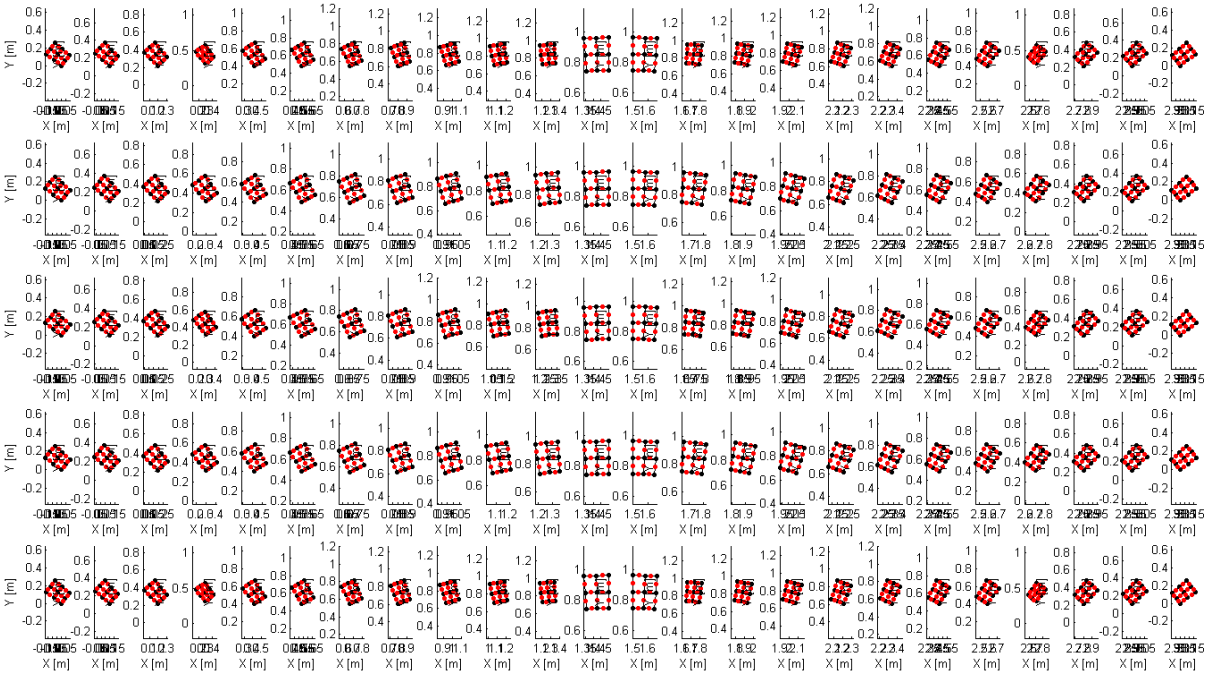

(b)

Figure 6-38: Partitioning strategy for (a) backfill and (b) arch barrel

6.2.4.2 Numerical results

Nonlinear analyses have been performed utilising the 3D description for *Bridge 3-3* described before. The numerical simulations have been carried out using 48 2.66 GHz Intel Xeon Processors X5650 cores. A wall-clock time limit of 60 hours has been assigned to each analysis. This has not allowed the prediction of the bridge failure, as most of the analyses stopped at a load of about 110kN because of the time constraint. However comparisons between the results obtained by the strip-model and those determined by the full 3D model enabled the investigation of the transverse behaviour of the bridge and the influence of the lateral walls on the bridge response.

Figure 6-39 shows the deformed shape at the last step of the nonlinear analysis, while Figure 6-40 compares the strip-model prediction against the load-displacement curve achieved by using the full 3D description. The latter curve shows higher stiffness which is mainly associated with the longitudinal stiffening contribution of the lateral walls.

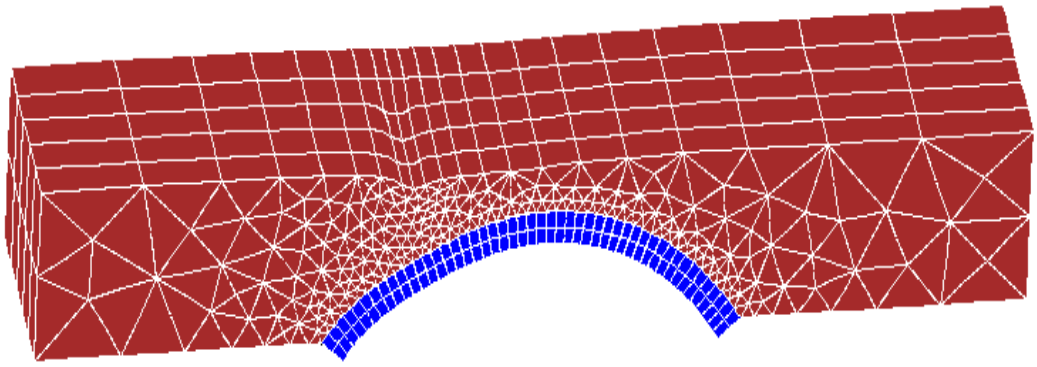

Figure 6-39: Deformed shape at last step of analysis

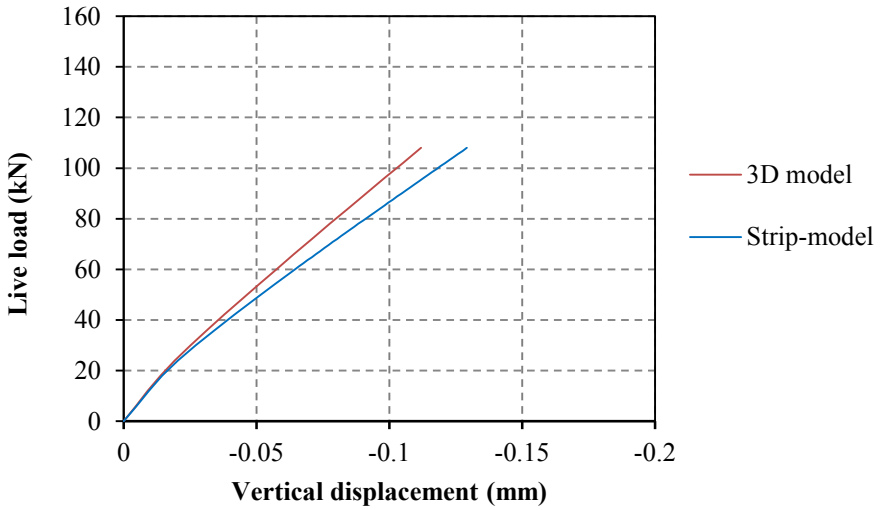

Figure 6-40: Load-displacement curves at quarter spans

The displacements at the quarter span along the arch width at different loading levels are displayed in Figure 6-41, where also the strip model predictions are shown. It can be seen that by increasing the load the displacement distribution becomes less uniform. This is due to the development of plastic deformations in the backfill (Figure 6-42). Thus, the displacements close to the spandrel walls are notably lower than those at the mid-width of the arch which are well approximated by the strip-model.

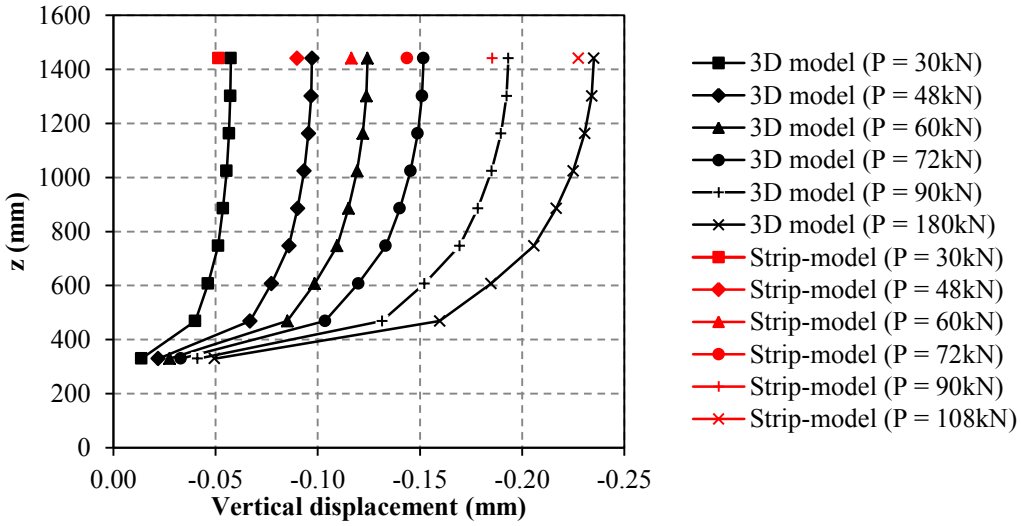

Figure 6-41: Displacement along the arch width at different loading levels for the 3D model of *Bridge 3-3*

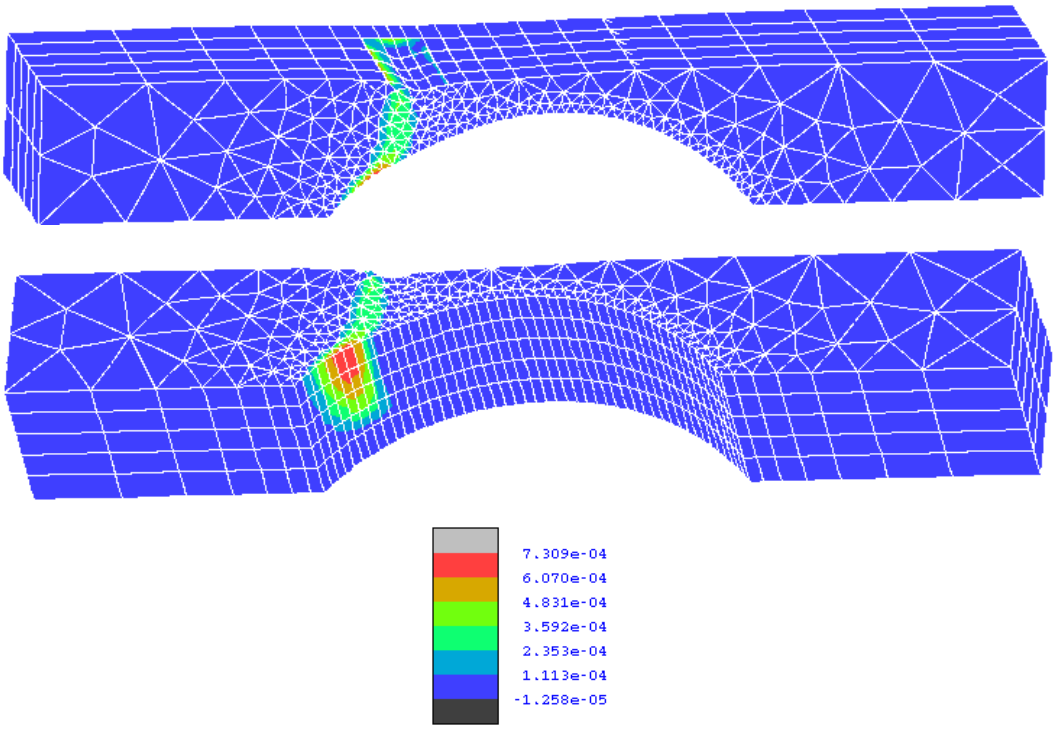

Figure 6-42: Equivalent von Mises plastic deformations of backfill at last step of analysis for the 3D model of *Bridge 3-3*

The plastic deformations in the backfill are not uniform (Figure 6-42) because of the transverse effects and the interaction with the lateral wall. The maximum values are located close to the arch mid-width. The transverse effects give rise also to notable normal stresses in the arch (Figure 6-43) along the transverse direction. At higher loading level these may induce the development of longitudinal cracks in the arch barrel.

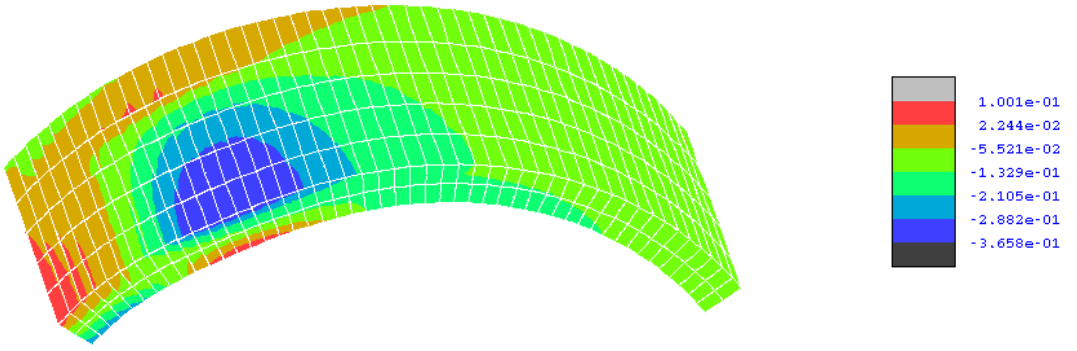

(a) Longitudinal stress σ_{xx}

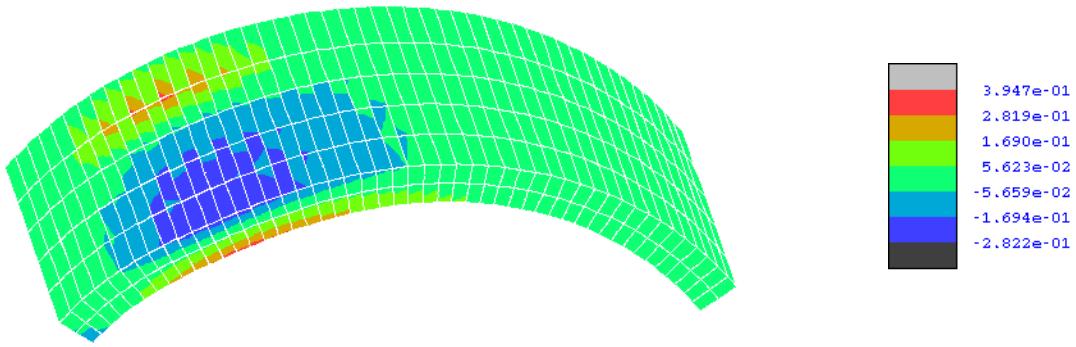

(c) Transverse stress σ_{zz}

Figure 6-43: Stress contour for the masonry arch barrel of the 3D model of *Bridge 3-3*

The influence of the lateral wall characteristics on the arch response has been analysed comparing the numerical results obtained adopting different Young's modulus values for the lateral wall. Three different values of the elastic modulus E_s = 5000N/mm^2, 10000N/mm^2, and 16000N/mm^2 have been considered. These three values represent different types of brickwork, in which 16000N/mm^2 is a reference value reported in the literature for masonry structures made of new brickwork (Wang, 2004), while 5000N/mm^2 is suggested for historical brick-masonry.

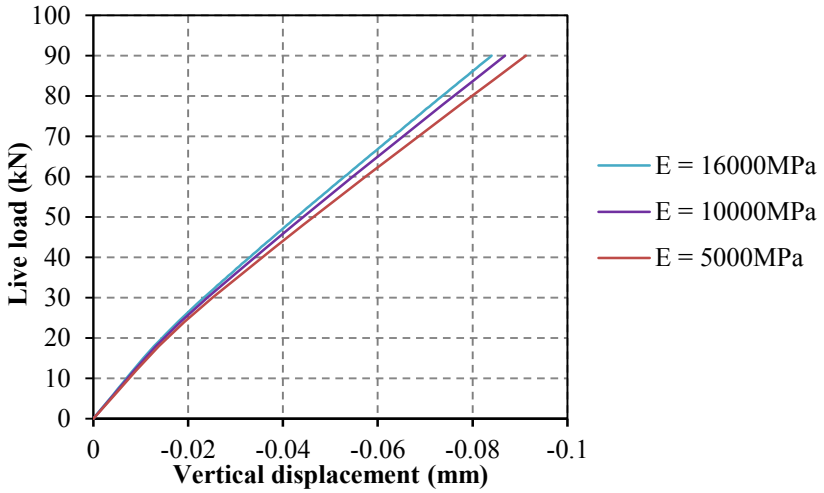

Figure 6-44: Load displacement curves for 3D model with different spandrel walls

Figure 6-44 shows the responses for the vertical displacement at mid-width quarter span of the arch barrel against the applied load. It can be noticed that, in this specific case, the initial stiffness of the bridge along the longitudinal direction is only marginally influenced by the spandrel wall elastic properties. The same can be seen for the evolution of the transverse displacements shown in Figure 6-45, where the displacements across the arch width are only slightly affected by the lateral wall stiffness. On the other hand, the maximum values of plastic deformations in the backfill (Figure 6-46) and the normal stresses along the longitudinal (Figure 6-48) and the transversal direction (Figure 6-49) in the arch barrel (Figure 6-47) and in the lateral walls seem to be more dependent on the lateral wall stiffness, where the model with highest Young's modulus for the lateral wall shows highest plastic deformation and stress values.

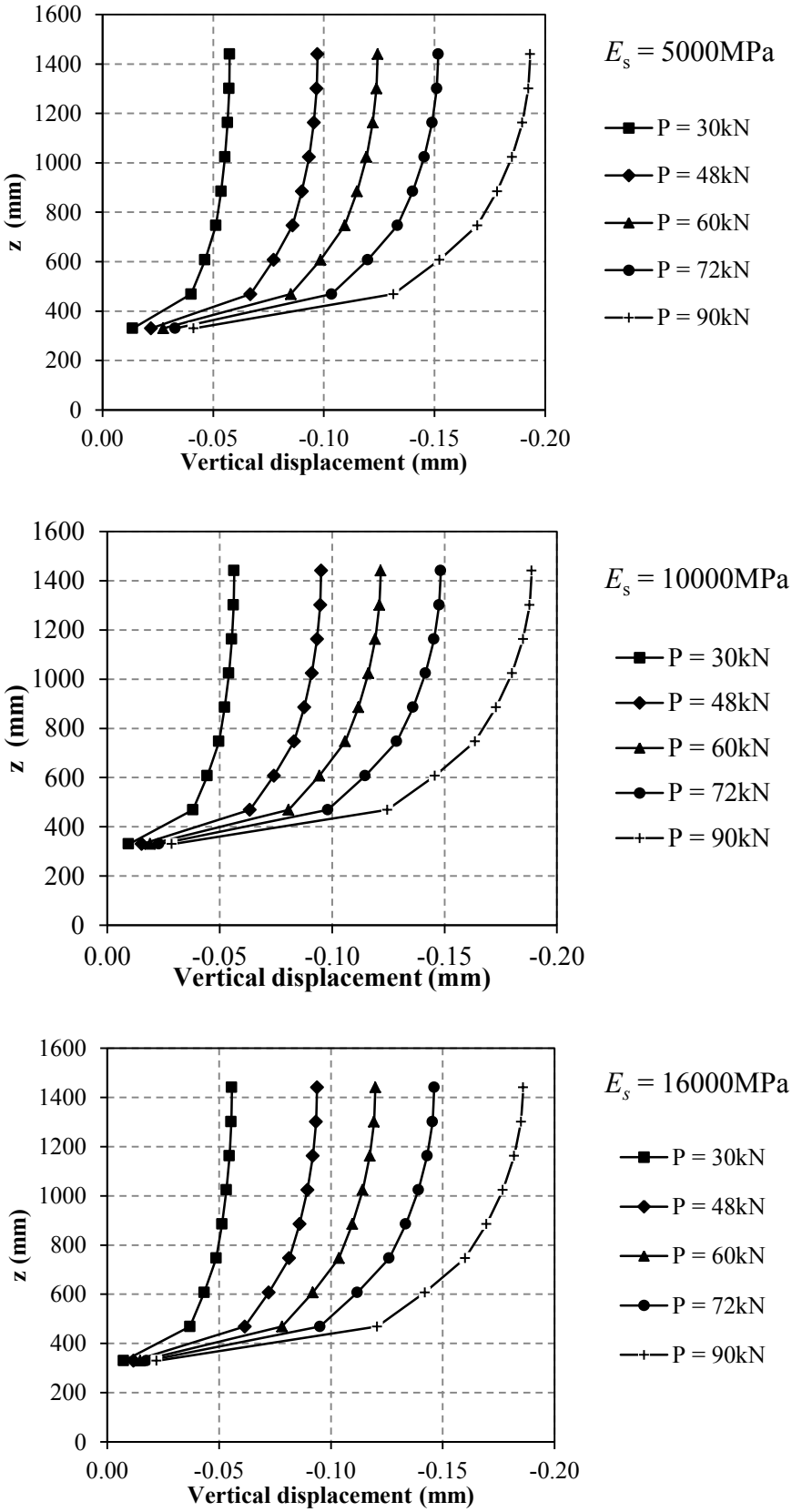

Figure 6-45: Vertical displacements across the width for bridges with different spandrels

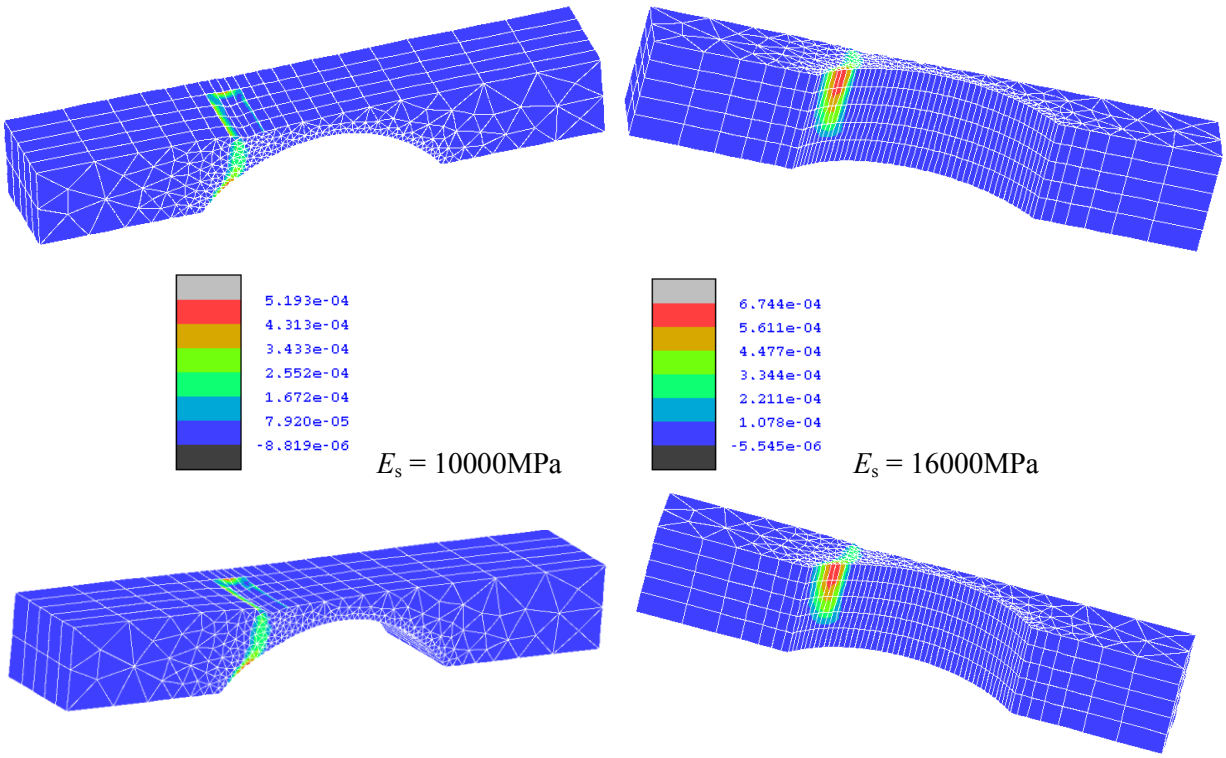

Figure 6-46: Equivalent von Mises plastic deformations in backfill for bridges with different spandrels

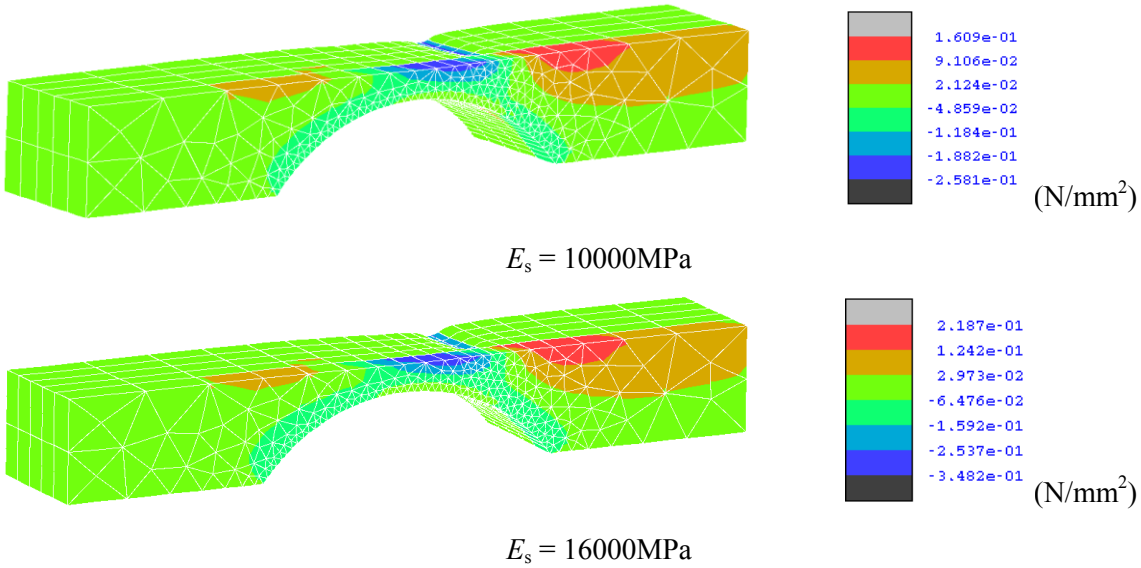

Figure 6-47: Spandrel wall longitudinal stress contour for bridges with different spandrels

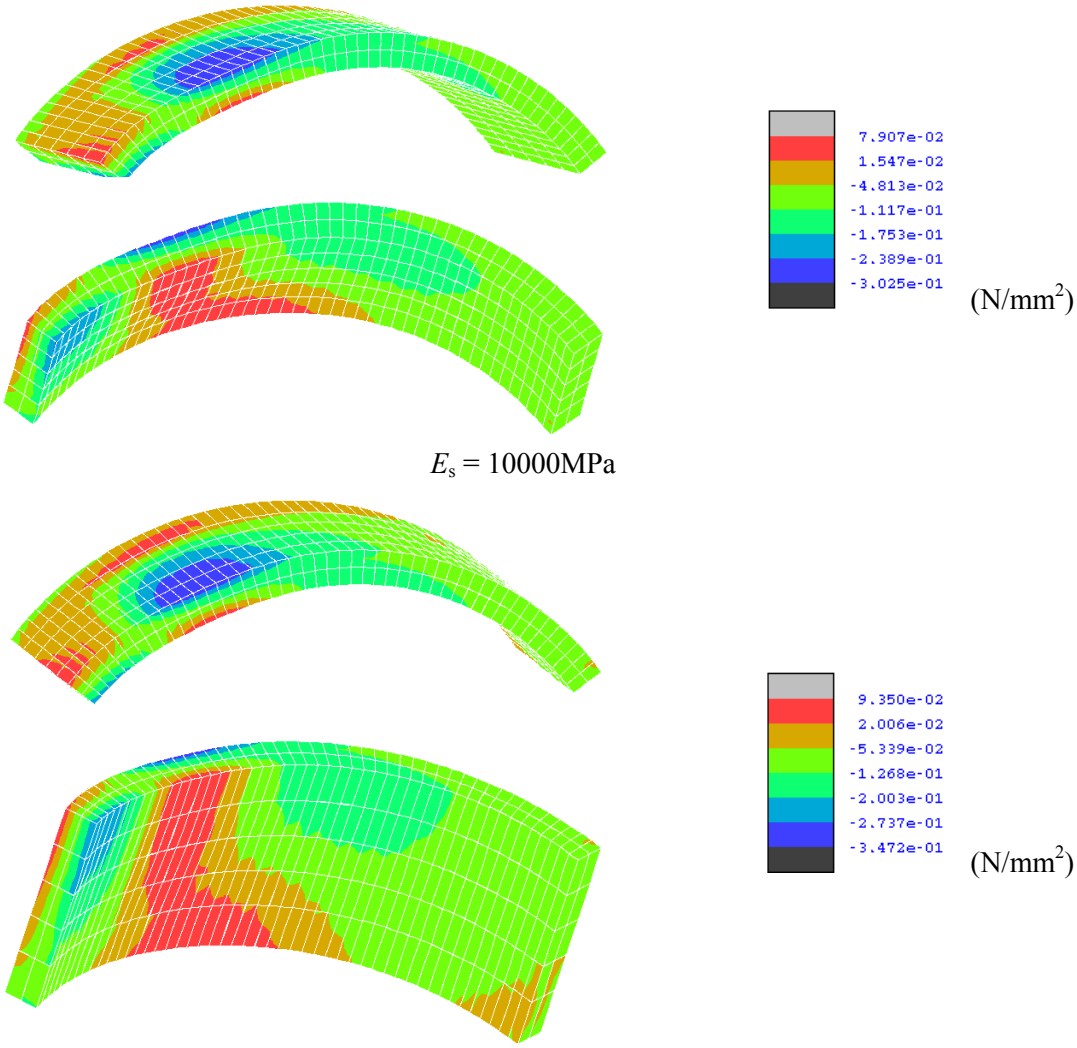

Figure 6-48: Arch longitudinal stress contour for bridges with different spandrels

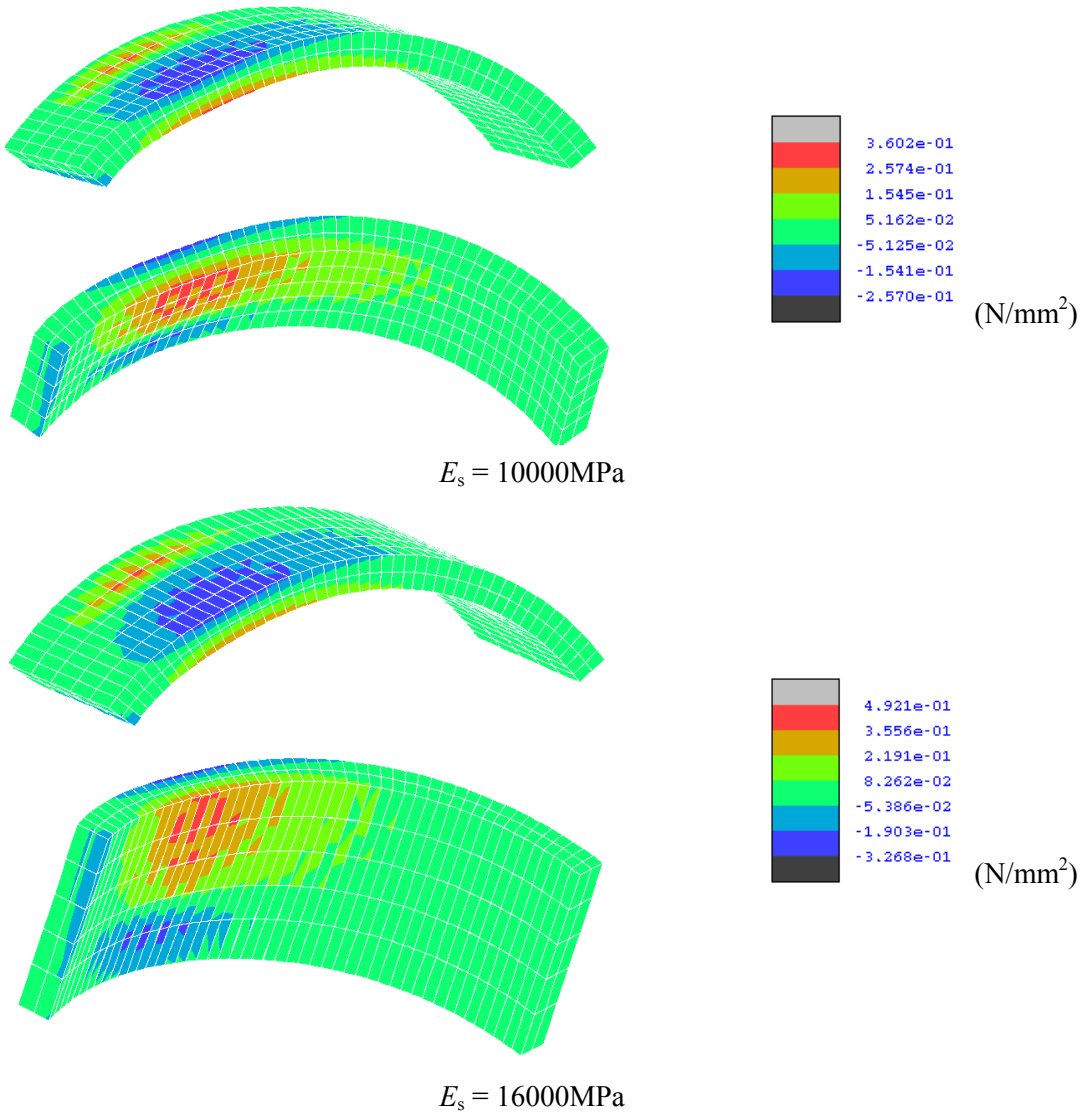

Figure 6-49: Arch transverse stress contour for bridges with different spandrels

6.3 Analysis of a large stone-masonry bridge

According to the proposed numerical strategy for masonry arch bridges, the detailed 3D FE model is incorporated within an advanced partitioning approach (Jokhio, 2012; Jokhio & Izzuddin, 2013) to improve computational efficiency. In this section, the computational performance provided by using different partitioning techniques for the analysis of a realistic stone-masonry bridge is investigated.

The analysed structure corresponds to the Bargower Bridge, a 10m single span stone-masonry arch bridge which was constructed in 1895 with a semi-circular profile. In 1986, the bridge was tested to collapse within the scope of a research program conducted by the Transport and Road Research Laboratory (Hendry et al., 1986a). The principal geometry of the bridge is reported in Table 6-6.

Table 6-6: Principal geometry for *Bargower* Bridge (Hendry et al., 1986a)

Arch	Span (mm)	Rise (mm)	Ring thickness (mm)	Width (mm)	Number of units
	10000	5000	558	8680	53
Backfill	Depth at the crown (mm)		Width (mm)		Length (mm)
	1200		8680		1000
Spandrel walls	Depth at the crown (mm)		Thickness (mm)		Length (mm)
	1200		1400		1000

6.3.1 Model description

As before, the mesoscale strategy for brick\block-masonry developed in (Macorini & Izzuddin, 2011) is considered for representing the stone-masonry arch taking into account the actual masonry bond on the face of the bridge. On the other hand, the backfill and the lateral walls are modelled using 15-noded solid elements. Thus the adopted FE mesh (Figure 6-50) consists of 53×6 solid elements, 52×6 interface elements for radial bed joints and 53×5 for circumferential mortar head joints and potential fracture planes in the stone blocks. Other 53×6 interface elements are used to represent the physical interface connecting the arch barrel to the backfill. Fixed supports are assumed at the two springings to account for the rigid abutments. Besides, the bottom surfaces of the backfill at each side of the arch barrel are also fixed.

Elastic analyses have been carried out applying a line load (total load P = 100kN) at the top of the backfill at the third span of the arch in 5 steps. The elastic material properties for the component materials used in the analyses are reported in Tables 6-7, 6-8 and 6-9.

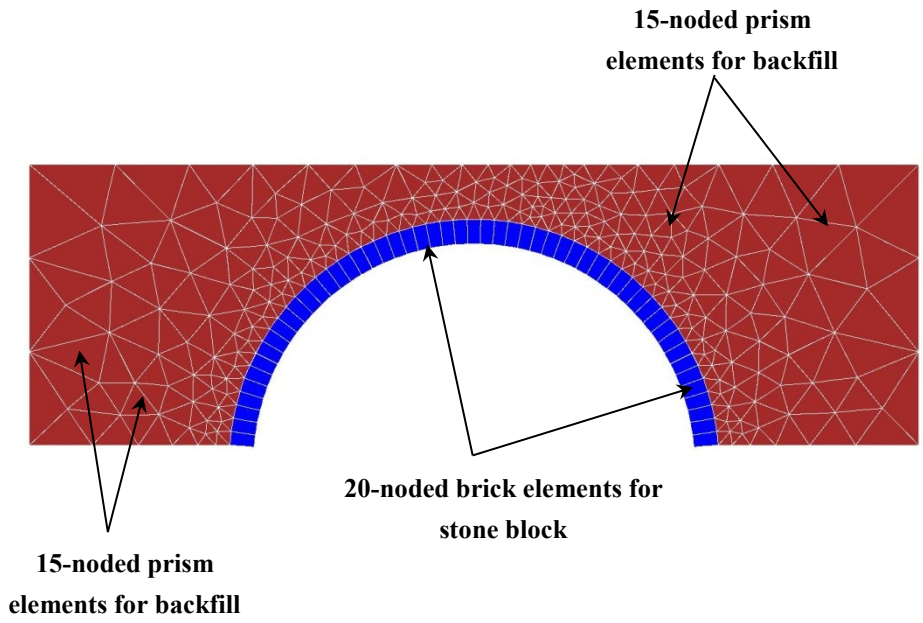

(a) Elevation view

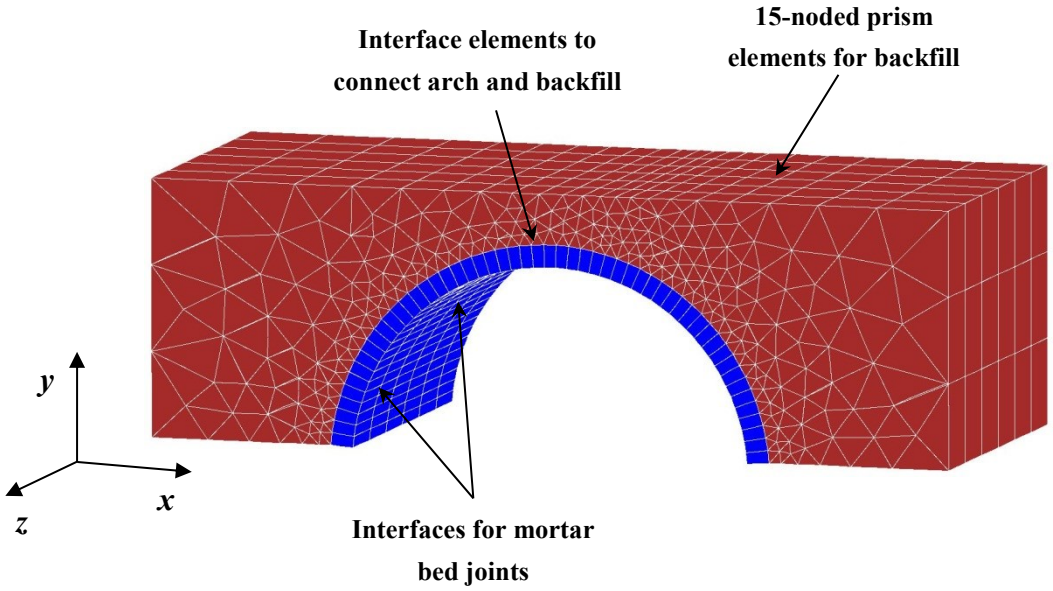

(b) 3D view

Figure 6-50: FE mesh for the *Bargower* Bridge (a) elevation and (b) 3D view

Table 6-7: Elastic properties of stone units for elastic analysis of *Bargower* Bridge

	Elastic modulus E (N/mm^2)	**Poisson's ratio v**
Stone block	1.41×10^4	0.15

Table 6-8: Elastic properties of mortar interface elements for elastic analysis of *Bargower* Bridge

	Normal stiffness K_n (N/mm^3)	**Tangent stiffness K_t (N/mm^3)**
Mortar interface	90	40
Stone-stone interface	1×10^5	1×10^5

Table 6-9: Elastic properties of backfill for elastic analysis of *Bargower* Bridge

Elastic modulus, E (N/mm^2)	**Poisson's ratio v**	**Unit weight (kN/mm^3)**
500	0.20	19.1

6.3.2 Computational efficiency and solution accuracy

As before, to improve computational efficiency the detailed model for the bridge has been implemented into the partitioning approach developed previously at Imperial College (Jokhio, 2012). The performance provided by using different partitioning techniques has been compared in terms of speed-up *S*. As discussed in Chapter 4, this is usually defined as the ratio between the wall-clock time required by a monolithic simulation and that needed by a partitioned model. However in this specific case, the monolithic model required an excessive memory allocation which did not allow a numerical simulation using a serial code. Thus a model with only two partitions has been assumed as the reference model for calculating *S*. In this "basic" partitioned model, one partition represents the backfill and the other the masonry

arch. The parent structure corresponds to the set of nodes at the partition boundaries between the two domains.

The characteristics of the different partitioned models are reported in Table 6-10. These include models with flat partitions, hierarchic partitions and partitions with master-slave coupling at the partitioned boundary. For each model, the table presents the number of partitions along the longitudinal (x) and transverse (z) directions, the partition level (e.g. 1 for flat partitioning, > 1 for hierarchic partitioning) and the number of processors employed in the numerical simulations. Also the analyses considered in this section were performed using 2.66 GHz Intel Xeon Processors X5650 cores. Again, each partitioned model is named as P-*n-flat/hier/mslc/hiermslc*, where *n* stands for the number of child partitions, *flat* for single level partitioning method, *hier* means multi-level hierarchic paritioning, *mslc* means single level partitioning with multi-dimensional master-slave coupling at partition boundary and *hiermslc* multi-level hierarchic paritioning with master-slave coupling.

All the FE meshes have been generated using *Caim* (Rodriguez-Villares, 2014). Figure 6-51 illustrates the elevation of the subdivision in super-elements at the lowest hierarchical level for some of the analysed models.

Table 6-10: Characteristics of partitioned models and speed-up values

	Arch partition *z* *x*	Backfill partition	No. Arch levels	No. Backfill levels	No. Processors	S
P-2-flat	1	1	1	1	4	-
P-2-mslc			1	1	4	1.47
P-8-flat	01×02	03×02	1	1	12	1.26
P-8-mslc			1	1	12	1.89
P-30-flat	01×03	09×03	1	1	34	1.11
P-30-mslc			1	1	34	1.63
P-30-hier			1	2	37	1.12
P-30-hiermslc			**1**	**2**	**37**	**2.22**
P-60-hier	01×06	18×03	2	3	48	0.69
P-60-hiermslc			2	3	48	1.95
P-141-hier	01×06	45×03	2	3	48	0.49
P-141-hiermslc			2	3	48	1.28
P-188-hier	53×01	45×03	1	3	48	0.35
P-188-hiermslc			1	3	48	0.82

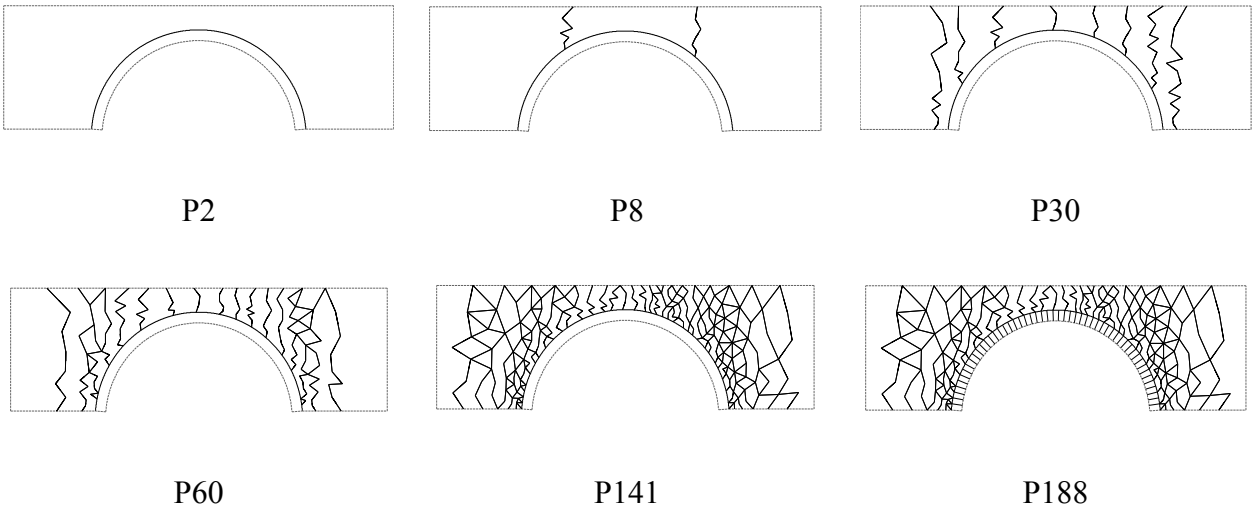

Figure 6-51: Child structures at lowest hierarchical level used for the different partitioned models of *Bargower* Bridge

Table 6-10 reports also the *S* values for the different models, where the wall-clock time for the "basic" partitioned model is t_{sm} = 6,793s, while the fastest execution took t_{P030} = 3,066s. This is associated with the model *P-30-hiermslc* which utilises master-slave coupling at the partition boundaries. Similar results have been obtained in the mesoscale partitioned analysis of masonry arches (see Section 4.4.2). However the use of hard (e.g. master slave) coupling leads to some errors in the solution as shown in Figure 6-52, where the normal stresses in the masonry bridge modelled using alternative partitioning techniques are compared. It can be seen that the models employing master slave coupling predict higher local stresses which is due by the use of rigid internal constraints.

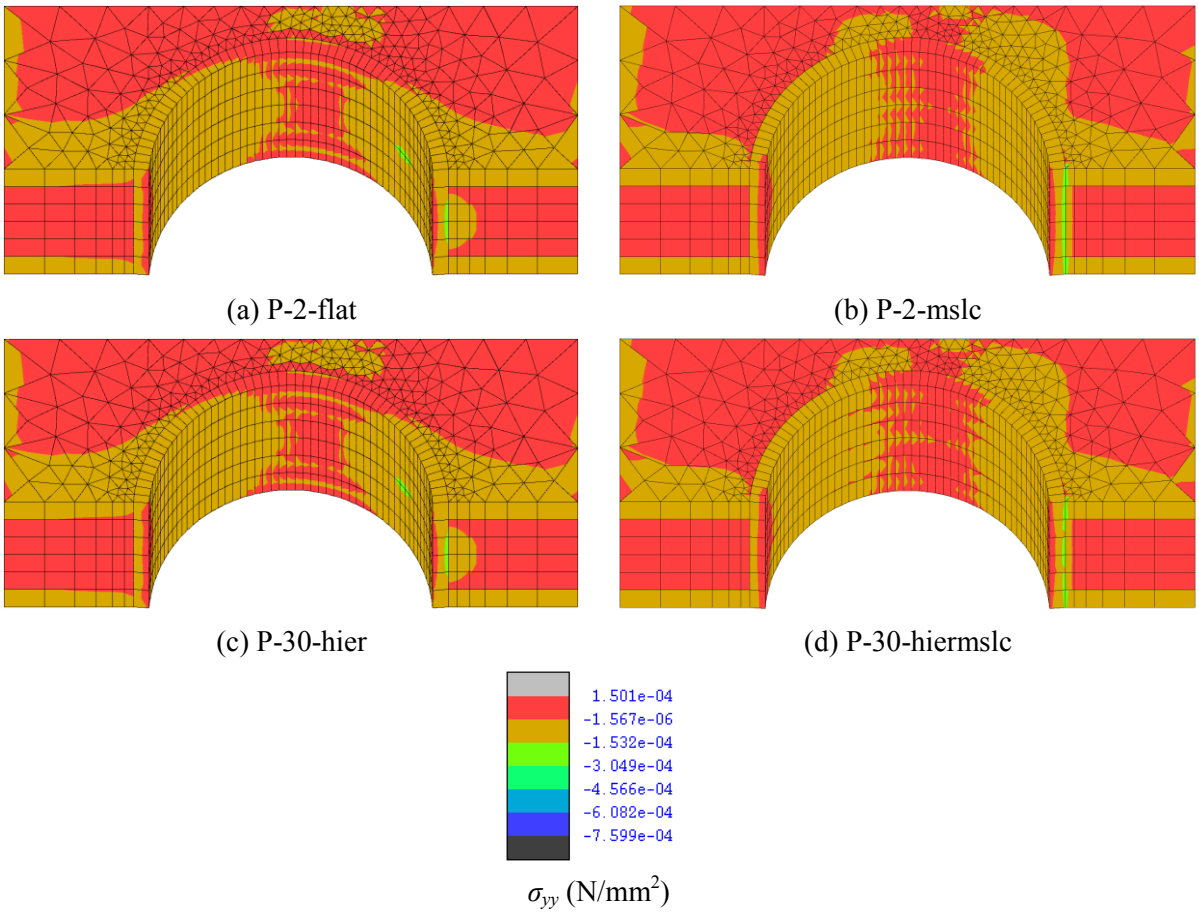

Figure 6-52: Normal stress distribution along the vertical direction at the last step of analysis

6.4 Conclusions

In this chapter the accuracy and potential of the proposed detailed modelling strategy for masonry arch bridges has been shown. Initially a simplified and efficient strip-model, developed assuming rigid spandrel walls, has been used in the numerical-experimental comparisons of the structural response of a brick-masonry bridge in terms of the ultimate loading capacity and initial stiffness. It has been shown that the proposed model enables an accurate prediction of the cracking in the arch, and to capture the actual collapse mechanism providing a good prediction of the initial stiffness and the load capacity. In this respect the contribution of the backfill is critical, where an explicit modelling of the backfill domain including its elastic and plastic characteristics is required to achieve realistic results. Moreover it has been found that also the representation of the physical interface between the arch and the fill plays a significant role, and an adequate nonlinear description allowing for separations and plastic sliding should be used for taking into account its contribution.

The strip-model has been used in parametric studies to analyse the influence of the backfill material and brickwork parameters on the response, and the effects of the loading position, the geometrical characteristics of the arch and potential movement at the abutment. It has been found that a variation of the fill parameters within realistic limits can lead to a significant change of the initial stiffness and the ultimate load, but not in the collapse mechanism. On the other hand, defects in the brickwork may cause more substantial changes in the response, where the cracking pattern is governed by ring separation which leads to a notable reduction of the load capacity. As for brick-masonry arches (see Chapter 5), the loading position and the arch shape influence the development and location of the cracks in the arch, where ring separation can occur in shallow arches also with good quality brickwork. Different failure mechanisms induced by movements at the abutment have also been investigated, finding that they are associated with a different number and position of radial cracks, and that these mechanisms generally show a more ductile response when compared

with the failure behaviour of masonry arches caused by support movements which is more brittle.

Full 3D analyses have been performed considering an accurate 3D description for the bridge. Due to the significant computational cost, and the limit in the computing time (60 hours), the numerical simulations did not allow the investigation of the failure mechanism. However they provided significant information on the interaction between the different bridge components leading to a complex longitudinal and transverse response.

Finally the computational efficiency guaranteed by the use of different partitioning strategies has been investigated. As in the case of masonry arches, it has been found that the use of master-slave coupling at partitioned boundaries provides the highest speed-up but it introduces errors mainly in the stress distribution. In the case of masonry arch bridges, the use of master-slave coupling may introduce more errors because the arch-fill interaction is dominated by the behaviour of interface elements between the arch and the fill which cannot be replaced using rigid connection. Thus further research should be carried out to enhance the speedup of the proposed advanced modelling technique in analysing large masonry arch bridges.

CHAPTER 7

Conclusions and Future Work

7.1 Introduction

Previous experimental research (e.g. Page, 1993; Hendry et al., 1986b) conducted to study the behaviour of masonry bridges under static loading showed that the response up to collapse derives from a 3D interaction between the different structural and non-structural components, eventually leading to the collapse of the arch barrel. Current practical assessment methods founded upon the elastic (e.g. Pippard & Chitty, 1951) and plastic (e.g. Heyman, 1982) principles and most of the advanced modelling techniques for masonry bridges based upon 1D (e.g. Crisfield, 1984) or 2D (e.g. Choo, Coutie & Gong, 1991b) representations disregard such 3D interaction. Moreover most of previous modelling approaches (e.g. Boothby & Roberts, 2001) describing the 3D geometrical characteristics of masonry bridges employ the macroscopic approach for representing material nonlinearity at the structural scale, thus they do not allow for the specific masonry bond and the consideration of potential defects in the brickwork, which may determine the behaviour of these complex structural systems. To overcome the intrinsic limitations of current response prediction techniques for masonry bridges, this research has been devoted to developing a novel detailed 3D modelling approach for masonry arches and bridges, and the use of this advanced strategy in nonlinear analysis for accurate response predictions. This is to enhance the understanding of the actual response up to collapse, considering different geometrical and material characteristics, loading and

boundary conditions. The research objectives stated in Chapter 1 have been met by completing a research program comprising four main parts, which were described in Chapters 2 to 6. The main results are discussed in the conclusions below, which are then followed by some proposals for future work on the modelling and analysis of masonry arch bridges.

7.2 Conclusions

The main results achieved in this research, which concern (i) the development of an accurate mesoscale description for brick/block-masonry arches, (ii) the nonlinear analysis of masonry arches subject to static loading, (iii) the development of a 3D modelling strategy for masonry bridges and (iv) the nonlinear analysis of realistic masonry bridges under static loading, are discussed below.

7.2.1 Mesoscale description for brick/block-masonry arches

The use of an advanced mesoscale strategy for brick/block-masonry previously developed at Imperial College (Macorini & Izzuddin, 2011) has been considered to overcome the inherent limitations of previous 3D modelling approaches for masonry arches. Solid and nonlinear interface elements are employed to offer an accurate prediction of the development of damage and cracks in the masonry. In the case of large arches, a partitioning approach allowing for parallel computation (Jokhio & Izzuddin, 2013; Jokhio, 2012) is adopted to increase computational efficiency. Moreover a specific geometrical description for skew arches has been developed, considering the rules for the helicoidal method used to build old skew arches in masonry bridges. The accuracy and the effectiveness of the adopted mesoscale modelling approach have been investigated. Experimental-numerical comparisons have been carried out, showing that the proposed numerical description allows for a realistic response prediction up to collapse. The development of damage and the most critical failure mechanisms of multi-ring square and skew arches can be predicted with good accuracy. Besides, parametric studies have been conducted to investigate the influence of the mesoscale

material parameters on the response prediction, and to define the most computationally efficient mesoscale modelling strategy for square and skew arches. Moreover, it has been found that in the case of square arches under line loads applied uniformly across the width of the arch, an efficient strip-model, accounting for the actual masonry bond only on the face of the arch, provides accurate results. On the other hand, when analysing skew arches a "full" 3D description describing the actual 3D masonry bond should be considered for accurate response predictions. Finally, the efficiency provided by different partitioning schemes has been assessed. Significant speed-ups have been obtained when a large number of partitions and master-slave coupling (Jokhio, 2012) at the partition boundaries are used. In this case, as opposed to the use of standard flat or hierarchic partition techniques, some local errors, especially in the stress distribution at the partition boundaries, may affect the numerical results.

7.2.2 Nonlinear analysis of brick/block-masonry arches

The response up to collapse of square and skew brick-masonry arches has been investigated using the proposed mesoscale description, and considering the effects of (i) rise-to-span ratio, (ii) loading position, (iii) masonry bond and defects in the brickwork, (iv) abutment stiffness and (iv) support movements. It has been found that the rise-to-span ratio considerably influences the response. Deep arches or arches with an intermediate rise-to-span ratio, such as 1:4, generally show a typical four hinge mechanism, while shallow arches typically with rise-to-span ratio smaller than 1:8 may fail by a combination of radial cracks and ring separation. Moreover the failure mode strongly depends upon the load position, as line loads close to the springings may induce a brittle collapse also for arches with high rise-to-span ratio. It has also been shown that defects (e.g. weak material, mortar debonding) in the brickwork generally lead to ring separation even at very low loading levels. On the contrary, in masonry arches without defects, ring separation can be rarely found. Further analyses have confirmed that brick-masonry arches can support live loads also after the formation of a

mechanism due to differential support movements. This additional load bearing capacity depends upon the mount of abutment displacement.

7.2.3 Mesoscale description for brick-block-masonry bridges

According the proposed modelling strategy for masonry bridges, the mesoscale modelling technique for masonry arches described before has been coupled with an effective nonlinear modelling description for the backfill and the arch-backfill interaction. In this respect, an accurate and robust elasto-plastic model for soil material has been selected and implemented into ADAPTIC (Izzuddin, 1991). This is used within a continuum description with solid elements to represent the backfill and the lateral walls. The arch-backfill interaction is modelled by nonlinear interface elements, which consider the frictional characteristics of the physical interface between the arch and the fill. As before, to improve computational efficiency, the detailed 3D description is incorporated within a partitioned approach developed previously at Imperial College (Jokhio & Izzuddin 2013; Jokhio, 2012).

7.2.4 Nonlinear analysis of brick-masonry bridges

The accuracy of the proposed detailed modelling strategy for masonry arch bridges has been checked in numerical-experimental comparisons. Initially, simplified and efficient strip-models have been used. It has been shown that the proposed modelling approach enables an accurate prediction of cracking in the arch and the actual collapse mechanism, providing a good prediction of the initial stiffness and the load capacity. In this respect the contribution of the backfill is critical, where an explicit modelling of the backfill domain including its elastic and plastic characteristics is required to achieve realistic results. The strip-model has been used in parametric studies to analyse the influence of the backfill material and brickwork parameters on the response, and the effects of the loading position, the geometrical characteristics of the arch and potential movement at the abutment. It has been shown that defects in the brickwork may cause substantial changes in the response,

where the cracking pattern is governed by ring separation which leads to a notable reduction of the load capacity. Different failure mechanisms induced by movements at the abutment have been investigated, finding that they are associated with a different number and position of radial cracks. Full 3D analyses have been performed considering an accurate 3D description for the bridge. These have shown the 3D effects including a non-uniform distribution of stresses along the arch width under static loading confirming the potential of the proposed modelling strategy for a realistic response prediction.

7.3 Future work

Further research is required toward the definition of efficient and accurate numerical strategies for representing the complex response of masonry arch bridges. This comprises experimental and numerical research. Additionally, the proposed advanced modelling approach could be used as a substitute for experimental tests towards the enhancement and calibration of existing practical assessment methods for masonry arches and bridges.

7.3.1 Experimental work

Previous experimental programs on masonry bridges did not provide detailed information on the mechanical characteristics of the component materials. In future experimental research, experimental tests on masonry arch and bridges should be coupled with specific material tests providing detailed information on the “mesoscale” material properties. This will allow a more effective validation of the proposed modelling approach. Additionally, specific experimental techniques to be used on site on existing structures should be developed again to obtain mesoscale material parameters. This will allow the use of the proposed numerical strategy for an accurate analysis of existing structural systems.

7.3.2 Numerical research

According the present research, arch-fill interaction has significant influence on the overall behaviour of masonry arch bridges. In the proposed 3D model for masonry arch bridges, nonlinear interface elements are employed at the physical arch-fill interface. However, this technique requires perfectly matching meshes for the two domains at their actual interface. This renders the FE mesoscale representation for bridges with skewed arch barrels impractical. To overcome this intrinsic limitation, contact mechanics techniques enabling the representation of frictional contact between two domains with non-matching meshes could be used. Moreover, as the use of the partitioning approach for the analysis of masonry arch bridges has provided increased computational efficiency with relatively low speed-up, further research is required to improve this advanced modelling strategy especially when applied to the analysis of complex systems as masonry bridges.

REFERENCES

Abbo, A. J. (1997) *Finite element algorithms for elastoplasticity and consolidation.* PhD Thesis. University of Newcastle.

Abbo, A. J. & Sloan, S. W. (1995) A smooth hyperbolic approximation to the Mohr-Coulomb yield criterion. *Computers & Structures.* 54 (3), 427-441.

Agrawal, S. R. (1973) Survey and Tabulation Method of Assessment and Strengthening of Masonry Arch Bridges. *Journal of the Institution of Engineers (INDIA).* 53, 148.

Ashour, A. F. & Garrity, S. W. (1998) An upper bound analysis for the strength assessment of masonry arch bridges. *Arch Bridges–History, analysis, assessment, maintenance and repair, Proc. Second Int. Arch Bridge Conference.* pp.139-146.

Azevedo, J. & Sincraian, G. (2001) Modelling the seismic behaviour of monumental masonry structures. *International Millennium Congress Archi 2000. September 10-12, Paris, France.* UNESCO. pp.498-504.

Barlow, W. H. (1846) The existence of the line of equal horizontal thrust in arches, and the mode of determining it. *Proceedings of the ICE.* Paper No.728.

Bathe, K. J. (1996) *Finite element procedure.* Upper Saddle River, New Jersey, Prentice Hall.

Beare, M. (1993) Bridges: repairing old and new. *Construction Repair.* 7 (1), 6-8.

Boothby, T. E. & Roberts, B. J. (2001) Transverse behaviour of masonry arch bridges. *Structural Engineer.* 79 (9), 21-26.

Boothby, T. E. (2001) Load rating of masonry arch bridges. *Journal of Bridge Engineering.* 6 (2), 79-86.

Brencich, A. (2009) Assessment of Masonry Bridges: Numerical and Theoretical Approaches, Trends in Civil and Structural Engineering Computing. In: Topping, B. H. V., Costa Neves, L.

F. & Barros, R. C. (eds.). *CSETS: 22 Trends in Civil and Structural Engineering Computing.* Stirlingshire, Scotland, Saxe-Coburg Publications.

Brencich, A. & Colla, C. (2002) *The influence of construction technology on the mechanics of masonry railway bridges.* Crowthorne, UK, Transport Research Laboratory. Report number: 17.

Brencich, A. & De Francesco, U. (2006) Closure to "Assessment of Multispan Masonry Arch Bridges. I: Simplified Approach" by Antonio Brencich and Ugo De Francesco. *Journal of Bridge Engineering.* 11 (2), 259-261.

Brencich, A. & Morbiducci, R. (2007) Masonry arches: historical rules and modern mechanics. *International Journal of Architectural Heritage.* 1 (2), 165-189.

Brocks, W., Cornec, A. & Scheider, I. (2003) Computational aspects of nonlinear fracture mechanics. In: Milne, I., Ritchie, R. O. & Karihaloo, B. (eds.). *Comprehensive Structural Integrity - Numerical and Computational Methods.* Oxford, Elsevier. pp. 127-209.

Castigliano, C. A. P. (1879) *Theorie de l'equilibre des systemes elastiques et ses applications. [Elastic stresses in structures]* Trans. Andrews. London, Scott Greenwood and Son.

Cavicchi, A. & Gambarotta, L. (2007) Lower bound limit analysis of masonry bridges including arch–fill interaction. *Engineering Structures.* 29 (11), 3002-3014.

Cavicchi, A. & Gambarotta, L. (2005) Collapse analysis of masonry bridges taking into account arch–fill interaction. *Engineering Structures.* 27 (4), 605-615.

Chen, W. & Baladi, G. Y. (1985) *Soil plasticity :theory and implementation.* Developments in geotechnical engineering. Amsterdam; Oxford, Elsevier.

Chisari, C., Macorini, L., Amadio, C. & Izzuddin, B. A. (2013) Identification of Brick-Masonry Material Properties Through Inverse Analysis and Genetic Algorithms. In: Topping, B. H. V. & Iványi, P. (eds.) *Proceedings of the Fourteenth International Conference on Civil, Structural and Environmental Engineering Computing. September 3-9, Cagliari - Sardinia - Italy.* Stirlingshire, UK, Civil-Comp Press.

Choo, B. S., Coutie, M. G. & Gong, N. G. (1991a) The effect of cracks on the behaviour of masonry arches. *Proceedings of the 9th International Brick/Block Masonry Conference. Berlin.* pp.948-955.

Choo, B. S., Coutie, M. G. & Gong, N. G. (1991b) Finite-element analysis of masonry arch bridges using tapered elements. *ICE Proceedings.* 91 (4), 755-770.

Choo, B. S., Coutie, M. G. & Gong, N. G. (1990a) Analysis of masonry arch bridges by a finite element method. *Proc. of 4th Rail Bridge Centenary International Conference. Edinburgh.* pp.381-392.

Choo, B. S., Coutie, M. G. & Gong, N. G. (1990b) The application of the finite element method to the study of cracking in masonry arch bridges. *Proc. of the International Congerence on Applied Stress Analysis. Nottingham.* pp.476-785.

Choo, B. S. & Gong, N. G. (1995) Effect of skew on the strength of the masonry arch bridges. In: Melbourne, C. (ed.) *Arch Brides: Proceedings of the First International Conference of Arch Bridges. 3-6 September, Bolton, UK.* London, Thomas Telford. pp.205-214.

Corradi, M. (1998) Empirical methods for the construction of masonry arch bridges in the 19th century. In: Sinopoli, A. (ed.).*Arch Bridges: History Analysis Assessment Maintenance and Repair.* Rotterdam, Netherlands, A.A. Balkema. pp. 25-36.

Crisfield, M. A. (1985a) Computer methods for the analysis of masonry arches. *Proc 2nd Int Conference on Civil and Structural Engineering Computing. December, London.* Edinburgh, Civil-Comp Press.

Crisfield, M. A. (1984) *A finite element computer program for the analysis of masonry arches.* Crowthorne, Transport Research Laboratory. Report number: Laboratory Report 1115.

Crisfield, M. A. & Packham, A. J. (1987) *A mechanism program for computing the strength of masonry arch bridges.* Crowthorne, Transport Research Laboratory. Report number: Research Report 124.

Crisfield, M. A. & Wills, J. (1986) Nonlinear analysis of concrete and masonry sutrctures. In: Bergan et al (ed.).*Finite element methods for nonlinear problems.* Berlin, Springer-Verlag. pp. 639-652.

Crisfield, M. A. Transport Research Laboratory (ed.) (1985b) *Finite eleement and mechanism methods for the analysis of masonry and brickwork arches.* Crowthorne, Transport Research Laboratory. Report number: Research Report 19.

Da Porto, F., Guidi, G., Garbin, E. & Modena, C. (2010) In-plane behavior of clay masonry walls: experimental testing and finite-element modeling. *Journal of Structural Engineering.* 136 (11), 1379-1392.

Davey, N. (1953) *Testing on road bridges.* Research Paper No.16, National Building Studies. London: HMSO, Her Majesty's Stationery Office.

Davey, N. (1949) Structural Engineering International. *Journal of the International Association for Bridge and Structural Engineering.* 9 (1).

Davey, N. (1947) *Testing of Highway Bridges.* Public Works, Roads and Transport Congress, S.l., s.n.

Dawe, D. (1974a) Curved finite elements for the analysis of shallow and deep arches. *Computers & Structures.* 4 (3), 559-580.

Dawe, D. (1974b) Numerical studies using circular arch finite elements. *Computers & Structures.* 4 (4), 729-740.

De Salvo, G. J., Gorman, R. W. & Imgrund, M. C. (1987) *ANSYS: Engineering Analysis System. User's Manual.* , Swanson Analysis Systems, Incorporated.

Department of Transport. (2001) Section 4, Part 4, BA 16/97 Amendment No.2, The assessment of highway bridges and structures. In: Anonymous *Design Manual for Roads and Bridges: Volume 3 Highway structures: Inspection and maintenance.* London, Department of Transport.

Drucker, D. C. & Prager, W. (1952) Soil mechanics and plastic analysis for limit design. *Quarterly of Applied Mathematics.* 10 (2), 157-165.

Dym, C. L. & Williams, H. E. (2011) Stress and displacement estimates for arches. *Journal of Structural Engineering.* 137 (1), 49-58.

Fairfield, C. A. & Ponniah, D. A. (1994) Model tests to determine the effect of fill on buried arches. *Proceedings of the ICE-Structures and Buildings.* 104 (4), 471-482.

Fairfield, C. A. & Ponniah, D. A. (1993) Geotechnical considerations in arch bridge assessment. *Highways & Transportation.* 40 (9), 11-15.

Fanning, P. J., Boothby, T. E. & Roberts, B. J. (2001) Longitudinal and transverse effects in masonry arch assessment. *Construction and Building Materials.* 15 (1), 51-60.

Fanning, P. J. & Boothby, T. E. (2001) Three-dimensional modelling and full-scale testing of stone arch bridges. *Computers & Structures.* 79 (29), 2645-2662.

Finite Element Analysis Ltd. (1993) *LUSAS user manual* (Version 12) Kingston upon Thames.

Ford, T., Augarde, C. & Tuxford, S. (2003) Modelling masonry arch bridges using commercial finite element software. *9th International Conference on Civil and Structural Engineering Computing, Egmond aan Zee, The Netherlands.* pp.2-4.

George, W. B. (1880) *A Practical and Theoretical Essay on Oblique Bridges.* Third edition. London, Crosby Lockwood.

Geuzaine, C. & Remacle, J. (2009) Gmsh: A 3-D finite element mesh generator with built-in pre-and post-processing facilities. *International Journal for Numerical Methods in Engineering.* 79 (11), 1309-1331.

Gilbert, M. (1993) *The behaviour of masonry arch bridges containing defects.* PhD Thesis. University of Manchester.

Gilbert, M. (2001) RING: a 2D rigid-block analysis program for masonry arch bridges. In: Abdunur, C. (ed.) *Proc. 3rd International Arch Bridges Conference. Paris.* pp.459-464.

Gilbert, M. & Melbourne, C. (1998) On the analysis of multi-ring brickwork arch bridges. *Proc. 2nd International Arch Bridges Conference, Venice.* pp.109-118.

Gilbert, M., Melbourne, C. & Smith, C. (2006) Discussion of "Assessment of Multispan Masonry Arch Bridges. I: Simplified Approach" by Antonio Brencich and Ugo De Francesco. *Journal of Bridge Engineering.* 11 (2), 257-259.

Gilbert, M. & Melbourne, C. (1994) Rigid-block analysis of masonry structures. *Structural Engineer.* 72 (21), 356-361.

Gramsammer, J. C., Kerzreho, J. P. & Odeon, H. (1999) The LCPC's APT Facility: Evaluation of Fifteen Years of Experimentations. *Proceedings of the 1st International Conference on Accelerated Pavement Testing. October, Reno, Nevada.* pp.18-20.

Hamilton, S. B. (1952) The historical development of structural theory. *ICE Proceedings: Engineering Divisions.* 1 (6), 374-402.

Harvey, B. (2004) Skew arch behaviour. *Structural Engineer.* 82 (5), 13-15.

Harvey, W. J. (1988) Application of the mechanism analysis to masonry arches. *The Structural Engineer.* 66 (5), 77-84.

Hendry, A. W., Davies, S. R., Royles, R., Ponniah, D. A., Forde, M. C. & Komeyli-Birjandi, K. (1986a) *Load test to collapse on a masonry arch bridge at Bargower, Strathclyde.* Crowthorne, U.K., Transport and Road Research Laboratory Department of Transport, TRL. Report number: Contractor Rep. No. 26.

Hendry, A. W., Davies, S. R. & Royles, R. (1985) *Test on stone masonry arch at Bridgemill - Girvan.* Crowthorne, Transport Research Laboratory. Report number: Contractor Report 7.

Hendry, A. W., Davies, S. R., Royles, R., Ponniah, D. A., Forde, M. C. & Komeyli Birjandi, F. (1986b) *Load test to collapse on a masonry arch brtidge at Bargower, Strathclyde.* Crowthorne, Transport Research Laboratory. Report number: Contractor Report 26.

Heyman, J. & Pippard, A. J. S. (1980) The estimation of the strength of masonry arches. *ICE Proceedings.* 69 (4), 921-937.

Heyman, J. (1982) *The masonry arch.* Chichester, UK, Ellis Horwood.

Heyman, J. (1969) The safety of masonry arches. *International Journal of Mechanical Sciences.* 11 (4), 363-385.

Hodgson, J. A. (1996) *The behaviour of skewed masonry arch bridges.* PhD Thesis. University of Salford.

Hughes, T. G. & Blackler, M. J. (1997) A review of the UK masonry arch assessment methods. *Proceedings of the ICE-Structures and Buildings.* 122 (3), 305-315.

Izzuddin, B. A. (1991) *Nonlinear dynamic analysis of framed structures.* PhD Thesis. Imperial College London (University of London).

Jokhio, G. A. (2012) *Mixed dimensional hierarchic partitioned analysis of nonlinear structural systems.* PhD Thesis. Department of Civil and Environmental Engineering, Imperial College London.

Jokhio, G. A. & Izzuddin, B. A. (2013) Parallelisation of nonlinear structural analysis using dual partition super elements. *Advances in Engineering Software.* 60, 81-88.

Jokhio, G. A. & Izzuddin, B. A. (2011) Parallelisation of nonlinear structural analysis using dual partition super-elements. *PARENG2011. April 12-15, Ajaccio, Corsica, France.*

Larnach, W. J. (1987) *Report on an investigation into the basis of the "MEXE" method for the assessment of the load carrying capacity of masonry arch bridges.* Christchurch, Royal Armament Research and Development Establishment. Report number: Contract Report.

LimitState Ltd. (2011) *Technical Note - The Influence of Arch Shape on masonry Arch Bridge Capacity* (LimitState: RING 3.0) LimitState Ltd.

Livesley, R. K. (1992) A computational model for the limit analysis of three-dimensional masonry structures. *Meccanica.* 27 (3), 161-172.

Livesley, R. (1978) Limit analysis of structures formed from rigid blocks. *International Journal for Numerical Methods in Engineering.* 12 (12), 1853-1871.

Loo, Y. C. & Yang, Y. (1991a) Cracking and failure analysis of masonry arch bridges. *Journal of Structural Engineering.* 117 (6), 1641-1659.

Loo, Y. C. & Yang, Y. (1991b) Tensile Strength, Strain Softening and the Failure analysis of Masonry Arch Bridges. In: Cheung, Lee & Leung (eds.). *Computational Mechanics.* Balkema, Rotterdam.

Lourenço, P. B. (1996) *Computational strategies for masonry structures.* PhD Thesis. Delft University of Technology.

Lourenço, P. B. & Rots, J. G. (1997) Multisurface interface model for analysis of masonry structures. *Journal of Engineering Mechanics.* 123 (7), 660-668.

Macorini, L. & Izzuddin, B. A. (2014) Nonlinear Analysis of Unreinforced Masonry Walls under Blast Loading Using Mesoscale Partitioned Modelling. *Journal of Structural Engineering.* 140 (Special issue: Computational Simulation in Structural Engineering, A4014002), 1-10.

Macorini, L. & Izzuddin, B. A. (2013a) Enhanced Mesoscale Partitioned Modelling for Unreinforced Masonry Structures. *Proceedings of the 14th International Conference on Civil, Structural and Environmental Engineering Computing. September 3-6, Cagliari - Sardinia - Italy.* Stirlingshire, UK, Civil-Comp Press. Paper 63.

Macorini, L. & Izzuddin, B. A. (2013b) Nonlinear analysis of masonry structures using mesoscale partitioned modelling. *Advances in Engineering Software.* 60, 58-69.

Macorini, L. & Izzuddin, B. A. (2011) A non-linear interface element for 3D mesoscale analysis of brick-masonry structures. *International Journal for Numerical Methods in Engineering.* 85 (12), 1584-1608.

McKibbins, L. D., Melbourne, C., Sawar, N. & Sicilia Gaillard, C. (2006) *Masonry arch bridges: condition appraisal and remedial treatment.* CIRIA C656. London, CIRIA.

Melbourne, C. (1998) The collapse behaviour of a multi-span skewed brickwork arch bridge. In: Sinopoli, A. (ed.).*Arch Bridges: History Analysis Maintenance and Repair.* Rotterdam, Netherlands, A. A. Balkema. pp. 289-294.

Melbourne, C. & Gilbert, M. (1995) The behaviour of multi-ring brickwork arch bridges. *Structural Engineer.* 73 (3), 39-47.

Melbourne, C. & Tomor, A. K. (2004) Fatigue Performance of Composite and Radial-pin reinforcement on Multi-ring Masonry Arches. Proceedings of the 4th conference on arch bridges. *Arch'04. November 17-19, Barcelona ,Spain.* pp.427-433.

Melbourne, C. & Walker, P. J. (1989) *Load test to collapse on a full scale model six metre span brick arch bridge.* Crowthorne, Transport Research Laboratory. Report number: Research Report 189.

Melbourne, C., Wang, J. & Tomor, A. K. (2007) A new masonry arch bridge assessment strategy (SMART). *Proceedings of the ICE-Bridge Engineering.* 160 (2), 81-87.

Melbourne, C., Gilbert, M. & Wagstaff, M. (1995) The behaviour of multi-span masonry arch bridges. *Proceedings of the 1st International Conference on Arch Bridges, Arch Bridges. 3-6, September, Bolton, UK.*

Melbourne, C. & Hodgson, J. (1995) The behaviour of skewed brickwork arch bridges. *Arch Bridges: Proceedings of the First International Conference of Arch Bridges.* pp.309-320.

Melbourne, C., Wang, J., Tomor, A., Holm, G., Smith, M., Bengtsson, P. E., Bien, J., Kaminski, T., Rawa, P., Casas, J. R., Roca, P. & Molins, C. (2007) *Masonry Arch Bridges Background document D4.7.* Sustainable Bridges. Report number: Deliverable D4.7.

Milani, G. & Lourenço, P. B. (2012) 3D non-linear behavior of masonry arch bridges. *Computers & Structures.* 110–111 (0), 133-150.

Moseley, H. (1835) Equilibrium of the arch. *Transactions of the Cambridge Philosophical Society.* 5, .

Navier, C. L. M. H. (1833) *Resume des lecons donnees a l'Ecole des ponts et Chaussees Sur l'aplication de la mecanique a l'etablissement des constructions et des machines.* Second edition. Paris, Carilian-Goery.

Nayak, G. & Zienkiewicz, O. (1972) Convenient form of stress invariants for plasticity. *Proceedings of ASCE,JSD.* 98, 949-953.

Ng, K. H., Fairfield, C. A. & Sibbald, A. (1999) Finite element analysis of masonry arch bridges. *Proceedings of the ICE Structures and Buildings.* 134 (2), 119-127.

Ning, J. & O, Y. (2008) Numerical simulation research of microcosmic flaws in masonry arch bridge. *Journal of Communication & Computer.* Vol. 5 (Issue 10), p18.

Oliveira, D. V. (2003) *Ph.D. Thesis: Experimental and numerical analysis of blocky masonry structures under cyclic loading.* PhD Thesis. University of Minho.

Page, A. W. (1981) The biaxial compressive strength of brick masonry. 71 (3), 893-906.

Page, J. (1989) *Load tests to collapse on two arch bridges at Strathmashie and Barlae.* Crowthorne, Transport Research Laboratory. Report number: Research Report 201.

Page, J. (1987) *Load tests to collapse on two arch bridges at Preston, Shropshire and Prestwood, Staffordshire.* Crowthorne, Transport Research Laboratory. Report number: Research Report 110.

Page, J. (1993) *TRL State of the Art Review: Masonry Arch Bridges.* London, UK, Her Majesty's Stationery Office.

Pippard, A. J. S. & Baker, J. F. (1968) *The analysis of engineering structures.* Fourth edition. US, American Elsevier Pub. Co.

Pippard, A. J. S. & Chitty, L. (1951) *A study of the voussoir arch.* London, Her Majesty's Stationery Office. Report number: Research Paper 11, National Building Studies.

Pippard, A. J. S. & Chitty, L. (1941) Repeated load tests on a voussoir arch. *Proc. ICE.* pp.79-86.

Pippard, A. J. S., Tranter, E. & Chitty, L. (1936) The mechanics of the voussoir arch. *Journal of the ICE.* 4 (2), 281-306.

Ponniah, D. A., Fairfield, C. A. & Prentice, D. J. (1997) Fill stresses in a new brick arch bridge subject to heavy axle-load tests. *Proceedings of the ICE-Structures and Buildings.* 122 (2), 173-185.

Potts, D. M. & Zdravkovic, L. (2001) *Finite Element Analysis in Geotechnical Engineering: Theory and Application.* London, UK, Thomas Telford Ltd.

Prentice, D. J. & Ponniah, D. A. (1996) New techniques in the elastic analysis of arch bridges using image processing. *Strain.* 32 (4), 139-144.

Rankine, W. J. M. (1862) *Civil engineering and applied mechanics.* London, Charles Griffin Co.

Rodriguez-Villares, A. (2014) *Analysis of large complex masonry structures using nonlinear interface elements and partitioned modelling.* MEng Dissertation. Imperial College London.

Rots, J. G. (1997) *Structural Masonry: An Experimental/Numerical Basis for Practical Design Rules (CUR Report 171).* Abingdon, Taylor & Francis.

Rouf, M. A. (1984) *Fundamental properties of brickwork with particular emphasis to brickwork arches.* PhD Thesis. University of Liverpool.

Royles, R. & Hendry, A. W. (1991) Modal tests on masonry arches. 91 (2), 299-321.

Simo, J. C. & Hughes, T. J. R. (1998) *Computational inelasticity.* New York, Springer.

Strand7 Pty Ltd. (2010) *Strand7 manual* (Edition 3) Strand7 Pty Ltd.

Sunley, V. K. (1990) The experimental investigation of defects. In: Sowden, A. M. (ed.).*The maintenance of brick and stone masonry structures.* , Taylor & Francis. pp. 62-80.

Thavalingam, A., Bicanic, N., Robinson, J. I. & Ponniah, D. A. (2001a) Computational framework for discontinuous modelling of masonry arch bridges. *Computers & Structures.* 79 (19), 1821-1830.

Thavalingam, A., Bicanic, N., Robinson, J. & Ponniah, D. (2001b) Computational framework for discontinuous modelling of masonry arch bridges. *Computers & Structures.* 79 (19), 1821-1830.

Towler, K. D. S. (1985) Applications of non-linear finite element codes to masonry arches. *Proceedings of the 2nd International Conference on Civil and Structural Engineering Computing. London.* Edinburgh, UK, Civil-Comp Press. pp.197-202.

Towler, K. D. S. & Sawko, F. (1982) Limit state behaviour of brickwork arches. *Proceedings of the 6th International Brick Masonry Conference. May, Rome.*

Walker, P. & Melbourne, C. (1988) Load tests to collapse of model brickwork masonry arches. *Proceedings of the 8th International Brick and Block Masonry Conference. January 1, Dublin, Eire.*

Wang, J. (2004) *The three-dimensional behaviour of masonry arches.* PhD Thesis. University of Salford.

Wang, J., Haynes, B. J. & Melbourne, C. (2013) A comparison between the MEXE and Pippard's methods of assessing the load carrying capacity of masonry arch bridges. Proceedings of the 7th International Conference on Arch Bridges. *ARCH'13. October 4-6, Trogir-Split, Croatia.* SECON-CSSE, Zagred, Croatia. pp.589-596.

Zienkiewicz, O., Humpheson, C. & Lewis, R. (1975) Associated and non-associated visco-plasticity and plasticity in soil mechanics. *Geotechnique.* 25 (4), 671-689.